Characterization of Low-dimensional Structures by Advanced Transmission Electron Microscopy

PROEFSCHRIFT

Ter verkrijging van de graad van doctor
aan de Technische Universiteit Delft,
op gezag van de Rector Magnificus Prof. ir. K.C.A.M. Luyben,
voorzitter van het College voor Promoties,
in het openbaar te verdedigen op
donderdag 9 juni 2011 om 10:00 uur

Door

Emrah YÜCELEN

Master of Science in Materials Science & Engineering
Christian-Albrechts Universität zu Kiel, Duitsland
Geboren te Istanbul, Turkije

Dit proefschrift is goedgekeurd door de promotor:
Prof. dr. H. W. Zandbergen

Samenstelling promotiecommissie:

Rector Magnificus	voorzitter
Prof. dr. H.W. Zandbergen	Technische Universiteit Delft, promotor
Prof. dr. C. Pappas	Technische Universiteit Delft
Prof. ir. L.M.K. Vandersypen	Technische Universiteit Delft
Prof. dr. H.W.M. Salemink	Technische Universiteit Delft
Prof. ir. T. J.H. Vlugt	Technische Universiteit Delft
Prof. dr. R.E. Dunin-Borkowski	Rheinisch-Westfälische Technische Hochschule Aachen
Dr. B. Freitag	FEI Electron Optics BV

Contents

Chapter 1

General Introduction

This is a general introduction to the experimental and theoretical methods used in this thesis. It will explain the arc-melting method for alloy production and the conditions for heat treatment. It will also discuss the importance of specimen preparation for transmission electron microscopy. Moreover, a brief introduction to transmission electron microscopy will be given and the methodology used to identify unknown structures will be described. Finally, principles of ab-initio quantum mechanical calculations will be explained briefly.

1.1 Introduction

Low-dimensional structures occur in many forms. Interfaces in bulk materials and in thin films are classical examples of low-dimensional structures. An interface connects two crystal of the same or different compositions and can extend in two-dimensions (planar) or one-dimension (line). Grain boundaries are the most common interface encountered in crystalline materials. The atomic configurations at grain boundaries will be determined by the degree of mismatch. Such a mismatch can occur at grain boundaries of the same compound due to rotation of the two adjacent grains, boundary planes and the relative displacement of the two grains. In the case of dissimilar compounds the interface can be more complex due to the difference between two unit cells.

Another important type of interface in materials is a boundary between constituent phases. Precipitate-matrix interfaces are such interfaces between dissimilar compounds. They can be considered as similar to interfaces in epitaxial thin films (or quantum heterostructures) often having a special relationship with the matrix. A more recent addition to low-dimensional structures is the class of materials that exists in two-dimensions as a sheet with the thickness of the sheet being only one atom thick. Isolated layers of graphite (known as graphene) and hexagonal Boron Nitride is a well-known example of such structures [1,2].

There has been much interest in low dimensional structures from both fundamental and applied points of view. Atomic configurations of grain boundaries, precipitate/matrix interfaces and thin films show a strong anisotropic character and thus have important consequences on the properties of the materials [3]. For example, precipitate/matrix interfaces determine the strength of the materials by resisting against the movement of dislocations [4]. In semiconductor heterostructures the movement of charge carriers can be confined to regions of lower dimensions [5]. This enables the production of short-wavelength light emitting diodes and semiconductor based lasers. The ideal graphene sheet shows excellent electronic mobility and only by confining the graphene sheets into a nanoribbon one can create a band gap. However the properties of graphene can be modified by creating

nanoribbons. Depending also on the atomic structure of nanoribbon edges, these nanoribbons can show either metallic or semiconductor behavior [6].

In order to understand the properties of these materials it is important to characterize their structure and composition at the highest level of resolution. Since its discovery, Transmission Electron Microscopy, TEM, has evolved to an ultimate characterization tool providing chemical and structural information at atomic resolution. The introduction of aberration correctors together with enhanced stability greatly improved the resolution and the precision of TEM. These new instruments allow the use of lower accelerating voltages such that beam sensitive materials can be imaged without destroying the structure as visible at atomic resolution.

This thesis presents a study of atomic configuration analysis of various low-dimensional structures by advanced transmission electron microscopy techniques; it is organized in two parts. The first part, Chapters 2 to 5, describes the microstructure of several aluminum alloys and nanoprecipitates in these alloys. The main focus of these chapters is the atomic scale study of structure of nanoprecipitates and nanoprecipitate/matrix interfaces using high resolution transmission electron microscopy and nano-beam electron diffraction techniques. Understanding the structure of these interfaces allows insight into how these nanoprecipitates grow and change in the aluminum matrix. The second part, Chapter 6[1], describes the optimized conditions for atomic resolution imaging at 80 kV accelerating voltage. These considerations are then applied to the study of the atomic structure of graphene sheets quantitatively. This enables the study of graphene and similar 2-dimensional crystals at atomic resolution and helps to understand the structure of these crystals.

---

[1] Partly Published in *Microscopy Today*, Volume19, Issue 03 May 2011, pp 10 – 14 and in *Carbon*, Volume 49, Issue 2, February 2011, Pages 556-562.

1.2   Alloy Production and Heat Treatments

1.2.1 Alloy Production

This thesis documents a study of binary alloys of Al-Co, Al-Ni and Al-Zr (with Fe). The alloys, which are discussed in Chapters 2 and 3, were received from the Corus R&D department. The alloys were cast in cylindrical steel ingots measuring 2 cm in diameter and 10 cm in height. The Al-Ni and Al-Zr alloys discussed in Chapters 4 and 5 were produced using an arc-melting unit available in the Van der Waals-Zeeman Institute of the University of Amsterdam. Al-Ni alloys were prepared using Al-6wt. % Ni master alloy and 99.999% purity Al. Al-Zr alloys were prepared from 99.999% and the highest-purity Zr available on the market[2]. An overview of alloys, casting methods and shapes is given in Table 1.1.

Table 1.1. Overview of the production method as-cast shape and the compositions (in at. %) of the alloys.

Alloy	Production Method	Cast Shape	Composition
Al-Co (Chapter 2)	Ingot Casting (Corus)	Cylinder	**0.0092 at. % Co, Fe is impurity level** (lower than max solid solubility)
Al-Ni (Chapter 3)	Ingot Casting (Corus)	Cylinder	**0.0092 at. % Ni , Fe is impurity level** (lower than max solid solubility)
Al-Ni (Chapter 4)	Arc-Melting (UvA)	Knob-like	**0.097 at. % Ni, Fe is impurity level**
Al-Zr (Chapter5)	Arc-Melting (UvA)	Knob-like	**0.06 at. % Zr, 0.009 at. % Fe** (lower than max solid solubility)

---

[2] Sigma-Aldrich

The arc-melting technique involves pre-mixing alloying elements and then melting them with the help of an arc emanating from a tungsten tip. The design of the arc-melting unit in the Van der Waals-Zeeman Institute is shown schematically in Fig. 1.1. Pre-mixed elements (hereafter referred to as a "mixture") were melted in 5-cm-wide and 2-cm-deep Cu dishes. Cooling water circulates beneath the dishes to prevent the Cu from melting. A protective argon atmosphere is used to avoid oxidization of the mixture during melting, which is crucial because once oxide layers have formed, they cannot be melted due to the high stability of oxides. Therefore before melting, the experiment chamber is pumped down to a pressure of 10^{-5} torr, then filled with argon gas.
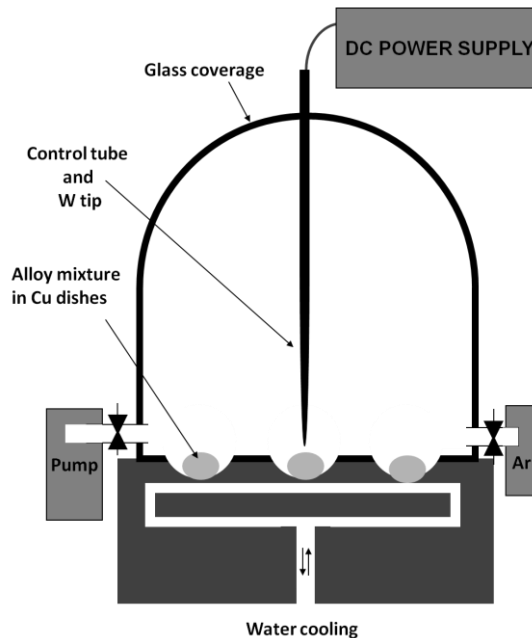

Figure 1.1 Schematic rendition of arc-melting facility in the Van der Waals-Zeeman Institute of the University of Amsterdam.

Heat created by the arc melts the upper part of the mixture, leaving the bottom part not entirely melted because of the water cooling below. Therefore in order to ensure compositional homogeneity of the alloy, the mixtures are re-melted several times from the bottom parts in contact with the water-cooled Cu dish. This process produces knob-shaped samples, illustrated in Fig. 1.2, that are approximately 2 cm wide and 0.8 cm high.

The drawback of knob-shaped alloys is that they do not provide enough samples for different heat treatments, nor for TEM sample preparation. To solve this problem, knob-shaped alloys were deformed into a slab geometry; i.e. they were flattened by a hydraulic press and then cold-rolled as shown in Fig. 1.2.
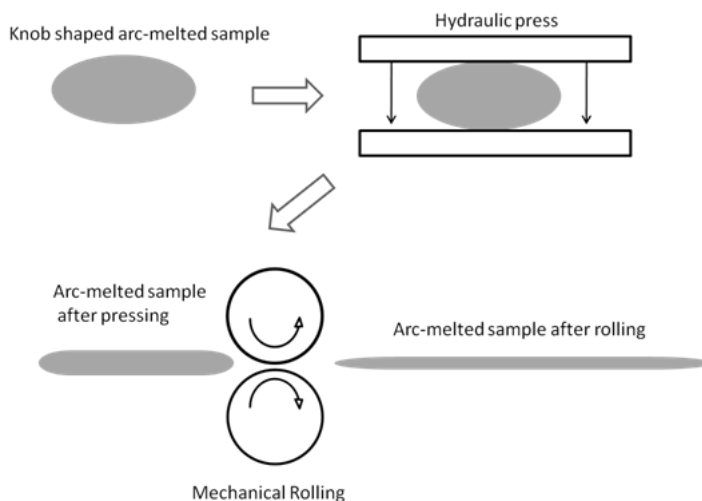

Figure 1.2 The knobs were deformed to slab geometry in a hydraulic press. Sufficiently thin slabs (approx. 3-4 mm) were cold-rolled to produce disks roughly 1.5 mm thickness and approx. 50 mm in diameter. Between the pressing and rolling steps, the alloy was subjected to thermal treatment. This facilitated further deformation of the slab and also enhanced the homogeneity of the alloy.

1.1.2 Heat Treatments

As-cast ingots and arc-melted alloys were homogenized at suitable temperatures to maximize the amount of solute atoms in the solid solution. This treatment is essential to enhance chemical homogeneity and to avoid any possible segregation, which are common characteristics of as-cast alloys. The as-cast microstructure of the alloys studied in this thesis consists of small grains with low-angle grain boundaries due to grain refining effects of Co, Ni and Zr. In addition, the microstructure of heavily deformed arc-melted alloys has a high dislocation density. These factors significantly change the precipitation behavior of the alloy-altering diffusion speeds and provide easy nucleation sites for solute atoms. Therefore the effect of these factors on the

precipitation is avoided after the homogenization treatment, which leads to larger, recrystallized grains.

Owing to the different diffusivity of Zr compared to that of Co and Ni, Al-Zr alloys were homogenized longer [7,8]. The Al-Co and Al-Ni alloys were kept at 20 degrees below the eutectic temperature for 24 hours, i.e. at 913 K and 893 K, respectively. The Al-Zr alloy was kept at 913 K for 120 hours. The homogenized cylindrical ingots were cut into 3-mm-thick disks for annealing. Prior to annealing, the disks were re-homogenized to compensate for possible heating and its effect on the microstructure during mechanical cutting.

After the homogenization treatment, the disks and sheets were quenched in an ice/water mixture to ensure a maximum number of alloying elements in the Al solid solution (see Table1.1). Quenched alloys were heated to various temperatures to obtain precipitation from a solid solution. Overview of annealing temperatures and holding times used for each alloy are presented in Table 1.2.

Table 1.2 Holding times for annealing temperature and alloys.

	473 K	573 K	698 K	823 K
Al-Ni	4 hours	4hours	4 hours	4 hours
Al-Co	-	4 hours	4 hours	4 hours
Al-Zr	-	20 hours	20 hours	-

1.3 Specimen Preparation of Alloys for Transmission Electron Microscopy

The samples to be investigated by transmission electron microscopy (TEM) have to be prepared in such a way that the finished TEM sample should contain electron-transparent regions. For this purpose, a combination of several different thinning methods is applied [9].

The main steps of the TEM specimen preparation procedure of Al alloys employed in this study are presented in Fig. 1.3. The first step is coarse thinning by mechanical

grinding a thin disk of the sample using SiC abrasive papers, followed by mechanical polishing to flatten the surface of the disk to be shiny and scratch-free. Depending on which final step of sample preparation is chosen, samples can be mechanically thinned down to 20 μm. 150-μm-thick disks are suitable for electropolishing. On the other hand, thin disks, 10-20 μm, are preferred for quick ion beam polishing. Details of electropolishing and ion beam polishing techniques are given below.
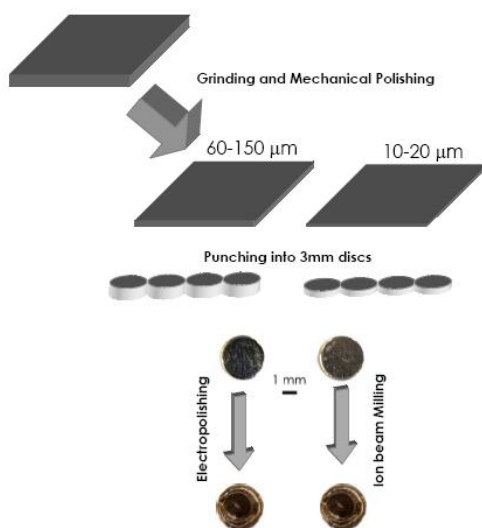

Figure 1.3 Schematic rendition of specimen preparation procedure.

1.3.1 Electropolishing

Electropolishing is a rather quick method to obtain thin, electron-transparent foils with a small amount of mechanical damage (usually bending near hole regions). Most of the TEM specimens in this study were prepared by electropolishing using Struers TENUPOL 3 and TENUPOL 5 devices. A common twin jet electropolishing cell is shown schematically in Fig. 1.4.

The electrolyte is poured via a pump and nozzle system through two jets on either side of the anode specimen. A voltage is applied in order to produce a current, which causes anodic dissolution of the specimen and thus creates a polished surface. The voltage has to be set accurately; when it is set too low (between a and b in the curve

shown in Fig 1.4(b)), an etched surface will appear because most reactive parts on the sample will be attacked. On the other hand when the voltage is set too high (between d and e), hydrogen gas starts to form on the surface of the specimen, causing an increase in current. This regime is called pitting and many holes are formed in the specimen, although the specimen is still polished. As shown in Fig. 1.4, good polishing occurs on the plateau between c and d. The electrolyte used in this study was a solution of 10 % perchloric acid and 1% nitric acid in methanol [10], which was cooled to a temperature of 253 K in order to obtain a more controlled polishing process. The typical operating voltage was between 15 and 20 V, and the measured current was between 0.5 and 1 A.
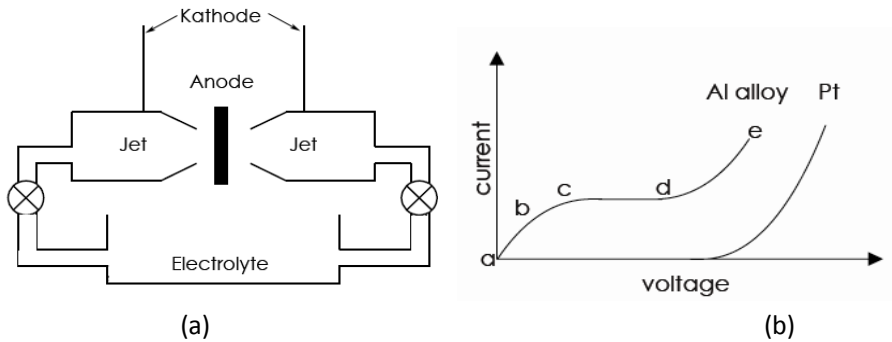

(a)   (b)

Figure 1.4 (a) Electrochemical polishing cell and schematic drawing of the twin-jet TENUPOL devices. (b) Corresponding voltage-current diagram [3].

1.2.2   Ion Beam Polishing

In the ion beam milling machine [9], the polished surfaces of a thin sample are bombarded with argon ions of energies of between 2 and 5 kV at various glancing angles. The best result is achieved with a low ion-incident angle such as $3\text{-}5^{0,}$ for which little implantation of Ar ions occurs compared to higher ion-incident angles such as 10^0. Operation at low angles increases the thinning time. Although Al is a good heat conductor, longer ion beam milling operation and Ar implantation might still create vacancies in the Al matrix, which strongly change the diffusion characteristic of solute atoms in Al alloys. Therefore it is important to work with very thin samples and low ion-incident angles to obtain successful and artifact-free samples from Al alloys.

1.2.3 Discussion of TEM Specimen Preparation from Aluminum Alloys

Specimen preparation is an ultimate restriction to successful transmission electron microscopy investigations and thus deserves careful attention. To obtain samples that represent true nano-microstructures of the alloy, it may not be sufficient to employ only one preparation method. For example, in Al-Zr and Al-Ni alloys the fine precipitates remained in the matrix when the electropolishing voltage is less than 20 V. But the big particles formed during solidification were lost, as these particles probably drop from the thinner part of the foil due to gravity during the electron polishing process. Electropolishing may bring another unwanted effect of a height difference between the precipitate and matrix on the specimen, which comes from the different polishing speeds between the precipitates and the Al matrix. In extreme cases, numerous small particles protrude or particles are etched heavily, leaving few nanometer-thick particles/precipitates at the surface of TEM samples. In these cases it is difficult to perform quantitative electron diffraction and quantitative electron microscopy studies on the parts of interest of these specimens. Therefore in such cases we used electropolishing for pre-thinning, followed by ion beam polishing to produce electron-transparent regions.

It should be noted that Focused Ion Beam, FIB, could constitute a novel specimen preparation technique in the future. For example, Omniprobe techniques could be used to prepare many lamellas that can then be attached to a single metal grid. This also allows further thinning of the lamellas to make them suitable for high-resolution imaging. In this way, multiple lamellas can be studied in TEM simultaneously without changing the TEM holder, which would highly improve the vacuum environment and reduce the holder-related drift. As FIB technology advances, it will become a feasible tool to obtain thin and almost damage-free samples for HR(S)TEM investigations

1.4 Transmission Electron Microscopy [3]

According to Rayleigh's criterion, the resolution of a microscope, which is the distance, R, between two details just separable from one another, is given as

$$R = 0.61 \frac{\lambda}{\sin \alpha} \qquad\qquad 1.1$$

for illumination with incoherent sources, where λ is the wavelength of the radiation and α the maximum angle between incident and scattered beams, determined by the opening angle of the objective lens. The resolution of a microscope is therefore restricted by the wavelength of radiation. For example the resolution of a light microscope is limited to within the visible region of the electromagnetic spectrum, where wavelengths range between 600-400 nm. Resolutions of as high as 300 nm can be achieved with modern light microscopes [11].

It has long been known that X-rays have much shorter wavelengths than visible light. However for a long time it was not possible to build an X-ray microscope with the same principles as optical microscopes because X-rays could not be manipulated by refractive lenses.[4]

It was Davisson and Germer's discovery of the wave behavior of electrons that led Ernst Ruska and Max Knoll to develop the most powerful imaging instrument of the 20th century, namely the transmission electron microscope. Since becoming commercially available, transmission electron microscopy has proved itself to be the most advanced and sophisticated technique to characterize any kind of matter, regardless of whether it is organic or inorganic. Today, transmission electron microscopy is a well-established characterization technique used in laboratories across the world.

---

[3] The entire section was adapted from References 9,13,14,15,16

[4] Recently it has become possible to build X-ray microscopes by using so-called diffractive lenses where x-rays can be manipulated by nanometer-sized layered optical elements, reflective mirrors and Fresnel zone lenses [12]. The X-ray microscopes are used mainly for tomography purposes [12].

1.4.1   Electron Beam-Matter Interaction

Unlike electromagnetic radiation-object interaction, interaction of electrons with matter is much stronger because of the electrostatic (Coulomb) interaction between the incident electrons and the atoms in the matter. As a result, numerous elastic and inelastic scattering events occur. Figure 1.5 shows the products of electron beam–specimen interaction for fast electrons traveling through matter.

Elastic scattering arises from interactions of incident electrons with the electrostatic potential of the atom (the result of Coulomb interaction between electron-electron and electron-nuclei) and provides the most important contribution to the contrast in (S)TEM images. Elastically scattered electrons suffer virtually no energy loss.

Interaction of incoming electrons with the electrons of the atom results in inelastic scattering of the incident electrons. Inelastically scattered electrons, on the other hand, lose energy and become concentrated within smaller scattering angles. Any event between the electron beam and matter results in a loss of energy, and/or a change in momentum of the incident beam electrons must produce an equivalent amount of energy in some other form. There are numerous forms of energy phenomena produced during electron beam–matter interaction, and all of these have the potential to provide important information about the nature of the specimen. The inelastic events may result from many electron–matter interactions, e.g. phonon excitations, plasmon excitations, intraband and interband excitations, ionization of inner shell electrons, and Bremsstrahlung.
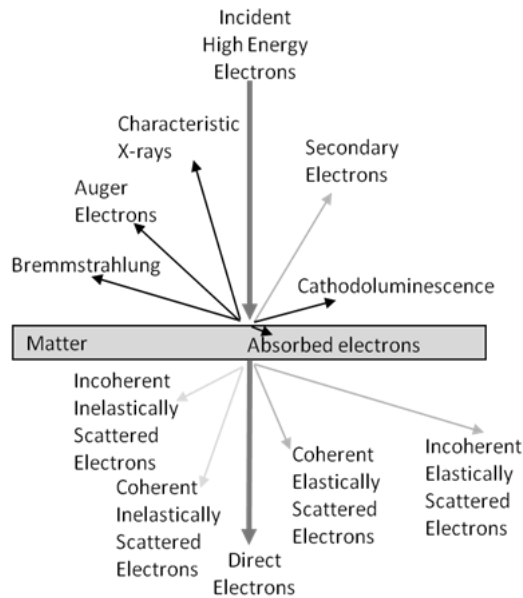
Figure 1.5 Interaction between incident electron beams and matter [9].

Among all these inelastic events listed above, ionization of inner-shell electrons is the most important one because the produced signals directly reflect the chemical state of the analyzed specimen. This occurs when a primary electron beam has enough energy to "knock out" an electron from one of the tightly bonded inner atomic shells. An atom that loses its inner-shell electron, usually called an ionized atom, is highly unstable. The empty state will then be filled by an electron from one of the outer shells. The atom is relaxed by emitting X-rays with corresponding energy (see Fig. 1.6). As the energies of the emitted X-rays will be different for each element, they are called characteristic X-rays and thus can be used to determine atomic species in the analyzed volume.

During the ionization of the atom, the incident electron beam transfers part of its energy and momentum to the atom. This results in an energy loss of the transmitted electrons. The energy required to eject a core-shell electron of the atom depends on its atomic number. For instance, it takes 55 eV to eject an electron from a K shell of a Li atom, whereas it takes 99 keV to do the same for U [13]. The detected energy loss of the primary electron caused by the core shell excitation is often called the "ionization edge" specific to orbital names, e.g. K edge, L1 edge etc. These "ionization

edges" provide not only the elemental information but also bonding effects and details of the electronic structure.

In addition to the core shell excitations, plasmon excitation causes energy losses. These are generated as a result of collective oscillations of valence electrons. The detected plasmon energy can therefore reflect the free-electron density of the materials.

1.4.2 Chemical Analysis with TEM

The first step in identifying phases is usually a chemical analysis. This is done in TEM by collecting and analyzing characteristic X-rays or the energy loss of an incident electron beam. Characteristic X-rays can be collected by solid-state detectors known as Energy Dispersive X-rays Spectrometry (EDX). The energy loss of an incident beam can be accessed by using a spectrometer (serial detection) or an imaging filter (parallel detection) attached below the microscope column, known as Electron Energy Loss Spectroscopy (EELS). An EELS spectrum reveals a wealth of chemical and electronic state information about the specimen.

EDX provides a quick way to identify and quantify the elements, whereas the EELS method has many other advantages, such as the capability of obtaining information about chemical bonding and good spatial resolution. In addition, EELS is particularly appropriate for light elements. In general, EELS spectra offer more information about the chemical state of the atoms. The variation of edge onset and shape reflects the bonding effects in the atom. EEL spectra can also be classified more specifically. Depending on the excitation level of the ejected electron, unoccupied states of the atom can be probed by EELS. This technique is known as Electron Loss Near Edge Structure (ELNES) and is often used to determine the electronic structure change in allotropic forms of elements and compounds. In addition, one can also deduce the coordination of the atom. Plasmon losses in EELS spectra are also resources of important information. Plasmon peaks offer a practical way to measure thickness of electron transparent samples and has been shown to give 10% accuracy [14]. The ratio between the total intensity of the spectra and the intensity of the zero loss peak gives the ratio between the thickness and the mean inelastic scattering path. The absolute determination of the thickness requires values of the inelastic mean free path [14].

In this work, EDX has been used primarily for identification and, to a lesser degree, quantification purposes. Thus, more a detailed knowledge of the EDX technique is required in order to be aware of the limitations and the resolution of this technique.
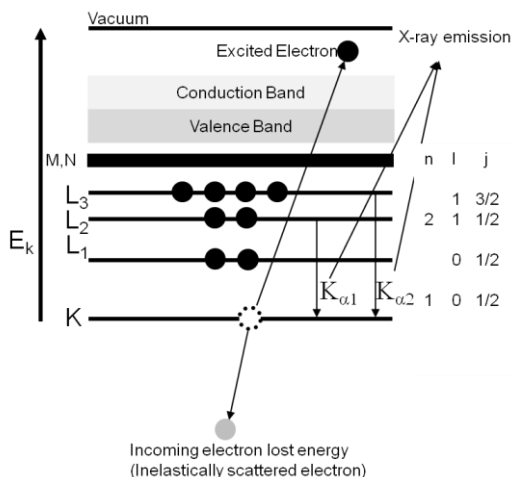

Figure 1.6 Electronic subshells of an atom with quantum numbers *n*, *l*, *j*. Ionization of the K shell and the emitted X-rays as a result of possible transitions are shown. Quantum mechanical selection rules govern the possible transitions, $\Delta l = \pm 1$ and $\Delta j = 0, \pm 1$. Therefore only L_2 and L_3 shells can provide an electron to fill a vacancy in the K shell resulting from X-ray emissions. These are denoted $K_{\alpha 1}$ and $K_{\alpha 2}$, respectively [adapted from 13].

In the EDX system the X-rays are collected by a semiconductor (Li-implanted Si) detector protected by an ultrathin window cooled to liquid nitrogen temperature to prevent thermal noise and the diffusion of the dopant Li atoms. The Si(Li) detector creates electrons and holes according to the quantum energy of impinging X-rays. These electrons and holes are then separated by applying a reverse bias, collected as a charge pulse, further processed by a computer system, and displayed as a spectrum such as the one shown in Fig. 1.7. The EDX spectrum comprises a background produced by the Bremsstrahlung X-rays and by peaks characteristic to the chemical elements of the material. It is quite straightforward to identify the elements beyond boron when the peaks do not overlap. For lighter elements, the excess energy after the relaxation of excited atoms is mainly carried off by Auger electrons (94% of the relaxation process). The efficiency of the EDX system to detect light elements is therefore low. Moreover, the emitted X-rays from a TEM specimen are largely absorbed by the window and also on the detector surface as well as by the specimen

itself. Therefore elemental analysis of light elements by EDX is less effective than for heavy elements.

It is difficult but straightforward to quantify the EDX spectrum if there are no overlapping peaks. Otherwise, deconvolution of overlapping peaks is required. Deconvolution usually yields poor results for close elements. Other than overlapping peaks, an important practical concern arises due to the channeling effect of incident electrons. The intensity of emitted X-rays depends on crystal orientation and can be reduced as much as 50% for zone axis orientations [9]. Therefore it is important to avoid zone axis orientation when collecting EDX spectra. On the other hand, the channeling effect of electrons is useful for distinguishing the substitutional and interstitial-type atoms and for locating impurity atoms. This technique is known as *atom location channeling enhanced microanalyses* (ALCHEMI) [9].

The EDX quantification procedure takes into account the link between the weight fraction and the generated intensities (ionization cross section) and between the generated intensity and the measured intensity (absorption and fluorescence effects). The measured intensity of an element depends on the other elements present in the sample. For thin samples, where fluorescence and electron absorption are negligible, the weight fraction of the elements are linked by

$$W_A/W_B = k_{AB}(I_A/I_B)_m, \qquad\qquad 1.2$$

where W is the weight fraction, I_m the measured intensity and the subscripts represent the element. The *Cliff-Lorimer ratios* are represented by k_{AB}. They can be measured with thin standard specimens of known composition (Cliff-Lorimer method) or calculated for each pair of elements if their ionic cross sections, fluorescence yields and detector efficiencies are known (standardless method). Then, the ratios are used for other samples containing the corresponding elements. The Cliff-Lorimer method is the most precise one, but it requires a considerable work before yielding the first results.

In this thesis, all quantifications were performed with the standardless method because the theoretical k values for the transition elements are reliable. It should be noted that the spatial resolution corresponds directly to the probe size of the microscope if the measurement is done on the thinner parts of the sample. Otherwise the effect of beam broadening has to be included.
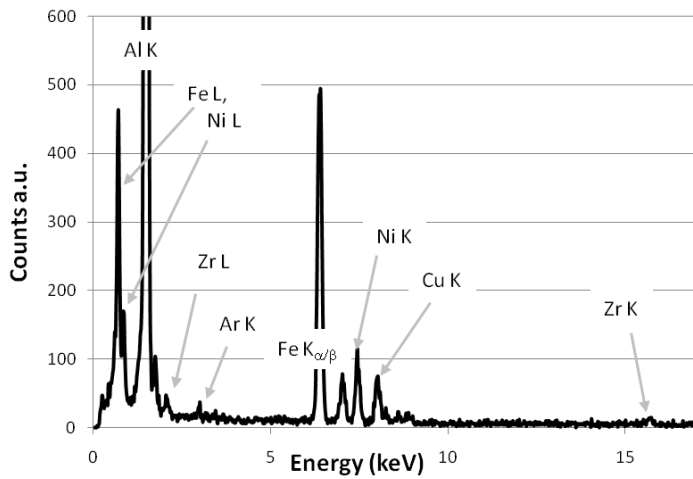
Figure 1.7 EDX spectra obtained from an Al intermetallic on the grain boundary found in an Al-Zr alloy. It is important to note that the CuK signal is caused by the specimen holder and can be avoided by using a low background holder. Ar K signal is due to implantation of Argon during ion beam polishing

1.4.3 Remarks on EDX Measurements

Compositions of intermetallic particles and precipitates observed in this thesis were checked by EDX. However it often proved to be difficult task because of the morphology and the position of the intermetallic phases distributed in the Al matrix. For example, the quantification of EDX data was not attempted for the plate-like precipitates because the small thickness of the precipitates and their geometry after electropolishing often makes it difficult to interpret the results of quantification. It was frequently observed that precipitates are etched differently than the Al matrix during electropolishing. In such cases, precipitates do not cut the TEM foil from top to bottom, but they are either embedded or protruded. A significant amount of Al signal can then be incorporated in quantification, which may lead one to conclude the wrong stoichiometry of the intermetallic phase. In these cases, the EDX results need to be checked carefully by means of other techniques.

1.4.4 Basics of (Scanning)Transmission Electron Microscope

A transmission electron microscope can be divided into three parts according to their optical functions: (1) the illumination part; (2) the objective lens system (image-forming part) and (3) the magnification part. In addition to optical elements, modern microscopes are equipped with beam and image deflection coils, electron beam monochromators, aberration correctors, several solid-state detectors, and in-column and post-column elements which utilize various types of signals produced as a result of the interaction between the electron beam and the specimen as described in the previous section.

Figure 1.8 (a) is a schematic drawing of the main elements of a transmission electron microscope. The illumination system of modern electron microscopes is generally equipped with a Schottky emission gun or, to a lesser extent, with a cold field emission gun as its electron-emitting source. These emitters provide higher brightness and lower energy spread than conventional W or LaB_6 electron sources at the expense of complicated electronic circuits and better vacuum conditions required around the emitting tip.

A gun lens is used to form and control a virtual source, which is a first crossover in front of the gun. The first condenser lens controls the size of the virtual source. The second and third condenser lenses are used to control the illumination on the specimen. Varying the strength of these lenses, for instance, it is possible to make a parallel (smaller than 0.5 mrad) or strongly converged electron beam on the specimen. Traditionally, transmission electron microscopes contain two condenser lenses to vary the size of the electron source size (spot size) and illuminated area. Recent transmission electron microscope models are equipped with three condenser lens systems, which provide parallel illumination for a range of illumination sizes (100 nm – 50 μm) and offer a range of convergence angles without changing and beam limiting the aperture size and/or the current of an objective lens.

Most of the electrons that pass through the specimen are scattered elastically in the case of very thin specimens. An objective lens focuses on electrons that left the bottom surface of the specimen and forms the magnified image of the specimen. In modern electron microscopes the specimen is placed inside the objective lens and an additional lens, the so-called mini-condenser lens, is placed above the upper objective pole piece. This creates the objective lens' pre-magnetic field and serves to control the illumination of the electron beam on the specimen.

A diffraction lens is used to form an image of the diffraction pattern. The strength of the diffraction lens can be adjusted so that the front focal plane of the diffraction lens coincides with the back focal plane of the objective lens. In the imaging mode, the strength of the diffraction lens is adjusted so that the image plane of the intermediate lens coincides with the image plane of the objective lens. Projector lenses are used to further magnify a diffraction pattern or an image of the specimen. The schematic of a modern TEM column and ray diagrams in different operating modes is displayed in Fig. 1.8. In addition to electro-magnetic lenses, several dynamic deflection coils are positioned along a TEM column to adjust the beam position and angle, which are also used to raster the electron beam on the specimen to form STEM images.
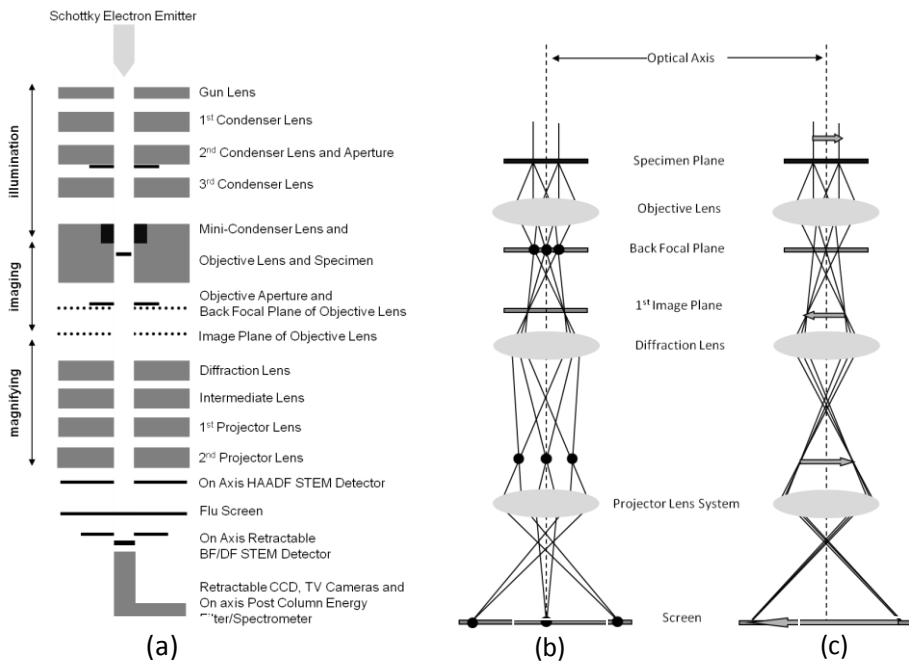

Figure 1.8. (a) Schematic rendition of a modern TEM column. Ray diagrams for (b) diffraction and (c) imaging mode. For the sake of clarity, intermediate and projector lenses are not included in the drawings.

1.4.5   Imaging with Electrons

Images observed in (S)TEM can be classified in terms of four contrast mechanisms:

- Diffraction contrast (TEM, STEM)

- Mass contrast (TEM, STEM)

- Atomic number contrast (STEM)

- Phase contrast (HRTEM, STEM, Lorentz microscopy)

Varying the intensity of the diffracted beams across the specimen yields an image with diffraction contrast. In the case of precipitates and matrix systems, the variation of the diffracted beam intensity induced by the microstructure can be mapped by selecting the desired diffraction spot using small objective apertures. This can provide valuable information about the microstructure [9]. The phase contrast arises from the interference of the primary beam and the diffracted beams. The phase contrast mechanism is responsible for the appearance of lattice fringe images. The atomic number and mass contrast are due to the difference between the scattering powers of the elements that constitute the specimen. Mass contrast is the main contrast mechanism for amorphous and organic specimens and is responsible for the high-resolution STEM images acquired by a high-angle annular dark-field detector.

Modern transmission electron microscopy observations can be also grouped into three main categories:

1. Static beam transmission electron microscopy: Image formation due to diffraction, mass and phase contrast of scattered electrons. The main techniques are bright field, dark field, weak beam dark field imaging (diffraction contrast), high-resolution electron microscopy.

2. Scanning transmission electron microscopy: A focused electron beam of variable sizes (from a few nanometers down to sub-Ångstrom) is scanned across the specimen and transmitted electrons are collected in reciprocal space by various types of detectors to form an image. By varying the camera length, different types of image contrast can be produced. The most known one is Z-contrast imaging, which reveals the atomic number differences across the scanned area.

3. Analytical electron microscopy: Signals generated as a result of electron beam–specimen interaction and can be used to determine the chemistry of the specimen. The power of analytical electron microscopy is the availability of high spatial resolution in combination with STEM imaging. The main analytical tools available in commercial (S)TEMs:[5]

- Energy-dispersive X-ray analysis of characteristic X-rays emitted from the specimen.
- Electron energy loss spectroscopy of transmitted electrons.

1.4.6 High-Resolution Transmission Electron Microscopy

Details of the image-formation process in High Resolution Transmission Electron Microscopy, HRTEM will be given and discussed in Chapter 6. In this part only brief introduction to HRTEM is given.

High-magnification images crystalline materials, oriented along one of the low-index zone axes[6], obtained with Field Emission Gun, FEG,instruments show contrast variations that are perceived as discrete peaks. Such images are generally referred to as lattice images and only under certain conditions do they correspond to atom columns and can thus yield atomic-resolution images of the materials. This technique is broadly known as high-resolution transmission electron microscopy (HRTEM). The phase relationship between the electrons leaving the specimen is responsible for the image formation in HRTEM, and the contrast of HRTEM images depends severely on the sample thickness.

In a TEM, when a crystalline sample, oriented along a low-index zone axis large number of diffracted beams are formed at the back focal plane of the objective lens. These beams recombine at the image plane of the objective lens, magnified by the projector lens system and thus periodic lattice fringe images are observed. As stated above, there is no one-to-one correspondence between the projected atom positions

---

[5] Auger detectors and cathodoluminescence detectors were also developed, but their incorporation into commercial instruments is very limited.

[6] A zone axis is a lattice row parallel to the intersection of two (or more) families of lattices planes. It is denoted by [u v w].

of the crystal structure viewed along a specific zone axis and the contrast of HRTEM images. For interpretation of HRTEM images, an image simulation is usually essential.

1.4.7 Scanning Transmission Electron Microscopy[7]

Scanning an electron beam over a sample and using forwardly scattered electrons to generate images is known as Scanning Transmission Electron Microscopy, STEM. It is a very powerful technique capable of atomic-resolution imaging and analysis.

Historically, STEM was a dedicated instrument capable only of imaging in the scanning mode. It required a very skilled operator and was limited to a small community. Improvements on the electronics and mechanical stability of TEMs, combined with the high-brightness electron sources, turned classical TEMs into a very powerful STEM imaging tool. Today, STEM has long become widely available to the research community in academia as well as in industry.

In particular, Z-contrast High-Angle Annular Dark-Field, HAADF, technique is often used today for atomic-scale imaging. Unlike HRTEM images, Z-contrast images are formed by electrons that are elastically scattered at high angles (50–150 mrad) and are dependent on the atomic number approximately as $Z^{1.7}$. There is no coherence relationship between high angle scattered electrons because they are mutually independent. Therefore, for incoherent scattering, the intensities I from individual scatterers (atoms) are added, rather than the wavefunction amplitudes ψ. The phase relationship of scattered beams and their interference, which are important considerations for HRTEM imaging, are not relevant for Z-contrast STEM imaging. Each atom can be considered an independent scatterer because there is no constructive or destructive interference between the phases of wavefunctions emanating from the different atoms. The incoherent nature of Z-contrast STEM imaging enables direct interpretation of these images in terms of atom types and positions [19].

The Z-contrast STEM images are formed by collecting high-angle elastically scattered electrons with an annular dark-field detector (Fig. 1.9). An annular detector of this type captures a large fraction of the high-angle intensity, providing an efficient dark-field imaging mode. The angle of high angle elastic scattering is larger than that of

---

[7] Adapted from References 14,17,18

typical Bragg diffracted beams[8], and the relevant part of the scattering potential is one order of magnitude smaller than typical atomic dimensions. The effective size of the atomic scattering potential (typically 0.01–0.03 nm) is also about one order of magnitude smaller than the size of the electron-beam probe of modern medium-voltage field-emission STEMs (typical probe size for high-resolution work varies between 0.2 and 0.05 nm). Figure 1.10 illustrates image formation for STEM. A vertical column of atoms can therefore be understood as a very sharp object in the plane of the sample. The image resolution is the convolution of this "δ function" with the spatial profile of the probe current together with any beam broadening that occurs as the electrons propagate through the sample. Owing to the large cross section for elastic scattering, however, it is possible to use thin specimens to minimize beam broadening. A phenomenon called "electron channeling" also helps to minimize beam broadening.
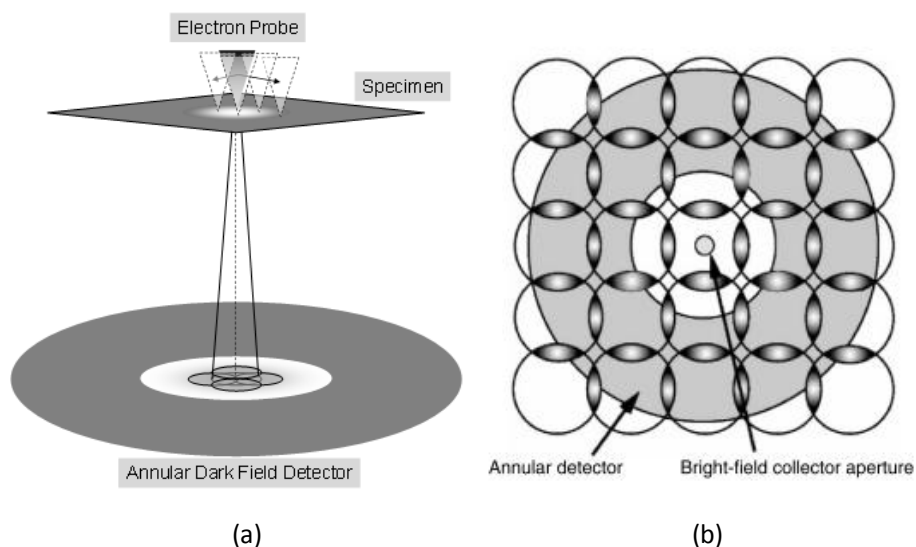

(a)   (b)

Figure 1.9 (a) Schematical rendition of geometry of STEM. (b) Bird's eye view of common detector types used in STEM [19].

---

[8] Zero order Bragg diffraction is typically up to 30-40 mrad but high angle elastic scattering is 50-150 mrad [17].
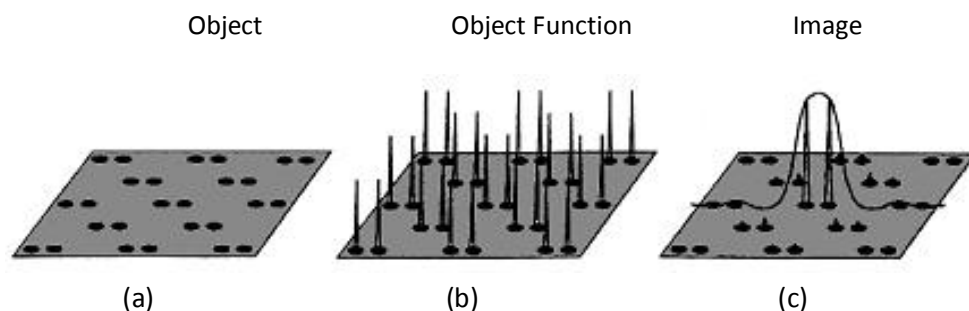
Object	Object Function	Image

(a)	(b)	(c)

Figure 1.10 The specimen in (a) represent <110> oriented diamond-like structure and black dots indicate atom columns. High angle scattering potential of the specimen is represented as the object function in (b). The image formation in (c) can be considered as a convolution of the electron probe and the object function. As the electron probe raster the specimen it maps out the high angle scattering power of the specimen [14].

The electron optical ray path for STEM imaging in a modern microscope (the TEM used in this thesis for STEM imaging) is schematically shown in Fig. 1.11. Electrons emitted from FEG are demagnified by the gun lens (gun lens setting in the microscope) and the 1st condenser lens (spot size setting in the microscope). The zoom system (2nd and 3rd condenser lenses) forms a beam path with very little convergence (see Fig. 1.11). As electrons are almost parallel, the upper field of the objective lens therefore focuses them into a small spot on the specimen plane and convergent beam diffraction pattern formed on the back focal plane of the objective lens. When electron beam is scanned on the sample the intensity in the back focal plane changes as a function of the scattering angle for each scan position. These variations of intensity can then be mapped using either a bright-field or an annular dark-field detector, which yields images via the phase contrast mechanism. When elastically scattered electrons at higher angles are collected using a suitable detector and camera length, incoherent images known as Z-contrast images are formed.

The disk formed in the back focal plane contains the shadow image of the sample that is infinitely magnified when the electron probe is focused on the sample. When the electron probe is defocused, sample details can be seen within the shadow image. The shadow image is called a Ronchigram after the Italian physicist Vasco Ronchi, and is widely used for correcting aberrations present in the electron probe to achieve highest possible resolution in STEM imaging.
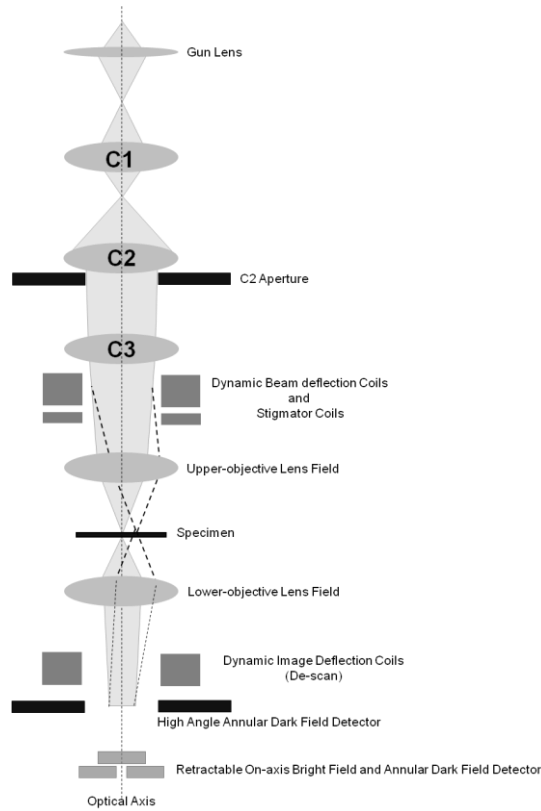
Figure 1.11 Ray diagram for STEM mode in a 3-condenser-lens TEM.

The best possible resolution in STEM requires a small coherent electron probe. Several parameters that have serious effects on the shape and size of the probe have to be balanced/optimized [17,18]. These effects can be summarized as

- The convergence angle of the electron probe (illumination semi angle), α, in combination with the spherical aberration, C_S, of the objective lens causes a disk of blurring (also known as disk of least confusion) and its contribution to the probe size is $D_{C_S} = 0.25 C_s \alpha^3$. C_S is 1.2 mm for conventional microscopes. C_S is set to 0.002 mm for aberration corrected STEM.

- The diffraction effect (Rayleigh criterion given in Eq1.1). This causes a blur of the probe even when it would have been focused at a perfect point. The size

of this diffraction blur disk is $D_D = 0.61\dfrac{\lambda}{\alpha}$. λ is the wavelength of the electrons. It is apparent the diffraction limit reduces with increasing the acceleration voltage (electron wavelength at 300 kV is 0.00169 nm while at 80 kV is 0.00476nm).

- The geometrical size of the FEG source on the sample is denoted D_{GEO} which is due to finite brightness of FEG. It varies with the illumination angle, inversely.

In a simplified approach these factors can be assumed to be Gaussian. Hence the final probe size can be estimated from the geometric mean of D_{GEO}, D_{Cs}, and D_D. It is obvious that the probe size is smallest when the contributions D_{GEO}, D_{Cs}, and D_D are smallest. Making the image of the source smaller is achieved merely by increasing the gun lens and or spot size at the expense of the beam current. Even if the image of the FEG source were made infinitely small, this would not result in a sub-angstrom probe because the spherical aberration disk, D_{Cs} and the diffraction disk, D_D are interrelated and cannot be made small simultaneously. Therefore these two contributions need to be balanced against each other.

The electron wave in front of the objective lens's upper field can be considered a plane wave with a single k wave vector because the beam becomes almost parallel. Thus the point q in the front-focal plane of the objective lens corresponds to a partial plane wave converging at an angle α to the sample and related to semi angle, by **q**=α/λ which is valid for paraxial rays. The phase shift experienced by the electron wave after passing the upper field of the objective lens (astigmatism and other high-order aberrations are ignored) is given as

$$\chi(\vec{q}) = \pi \left[\lambda \Delta f \, \vec{q}^{\,2} + \frac{1}{2} \lambda^3 C_s \, \vec{q}^{\,4} \right] \qquad 1.3$$

Δf is defocus. The aberration wave function can written as

$$\psi(\vec{q}) = e^{-i\chi(\vec{q})} \qquad 1.4$$

$$(FT[\psi(\vec{r})])^2 = \left| \int_0^{g\,max} e^{i\chi(\vec{q})} d^2\vec{q} \right|^2$$

1.5

A Fourier transformation in Eq. 1.5 yields the shape of the probe (which is the point spread function). This is the intensity distribution of the focused probe on the sample.

Following Weyland and Muller's approach [14] for finding optimum conditions for incoherent STEM imaging (for a non-C_S corrected instrument), we must first find the optimum defocus value (Scherzer defocus for the STEM imaging) to balance the spherical aberration for the maximum allowed phase shift of $\lambda/4$ (which is $\pi/2$) condition,

$$\chi(\vec{q}) \leq \pi/2 .$$

1.6

The next step is to obtain the optimum probe convergence angle at the limit of the spherical aberration. This can be solved when the convergence angle, α, (which is $q\lambda$) satisfy the Eq.1.7 for the optimum defocus setting. Therefore we can have the conditions for high-resolution STEM imaging

$$\alpha_{max} = \left(\frac{4\lambda}{C_s} \right)^{1/4}$$

1.7

$$\Delta f_{opt} = \left(C_s \lambda \right)^{1/2}$$

1.8

Under these conditions the point-spread function of the probe is sharply peaked and the tails of the probe are surpassed. Full Width at Half Maximum, FWHM, of the point-spread function is defined as the probe size and is therefore the resolution of the STEM probe for incoherent imaging. The optimum resolution for incoherent STEM imaging [14,17,18] is

$$d_{optimum} = 0.43 C_s^{1/4} \lambda^{3/4}$$

1.9

STEM was heavily used during preparation of this work. Therefore special attention was paid to choosing the right operating settings to avoid the influence of the probe

shape during image formation. For high-resolution STEM work to the highest resolution in our non-probe C_s-corrected 300 kV S(TEM). Δf is found to be 45 nm and the maximum convergence angle is chosen to be 10 mrad in order to balance the effect of C_S. Therefore the highest resolution of 0.14 nm is obtained.

For our 300 kV (S)TEM we used a defocus of 45 nm and a maximum convergence angle of 10 mrad for HRSTEM work. In our TEM equipped with a hardware probe aberration corrector, aberrations can be corrected up to 25 mrad (limit of the corrector technology). Therefore, we used a convergence angle of 25 mrad and a defocus very close to zero for aberration corrected STEM imaging.

As can be seen in Fig 1.12, it is important to use the right defocus value to minimize the probe tails. Using different defocus values makes it possible to obtain narrower probe, but this increases the intensity of the probe tails, which in turn increases the total background of the STEM images. Therefore the contrast and sharpness of images from interfaces and small precipitates (embedded in the parent matrix) are made dramatically worse due to the intensity spreading of probe tails. This makes it difficult to analyze HR-STEM images. Another consequence of probe tails is the mixture of the chemical signal acquired across the interface, which causes the artificial broadening of chemical profiles extracted from such experiments.

The effect of defocusing the objective lens on the probe shape for optimized and non-optimized settings is demonstrated in Fig. 1.12.
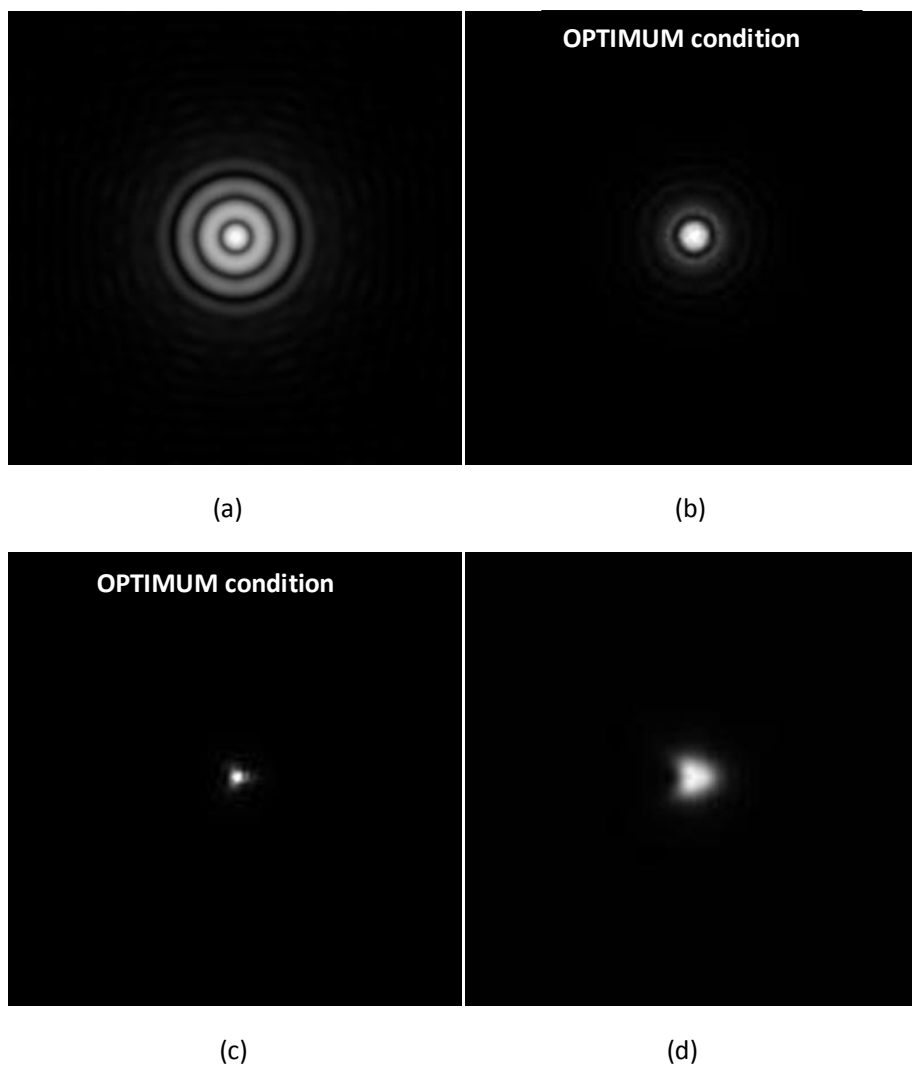
(a)

(b)

(c)

(d)

Figure 1.12 Calculated probe shapes usind Dr. Probe [20] for different defocus values at different convergence angles (non-probe Cs-corrected vs probe Cs-corrected) and different defocus values (a) 10 mrad with no defocus, (b) 10 mrad 55 nm underfocus: **OPTIMUM condition**, (c) 25 mrad no defocus: **OPTIMUM condition** (d) 25 mrad 10 nm underfocus. Effect of residual aberrations can be clearly seen in underfocused C_s-corrected probe.

1.5   Strategy for identification of and structure determination unknown phases

Interfaces in crystals are of great importance in the mechanical, physical and chemical properties of materials. The atomic configuration at interfaces is related closely to the conditions of nucleation and growth. To understand and then control the process of crystal growth, it is beneficial to study interface properties, including dislocations, planar defects, cracks, adsorption layers, etc. It has long been recognized that our understanding of interface properties depends strongly on the availability of information about the atomic configuration of the interface, which is in an interesting and challenging study area. Since the 1970s, the development of high-resolution transmission electron microscopy has provided a tool to observe the crystal structure directly [21], when the sample is sufficiently thin.

Through-focus exit wave reconstruction technique [22] can be applied to retrieve electron wave at the exit surface of the specimen which can be used to model interface structure since such images are free from phase shifts introduced by the objective lens. On the other hand this technique requires very thin samples and therefore it is difficult to apply it to the precipitates formed in dilute alloys since the chance to get precipitates near the hole may be very low. Combined with quantitative electron diffraction, through focus exit wave reconstruction method was successfully used to determine the structure of precipitates formed in Al-Mg-Si alloys which were unknown to scientific community for long time [23,24,25].

Structure determination of crystals using diffraction intensities, is not straightforward, mainly because the only intensities are recorded and the phase information is lost. If the phase information can also obtained, inverse Fourier transform of structure factors would give to 3-d map of scattering potential of the crystal. To overcome phase problem, several methods are developed which are mostly x-ray and neutron diffraction based. Kinematic nature of X-ray and neutron diffraction makes possible very accurate structure determination [26]. Electron diffraction, on the other hand, is hardly used because it suffers dynamical scattering and intensities are modified accordingly. Thus to use electron diffraction intensities for structure determination, dynamical events has to be taken to into an account [27].

Usually structure determination procedure needs a good starting structure model. This can be obtained by combination of several ways:

- Chemical analysis: Chemical analysis is the first step for the identification of unknown phases. By knowing rough composition possible structures can be guessed.

- Lattice parameters, unit cell and symmetry determination from electron diffraction pattern: They provide necessary information to identify and build a model.

- Exit wave reconstructed from HRTEM images, atomic imaging in STEM. It can provide rough position of atoms. Z-contrast sensitive imaging in STEM can reveal the position of different atomic species.

- Structural chemistry knowledge: It is often useful since many intermetallic compounds formed in Al alloys form in similar structures. Therefore it is possible to use known structure as an initial model by adjusting lattice parameters and substituting the atom types.

1.6 Quantum mechanical first-principles calculations[9]

Understanding the complexities of phase stability in alloys is a classic problem in materials science. The rich variety of ordered compounds, solid solutions, and metastable intermetallic phases with and without structural defects observed in aluminum and its alloys makes Al alloys is very useful to prove theories of phase stability. The stability of these Al-rich phases is not only of scientific but also technological interest, simply because understanding of phase stability is an ultimate need for a design and control of alloy properties.

---

[9] Adapted from the reference 29.

First-principles electronic structure calculations, based on density functional theory have become a widely used tool in the exploration of crystal structures and alloy phase stability [28]. Due to the predictive nature of these methods, as well as continuing improvements in physical accuracy, algorithms and computational power, first-principles methods are increasingly gaining acceptance as a powerful tool in structure refinement of crystals, defect structures, interfaces alloy design and successfully applied to predict phase stability of early stage metastable precipitates in 6xxx Al alloys [24,28].

First principles calculations are based on solving of the Schrödinger equation for many-particles system which is composed of positively charged nuclei and electrons. Hamiltonian for many-particle system is

$$H = \frac{-\hbar^2}{2}\sum_i \frac{\nabla^2_{R_i}}{M_i} - \frac{\hbar^2}{2}\sum_i \frac{\nabla^2_{r_i}}{m_e} - \frac{1}{4\pi\varepsilon_0}\sum_{i\neq j}\frac{e^2 Z_i}{\left|\vec{R}_i - \vec{r}_i\right|} + \frac{1}{8\pi\varepsilon_0}\sum_{i\neq j}\frac{e^2}{\left|\vec{r}_i - \vec{r}_j\right|} + \frac{1}{8\pi\varepsilon_0}\sum_{i\neq j}\frac{e^2 Z_i Z_j}{\left|\vec{R}_i - \vec{R}_j\right|} \quad 1.10$$

$$H = T_N + T_e + V_{e-N} + V_{e-e} + V_{N-N} \quad\quad 1.11$$

Where M_i is the mass of the nucleus position at $\mathbf{R}_i$ and m_e is the mass of an electron at position $\mathbf{r}_i$. The first two terms of the Hamiltonian are the momentum operators represent kinetic energy of the particles. The last three terms are the contributions of Coulomb interactions between electrons and a nucleus, between electrons and between nuclei. This equation cannot be solved exactly and several approximations exist to provide solutions.

The first approach to tackle many-particle problem was proposed by and Born-Oppenheimer in which the nuclei is considered to be fixed and electrons are in instantaneous equilibrium with them. This approximation reduces the kinetic energy term between nuclei in the Hamiltonian and the potential energy term due to Coulomb interaction between nuclei becomes a constant.

$$H = T_e + V_{e-N} + V_{e-e} \quad\quad 1.12$$

Thus Born-Oppenheimer approximation can be effectively used for structure refinement. First, equilibrium electronic states have to be calculated for the model structure containing all nuclei type and positions. The next step is the minimization of the Hamiltonian by moving the nuclei to their equilibrium positions. To do this, forces and stress tensors are calculated from electron states, are used to determine the

search direction for finding equilibrium positions of the nuclei, hence the atom positions in the crystal structure.

Though the Born-Oppenheimer approximation simplify the many-particle problem it is still difficult to find solution for Hamiltonian in Eq.1.12 due to correlation property of the electrons which plays important role in superconductivity and quantum Hall effects. On the other hand for many properties of solids correlation of the electrons does not play crucial role. Such properties include, optical conductivity, ohmic conductivity and the most important (for the scope of this thesis) cohesion. Therefore the many-particle problem can be further simplified into a single quantum mechanical particle picture, apparently also ignoring quantum mechanical of behavior of ions.

Several approaches exist to reduce many-particle problem to a single particle states. These are Hartree, Hartree-Fock and Density Functional Theory, DFT. For solids DFT is currently most widely applied method. According to DFT, there is one-to-one relation between total density of electrons, $\rho(\vec{r})$ at ground state and the Coulomb potential arising between electrons and nuclei, V_{e-N}. This allows solving many-particle wavefunctions as the single-particle equations.

$$H_{KS}\phi_i = \varepsilon_i\phi_i \tag{1.13}$$

And total density of electrons, $\rho(\vec{r})$, at ground state, for N electron can be expressed as

$$\rho(\vec{r}) = \sum_{i=1}^{N}\phi_i(\vec{r})^*\phi_i(\vec{r}) \tag{1.14}$$

The Hamiltonian, known as Kohn-Sham Hamiltonian, is expressed as

$$\hat{H}_{KS} = \hat{T}_0 + \hat{V}_H + \hat{V}_{XC} + \hat{V}_{e-N} \tag{1.15}$$

$$H_{KS} = \frac{-\hbar^2}{2}\sum_i \frac{\nabla^2_{\vec{r_i}}}{m_e} + \frac{e^2}{4\pi\varepsilon_0}\int \frac{\rho(\vec{r}')}{|\vec{r}-\vec{r}'|}d\vec{r}' + V_{XC} + V_{e-N} \qquad 1.16$$

The third term is the correlation potential for the electrons and at it is stated above it is largely unknown. Two widely accepted approximations exist for finding the exchange-correlation term; Local-Density Approximation, LDA, and Generalized Gradient Approximation, GGA. These approximations relate the correlation term to the ground state electron density. For LDA the correlation potential can be expressed as

$$E^{LDA}_{XC} = \int \rho(\vec{r})\varepsilon_{XC}\left(\rho(\vec{r})\right)d\vec{r} \qquad 1.17$$

With this equation 1.16 is solvable. In many cases solutions provided with these approximations give quite accurate results and verified by experimental studies.

For solids there are two ways to solve the equation 1.16. All electron states (including core and valance states) can be calculated. Therefore the fine electronic structure of core electrons can also be calculated. Alternatively only valence electrons can be accurately determined. This is known as the pseudo-potential method where core electrons are not included in the calculations since they do not interact with the electrons of other atoms and are not strongly affected by the chemical bonding. This approximation greatly reduces the computation time for the calculations [29].

References

1. A. Geim et al., *Nature Materials*, **6** 183 (2007)
2. M. Corso et al., *Science*, **303** 217 (2004)
3. A.P.Sutton, W.Balluffi, *Interface in Crystalline Materials*, Oxford University Press (2006)
4. R.W. Cahn, P. Haasen (editors), *Physical Metallurgy*, Elsevier Press (1996)
5. K. Barnham, D. Vvedensky (editors), *Low-Dimensional Semiconductor Structures: Fundamentals and Device Applications*, Cambridge University Press (2001)

6. M. Fujita et al., *J. Phys. Soc. Jpn.*, **65** 1920 (1996)
7. L. F. Mondolfo, *Aluminum alloys : structure and properties*, (1976)
8. R. Lok, *Microchemistry of Al Alloys*, Ph.D Thesis TU Delft, (2006)
9. D. William, B. Carter, *Transmission Electron Microscopy: A Text book for Materials Science*, Plenum Press (1996).
10. V. Sechnikov, private communication
11. D.B. Murphy, Fundamentals of light microscopy and electronic imaging, Academic Press (2001)
12. M.Bass, *Handbook of Optics, Volume 3*, (2001)
13. L.Reimer, H. Kohl, *Transmission Electron Microscopy: Physics of Image Formation*, Springer (2008).
14. B. Fultz, J. Howe, *Transmission Electron Microscopy and Diffractometry of Materials*, Springer (2005)
15. D. Shindo, T. Oikawa, *Analytical Electron Microscopy for Materials Science*, Springer (2002)
16. J. Spence, *High Resolution Electron Microscopy*, (2002)
17. E. Kirkland, *Advanced Computing in Electron Microscopy*, Plenum Press (2002)
18. M. Weyland et al., *FEI Nano solutions*, **Issue 1** 24 (2005)
19. S.J. Pennycook, *Ultramicroscopy*, **30** 58 (1989)
20. Dr. Probe by Juri Barthel, Forschung Zentrum Juelich
21. S. Iijima, *J. Appl. Phys.*, **42** 5891 (1971)
22. D. Van Dyck et al, *Ultramicroscopy* **64** 99 (1996)
23. H.W. Zandbergen et al, *Science*, **29** 1221 (1997)
24. J.H. Chen et al, *Science*, **312** 416 (2006)
25. H.W. Zandbergen et al, *Nature*, **372** 759 (2002)
26. J. Cohen, M. Schwartz, *Diffraction for Materials Science*, Springer (1979)
27. J. Jansen et al. Acta. Cryst., **A54** 91 (1998)
28. C. Wolverton. *Modelling Simul. in Mater. Sci. Eng.*, **8** 323 (2000)
29. E. Kaxiras, *Atomic and Electronic Structure of Solids*, Cambridge University Press (2003)

Chapter 2

Transmission Electron Microscopy Study of Precipitation in a Dilute Al-Co Alloy

2.1 Introduction

Cobalt is an important element for many technological materials, from magnets to superalloys and implant materials. However, its use in aluminum alloys is not common. Most of the research on Co containing Al alloys was mostly performed between the two World Wars without success. Until now, no commercial aluminum alloys with Cobalt as main alloying element or as a trace element exist [1,2].

Thus very limited information is available on the precipitation of Co in conventional Al alloys. On the other hand, with the advances of rapid solidification techniques to develop high-strength, high-temperature aluminum alloys achieved during the 1980s, the Al-Co system together with Fe, Cu and Ni additions gained popularity due to the discovery of quasicrystalline phases [3]. In publications on rapidly solidified Al-Co alloys, high Co concentrations were preferred, because rapid solidification would allow an increase in the cobalt in aluminum and therefore would achieve a higher density of precipitated particles [4,5].

The equilibrium phases of the Al-rich part of the Al-Co phase diagram shown in Fig. 2.1 are: (1) FCC Al solid solution and (2) monoclinic Al_9Co_2, which is formed peritectically from the melt [6].

The Al_9Co_2 phase has a monoclinic unit cell with lattice parameters, which, determined from X-ray diffraction, are

a = 0.8565 nm, b = 0.629 nm, c = 0.6213 nm, β = 94.76^0 [7]

It has $P2_1/a$ space group. The unit cell contains 22 atoms: 18 Al atoms and 4 Co atoms. Each Co atom has nine Al atoms as nearest neighbors.

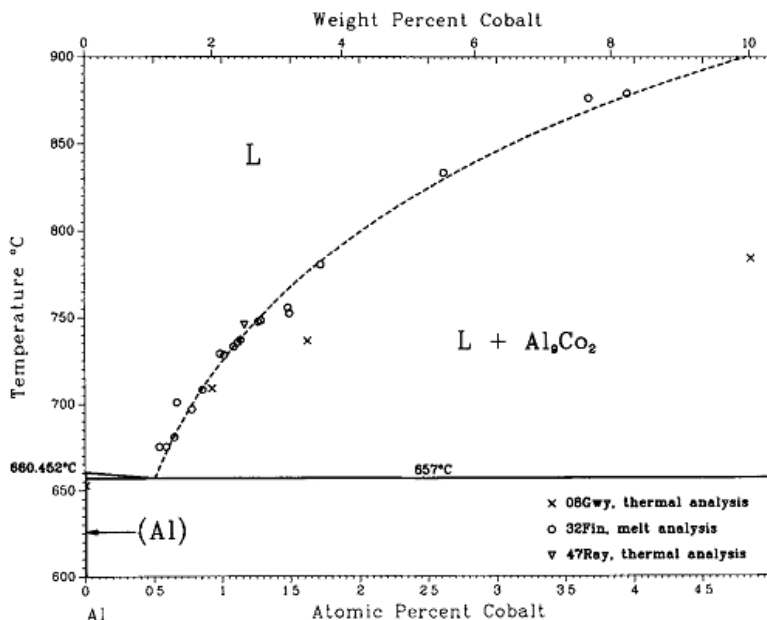**Figure 2.1** Al-Co phase diagram [6]. Below the eutectic temperature there exist two phase region with Al and Al_9Co_2.

Suryanarayana and Van Tendeloo [3] reported that the important phase in Al-rich Al-Co alloys is the Al_9Co_2 intermetallic phase. In addition to Al_9Co_2 those authors also reported a metastable Al_4Co phase in the samples annealed below 673 K. Microstructures of rapidly solidified Al-Co alloys contain Al_9Co_2 precipitates in the shape of Widmanstätten plates formed on {100} planes of the Al matrix. After indexing the electron diffraction patterns, these precipitates were reported to show the following orientation relationship [4]

$$(100)_{Al9Co2}//(001)_{Al}, (031)_{Al9Co2}//(100)_{Al}$$

In order to obtain information on the shape, size and structures of precipitates formed in low Co Al-Co alloys, we have investigated the details of precipitation in dilute Al-Co alloy using high-resolution electron microscopy and nano-beam electron diffraction.

2.2 Experimental Details

The experiments were performed on Al-Co alloy with 0.0092 at% Co. Thus the concentration of Co is just below the maximum solid solubility of Co at eutectic temperature. The as-cast alloys were homogenized at 893 K for 24 hours in an air furnace and then quenched in water at 293 K.

For the transmission electron microscopy investigations a Philips CM300 UT/FEG and a FEI TECNAI F20 operating at 300 and 200 kV, respectively, were used. The microscopes are equipped with fast and slow scan cameras and EDX detectors. Images and diffraction patterns were recorded on a slow scan CCD (charged coupled device) camera. Owing to the low density of precipitates and their small size, nano-beam electron diffraction instead of selected area diffraction was employed in the CM300 UT/FEG TEM to obtain the diffraction patterns from single precipitates.

2.3 Results and Discussion

According to the phase diagram, the solidification of dilute alloy containing 0.15 wt% cobalt will result in Al and Al_9Co_2. Indeed, TEM samples prepared from the as-solidified condition (see Fig. 2.2) contain globular Al_9Co_2 particles called "primary particles". The sizes of these particles vary between 1 and 4 µm. Homogenization heat treatment at 913 K dissolves the cobalt-containing primary particles in the Al matrix, provided that the as-solidified samples are kept at the homogenization temperature for a sufficiently long time. Quenching from the solid solution temperature results in a supersaturated solid solution of the cobalt atoms in the Al matrix.
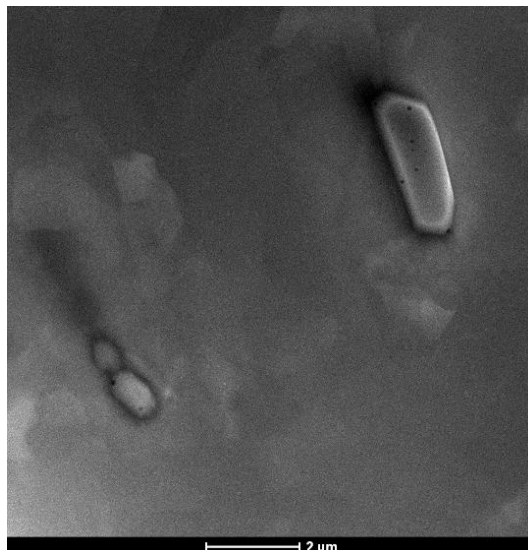
Figure 2.2 Dark-field STEM image of the microstructure of as-cast state of binary Al-Co alloy. Particles formed during solidification (called primary particles) of Al_9Co_2 are identified in the microstructure.

After annealing, few plate-like precipitates could be observed; 5-6 plates were observed inside the Al grains in the approximately 5 μm field of view. The size of these plate-like precipitates ranges from 70 to 120 nm. Occasionally very small plates a few unit-cells wide were also observed. The average thickness of the plates is 5 and 10 nm for heat treatments of 573 and 698 K, respectively. Images of such plate-like precipitates obtained under [013]Al and [001]Al are presented in Fig. 2.3. These plates have a characteristic plate-like aspect ratio, where the ratio of plate length to thickness is higher than 10. Annealing at 823 K changes the morphology of the plates. An example of such a precipitate can be seen in Fig. 2.4. Compared to plates observed in the samples annealed at lower temperatures, the precipitates observed at 823 K become up to 60 nm thick and consequently have a lower aspect ratio. However, plates formed after annealing at 823 K do not lose their orientation relationship with the Al matrix.

Due to low density of precipitates crystal structure of the plate-like precipitates cannot be studied by selected area diffraction since the intensities of the precipitate reflections will be far too weak. Therefore the precipitates were studied by nano-beam electron diffraction. Electron diffraction patterns obtained along $<001>_{Al}$ and $<130>_{Al}$ directions on single precipitates are presented in Fig. 2.5.

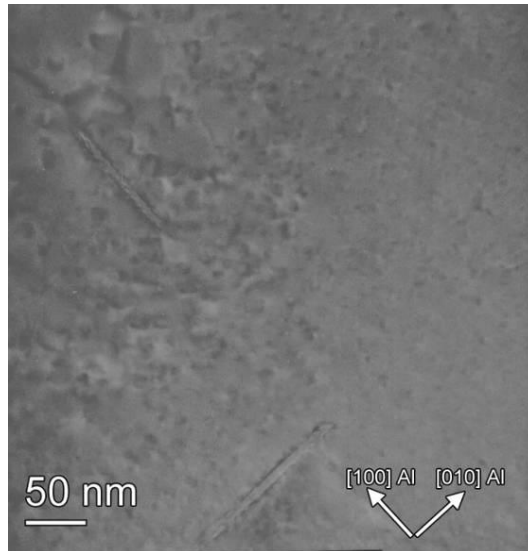**Figure 2.3** Bright-Field TEM image obtained along [100]Al in the microstructure of the 573K annealed Al-Co alloy contain plates-like precipitates. These precipitates are oriented along [001] and [010] Al directions shown by arrow.
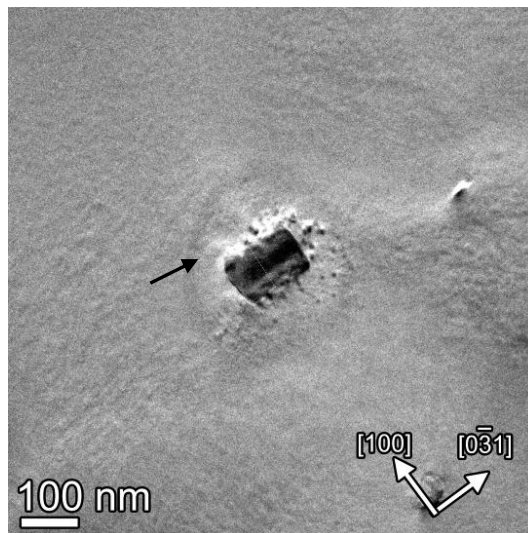

Figure 2.4 Bright-Field TEM image of a plate like precipitate along <013>Al direction formed at 823 K. The Ring (indicated by a black arrow) around the particle is due to carbon contamination deposited at the edges of the electron beam during imaging.

The electron diffraction patterns can be indexed with a monoclinic unit cell with

a= 0.861 nm, b= 0.625 nm, c= 0.621 nm, β= 94.5^0

The electron diffraction patterns can be indexed with a monoclinic unit cell with a= 0.861 nm, b= 0.625 nm, c= 0.621 nm and β= 94.5°. This indicates that precipitates belong to the Al_9Co_2 phase. Lattice parameters were obtained from electron diffraction patterns (DPs) and fast Fourier transformations (FFTs) of high-resolution images. The Al lattice was used as an internal calibration for DPs and FFTs, which allows the accurate determination,[1] especially using FFTs of HRTEM images, of the lattice parameters of Al_9Co_2 precipitates. With this approach, an accuracy of the order of a few picometers (about 0.2-0.3 %) can be achieved. The variation between the determined lattice parameters of Al_9Co_2 precipitates was scattered around the accuracy of the measurement.

Diffraction patterns of precipitates taken along [013], [010] and [001] Al zone orientations are displayed in Fig 2.5 indexed as [013] [001] and [010] Al_9Co_2.

Electron diffraction patterns as well as HRTEM images obtained along in different directions of the Al matrix show that (Fig 2.6) that precipitate 200 planes and the 200 spot of Al lie on the same direction. In Fig. 2.5 (a) one can also see that the 010 spot of the precipitate lie along the [031]Al. Therefore plates of the precipitates form Al {200} (see HREM images in Fig 2.7) and grow along <013> direction of Al. Based on these founding the following orientation relationship is obtained between Al_9Co_2 precipitates and Al matrix;

$(100)_{pr}$ // $(100)_{Al}$ $[010]_{pr}$ // $[031]_{Al}$ and $[001]_{pr}$ // $[01\text{-}3]_{Al}$

In order to verify orientation relationship and explain the features in the experimental diffraction patterns, kinematical diffraction patterns were simulated using JEMS[2] [8]. They are presented in Fig 2.5 (e) and (f). First of all, the experimental diffraction patterns show slight a mistilt. In Fig 2.5 (b) and (c), the diffraction patterns show the presence of 100 and 010 spots where as the electron diffraction pattern in Fig. 2.5 (d) does not have.

This is not in agreement with the space group of Al_9Co_2 reflections which requires h00, h=2n+1 and 0k0, k=2n+1 conditions are extinct, under kinematical diffraction

---

[1] Compared to X-ray diffraction data, the accuracy is about 10 times worse. Therefore, in a crystal structure analysis of nanosized unknown crystals, lattice parameters can be determined from HRTEM and can be further refined with X-ray powder diffraction.

[2] Available from: http://cimewww.epfl.ch/people/stadelmann/jemswebsite/jems.html

conditions. For the [001] and [013] zone axis orientations multiple scattering events causes the presence of symmetry forbidden h00 and 0k0 reflections (for an explanation see Chapter 3).
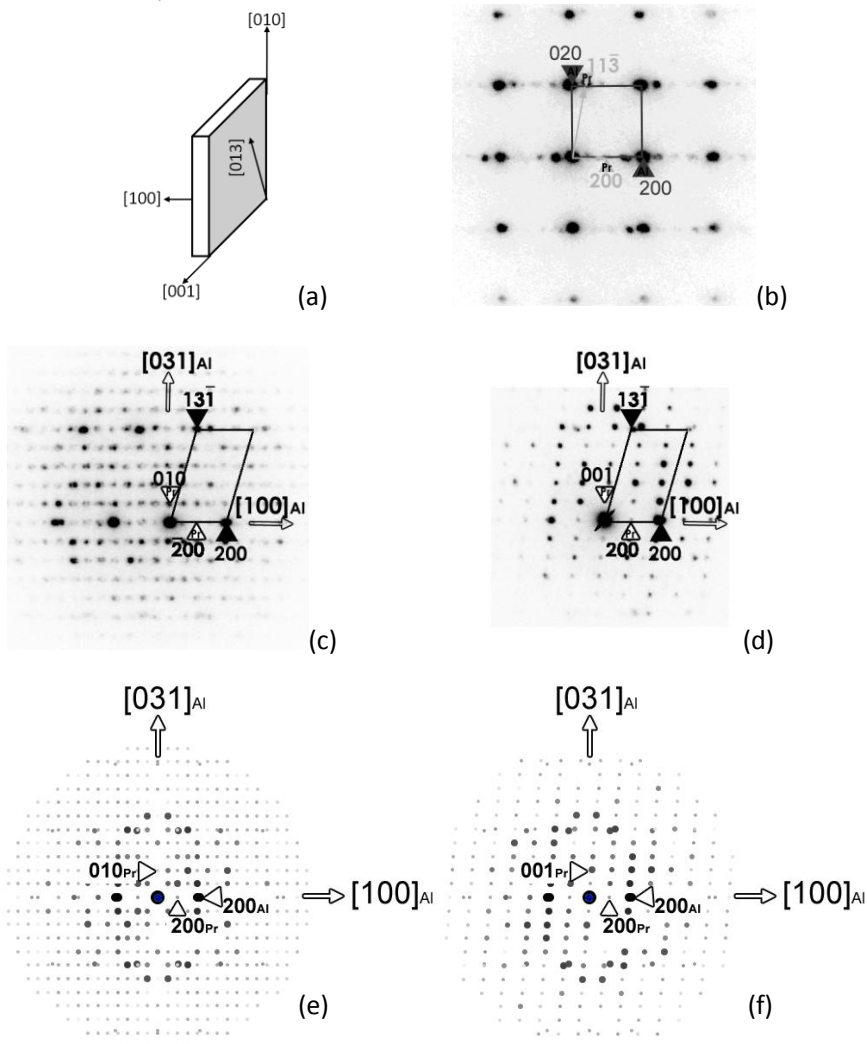

(a)

(b)

(c)

(d)

(e)

(f)

Figure 2.5 (a) Schematic representations of Al$_9$Co$_2$ plate-like precipitates and crystallographic directions. Nano-beam electron diffraction patterns recorded from plates under <001> and <013> oriented Al matrix. Experimental diffraction patterns from Al$_9$Co$_2$ (b) [013], (c) [001], (d) [010] orientations (e) and (f) are simulation of precipitate/matrix diffraction patterns according to orientation relationship given in the text under kinematical scattering conditions for [001] and [010] orientation of Al$_9$Co$_2$, respectively.

Typical examples of HREM images of the plate-like precipitates obtained from samples annealed at 573 and 698 K are presented in Fig. 2.6, which also indicates the unit cell projections and crystallographic directions. Fig. 2.6 (a) shows a [001]-oriented plate formed at 573 K, for which the plate thickness is 5 nm. Fig. 2.6 (b) shows an HREM image of a plate observed in the 698 K annealed sample. This is the thickest plate width, 10nm, observed in 698 K annealed samples.

The Al_9Co_2 precipitates formed as a result of the decomposition of a supersaturated Al solid solution formed by conventional quenching or by rapid solidification are very similar. First of all, the plate-like precipitates reported in this chapter and dispersoids in the studies published in [4] and [5] possess the same orientation relationship. Despite notation differences encountered in the literature, precipitates, plates and dispersoids are all Al_9Co_2 and have a plate-like shape. The main difference is the aspect ratio of the plates (see also Chapter 3). In the study reported here, the thickness of the plate-like precipitates varies between 5-10 nm and their length can be as much as 200 nm for the samples annealed at 573 and 698 K, for which an aspect ratio of 12-14 is found. In samples annealed at 823 K, the plate thickness can be up to 60 nm, whereas the plate length is around 120 nm. This yields a very low aspect ratio of around 2.

In rapidly solidified alloys under similar annealing conditions, the aspect ratio of the precipitates is generally lower than that of the plates formed in this study under similar annealing conditions. Images of plate-like shapes presented in the work of Suryanarayana et al. [4] suggest an aspect ratio of 2-3, where plate shape is not directly obvious. In the literature, plates with low aspect ratios are usually called dispersoids.
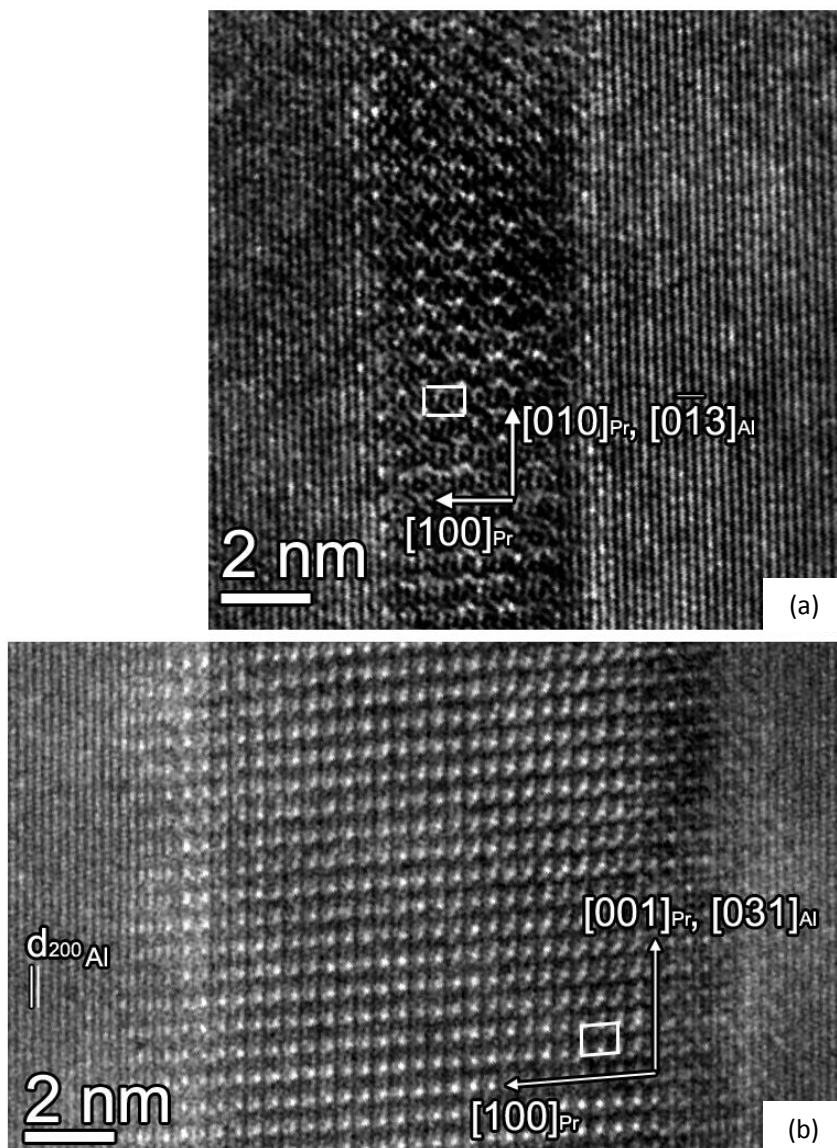
Figure 2.6 HRTEM pictures of Al_9Co_2 plates acquired along the <013> zone axis of Al. Plate sections imaged along (a) [001] (b) [010] zones at (a) 573 K, (b) 698 K, respectively. Unit cell projections are outlined in white color. Arrows indicate the crystallographic directions of Al matrix and Al_9Co_2 structure.

Occasionally very small plates only a few nanometers long and a few atomic layers thick were observed. An example of such a plate is shown in Fig. 2.7. Its shape is very

similar to the ones observed in dilute Al-Ni alloys (see Chapter 3 of this thesis). In the HRTEM images of these very small plates, the periodicity along the long plate direction and the perpendicular direction suggest that these precipitates have a structure very similar to Al_9Co_2. Formation of these very small plates must be due to a change in the nucleation rate during precipitation as supersaturation decreases and the nucleation rate becomes slower. It is safe to conclude that these small plates represent the early stages of Al_9Co_2 plates.

Since these precipitates have thin plate-like shape, the misfit is almost zero along the plate and relatively large misfit is expected (6%) perpendicular to the plate direction due to difference between (200)Al and (400)Al_9Co_2 planes. The thickness of the precipitate in Fig. 2.7 (a) is about 4 {200}Al planes, while the one in Fig. 2.7 (b) is thicker and extend over 12 {200}Al planes (appx 2.5 nm). Fourier filtering applied on the high resolution images in Fig.2.7 to study the details of misfit perpendicular to the plate direction. Inverse Fast Fourier Transform, FFT, formed after masking of 200Al spots in FFTs. Such images contain fringes that represent the {200}Al planes and shows no mismatch for the precipitate in Fig 2.7(a) and a misfit dislocation for the precipitate in Fig. 2.7(b). This is logical because the precipitate shown in Fig. 2.7(c) is thicker and structurally rather well developed compared to the one in Fig. 2.7(a).

It is often cited in the literature [9,10] that precipitation of intermetallics formed between aluminum and transition metals is difficult to happen. Nucleation of an intermetallic phase within Al matrix creates precipitate/matrix interface. This interface is often semi-coherent or incoherent to matrix crystal structure and its formation requires higher energy than the reduction in a volume free energy after formation of a new phase. The net energy needs to be supplied for precipitation is expressed as activation energy barrier. A higher the interfacial energy therefore results higher the activation energy barrier for the nucleation. It is obvious that intermetallics with semi-coherent and incoherent interfaces are difficult to form thorough homogeneous nucleation.

Therefore precipitation in matrix is often assisted by defect sites such as dislocations and low grain boundaries. The disorder at such sites reduces the high energy barrier for the creation of precipitate/matrix interface. As a result, precipitation products are dominated by heterogeneously nucleated precipitates. On the other hand this study shows the formation of early stage of plate like precipitates in Al matrix without presence of defect sites other than vacancies. As the plate-like precipitates get thicker the elastic strain at the plate/matrix interface is relaxed by introducing misfit dislocations as it can be seen in Fig. 2.7(c) and (d). It is obvious from HRTEM images in

Fig 2.6 and 2.7 that early stages of plates and well developed plates posses the same structure and exhibit the same orientation relationship with Al matrix.

Van Tendeloo et al. discussed the possibility of the existence of small precipitates of Al_4Co composition [3]. This phase is structurally analogous to ordered Au_4Mn. Such a precipitate was not observed in the present study. In addition, the proposed Al_4Co phase was not found in Grushko's extensive experimental study of the Al-Co phase diagram [11], nor in the theoretical study of Widom et al. on the comparison of cohesive energies of different experimental and hypothetical intermetallic structures in the Al-Co system [12].
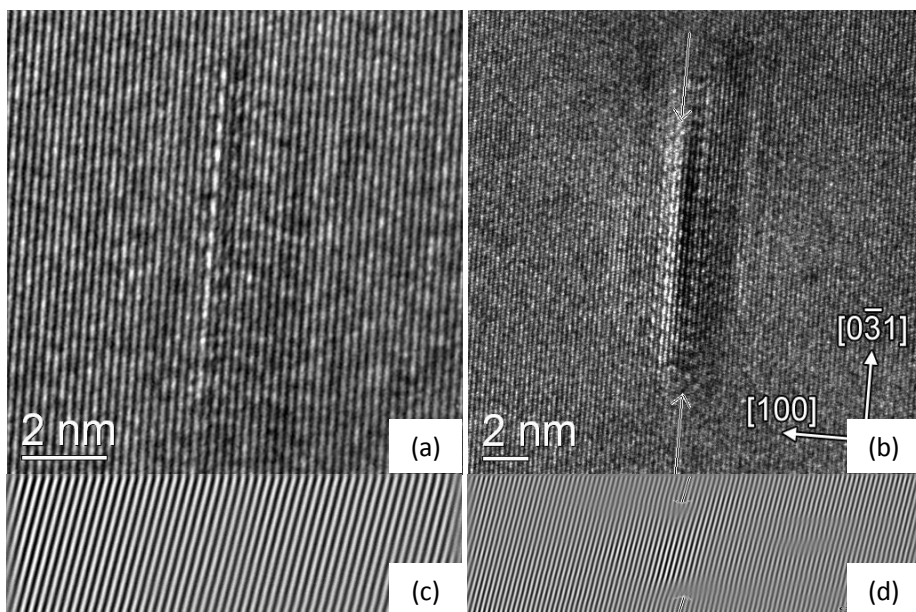
Figure 2.7 (a),(b) Very small plate like Al_9Co_2 precipitates seen through <013> zone axis of aluminum. 200 spots of aluminum were masked in FFTs to create interference image of 200 planes (c), (d) inverse FFT after masking FFT of the images in (a),(b). Inverse FFT in (c) indicates that plate in (a) is coherent and thus shows perfect lattice planes. Inverse FFT in (d) of the plate-like precipitate in (b) shows misfit dislocations at the ends of the plate. Inverse FFT images are compressed in order to avoid aliasing. Note the HRTEM images have different pixel sizes therefore the lattice planes seen in IFFTs have different scales.

References

1. L. F. Mondolfo, *Aluminum alloys : structure and properties*, (1976)
2. J.R. Davis, *Aluminum and Aluminum Alloys*, (1993)
3. B. Grushko et al, *J. Allys, and Comp.*, **233** 279 (1996)
4. G. van Tendeloo et al, *J. Mater. Res.*, **2** 547 (1987)
5. C. Suryanarayana et al, *Bull. of Mater. Sci.*, **17** 121 (1994)
6. B. Predel, Al-Co phase diagram, *Springer Materials Landolt-Börnstein Database*
7. A.M.B.Douglas, *Acta Cryst.*, **3** 19 (1950)
8. P.A. Stadelmann, *Ultramicroscopy*, **21** 13 (1987)
9. R. Cahn, P. Haasen (editors), *Physical Metallurgy*, Elsevier (1996)
10. D. Porter, K. Easterling, *Phase Transformation in Metals and Alloys*, Chapman-Hill (1996)
11. B. Grushko et al, *Z. Metallkd*, **88** 379 (1997)
12. M. Widom et al, *Phys. Rev. E*, **61** 4171 (2000)

Chapter 3

Detailed TEM Study of Precipitates and Particles Formed in Dilute Al-Ni Alloys

This chapter presents the results of studying small plate-like precipitates of Al_9Ni_2. The morphology and the orientation relationship of these precipitates were determined using nanobeam electron diffraction and HRTEM. Numerous structural and planar faults were observed in Al_9Ni_2 precipitates. The crystallographic relationship of the structural faults was derived.

3.1 Introduction

Nickel based Al alloys have been the subject of research for many years due to the extremely high tensile strength of these alloys. Especially the solidification of the eutectic composition (Al – 6.2 wt % Ni), where Al_3Ni fibers forms in the Al matrix, yielding an $Al-Al_3Ni$ composite structure, has been studied extensively [1]. In $Al-Al_3Ni$ composite, Al_3Ni fibers are also deformable at high temperatures and improve the ductility of the composite.

It is generally accepted that adding nickel to commercial aluminum alloys improves their strength as well as their corrosion properties in aqueous solutions at high temperatures [2,3]. On the other hand, dilute Al-Ni alloys have not attracted great interest—neither commercially nor scientifically— because of their poor age hardening response and limited number of intermetallic phases that can be formed during different thermo-mechanical treatments as compared to other Al-rich   Al-TM alloys.[1] Only a few wrought Al alloys with Ni, often together with Fe, is available commercially;

- Alloys of 2xxx series: 2007 and 2014A, less than 0.2 wt % Ni.

- AA8001 series wrought Al alloys with Ni and Fe as main alloying elements, which is recommended for applications in aqueous environments above 373 K in nuclear power-generation applications. The effects of irradiation and void formation in this alloy were also studied by in-situ High Voltage TEM [4].

In addition to these examples, Wada et al. suggested that dilute Al-Ni alloys can be considered a suitable candidate for superconductor solenoid shielding applications because of their low change in residual resistivity ratio and good strength properties as required for a solenoid construction [5,6].

3.2 Al-Ni System

3.2.1 Formation of Al-Ni Precipitates from Solid Solution

Nickel has a very low solubility value in Al compared to similar transition metals. At the eutectic temperature, 913 K, only 0.0121 at. % Ni can be incorporated in the Al

---

[1] Well-known systems are Al-Fe, Al-Cr and Al-Mn with many intermetallic compounds.

solid solution [2]. This value drastically decreases with decreasing temperature. For example, at 600 K, the solubility of Ni decreases to 0.0006 at %, and at room temperature practically no Ni can be kept in solid solution under equilibrium conditions. Alternatively, rapid solidification techniques such as splat cooling can enhance the Ni content of the solid solution as much as 10 at. % [2].

The Al-rich part of the Al-Ni phase diagram shows that, under equilibrium conditions, Al-rich Al-Ni alloys consist of an α-Al and Al_3Ni phase [2,7,8]. One expects from the phase diagram that Al_3Ni phase is formed during the decomposition of supersaturated solid solution. This phase has an orthorhombic unit cell with Pnma space group symmetry. Its lattice parameters (after X-ray diffraction) are a = 0.6611 nm, b = 0.77366 nm and c = 0.8411 nm [9].

The first detailed investigation of the precipitation of dilute Al-Ni alloys was performed by Yamamoto and Tsubakino on a 0.01 at. % Ni-containing Al-Ni alloy [10]. These authors showed that the decomposition of supersaturated solid solution below 823 K resulted in the formation of precipitates of metastable Al_9Ni_2 phase in the microstructure, instead of a stable Al_3Ni phase. Al_9Ni_2 precipitates are found in the plate morphology.

The precipitation sequence in dilute Al-Ni alloys is generally accepted to be

Supersaturated solid solution → Al_9Ni_2 (metastable) → Al_3Ni (stable).

The Al_9Ni_2 phase crystallizes into a monoclinic cell with $P2_1/a$ space group symmetry and its lattice parameters are given as

$$a = 0.8685 \text{ nm}, b = 0.6232 \text{ nm and } c = 0.6185 \text{ nm},$$

after X-ray diffraction studies [11]. Al_9Ni_2 precipitates were found to exhibit an orientation relationship with Al matrix [9], which is given as

$$(001)_{Al}//(001)_{Pr} \& [-310]_{Al} // [010]_{Pr} .$$

Although the Al_9Ni_2 phase is metastable, its precipitates appear to be very stable, as shown by Yamamoto et al. [10], who found no change in Al_9Ni_2 precipitates after annealing the Al-Ni alloys at 793 K for 76 hours. They observed an Al_3Ni phase in the alloys after 330 h annealing at 823 K. In contrast to Al_9Ni_2 precipitates, Al_3Ni precipitates formed within an Al matrix do not show an orientation relationship with the Al matrix [10].

3.2.2 Growth Characteristics of Plate-like Precipitates

Continuous growth of coherent or semi-coherent interfaces, as is often the case for the broad faces of plate-like precipitates, is difficult because an attachment of a single atom to a flat interface will raise the interfacial energy and the atom will tend to detach itself. The growth problem can therefore be overcome if the interface contains series of ledges (a shelf that protrudes from a normal to a surface/interface) normal to the interface and atoms are able to move more easily across the ledges than across the coherent flat interface [12,13]. It is now generally accepted that plate-like precipitates, formed on low-index planes, thicken by a ledge mechanism [13]. The thickening of plate-like precipitates therefore depends on the kinetics of the nucleation and the growth of thickening ledges on the broad faces of the plates. Earlier studies on precipitate-thickening kinetics in Al-Ag and Al-Cu alloys [14-15] have concluded that the overall thickening kinetics is ultimately restricted by nucleation of new ledges. In these studies, plates have low-misfit values. The effect of a misfit between the plate-like precipitates and the Al matrix normal to the plate direction has been considered in Al-Cu-Mg-Ag alloys and concluded that elastic interactions between the misfitting coherent ledges and the significant strain field prohibit the coherent ledge nucleation [16].

3.2.3 Role of Iron Al-Ni Alloys

Iron is present as an impurity element in dilute Al-Ni alloys. According to the Al-rich part of the Al-Ni-Fe phase, the following phases can be in equilibrium with Al in the Al–Fe–Ni ternary system: Al_3Ni and $Al_9(Ni,Fe)_2$. Figure 3.1 represents the solidification surface projection and the distribution of phase domains in solid state in the Al corner of the ternary phase diagram [17]. The $Al_9(Ni,Fe)_2$ phase is formed according to the following peritectic reaction:

$$L + Al_{13}Fe_4 + Al_3Ni \rightarrow Al_9(Ni,Fe)_2 \,,$$
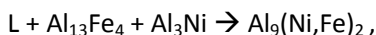
when Al-rich Al-Fe-Ni first solidifies the $Al_9(Ni,Fe)_2$ phase as a result of the triple eutectic, and then solidification is completed by a second eutectic reaction (L$\rightarrow$ Al_3Ni+Al) with the formation of the Al_3Ni phase. Therefore when the local concentration of Fe is consumed to form $Al_9(Ni,Fe)_2$ particles, the remaining amount of Ni forms Al_3Ni particles.
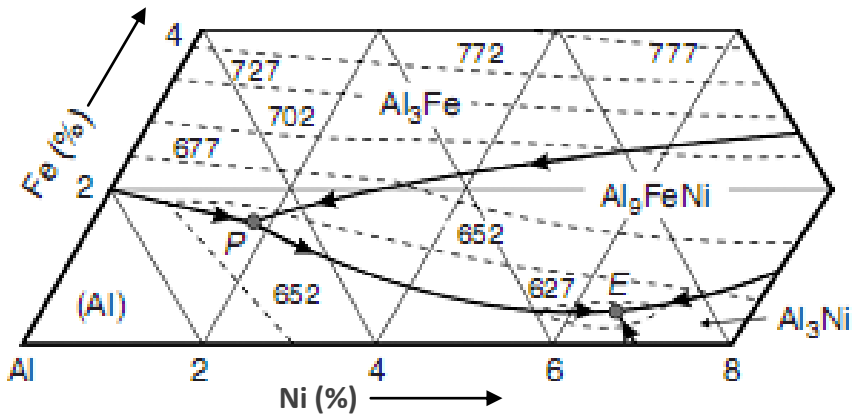
Figure 3.1 Liquidus projection of Al-rich corner of ternary Al-Fe-Ni phase diagram [17]. Axes of the diagram are the atomic percent concentration of Fe and Ni.

The higher thermal stability of the $Al_9(Ni,Fe)_2$ phase is due to a peritectic reaction. Al_3Ni dissolves during a homogenization treatment near the eutectic temperature, but the $Al_9(Ni,Fe)_2$ phase is remains undissolved.

This work presents a detailed analysis of precipitates formed in dilute Al-Ni alloys. As the precipitation sequence in this system has not been studied in detail in terms of homogenization-quenching-annealing sequences, the focus was on determining the nucleation location, size and structure of the precipitates that form during annealing, as well as on their crystallographic relation to the Al matrix.

3.3 Experimental

A binary Al-0.0092 at. % Ni alloy prepared from high-purity aluminum (99.995 %) and nickel (99.99 %) was produced by ingot casting (Chapter 1). The chemical composition of the alloy is listed in Table 1.1. The as-cast alloys were homogenized at 893 K for 24 hours in an air furnace and then quenched in water at 293 K.

For the transmission electron microscopy investigations presented here, a FEI TITAN, Philips CM300 UT/FEG and a FEI TECNAI F20 operating at 300 and 200 kV, respectively, were used. The microscopes are equipped with fast and slow scan cameras and EDX detectors. Images and diffraction patterns were recorded on a slow-scan CCD (charged coupled device) camera. Owing to the low density of precipitates

and their small size, nano-beam electron diffraction was employed in the CM300 UT/FEG TEM to obtain the diffraction patterns from single nanoprecipitates. With this technique a small condenser aperture of 10 μm, strong gun lens settings and small spot sizes were used to form a small, almost parallel, electron probe[2] of about 2 nm.
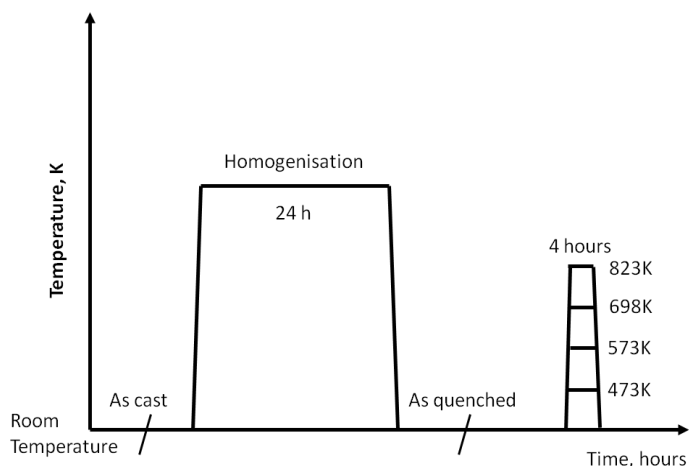

Figure 3.2 Heat treatment scheme for Al-Ni alloy. As-quenched alloys were kept in a refrigerator before annealing treatments to avoid early precipitation.

3.4 Results and Discussion

3.4.1 Primary Particles

This section reports the coarse intermetallic particles formed in the alloy during the solidification process. This type of investigation is important because the particles have to be dissolved in solid solution to obtain a significant amount of precipitation. As these particles are present in the as-cast specimens, they are called "primary particles". The as-cast structure of Al-Ni alloys consists of sub-micron-sized grains of the Al matrix with low-angle grain boundaries, Figs. 3.3(a) and (b). Al_3Ni and $Al_9(Ni,Fe)_2$ particles were detected using TEM, electron diffraction patterns and EDX, Figs. 3.3(c) and (d).   Long strings of particles (or a train of particles) were found in the

---

[2] The convergence angle of the electron probe was calculated from high-magnification diffraction patterns and was found to be around 0.46 mrad which indicates the almost parallel small electron probe.

microstructure, Fig. 3.3(b). A string can contain up to ten particles, the sizes of which range from 0.5 to 1 μm as seen in Fig. 3.3.

We did not observe an orientation relationship between the primary particles and the Al matrix. This is in contrast to the result found by Bendersky et al. [18], who observed $Al_9(Ni,Fe)_2$ particles with an orientation relationship in rapidly solidified Al-Ni alloys. The presence of an orientation relationship between particles and the Al matrix suggest that Al-Ni intermetallics form as a result of the decomposition of the solid state. The existence of primary particles that do not have an orientation relationship in the first place indicate that the formation of these particles does not result from the decomposition of the solid solution during cooling. Instead they can be formed in the melt. For the formation of strings of particles, two different mechanisms are proposed, as illustrated in Fig. 3.4.

The first mechanism, shown in Fig. 3.4(a) is adapted from Sato and Ohira [19], who showed that, at a slow/intermediate rate of solidification, strings of particles are formed in the regions between solidified Al cells/large grains where solute-rich liquid regions are present. This implies that we would expect to find primary particles, possibly at high-angle grain boundaries, formed via this mechanism. However, this is contradictory to the observed microstructure, where particles were located on low-angle boundaries.

The second proposal is based on the grain boundary pinning effect of nickel. It is known that adding Ni to Al, combined with fast solidification, hinders the growth of Al grains during solidification and results in refined grain size [2]. Therefore low-angle grain boundaries are expected to be rich in Ni. The BF-TEM image in Fig 3.3(b), as well as numerous BF-TEM and Z-contrast STEM images obtained on the as-cast samples, shows that the particles prefer to align at low-angle grain boundaries. Therefore, during solidification and cooling, it is possible that Ni-rich, low-angle grain boundaries can lead to the simultaneous nucleation of particles along a low-angle grain boundary. When these particles grow, they meet and form strings of particles, as shown schematically in Fig. 3.4(b).
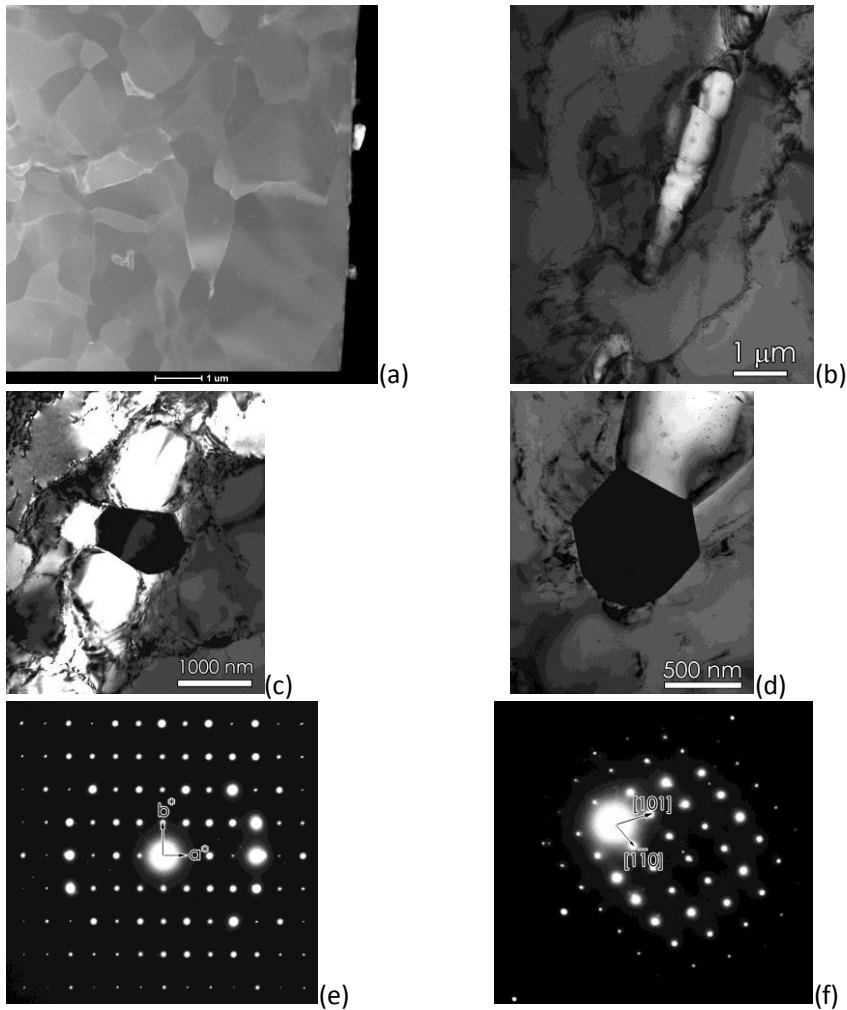
Figure 3.3 (a) Annular dark-field STEM image of as-cast Al-Ni alloy, which reveals a fine microstructure composed of small (less than 1 μm) primary particles with low-angle grain boundaries. The presence of grain boundaries is attributed to the channeling of electrons during scanning through areas with slight misorientations. This results in a difference in contrast. (b) Bright-field TEM image of a string of primary particles seen in the microstructure. (c) and (d) are TEM images of primary particles. They appear darker because the particles are under zone axis orientation. (e) and (f) are diffraction patterns taken from particles on (c) and (d), respectively. The diffraction patterns are identified as the $Al_9(Ni,Fe)_2$ and Al_3Ni phases, respectively.

As-cast alloys were homogenized at 933 K for 24 hours to dissolve the primary particles and then quenched in water at room temperature. These as-quenched samples were found to contain few primary particles that did not dissolve during homogenization. These particles have a globular shape and their sizes are around 1 μm. They were identified from SAD patterns as being the Al_9Ni_2 phase. Chemical analysis of these particles shows that they all contain Fe and Ni, see Fig. 3.5(b). Interestingly, no Al_3Ni phase was observed in the microstructure of the as-quenched specimen.

(a)   (b)
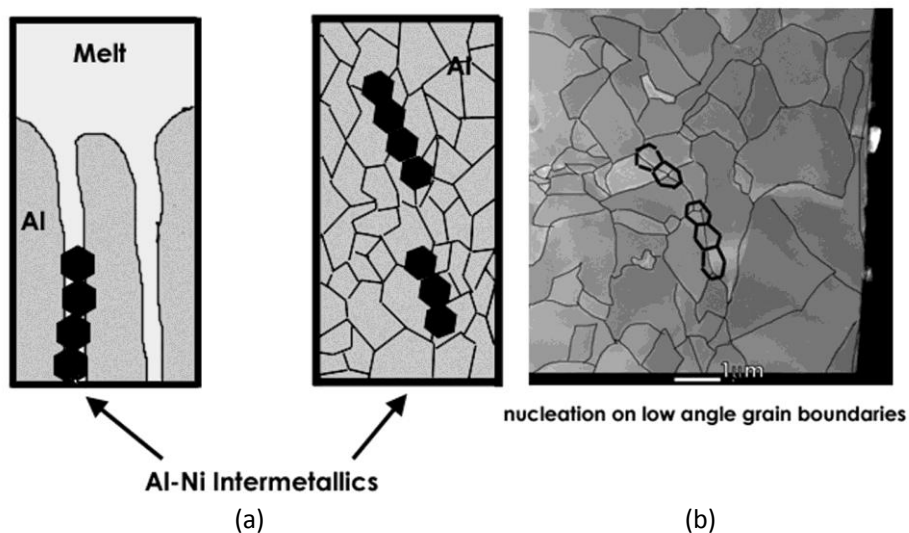
Figure 3.4 Schematic representation two different formation mechanisms of strings of intermetallics in an as-cast microstructure of Al-Ni alloy. (a) From the melt during slow cooling, (b) solid solution decomposition starts at low-angle grain boundaries during cooling.

The composition of primary particles and the Ni/Fe ratio were determined by EDX analysis. The quantification results for the particles are presented in Table 3.1. It is important to note that EDX spectra were collected from particles with similar thicknesses and avoiding zone axis orientations. Therefore the degree of X-ray absorption of Fe and Ni and fluorescence of Fe by Ni (K_α) radiation can be assumed to be similar for each spectrum, which allows the direct comparison of the quantification results. Particle numbers 1 to 8 presented in Table 3.1 shows the composition of the $Al_9(Ni,Fe)_2$ phase, whereas particles 9-10 are from the Al_3Ni phase observed in the as-cast alloy. The results of the quantification indicate the ideal compositions of Al_9Ni_2 and Al_3Ni. The small differences are attributed to the inaccuracies of standardless

quantification. Particles 5 and 8 yield Al-rich compositions. The difference to the Al_9Ni_2 composition is as high as 15%. In this case we assume the Al matrix must have contributed to the EDX signal due to specimen geometry.

The Fe/Ni ratio of the particles in the Al_9X_2 host structure varies between 5 and 3.8 (20 to 27%). The difference must be related to the local Fe content during formation of the $Al_9(Ni,Fe)_2$ phase.
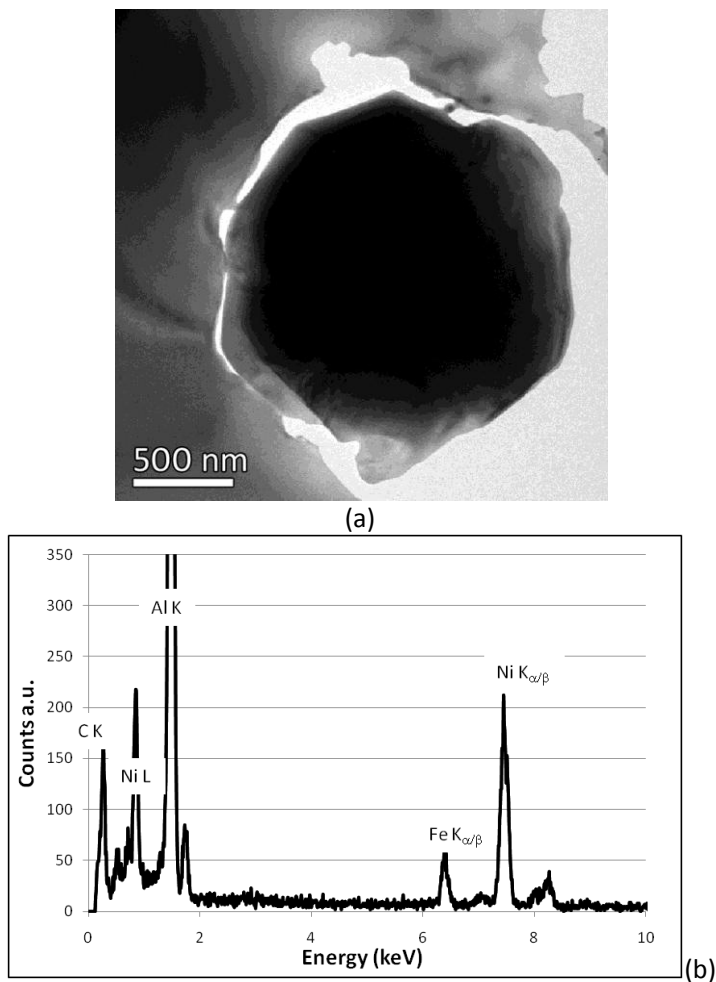

(a)

(b)

Figure 3.5 (a) Zero-loss filtered TEM image of a large particle formed during solidification of a dilute Al-Ni alloy and (b) EDX spectra obtained on the particle. C signal is due to contamination.
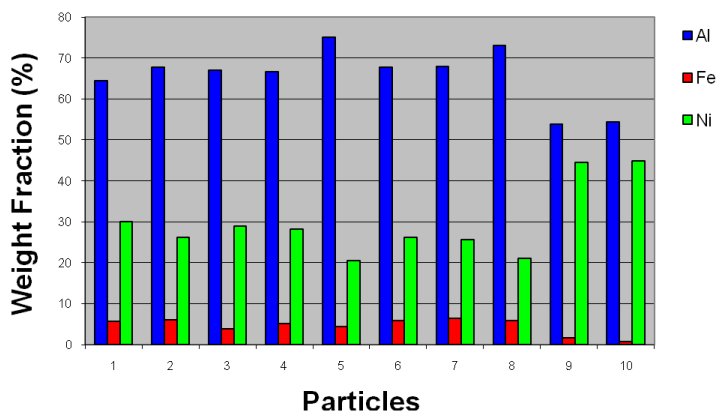
Table 3.1 Composition of coarse intermetallic particles (primary particles) found in Al-Ni alloys. The horizontal axis shows 10 discrete particles numbered from 1 to 10. Ideal composition of particles is given in the footnote[3].

3.4.2 Precipitates

Plate-like precipitates were observed in the microstructure of Al - 0.0092 at % Ni alloy after annealing at 473, 573 and 698 K. Figure 3.6 shows a HAADF image of the Al-Ni plates formed in the Al matrix observed along <100>Al, as well as a SAD pattern of precipitates and a BF image, all observed in a sample annealed at 573 K. The plate normal is directed along <100>Al. The thickness and length of these precipitates were analyzed using Z-conrast STEM and HREM images. For the sake of consistency, only [001]-oriented plates were used for measurements. As is evident in Fig. 3.6(d), precipitates have different lengths along the [010] and [001] axes. The plate thicknesses and lengths were measured for three temperatures: 473, 573 and 698 K. The mean thickness of the precipitates increases from 1 to 6 nm as the annealing temperature was raised from 473 to 698 K.

3

Wt. %	Al_9Ni_2	Al_3Ni
Al	67.63	58.2
Ni	32.37	41.8

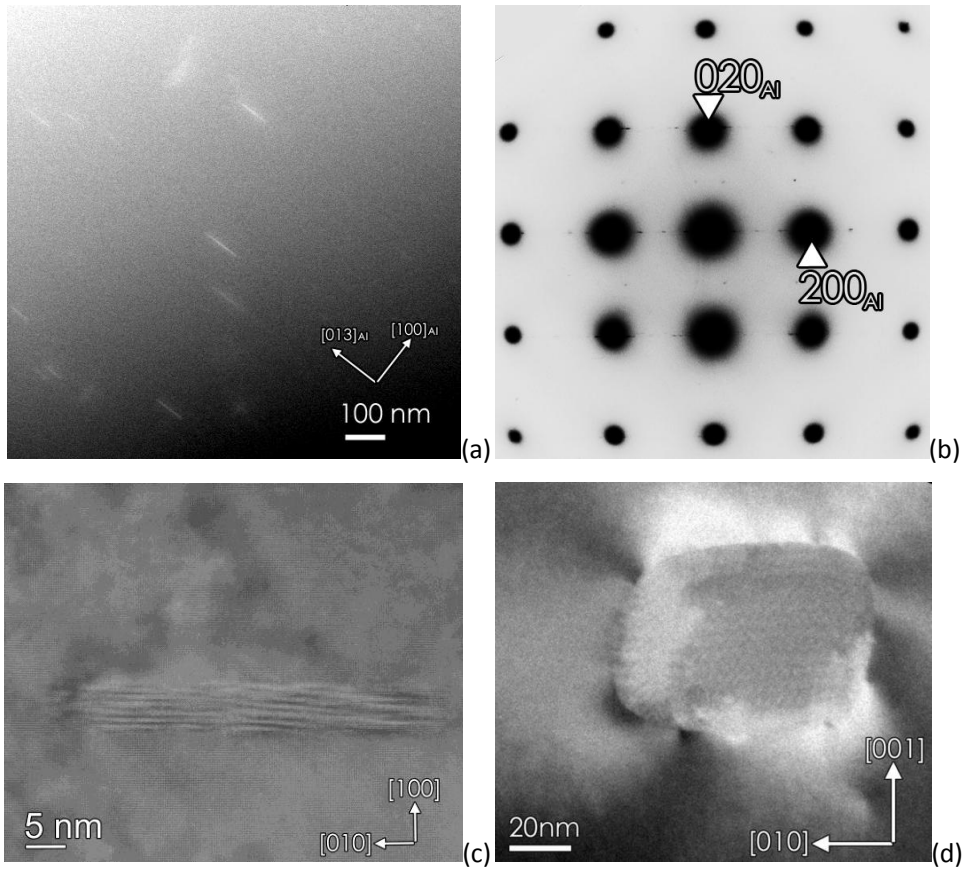**Figure 3.6** (a) Annular Dark Field STEM image obtained along the <013>Al on a sample annealed at 573 K. Sharp lines in the image are the precipitates viewed edge-on. (b) BF-TEM image of a plate-like precipitated viewed perpendicular to the plate direction. (c) BF-TEM image of a plate-like precipitate viewed parallel to plate direction. (d) Selected area diffraction pattern from the precipitates in presented in (b).

The length of the precipitates is found to range between 10 and 250 nm. The distribution of the lengths and length-thicknesses of these precipitates is different for the two annealing temperatures 573 and 698 K; they are presented Figs. 3.7(a) and (b). As the number of precipitates in the microstructures of samples annealed at 473 K was far too low to draw statistical conclusions, the data are not included in the distribution graphs. The thickness of precipitates we observed was around one unit cell in the [100] direction and the length was around 10 nm. Such an HREM image from a precipitate of a sample annealed at 473 K can be seen in Fig. 3.8. For the

specimen annealed at 573 K, the mean length of the precipitates is 82 nm with a mean thickness of 4.8 nm. The shortest precipitate length measured for the sample annealed at 573 K is 30 nm with a thickness of 2 nm, and the longest precipitate is 225 nm with a thickness of 7.7 nm. The mean length for the specimen annealed at 698 K is 132 nm with a mean thickness of 6.3 nm. In the investigation of the sample annealed at 698 K, the shortest precipitate is 70 nm long and the longest one is 250 nm long. The relationship between the precipitate length and thickness of the samples annealed at 573 and 698 K is presented in Fig. 3.7(c).

It is obvious that, at all three annealing temperatures, the growth/thickening mechanism of the plates follow the same path. The graph in Fig. 3.7(c) shows two trends. In the early stage of plate growth up to approximately 100 nm, the slope and thickening of the plate is faster than during the phase where the precipitates are longer than 100 nm.

Ledge formation and movement are responsible for the coarsening of plate-like precipitates. Two factors define the thickening kinetics of plates. The first is the supply of solute[4] atoms via bulk diffusion, which leads to solute atoms to the plate matrix interface and to the existing ledge. The second factor is the nucleation of the ledges at the interface. The former defines diffusion-controlled process whereas the latter is interface-controlled and often slower than diffusion-controlled processes. The faster thickening of the small plates indicates that, once the ledge is formed, diffusion of Ni to the ledge is fast and therefore the ledge can propagate easily in the early stage of the precipitates. However, as the plates become thicker, the supply of Ni atoms to the existing ledges is lowered, thus slowing the plate-thickening process.

---

[4] Solute, a substance dissolved in solvent, forming a solution.
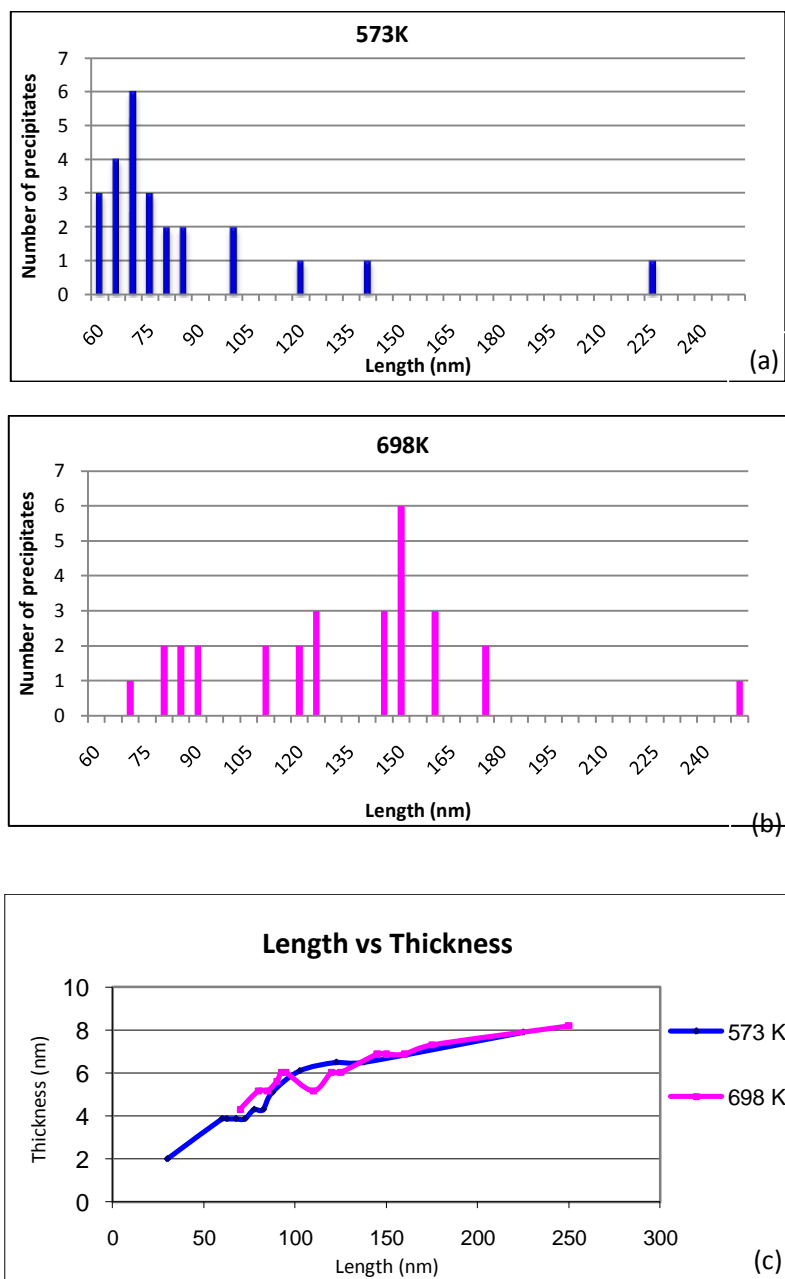
Figure 3.7 Distribution of the length of plates measured in samples annealed at (a) 573 K and (b) 698 K; (c) change of plate thickness for different plate lengths.
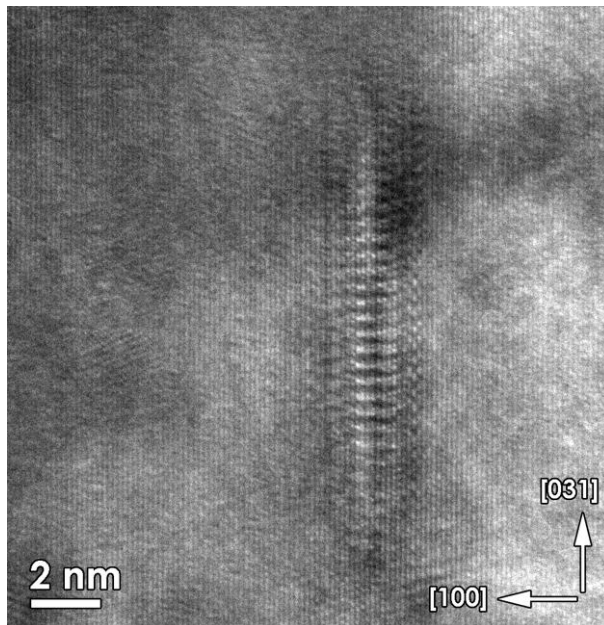
Figure 3.8 HRTEM image of a precipitate observed in sample annealed at 473 K. Al matrix is oriented along <013>. Precipitate shows high degree of coherency with Al matrix.

After annealing at 823 K, plate-like precipitates can no longer be observed but bigger and irregularly shaped precipitates were found both at grain boundaries and inside Al grains. The size of these precipitates was in the range of several hundreds of nanometers. Images of these grain boundary and matrix particles are shown in Fig. 3.9.
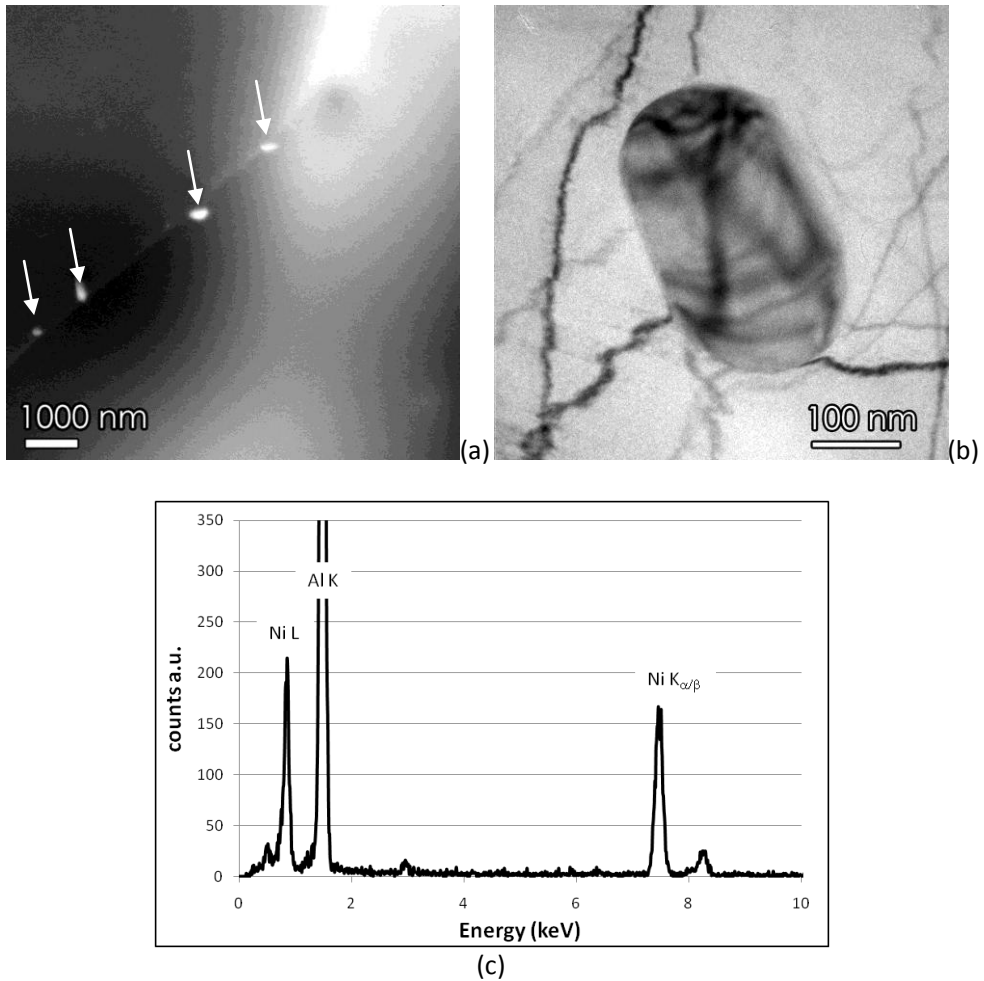
Figure 3.9 (a) HAADF image of grain boundary precipitates (indicated by white arrows) (b) Bright-Field TEM image of a matrix precipitate formed in the microstructure of Al-Ni alloys annealed at 823 K for 4 h. These precipitates show no orientation relationship with the Al matrix. (c) EDX spectra obtained from the matrix precipitate. No Fe was detected in the Al_3Ni precipitates.

Analysis of the nano-beam electron diffraction patterns and HRTEM images, taken at the samples annealed at 573 and 698 K, show that the plate-like precipitates are metastable Al_9Ni_2 phase with monoclinic unit cell. The averaged lattice parameters are

a= 0.868 nm, b= 0.626 nm, c= 0.619 nm and b= 96.5˚.

The rectangular precipitates in the sample annealed at 823 K were found to be the orthorhombic Al_3Ni phase with lattice parameters calculated from the diffraction patterns,

a= 0.67 nm, b= 0.84 nm, c= 0.43 nm.

Al_3Ni phase was observed only in the samples annealed at 823 K. Precipitation of Al_3Ni was observed both at grain boundaries and the matrix. The number of matrix precipitates is less than the number of grain boundary precipitates. EDX spectra from precipitates at both locations show no difference in their chemical composition. Unlike Al_9Ni_2 precipitates they show no orientation relationship with the Al matrix.

Quenched-in vacancies must play a role in the formation of the Al_9Ni_2 phase, as suggested by Yamamoto et al.'s resistivity measurement study on the decomposition of an Al(Ni) solid solution [10]. They can enhance the diffusion of solute atoms during annealing. In addition to this they can form clusters and dislocation loops, where heterogeneous nucleation takes place. However, at higher annealing temperatures, quenched-in vacancies will disappear quickly, leaving no room for heterogeneous nucleation to take place.

At annealing temperatures above 823 K, precipitates of the stable Al_3Ni phase form in the Al matrix and on high-angle grain boundaries. Most of the Al_3Ni phase prefers to form at grain boundaries and few of them are able to nucleate in the Al matrix. The Al_3Ni phase has an orthorhombic crystal structure and is structurally less similar to the Al lattice than Al_9Ni_2 is. A notable difference between two crystal structures is that, the more Ni is present in the Al_3Ni crystal structure, the more it loses the layered character of the Al_9Ni_2 structure. Despite the high driving force to reduce the free energy by forming the Al_3Ni phase, the relatively high activation energy barrier due to the incompatibility of the Al_3Ni structure with the Al matrix prevents the easy nucleation of Al_3Ni. Therefore, at annealing temperatures below 823 K, Al_9Ni_2 precipitates form instead of Al_3Ni precipitates. The Al_3Ni phase can overcome the activation energy barrier only at temperatures above 823 K. But at such conditions most vacancies and lattice defects are also annealed out, otherwise they can facilitate the nucleation of Al_3Ni by lowering the interface energy, creating heterogeneous nucleation sites. Under these conditions the formation of incoherent Al_3Ni precipitates takes place heterogeneously mainly at grain boundaries. This explains the reason why Al_3Ni is difficult to form in the matrix but not at the grain boundaries.

3.4.3 Composition of Precipitates and Incorporation of Fe in the Precipitates

Several EDX line scan experiments were performed in STEM mode. The EDX spectra collected during line scan experiments on Al_9Ni_2 and Al_3Ni precipitates and their results are presented in Fig. 3.10-11. The EDX spectra were then quantified with the EMISPEC software package using standardless quantification. Figure 3.11 shows the extracted weight concentrations of elements versus scan length. The quantification results (compared to the results from primary particles) show a lower Ni concentration. This is understandable because particles are embedded in the Al matrix and a significant amount of Al is therefore present in the collected spectra.

As the Al_9Ni_2 phase can host Fe, as was shown for primary particles formed during solidification, Fe dissolved in a saturated solid solution can be incorporated into the Al_9Ni_2 phase during the precipitation process. EDX was employed to check the presence of Fe in the plate-like precipitates and the Al_3Ni grain boundary precipitates. No Fe was detected in the grain boundary precipitates. Fe and Ni K_α raw signals obtained on the EDX detector from the plate-like precipitate, shown in Fig. 3.10(a), during the line scan are displayed in Fig. 3.12. In this graph, the variation of the Fe K_α signal over the line scan follows almost the same path as the variation of the Ni K_α signal. Therefore, in the case of plate-like precipitates, Fe is incorporated into the Al_9Ni_2 structure.
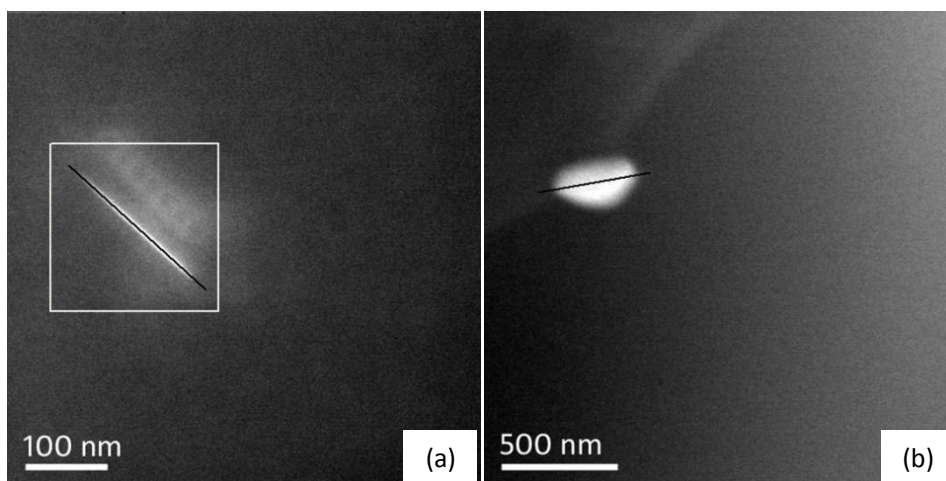

Figure 3.10 EDX Line scan experiments in STEM mode. (a) Precipitate in Al matrix (b) on a grain boundary precipitate. Imaging performed by a HAADF detector. The white rectangle box in (a) is used to correct the drift during the experiment. EDX spectra were collected along the black lines.
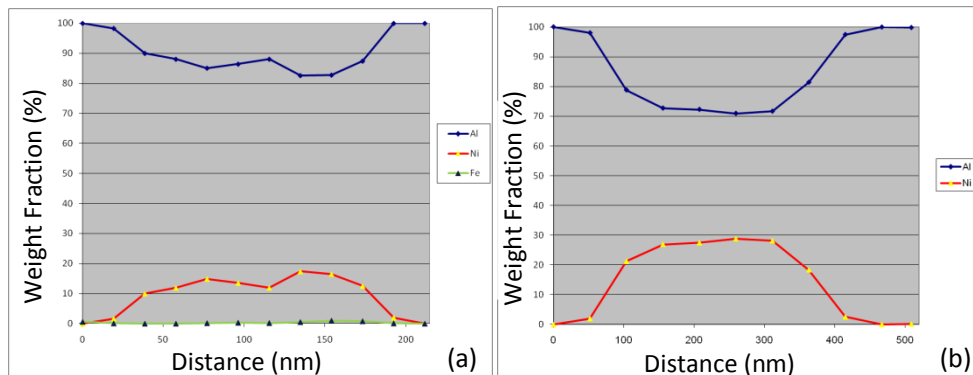
Figure 3.11 Weight fractions extracted from EDX spectra collected during line scan experiments shown in Fig. 3.10. (a) Precipitate in Al matrix (b) Grain boundary precipitate. Data collection points along the profile are indicated by small triangles on the curve.
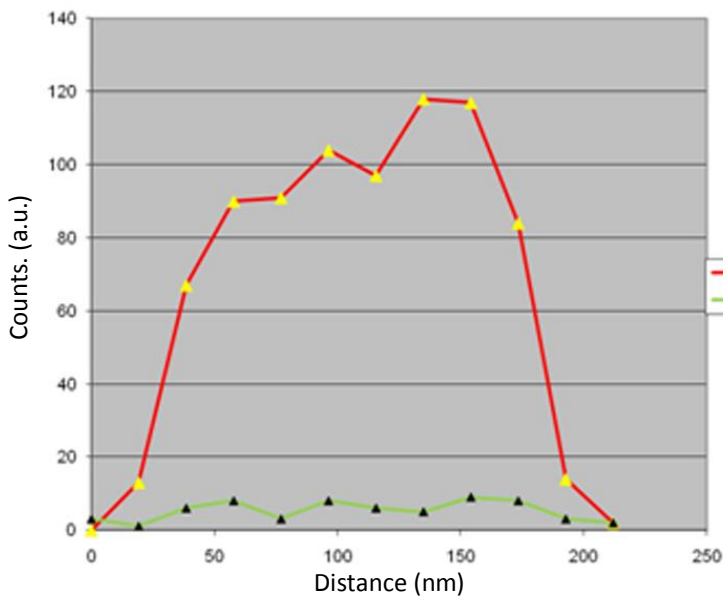

Figure 3.12 Profile of the integrated intensities for Ni and Fe K_α signals obtained in Fig. 3.9(a). Data collection points along the profile are indicated by small triangles on the curve.

3.4.4 Orientation Relationship and Structural Details of Al_9Ni_2 Precipitates

Figure 3.8 shows an HRTEM image of an Al_9Ni_2 precipitate observed in an early stage of precipitation of a sample annealed at 473 K. This HRTEM image as well as other images we recorded clearly indicates the presence of coherency between Al_9Ni_2 precipitates and the Al matrix as the long axis of the plate is directed along <013>Al and the plate normal is along   <100>Al. Nano-beam electron diffraction patterns taken from two Al_9Ni_2 precipitates found in a sample annealed at 698 K under [100] Al are shown in Figs. 3.13(a) and (b). The strongest spots in the diffraction patterns belong to <001>Al. The spots that have smaller reciprocal distances than that of Al and are aligned along the principle directions of the Al reciprocal lattice belong to monoclinic Al_9Ni_2. They were found to have originated from the [013], [031] zone axes diffraction patterns, respectively.   The diffraction patterns presented in Figs. 3.13(c) and (d) were taken along the [013]Al zone axis (obtained by tilting 18 degrees along $[100]_{Al}$).   In Fig. 3.13(c) the diffraction pattern of the precipitate is indexed as [001]. This orientation shows that in the reciprocal space, the [100] axis of the precipitate is parallel to [100]Al, and $[010]Al_9Ni_2$ is parallel to [031]Al. The diffraction pattern in Fig. 3.13(d) is indexed as $[010]Al_9Ni_2$. Simulated diffraction patterns for the precipitate/matrix configurations in Figs. 3.13 (c) and (d) are shown in Figs. 3.13(e) and (f). Superimposed kinematical diffraction patterns from Al and Al_9Ni_2 unit cells show a good match with the observed diffraction patterns in Figs. 3.13 (c) and (d). The appearance of $(100)Al_9Ni_2$ and $(001)Al_9Ni_2$ spots are due to double diffraction. For example, -130 and 2-30 spots, indicated by arrows in Fig. 3.13(e), produce the kinematically forbidden 100 reflection.
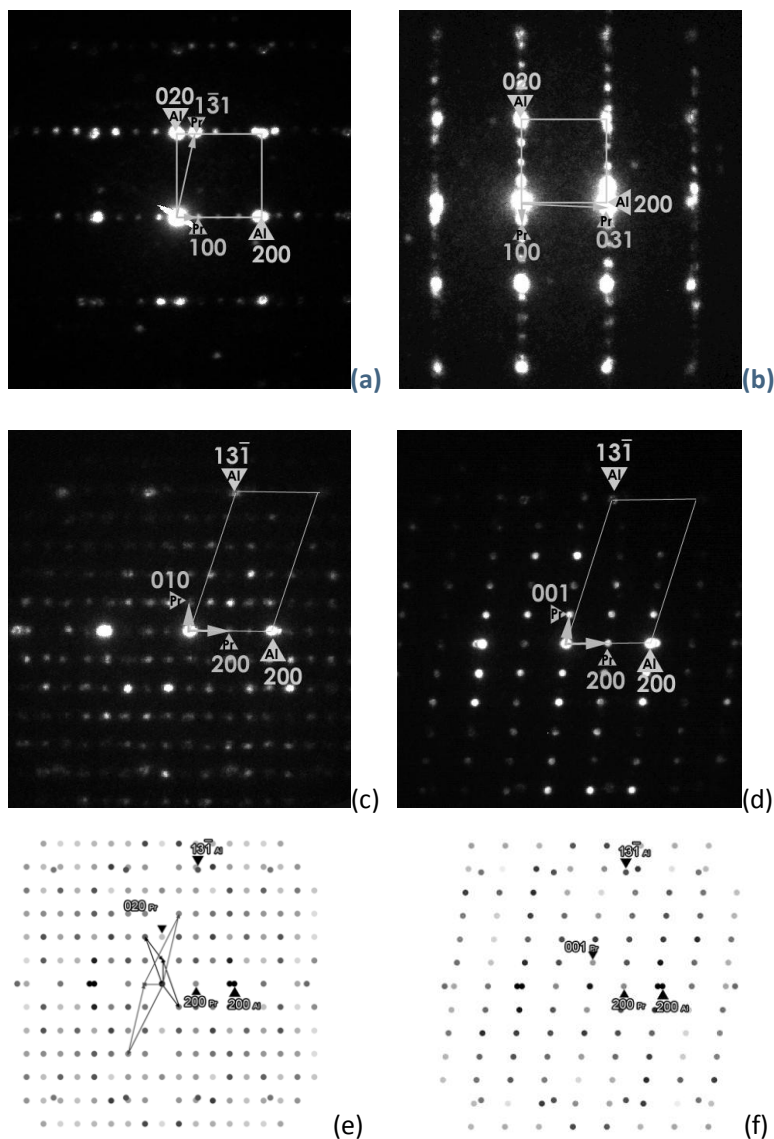
Figure 3.13 Nano-beam electron diffraction patterns obtained from Al_9Ni_2 plates under <100>Al zone axes. In (a) precipitates are under [013] zone axis, in (b) precipitates are under [031] zone axis. Nano-beam electron diffraction patterns obtained from Al_9Ni_2 plates under <013>Al zone axes, precipitates are under (c) [001] and (d) [010] zone axes. Simulated kinematical electron diffraction patterns of Al matrix and Al_9Ni_2 plates. (e) [013]Al // [001]Al_9Ni_2 and (f) [013]Al // [010] Al_9Ni_2. Arrows represent reciprocal lattice vectors, $\mathbf{g}_{2\text{-}30} + \mathbf{g}_{1\text{-}30} = \mathbf{g}_{100}$.

The diffraction patterns and HREM data indicate the following orientation relationship between Al_9Ni_2 precipitates and the Al matrix:

$$[010]_{Pr}//031_{Al} \text{ \& } (100)_{Pr}//\{100\}_{Al} .$$

The orientation relationship between Al and Al_9Ni_2 yields 24 variations of the Al matrix. Al_9Ni_2 plate-like precipitates can grow with their plate normal parallel to the {100} [(100), (010) and (001)] planes, and the plates can grow in 8 different <013> directions. The origin of the orientation relationship is a direct result of the resemblance of the atomic planes of Al_9Ni_2 to Al planes. The orientation relationship between Al_9Ni_2 plates and the Al matrix is illustrated in Fig. 3.14. It is evident in the schematic representation in Fig. 3.14 that Al-rich planes of Al_9Ni_2 and (100) Al planes have similar configurations. It is logical to consider the Al_9Ni_2 structure as being composed of alternating layers of pure Al and Al/Ni mixed planes. In Fig. 3.14(c) a perspective view of Al and Al_9Ni_2 unit cells is presented. For the sake of clarity, only a single Al plane (oriented in [013] direction) is shown in the left part of the picture. In the right part, an Al-rich plane of Al_9Ni_2 is seen. In the front part, only Al planes are shown and the next plane, composed of Ni and Al atoms, is omitted in order to demonstrate the resemblance between the two planes. Red dots represent Al atoms; blue dots represent Ni atoms. Cyan dots represent Al positions where two planes match. It is obvious that the planes of Al atoms in Al_9Ni_2 in [010] and [001] directions show a similar atomic configuration to [013]-oriented Al planes. Therefore it is natural for such a layered structure with a strong similarity to Al planes to form on {100}Al planes.

HRTEM, STEM and Bright-Field TEM images taken along $[010]Al_9Ni_2$ $[001]Al_9Ni_2$ and $[100]Al_9Ni_2$ indicate that precipitates have a plate-like geometry and that their shape is not disk-like but more like a thin rectangular prism with rounded edges, as can be seen in Fig. 3.6(c).

HREM images and diffraction patterns (Figs. 3.8, 3.12 and 3.13) show that (400) lattice planes of Al_9Ni_2 ($d_{(400)}$=0.215 nm) are parallel to the Al (200) planes ($d_{(200)}$= 0.20259 nm) and that the actual misfit value between these planes is 6.1%, as shown in Fig. 3.14(b). In the case of a complete relaxation of the misfit strain at semi-coherent interfaces by misfit dislocations, spacing between misfit dislocations is given by the ratio of the length of Burger's vector of a dislocation and the misfit value [13]. Therefore, along [100], one misfit dislocation can be expected for every 23 Al (200) planes, which is 4.6 nm. The HREM image in Fig. 3.15(a) shows the interface between (400) lattice planes of Al_9Ni_2 and Al (200). The thickness of this precipitate is 4.4 nm.

The Fourier filtered image of Fig 3.15(a) presented in Fig 3.15(c) shows the presence of a misfit dislocation at the precipitate/matrix interface. An extra (200)Al plane is present and the misfit dislocation indicated by the large arrow can be clearly seen. This dislocation has an edge character, and the Burgers vector of an edge dislocation in fcc structure is 1/2<110>Al, which is a common dislocation for fcc metals.

(a)

(b)

(c)

(d)

Red: Al atoms   Blue: Ni atoms   Cyan: Matching Al atoms on both structures
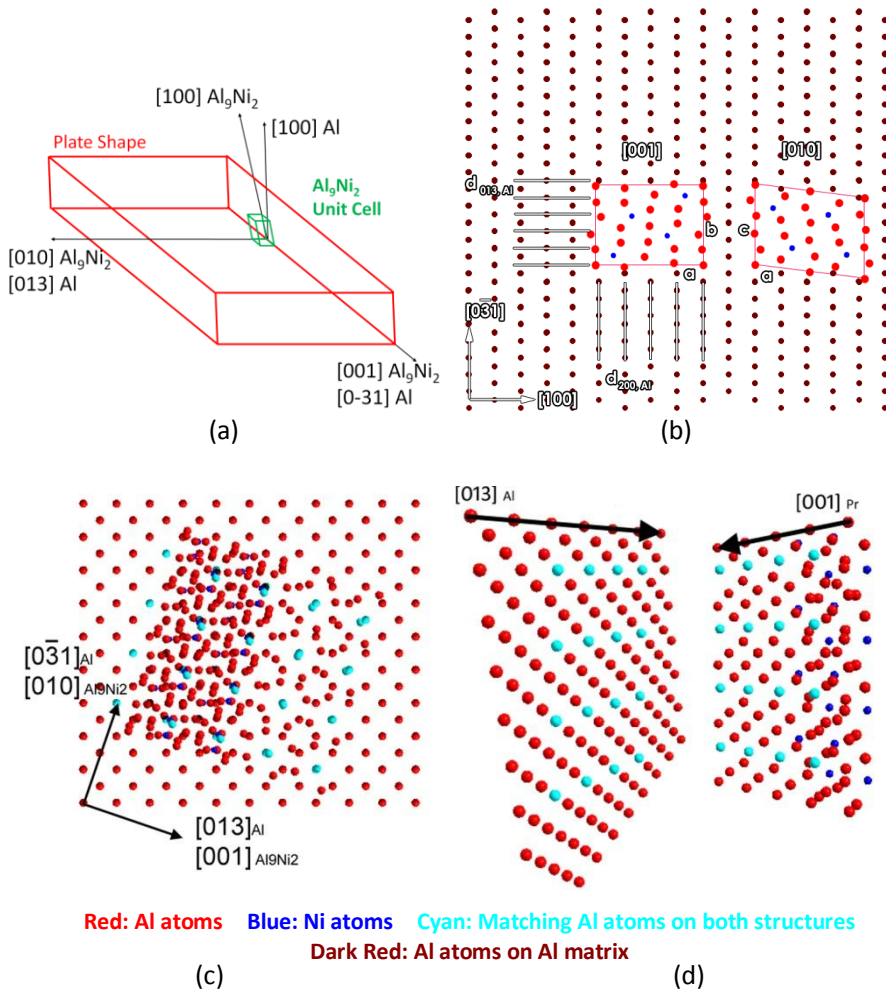**Dark Red: Al atoms on Al matrix**

Figure 3.14 (a) Schematic representation of an Al_9Ni_2 plate in an Al matrix. (b) Schematically represented orientation relationship between precipitates and Al matrix seen along $[013]_{Al}$. [001] and [010] unit cell projections of Al_9Ni_2 unit cell are superimposed on the Al lattice. (c) Interface between Al and Al_9Ni_2 seen through plate direction. (d) Perspective views of Al planes in Al and Al_9Ni_2 structures.
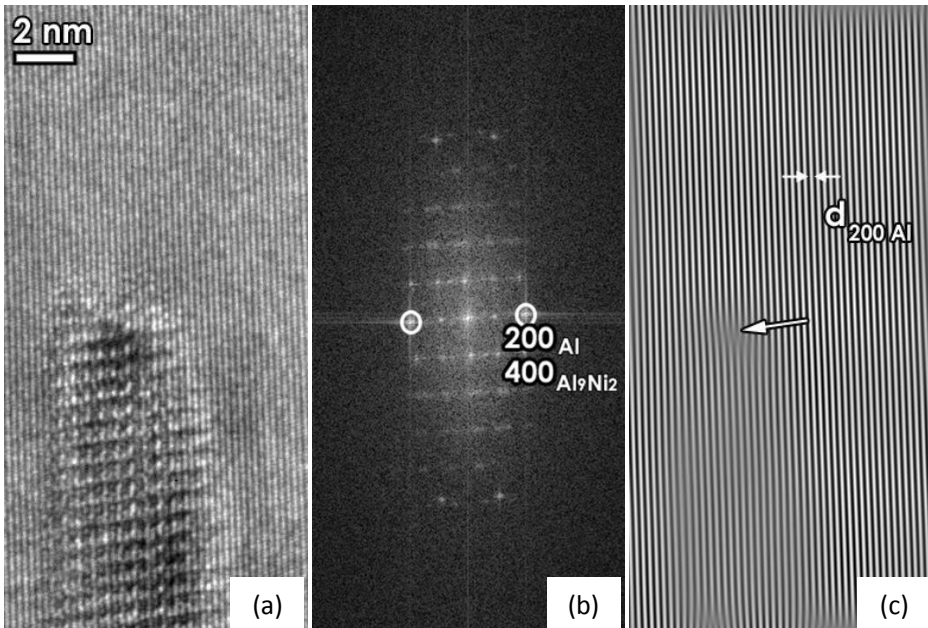
Figure 3.15 (a) HREM image of an end of an Al_9Ni_2 precipitate. (b) Details of the matrix-precipitate interface were studied by applying Fourier filtering to the FFT pattern of image (a) that contains the interface [15]. The circled regions indicate where the $(400)Al_9Ni_2$ and $(200)Al$ spots were masked in the FFT. Then the filtered FFT pattern was inverse-Fourier filtered. The result is the enhanced image of misfitting planes presented in (c).

An ideal misfit of 2.4% and 3.7 % exists between (001) and (010) planes of Al_9Ni_2 and 5 {013} planes of aluminum,[5] respectively (see Fig. 3.14). Therefore, in the growth direction of Al_9Ni_2 precipitates, one misfit dislocation is expected for every 11 nm in [001] and 10 nm in [010] Al_9Ni_2 directions. A BF-TEM image of a plate observed in the 573 K sample under [010] zone axis presented in Fig. 3.16 shows the (edge on, the interface is straight, not inclined) precipitate matrix interface with a strain contrast spacing of 13 nm.

---

[5] $d_{(001)Al9Ni2}$=0.628 nm, $d_{(010)Al9Ni2}$= 0.615 nm, $d_{(013)Al}$ = 0.128 nm.
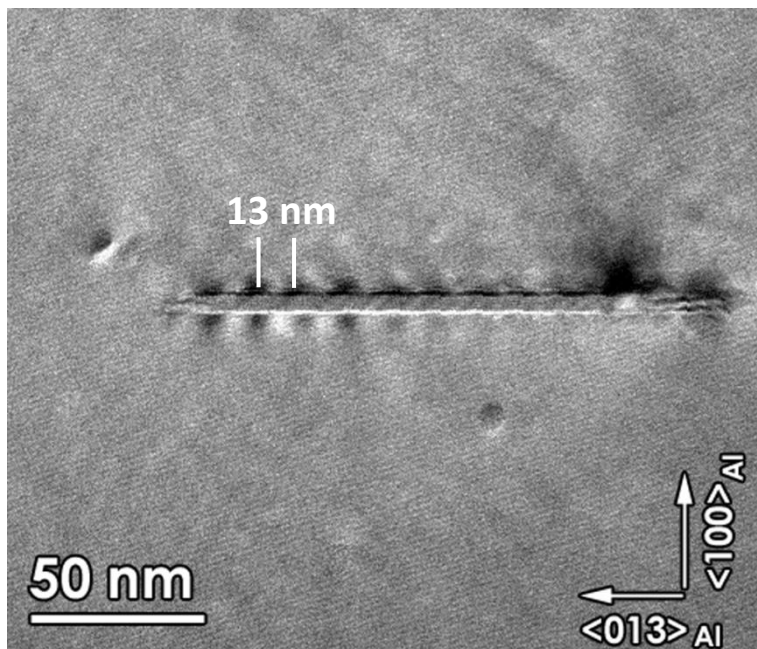
Figure 3.16 Edge-on Bright-Field TEM image of a precipitate seen through the $[013]_{Al}$ zone axis. Strain contrast as a result of the misfit between the plate and the Al matrix is visible at the interface. The spacing of strain contrast is 13 nm.

According to the orientation relationship, (010) planes of Al_9Ni_2 are parallel with (013) planes of Al, the misfit value between planes is 3.5%, and (001) planes of Al_9Ni_2 can be matched with (013) planes of Al introducing a misfit of 2.4%. Therefore the Al matrix must be strained to match with Al_9Ni_2 precipitates because, in general, an Al lattice must be more elastic than the Al intermetallics. The measured lattice parameters of the Al_9Ni_2 unit cell are slightly different from those found on bulk Al_9Ni_2 crystals, and the **b** axis of the Al_9Ni_2 unit cell can expand to match with Al planes, whereas the **c** value can be shortened to keep the unit cell volume unchanged. Therefore the misfit values on broad faces decrease in the [010] Al_9Ni_2 direction, whereas it increases in [001] Al_9Ni_2.   As is also shown above, strain contrast spacing is longer than expected value in the [001] Al_9Ni_2 direction. It can therefore be concluded that the misfit between Al_9Ni_2 precipitates and the Al matrix is smaller than the misfit between ideal Al_9Ni_2 structure and the Al lattice.

In the annealed samples, precipitates with planar faults and structural defects were often observed. Analysis of HRTEM images and electron diffraction patterns revealed

the presence of three different types of faults;

- Twin (Fig. 3.17)
- Twist (Fig. 3.19)
- Complex planar (Figs. 3.21-3.22)

The first type occurs as a simple twin, where one side of a precipitate appears to be mirrored relative to the other side. An HRTEM image of such a precipitate observed in the sample annealed at 573 K is shown in Fig. 3.17(a). In this image, the left and right parts of the precipitate are separated by a sharp interface and the parts appear to mirror each other. The nano-beam electron diffraction patterns taken from the left and right parts of the precipitate are presented in Figs. 3.17(b) and (c), respectively. These diffraction patterns can be indexed with that of $[010]Al_9Ni_2$ and related to each other by a 180° rotation of the **b** axis, defined by operation

$$\begin{pmatrix} 1 & 0 & 0 \\ 0 & \bar{1} & 0 \\ 0 & 0 & 1 \end{pmatrix}.$$
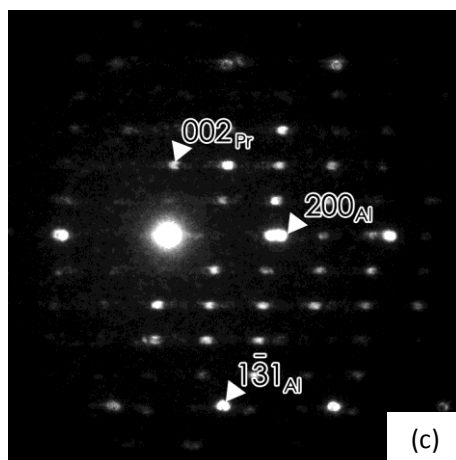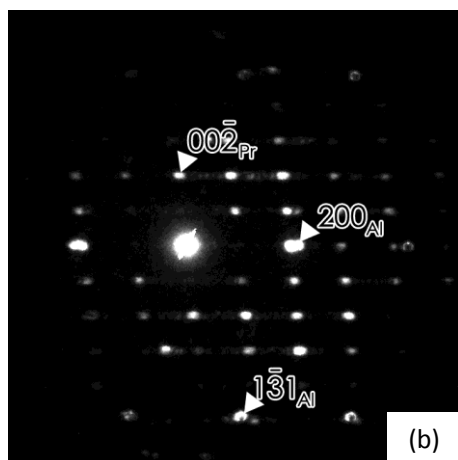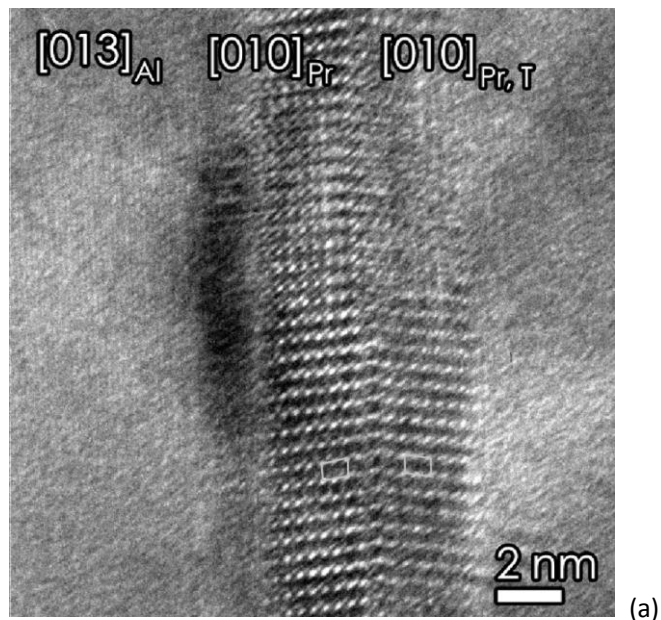
(a)

(b)

(c)

Figure 3.17 (a) HRTEM image of a twinned Al_9Ni_2 precipitate taken along [013]Al. The unit cell projections in twins shown in white. Twin regions are only 4 unit cell wide. (b) and (c) are nano-beam diffraction patterns from the left and right parts of the twin interface. Diffraction patterns are related by a mirror.

In Fig. 3.18(a) a simple model is displayed that explains the twinning of Al_9Ni_2 precipitates schematically. If the left part of the precipitate is indexed as [010] Al_9Ni_2, the right part of the precipitate, according to the rotation operation defined above, is

indexed as [0-10] Al_9Ni_2 and the right part can described as the inversion of the left part. As the right part has the same zone axis orientation as the left part, only inverted, it also follows the orientation relationship with the Al matrix. It is evident from the HRTEM image and diffraction patterns that the common plane in both parts are the $(100)Al_9Ni_2$ planes. This is the habit plane of the twin and it also coincides with $(200)Al$ planes in accordance with the orientation relationship. In Fig. 3.18(b) the twinned (using the atom positions given in Chapter 4) and the non-twinned unit cell of Al_9Ni_2 in the **b** direction is superimposed onto the [013]Al matrix according to the orientation relationship concluded in the previous section. At first glance at this illustration it is obvious that twinning the precipitate does not help to accommodate the elastic strain between the $(200)Al$ and $(400)Al_9Ni_2$ planes (6.1% misfit).

Red: Al atoms in Al_9Ni_2
Blue: Ni atoms
Dark Red: Al atoms on Al matrix
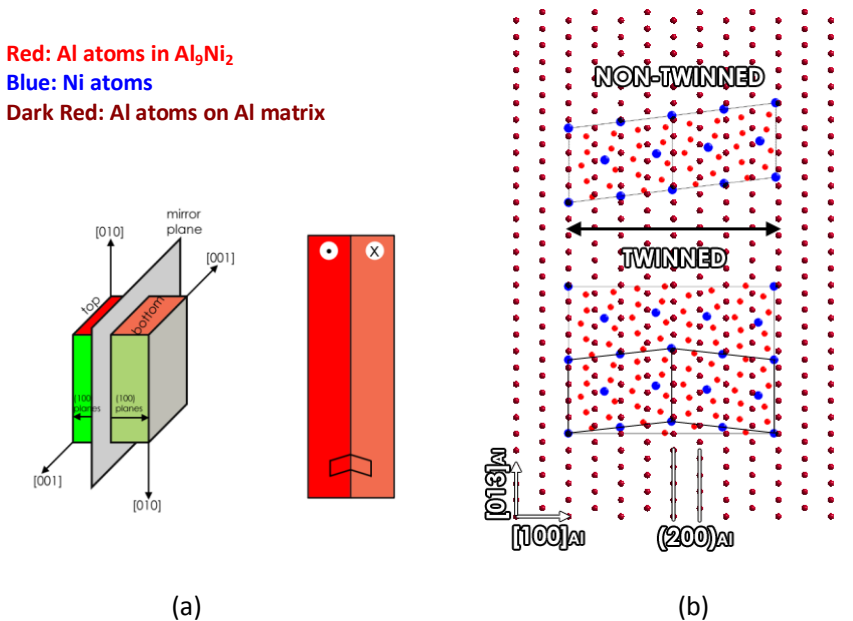
(a)   (b)

Figure 3.18 Twin-type fault formation in Al_9Ni_2 plates. (a) Crystallographic relationship between left and right parts of the precipitate. If the left part is chosen to be the [010] orientation, the right part has [0-10] orientation. (b) Superimposed Al matrix and twinned and non-twinned Al_9Ni_2 unit cells. Rectangle seen under twinned area defines a supercell that contains the twin.

The second fault type is a 90° rotation twin (called twist) observed frequently in samples annealed at 573 and 698 K. In the rare case of a well-grown precipitate as shown in Fig. 3.19, twist-type faults are clear to see (see also Z-contrast HRSTEM in

Chapter 4, Fig. 4.4). This precipitate contains three parts that are joined across $(100)Al_9Ni_2$ planes, which are rotated 90° relative to each other. Therefore, this precipitate can be considered a stacking of [010] Al_9Ni_2, [001] Al_9Ni_2 and [010] Al_9Ni_2-oriented precipitates. The twist formation is schematically represented in Fig. 3.20(a) and can be defined by the operation

$$\begin{pmatrix} 1 & 0 & 0 \\ 0 & 0 & 1 \\ 0 & 1 & 0 \end{pmatrix}$$

The **b** and **c** axes of the Al_9Ni_2 unit cell have very similar lengths and only differ by 2.3%. The HRTEM image in Fig. 3.19(c) shows the perfect matching when the axes are swapped at the interface by a 90° rotation, making the two axes equal. Moreover strain contrast is not observable at the interface. These findings suggest that the rotated planes match perfectly at the interface and the lattice mismatch of 2.3 % is elastically accommodated.

A closer look at the twist precipitate in Fig. 3.19(b) reveals that the precipitate has various ledges. The most notable ledges are on the right part of the matrix/precipitate interface, but these ledges are mainly responsible for the thickening of the plates. In Fig. 3.19(b), the interface between the twisted regions shows that the interface also has steps. Probably, the [001]-oriented middle part formed first and, during its growth, ledges formed. HRTEM images of many precipitates obtained along <013>Al were analyzed and most of the precipitates were found to contain twist faults, whereas only a few precipitates with twin faults were seen for all the samples. Al_9Ni_2 precipitates and, generally speaking, in Al_9X_2 phases, that contain neither twin nor twist faults have been reported in the literature.

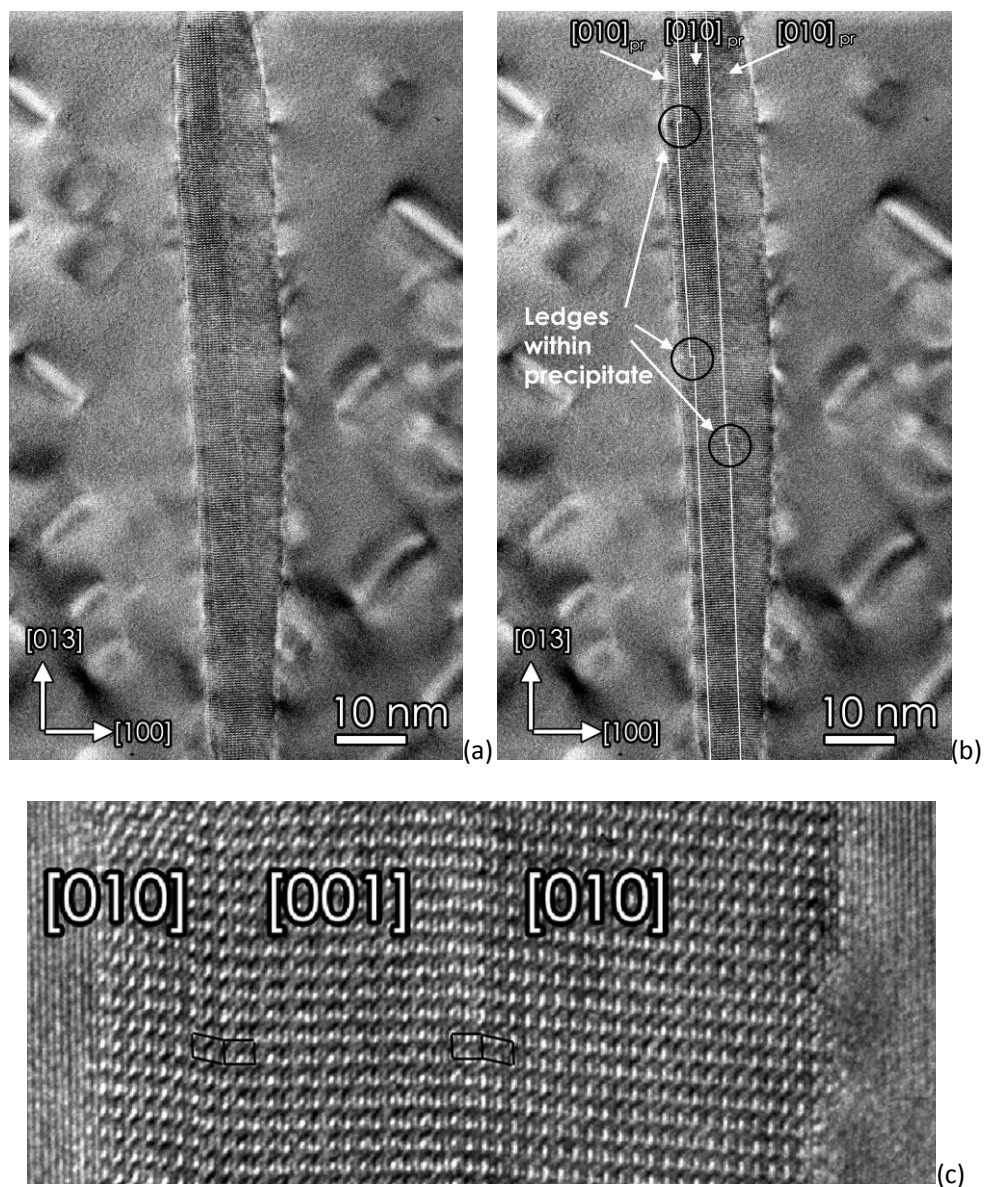**Figure 3.19** (a) BF-TEM image from a stacked precipitate. The bright disks in both parts of the precipitate are thought to be dislocation loops generated by electron beam irradiation. (b) Same image as (a) but with an overlay of lines to indicate the ledges. (c) HRTEM image of a portion of a precipitate seen in (a). Al_9Ni_2 unit cell projections along [010] and [001] zone axes are denoted in black.
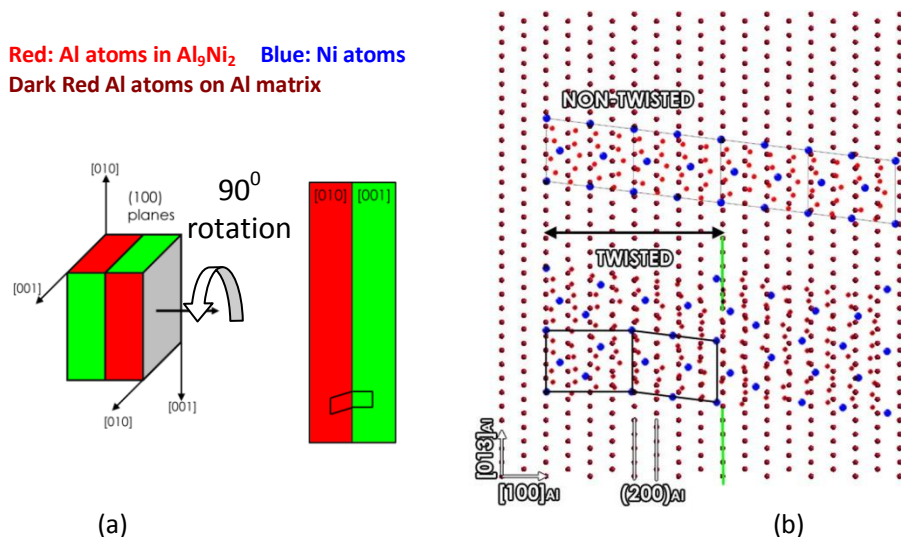
Red: Al atoms in Al$_9$Ni$_2$ **Blue: Ni atoms**
Dark Red Al atoms on Al matrix

(a)   (b)

Figure 3.20 Twist-type fault formation in Al$_9$Ni$_2$ plates. (a) Crystallographic relationship for a twisted precipitate. If the left part is [010]-oriented, the right part is [001]-oriented. (b) superimposed Al matrix and twisted and non-twisted Al$_9$Ni$_2$ unit cells. [010] and [001] projections are shown in black lines.

Apart from the structural defects (twins and twists), Al$_9$Ni$_2$ precipitates are also frequently found to contain planar faults regardless of the annealing temperatures but confined to shorter and thinner precipitates. An example of a diffraction pattern and HRTEM image taken from such a precipitate can be seen in Fig. 3.21. The diffraction pattern is streaked along [100] and it is even difficult to deduce the zone axis orientation of the precipitate. In some cases, planar faults are discernible. However, it is found that the type of planar faults is not unique and that it changes from precipitate to precipitate.   For example, Fig. 3.21(a) is the HREM image of a part of a precipitate, where the top part of the precipitate is shifted by ½<001> relative to the central part. Figure 3.22(a) shows an HRTEM image of a precipitate with planar faults. We analyzed the matrix-precipitate interface at the ends of the faulty precipitate in Fig. 3.22 by Fourier filtering. The Fourier-filtered interfaces presented in Fig. 3.22 were found to be without a misfit dislocation, in contrast to the precipitate in Fig. 3.15, which contains a misfit dislocation for the same plate thickness.
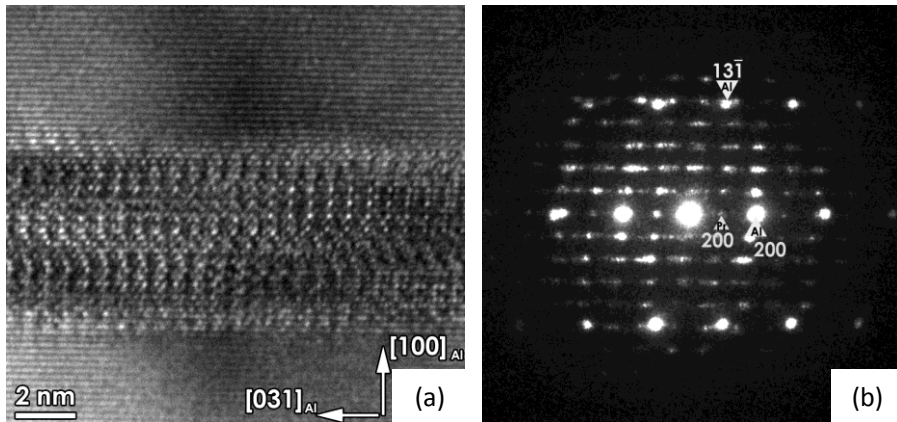
Figure 3.21 (a) HRTEM image of a precipitate seen through the $[013]_{Al}$ zone axis. The precipitate contains planar faults (b) Nano-beam diffraction pattern obtained on the precipitate. Diffraction pattern shows streaking.

Figure 3.22 HRTEM image of an end of an Al_9Ni_2 precipitate with planar faults. (b) Fast Fourier transform of (a), circled regions indicate (200) spots of Al and (400) spots of the Al_9Ni_2, masked. (c) Inverse Fourier transform image of masked FFT in (b). No misfit dislocation is present in (c). Contrary to the precipitate in Fig. 3.15 strain in small precipitates with planar faults are elastically accommodated.

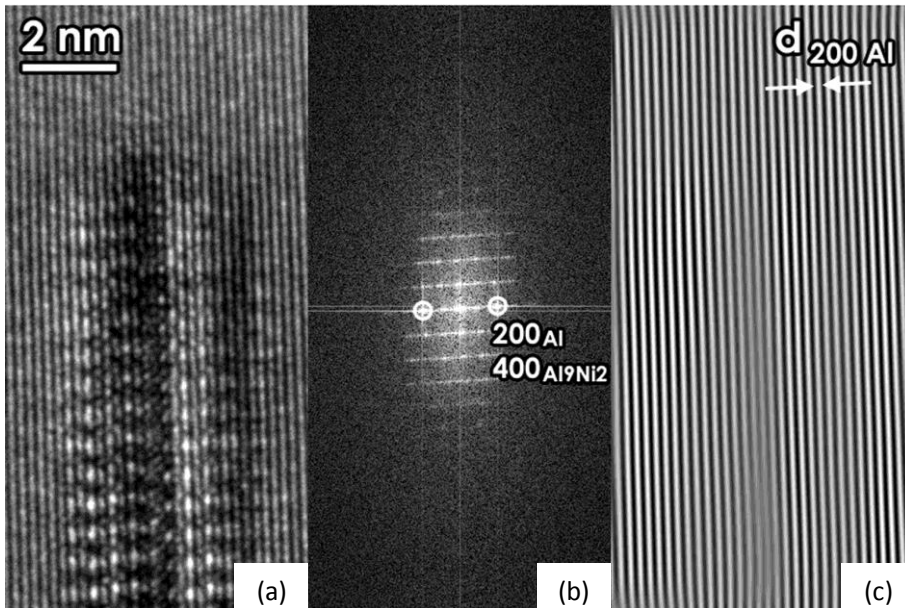The formation of twist and twin types of planar faults can be considered in light of the following mechanisms:

- Misfit between Al and Al_9Ni_2 structures can be reduced via formation of planar faults.

- Growth of Al_9Ni_2 precipitates in Al matrix. Small clusters that grow and nucleate in Al lattice in different directions can join during growth process. This mechanism may possibly explain the formation of twin and twist faults.

- Precipitate growth/thickening via ledge mechanism. Nucleation and propagation of ledges at the plate–matrix interface may form twinned and twisted precipitates.

The elastic strain field is an important factor for semi-coherent precipitates and determines the shape and aspect ratio of the precipitates [13]. When the elastic strain energy reaches a critical level, misfit strain is relaxed by accommodating misfit dislocations. This is shown for the Al_9Ni_2 precipitate in Fig. 3.15. On the other hand our analysis of the precipitates that contain planar faults shows no misfit dislocations at the plate/matrix ends. Al_9Ni_2 precipitates can be considered to be a stacking of alternating planes of pure Al and mixed Al/Ni planes (see Fig. 3.14) that form on elastically soft $\{100\}_{Al}$ planes. Therefore Al planes are stretched. In the early stage of the precipitates, this deformation might cause Al_9Ni_2 planes to deviate from their ideal structure, which in turn would cause changes in the structure of the precipitates. The presence of perfect precipitates together with precipitates with planar faults may also suggest the possible involvement of lattice/matrix dislocations on the formation of Al_9Ni_2 precipitates with planar faults. Lattice dislocations interrupt the symmetry and thus order of the lattices sites which easier nucleation of Al_9Ni_2 precipitates. On the other hand, this can cause deviation from ideal configuration of Al_9Ni_2 planar structure.

The second consideration is the nucleation and growth of separate neighbouring precipitates. During growth, these precipitates can eventually be joined. However, this is not a very plausible explanation, because the density of precipitates is low.

The most plausible mechanism for the formation of structural defects such as twists and twins can be explained with a ledge concept. It is known that the growth and thickening of plate-like precipitates with broad semi-coherent interfaces and large misfits at the end of the plate–matrix interface occurs via nucleation of steps of the

unit cell (half or full unit cell), known as ledges [12,13,14]. This is schematically shown in Fig. 3.23. Ledges form at the corner of the plates and propagate throughout the interface, resulting in a thicker plate. A local elastic strain field near the matrix–precipitate interface may cause distortion in lattice planes (as explained above) and it is possible that a ledge may form differently than the plate, assuming that low-energy interfaces are created. The change in the newly formed ledge compared to the plate must also be related to the Al matrix. Al_9Ni_2 precipitates have 24 variants within the Al matrix. When a ledge forms on a broad faces of a plate, it has to form on the same planes but might be rotated 180° or 90° in the plane while still satisfying the orientation relationship. When such ledges form and grow, the twin and twist structures form. The perfect precipitates without planar faults having misfit dislocations at the end of the precipitate, see Fig. 3.15(a), will provide locations for the ledge nucleation. When two ledges formed in different orientations as seen in Fig. 3.23(b) propagate and finally meet, another ledge can be formed at the joining site and this ledge can grow both ways and cover the entire interface. This mechanism can also explain the presence of steps seen in the interface between [010] and [001]-oriented regions in Fig. 3.19(b).
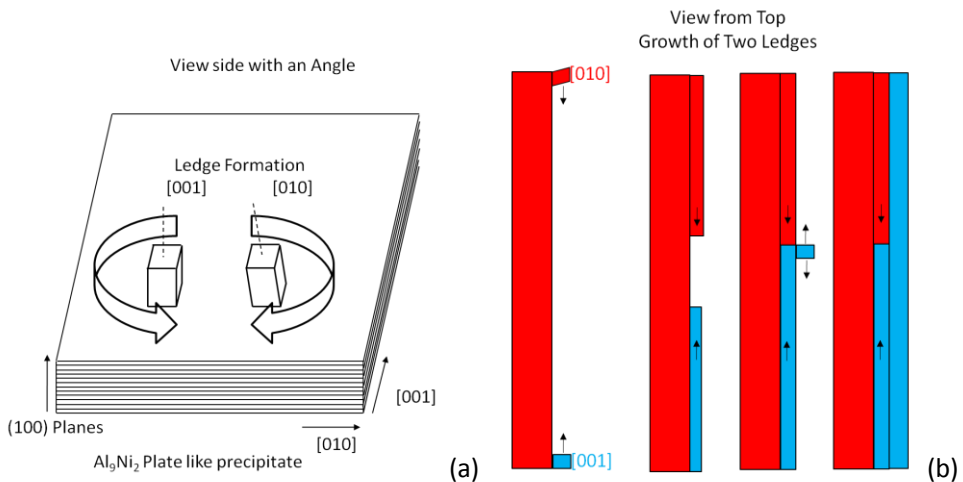
Figure 3.23 Illustration of the formation of A_9Ni_2 ledges, [001] and [010]. (a) For the sake of clarity, ledges are put on the broad face. Actually, ledge formation starts at the plate corners. The ledges still form on the same plane (100) as the plate itself, but they can rotate, assuming that the final interface between the ledge and the plate has small energy. (b) A plate seen from above. Blue represents [001] orientation; red represents [010]. Growth of two ledges with different orientations starting from the corner of the precipitate–matrix interface is illustrated.

3.5 Conclusion and Prospects

Impurity Fe was mainly consumed in large primary particles and has virtually no effect on the matrix precipitates. There may be very little change in lattice parameters, which cannot be detected by TEM. Another consequence of Fe in Al-Ni alloys that it stabilizes the Al_9Ni_2 structure, which might further increase the thermal stability of these precipitates at higher temperatures.

Upon annealing of quenched dilute Al-Ni alloys, metastable Al_9Ni_2 precipitates form instead of the stable Al_3Ni phase. The length of the Al_9Ni_2 precipitates changes as annealing temperature increase, whereas because of high degree of coherency between the precipitate and Al matrix their thickness stays almost constant for annealing temperatures between 573 and 698 K for a range of annealing times from 4 to 20 hours.

The Al_9Ni_2 precipitates have many planar and structural faults. The origin of planar faults is due to elastic strain effects. The accommodation of a misfit has important consequences for plate-like precipitates, making the nucleation of ledges difficult and therefore preventing the coarsening/thickening of the Al_9Ni_2 precipitates. As both perfect precipitates and precipitates with planar faults were observed, the formation of planar faults is due to pre-existing lattice defects.

The occurrence of structural faults such as twins and twists, on the other hand, is linked to the ledge mechanism, which is responsible for the thickening of the plate-like precipitates. Precipitates without planar faults, either strained or having misfit dislocations at the end of the precipitate, provide energetically favourable locations for ledge nucleation. A fault that occurs during nucleation can cause a change of orientation of the plate as the plate gets thicker.

Twist formation in Al_9Ni_2 precipitates is preferred over twin formation. However the interfacial details of twin and twist faults are unknown. The details of the interfaces and the reason for the preference of twist over twin will be explained in the next chapter with the help of interface models and energies calculated from models.

Finally, Al_9Ni_2 precipitates with their apparent thermal stability could be an interesting phase to modify the high-temperature properties of Al alloys with the proved

corrosion performance of Ni. Unfortunately, the main limitation of the use of nickel in the Al industry is its high price. However, as the results show, Fe can be used to form a $Al_9(Ni,Fe)_2$ phase if it can be dissolved during homogenization treatment. This will help to reduce the amount of nickel necessary to form Al_9Ni_2 plate-like precipitates. Bendersky showed that, by manipulating solidification rates, it is possible to form $Al_9(Ni,Fe)_2$ dispersoids with high volume densities [18]. A similar idea can be used if solid-state decomposition can be achieved while casting $Al_9(Ni,Fe)_2$ plates in other heat-treatable Al alloys that are sensitive to temperature. The high thermal stability of the $Al_9(Ni,Fe)_2$ phase will preserve the size and morphology of the plates, so other precipitation hardening phases can be produced without changing the $Al_9(Ni,Fe)_2$ plates.

References

1. B. Cantor, G. A. Chadwick, *J. Cryts. Grwth.*, **23** 12 (1974)
2. L. F. Mondolfo, *Aluminum alloys : structure and properties*, (1976)
3. J.R. Davis, *Aluminum and Aluminum Alloys*, (1993)
4. N.H. Packan, D.N. Braski, *J. of Nucl. Mater.*, **34** 307 (1970)
5. K. Wada et al, *IEEE Trans.*, **10** 1012 (2000)
6. A. Yamamoto et al, *Nucl. Phys. B*, **78**, 565 (1999)
7. W.L. Fink et al, *Trans AIME*, **111** 293 (1934)
8. B. Predel, Al-Ni phase diagram, *Springer Materials Landolt-Börnstein Online Database*
9. A.J. Bradley et al, *Phil. Mag.*, **23** 1049 (1937)
10. A. Yamamoto et al, *Scr. Mater.*, **37**, 1721 (1997)
11. C. Pohla, *Acta. Mater.*, **45** 2155 (1997)
12. D. Porter, K. Easterling, *Phase Transformation in Metals and Alloys*, Chapman-Hill (1996)
13. R. Cahn and P.Haasen (editors)., *Physical Metallurgy*,   Elsevier (1996)
14. V.F. Zackay and   H.I.Aaronson (editors), *Decomposition of Austenite by Diffusional Processes*, 387 Interscience -Wiley (1984).
15. W.M. Stoobs, G.R. Purdy, *Acta. Metall., Mater.*, **Vol 26**, 109 (1977)
16. C.R. Hutchinson et al, *Acta Mater.*, **49**, 2827 (2001)
17. Al-Fe-Ni Phase digaram. *ASM Handbook of Phase Diagrams*, (1998)
18. L. Bendersky, *Metall. Mater. Trans. A*, **16A**, 683 (1985)
19. T. Sato and G. Ohira, *J. of Cryst. Grth.*, **40** 78 (1977)

ADDENDUM

Nano-beam Electron Diffraction Study of an Al$_9$Ni$_2$ Precipitate

Yamamoto and Tsubakino have studied the precipitates in dilute Al-Ni alloys. In their early work, they studied the precipitation in Al-Ni alloys at temperatures below 573 K. Subsequently, they proposed that an Al(Ni) solid solution decomposes in three stages: (1) annealing of quenched-in vacancies, (2) an "unknown" phase (in later work confirmed as Al$_9$Ni$_2$) and (3) the Al$_3$Ni phase [1]. The proposed decomposition sequence is in agreement neither with our present work nor with a later study by Yamamoto et al. [2]. Therefore, the general conclusion is that Al$_3$Ni precipitates do not form in the microstructure of dilute Al-Ni alloys annealed below 823 K. That conclusion is supported by the present thesis.

Therefore, the question is how Yamamoto et al. found Al$_3$Ni precipitates in Al-Ni alloys annealed at 573 K. In their study [2], the authors reported the formation of plate-like precipitates in the microstructure. Selected area diffraction patterns taken from these precipitates along [112]Al contained a few spots (a rather insufficient amount of data) and were indexed as Al$_3$Ni. However, the key diffraction pattern (shown in Fig. A3.1) they used to conclude the presence of Al$_3$Ni does not contain interplanar spacings of Al$_3$Ni. Therefore, it is safe to conclude that the diffraction pattern is erroneously indexed. Such errors can easily arise during indexing of SAD patterns obtained from small and low-density precipitates simply because the intensity of some spots may be very low and not be visible in SAD patterns taken from thicker regions.

In order to explain the diffraction pattern in Yamamoto's work, I started with the superimposed stereographic projections of Al$_9$Ni$_2$ and Al according to the orientation relationship, see Fig. A3.2, proposed in Chapter 3. As can be seen in the stereographic projection, tilting [001]Al to [112]Al ends up with Al$_9$Ni$_2$ close to [122] orientation. To verify this, nano-beam electron diffraction employed on a single precipitate that is presented in Fig. A3.3(a). After tilting to [112]Al along the 110 axis, the precipitate is oriented near [122] Al$_9$Ni$_2$. The precipitate and its diffraction pattern are shown in Figs. A3.3(c) and (d). The tilting axis in reciprocal space and in real space is illustrated in Fig. 3.4.

This diffraction pattern is same as the one showed in the work of Yamamoto et al. The experimental diffraction pattern and the simulated diffraction patterns from [112]Al/[122] Al$_9$Ni$_2$ shown in Fig. A3.5 are a good match.
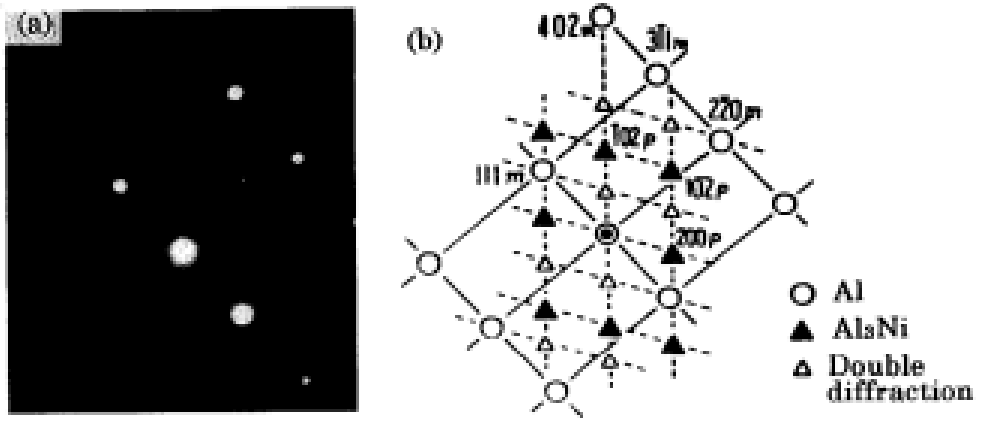
Figure A3.1 Tsubakino's diffraction patterns taken from reference [2].
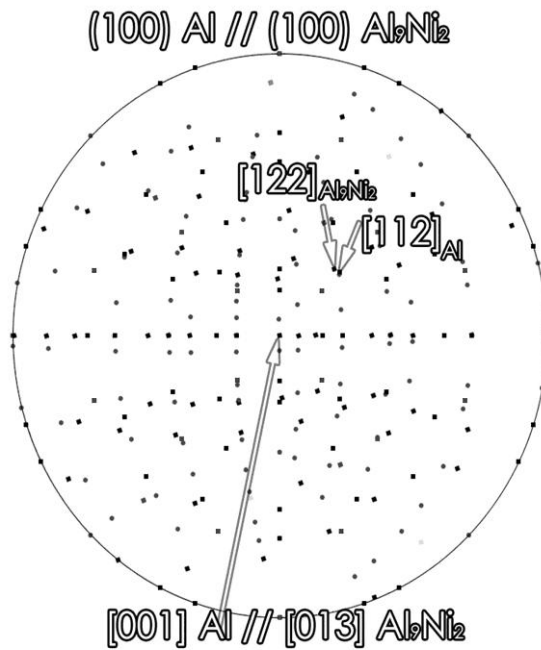
Figure A3.2 Superimposed stereographic projections of Al and Al_9Ni_2. [001]Al is almost parallel to [013] Al_9Ni_2.

(a)

(b)

(c)

(d)

Figure A3.3 (a) Al_9Ni_2 precipitate and (b) its nano-beam electron diffraction pattern seen through [001]Al. (c) Same precipitate and (d) its diffraction pattern after tilting to [112]Al zone axis. The tilting axis is [110]Al. Owing to the rotation between the image plane and the diffraction plane (in CM300UT/FEG), the diffraction patterns do not correspond directly to these images.

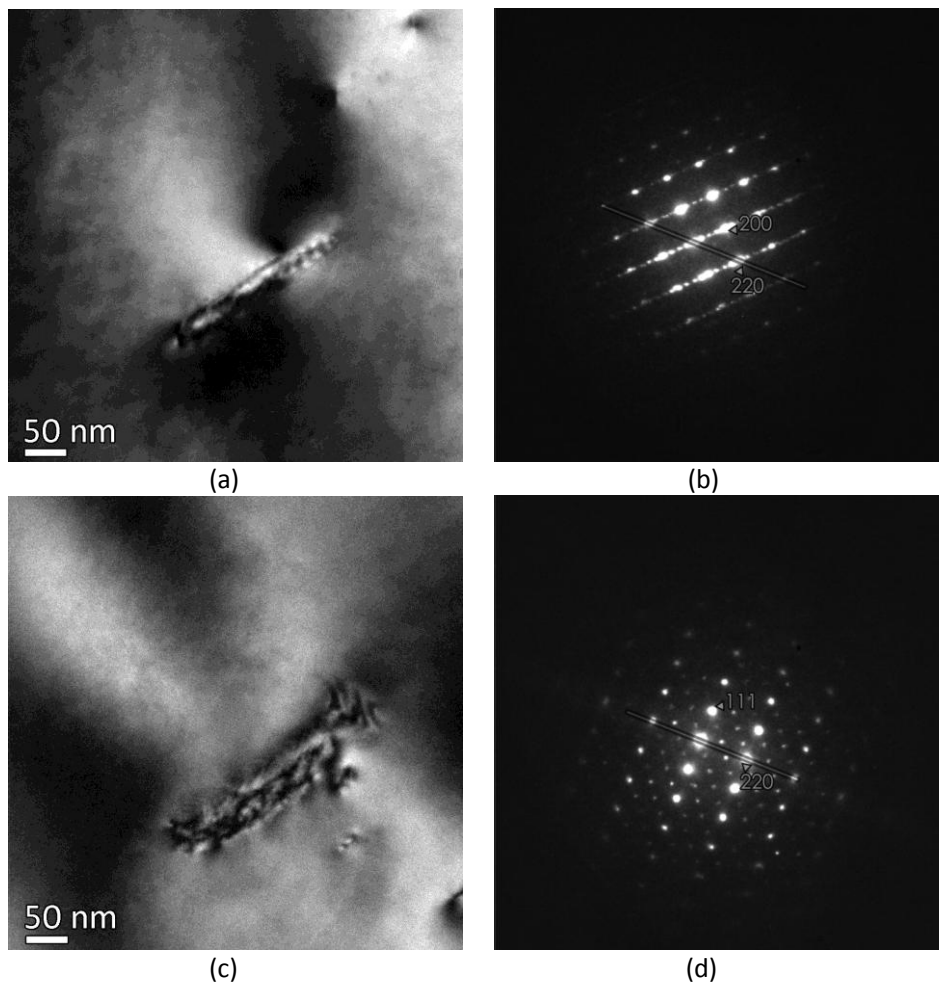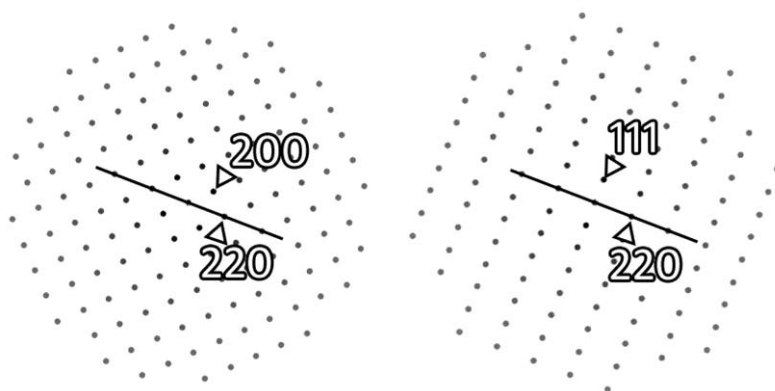**Figure A3.4** Schematic representation of tilting in reciprocal space along [110]Al. Please note that simulated kinematical diffraction patterns of Al are aligned to the experimental diffraction patterns in Fig A.3.3.

<center>(a)   (b)</center>
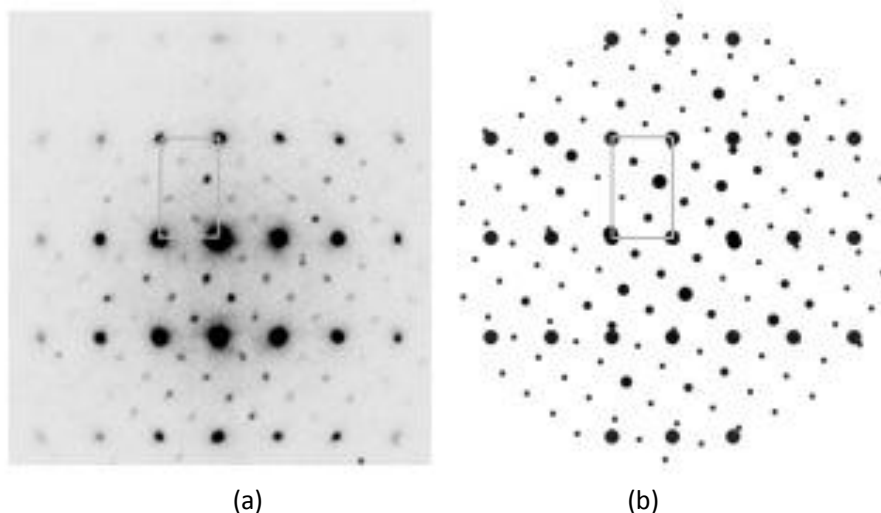
Figure A3.5 Experimental and simulated electron diffraction patterns. Zone axis orientation is [112]Al/[122]Al$_9$Ni$_2$. Rectangles in grey are inserted for easy comparison between the experimental and simulated diffraction patterns.

References

1. A. Yamamoto et al, *Scr. Mater.*, **37** 1721 (1997)
2. H. Tsubakino et al, *Mater.Sci. Forum*, **217-222** 901 (1996)

Chapter 4

Structure of Al$_9$Ni$_2$ precipitates in Al-Ni alloys

4.1 Introduction

Structure of Al$_9$Ni$_2$ phase and interfaces presented in the previous chapter are the subject of this chapter. The structure of Al$_9$Ni$_2$ phase has been refined using quantitative electron diffraction software and also from ab-initio first principles calculations.

The atomic structure of twin and twist interfaces shown in Chapter 3 were modeled and their formation energies were calculated.

4.1.1 Details of Al$_9$Ni$_2$ phase

A metastable Al-rich Al-Ni intermetallic phase was found in rapidly quenched Al-Ni alloys by Li and Kuo [1]. Based on SAD patterns the authors suggested that this phase is similar to a monoclinic Al$_9$Co$_2$ structure and named it as Al$_9$Ni$_2$. Later Pohla and Ryder [2] in their study on rapidly solidified Al-Ni alloys observed Al$_9$Ni$_2$ phase and determined its lattice parameter from X-ray diffraction data and deduced the reflection conditions of Al$_9$Ni$_2$ from XRD intensities as;

$$(h0l): \quad h=2n,$$
$$(0k0): \quad k=2n,$$
$$(h00): \quad h=2n,$$

which indicates that the space group is P2$_1$/a.

Table 4.1 Lattice parameters of Al_9Ni_2[2]. Standard deviations are given in parenthesis, is in the order of last digit.

Lattice Parameters by XRD [3]		
a (Å)	8.685(6)	
b (Å)	6.231(4)	$P2_1/a$
c (Å)	6.185(4)	
β	96.5^0	

4.1.2 Quantitative Electron Diffraction and Structure Refinement

Since the intensities of diffracted beams are not affected by post specimen imaging elements in the microscope, intensity of diffracted beams in electron diffraction patterns can be used to solve the structure of unknown phases. This procedure is the same as structure determination using X-ray diffraction, which is usually done by using either model refining or by Direct Methods [3], if the electron diffraction can be treated as kinematical in character. However, it is often difficult to obtain kinematical electron diffraction condition since the number of elastic scattering events is 10^5 times more for electrons than X-rays. Therefore electron diffraction should always be considered as a dynamical scattering event, in which results that the intensity of diffracted beams does not vary linearly with crystal thickness as for the kinematical case. In addition to dynamical scattering, electron diffraction patterns are usually recorded under zone axis condition and the curvature of Ewald sphere has to be taken into an account which implies that the crystal is not in the exact Bragg condition for most of the reflections.

The refinement of atom positions of Al_9Ni_2 phase was done using the ELSTRU software package [4], which includes several sub-programs to prepare the recorded electron diffraction for extracting intensities of spots in the diffraction patterns. Below, the steps for the structure determination from intensities of the diffracted beams in electron diffraction patterns are outlined.

-Recording of electron diffraction patterns on the image plates: Image plates are preferred because of the wider dynamic range they have than the CCD cameras. Therefore longer exposure times can be used to include reflections with low intensity reflections in the analysis.

-Obtaining initial model: A starting model for the structure to be refined is entered using 'Xatoms' program in ELSTRU.

-Suitable diffraction patterns are selected and the intensities of the diffraction spots are determined by, *Graphical Reduction of Electron diffraction Data*, GREED program in ELSTRU: Experimental diffraction patterns are indexed according to an initial model. Unwanted diffraction spots in the diffraction patterns are excluded since the diffraction patterns of precipitates always contains reflections of the Al matrix. Then first guess for the center of Laue circle is set. The data reduction part of the software determines the intensities of reflections which are written to a *.ii file. Each *.ii file is called a data set X.

The M̲ulti S̲lice L̲east S̲quares, MSLS, program performs the refinement: Data sets that contain intensity information of the reflections are the input for the MSLS program where the intensities calculated by multi-slice algorithm are adjusted with experimental intensities using least square fitting algorithm. First, scaling factor, thickness and center of Laue circle are refined. Next atomic coordinates, Debye-Waller factors and occupancies can be refined. The difference between the simulated and experimental data is expressed as reliability factor (R-factor). Successful structure refinement is achieved when R-factors are below 5 percent.

In this chapter, we studied the crystal structure of the Al_9Ni_2 phase and structural faults (twin and twist) using quantitative electron diffraction and ab-initio first principles calculations. No such structural faults have been reported in the literature. Interface energies of twin and twist structures were calculated from ab-initio first principles calculations.

4.2 Experimental

The Al-Ni alloy was produced by arc melting. The alloy contain 0.092 at.% Ni. The composition is given in Table 1.1 (Chapter 1). The precipitates studied in this chapter were formed after the heat treatments as described in Chapter 1.

Diffraction patterns used for quantitative analysis were recorded on the image plates using a Philips CM300 UT/FEG TEM operating at 300 kV. The diffraction patterns were taken by nano beam electron diffraction technique which details are given in Chapter 3. Imaging of precipitates was done on FEI Titan[3] TEM equipped with a HAADF detector.

4.3 Results and Discussion

As was shown in Chapter 3 the Al_9Ni_2 precipitates posses the following orientation relationship with Al matrix.

$$[010]_{Pr}//<031>_{Al} \ \& \ (100)_{Pr}//\{100\}_{Al}$$

Therefore it was easy to obtain diffraction pattern from at least two principal directions ([010] and [001]) of the Al_9Ni_2 precipitates. The 3rd direction, [100], is approximately 6 degree off from the $[100]_{Al}$ direction. In addition to this, along the $[100]_{Al9Ni2}$ orientation the viewing direction is parallel to plate normal and given the small plate thicknesses, 5nm, the diffraction pattern from [100] zone of the precipitates is not practically useful because overlapping with Al matrix which especially becomes stronger in thicker regions. Therefore only the diffraction patters taken along [010] and [001] orientations, (an example shown in Fig. 4.1), were used for quantitative treatment, which is already enough to determined three-dimensional crystal structure.

The lattice parameters were determined from the diffraction patterns. The Al lattice was used as internal calibration. This allows accurate determination of the lattice parameters of Al_9Ni_2 precipitates (presented in Table 4.2). With this approach accuracy of order of few pico-meter (about 0.2-0.3 %) can be achieved. The variation in lattice parameters determined for various Al_9Ni_2 precipitates was about same as the accuracy of the measurement. The space group and the reflection conditions of the Al_9Ni_2 precipitates was checked by tilting the Al_9Ni_2 precipitates along the [100] and [001] axes, therefore by tilting away from the zone axis orientation, possibility of double diffraction condition can be avoided (see Chapter 3 Figure 3.6). We verified that diffraction patterns indeed show the extinction conditions for $P2_1/a$.

Table 4.2 Al_9Ni_2 lattice parameters determined from electron diffraction patterns. The estimated errors in the order of last digits are given in the parenthesis.

Lattice Parameters of Al_9Ni_2 from electron diffraction patterns		
a (Å)	8.683 (1)	
b (Å)	6.261 (2)	
c (Å)	6.192 (2)	$P2_1/a$
β	96.5^0	

4.3.1 Structure model and refinement

Al_9Ni_2 structure belongs to a space group $P2_1/a$ as Al_9Co_2 structure. Furthermore, lattice parameters of both the structures are similar, differing slightly (see Chapter 2). Therefore atoms positions in Al_9Co_2 structure was used as a structure model for Al_9Ni_2, after readjustment based on Al-Ni distances found in stable Al_3Ni.
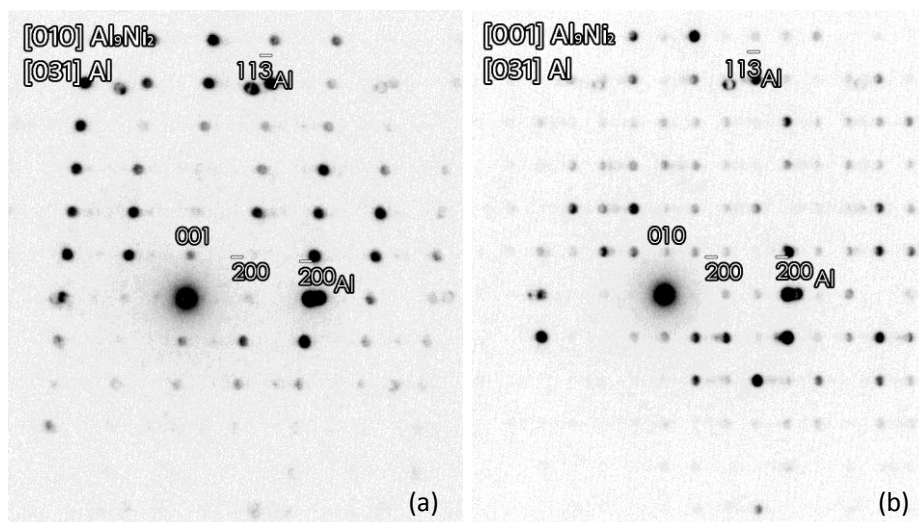

Figure 4.1 Electron diffraction patterns obtained on Al_9Ni_2 plate-like precipitates and recorded on image plates. (a) [010], (b) [001] zone axes. The diffraction patterns are slightly mistilted.

The multi-slice least square (MSLS) refinement method embedded in ELSTRU software package was used to refine the model structure. In Table 4.3, refined misorientations, estimated thickness and R-factors for 8 datasets are given.

Table 4.3 Electron diffraction data sets used for the refinement of Al_9Ni_2 structure. The estimated error in the order of last digit is given in the parenthesis.

Zone Axis	Thickness (nm)	h	k	l	R-factor(%)
[010]	82.8 (7)	1.7 (3)	0	-4.11(4)	15
[010]	340 (12)	0.327 (19)	0	-0.128 (10)	19
[010]	140 (10)	0.24 (4)	0	-0.298 (18)	9
[010]	72.9 (9)	0.41(7)	0	0.07 (3)	25
[010]	59.2 (8)	1.86 (10)	0	1.3 (5)	18
[001]	196 (4)	3.6 (6)	2.7 (5)	0	24
[001]	76 (4)	3.2 (3)	4.75 (17)	0	31
[001]	178(3)	-4.13(5)	-1.28(4)	0	22

The refined atom positions after MSLS are given in Table 4.4, but relatively high values of R-factors suggest that refinement procedure did not work efficiently and the refined atom positions cannot be used. On the other hand R-factors are lowest amongst the several alternative structures we tested. This suggests that our initial model is right.

Table 4.4 Atom positions (given in lattice coordinates) of Al_9Ni_2 structure after MSLS refinement.

Non-equivalent positions	x	y	z
Al1	0	0	0
Al2	0.2524(4)	0.0024(13)	0.4083(4)
Al3	0.5468(4)	0.120(11)	0.2157(5)
Al4	0.0023(4)	0.1742(12)	0.3585(6)
Al5	0.2373(4)	0.3016(12)	0.0825(6)
Ni	0.8418(17)	0.139(6)	0.2789(3)

The reason for the high R-factors might be due to planar faults and other structural defects present in the precipitates. The faults and defects cause overlapped spots and streaking in the diffraction patterns. The overlapped spots can be removed during the data reduction process. But streaks in the diffraction patterns cannot be removed successfully and thus still cause problems after data reduction. Moreover along the plate length the crystal is bent and this locally change the misorientation of the precipitates and assignment of right misorientation to the particular data set can be difficult, as the standard deviations given in Table 4.3 suggests. The other factor is that occupancy of Ni can be different in ideal Al_9Ni_2 structure than the Al_9Ni_2 structure of the precipitates.

MSLS calculations indicate that initial model is probably close to the ideal Al_9Ni_2 structure, but rather high R values were obtained. Therefore atom positions were also refined using the ab-initio first principles calculations using Vienna Ab-initio Simulation Package, VASP. In these calculations forces between the atoms are minimized by changing atom positions. The ab-inito refined atom positions and relaxed lattice parameters for ideal (bulk) Al_9Ni_2 structure is given in Table 4.5.

4.3.2 Description of Al$_9$Ni$_2$ structure

The Al_9Ni_2 structure contains 22 atoms (18 Al and 4 Ni) and can be best described as a layered structure. 2 by 2 by 2 unit cells of Al_9Ni_2 structure is displayed in Fig. 4.2. Al atoms lie approximately in a layers parallel to (100) planes (shown as green in Fig 4.2) at heights 0 and ¼. The Al atoms arranged in three groups, the first containing of atoms in the same layer and the two others in the layers on either side of the particular atom considered. Ni atoms form a distorted hexagon. These hexagons can be tiled in a close packed arrangement (see Fig. 4.3).

Table 4.5 First principles ab-initio refined lattice parameters and non-equivalent atompositions of the Al_9Ni_2 structure (given in lattice coordinates) after full relaxation.

Structure			Al_9Ni_2
Space group			$P2_1/a$
Cell dimensions	a (Å)		8.74
	b (Å)		6.26
	c (Å)		6.22
	α (°)		90.0
	β (°)		96.8
	γ (°)		90.0
Non-equivalent positions	**x**	**y**	**z**
Al1	0	0	0
Al2	0.267	0.0024	0.403
Al3	0.545	0.110	0.206
Al4	0.006	0.202	0.609
Al5	0.267	0.212	0.911
Ni	0.836	0.123	0.266
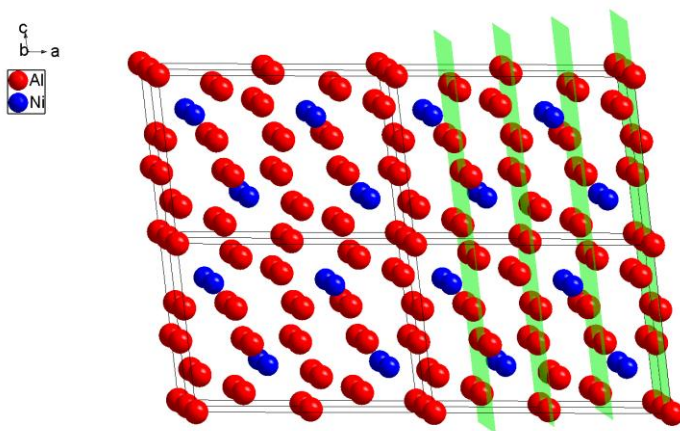
Figure 4.2 Al_9Ni_2 structure (2x2x2 unit cell) is seen along [010]. The (400) planes is designated seen in green.
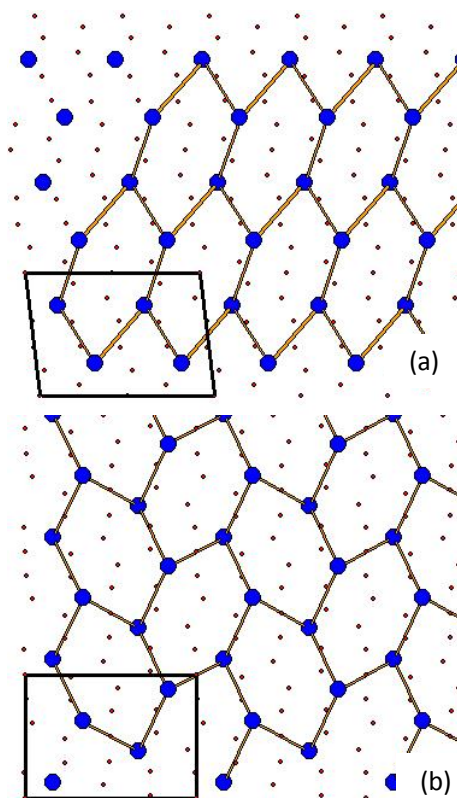
Figure 4.3 Al_9Ni_2 structure is seen along (a) [010] (b) [001]. Ni atoms are in blue. Al atoms (smaller) in red. Hexagons (seen in yellow)formed by Ni atoms can be tiled throughout the structure.

In the Al_9Ni_2 structure, Ni atoms have nine Al nearest neighbors. Three of the Al atoms have nine coordination, one is 10 coordinated and one is 12 coordinated. Analysis of interatomic distances (see Table 4.6) reveal Ni-Al distance is shorter than the Al-Al and Ni-Ni distances in their pure forms in fcc lattice. The average Ni-Al distance is 2.4947 Å (see in Table 4.6). Ni atoms are well separated (over 4 Å apart) and no Ni-Ni short distance is present. Short Al-Ni-Al distances ensure the distance between Al atoms residing on neighboring planes have inter-atomic distance that are close to Al-Al distance (2.84 Å) in Al fcc structure. The average Al-Ni interatomic distance has similar value for Al_9Ni_2 and stable Al_3Ni. But the average Al-Al distances differ greatly. Therefore compared to Al_3Ni where no Al rich planes with layered character is present Al_9Ni_2 shows resemblances to the Al lattice and therefore have layered character.

Table 4.6 Computationally refined lattice parameters and non-equivalent atomic positions of the basic Al_9Ni_2 structure (space group $P2_1/a$, No. 14) after full relaxation.

Atom 1	Atom 2	Count	d 1,2 [Å]	Atom 1	Atom 2	Count	d 1,2 [Å]
Al1	Ni1	2x	2.4385	**Al4**	Ni1	1x	2.5006
	Al5	2x	2.7271		Ni1	1x	2.5291
	Al4	2x	2.7471		Al1	1x	2.7471
	Al3	2x	2.7636		Al2	1x	2.7673
	Al5	2x	2.7963		Al5	1x	2.7787
Al2	Ni1	1x	2.4687		Al3	1x	2.8261
	Ni1	1x	2.5169		Al2	1x	2.8355
	Al5	1x	2.7532		Al3	1x	2.8579
	Al4	1x	2.7673		Al4	1x	2.8657
	Al4	1x	2.8355		Al2	1x	2.8833
	Al4	1x	2.8833		Al2	1x	2.963
	Al3	1x	2.8934	**Al5**	Ni1	1x	2.4476
	Al3	1x	2.8983		Ni1	1x	2.4871
	Al4	1x	2.963		Al1	1x	2.7271
Al3	Ni1	1x	2.5278		Al3	1x	2.7524
	Ni1	1x	2.536		Al2	1x	2.7532
	Al5	1x	2.7524		Al4	1x	2.7787
	Al1	1x	2.7636		Al1	1x	2.7963
	Al4	1x	2.8261		Al3	1x	2.9364
	Al4	1x	2.8579	**Ni1**	Al1	1x	2.4385
	Al2	1x	2.8934		Al5	1x	2.4476
	Al2	1x	2.8983		Al2	1x	2.4687
	Al3	1x	2.9335		Al5	1x	2.4871
	Al5	1x	2.9364		Al4	1x	2.5006
					Al2	1x	2.5169
					Al3	1x	2.5278
					Al4	1x	2.5291
					Al3	1x	2.536

4.3.3 Interface Modeling

Atom positions of ab-initio first principles refined structure of Al_9Ni_2 (given in Table 4.5) was used to derive structure of interfaces in precipitates with twist and twin

features. Modeled twin and twist structures were also refined using ab-inito first principles calculations.

Interface models were generated after Al-Ni and Ni-Ni interatomic distances and coordination number of Ni atom were taken into account to obtain a physically realistic model. In order to compare the interfacial energies directly, periodic interfaces along the [100] axis/plate normal/ of the Al_9Ni_2 structure were chosen. The misfit is easily accommodated along the perpendicular to the plate normal as was shown in Chapter 3 (13 nm spacing between misfit dislocations see Fig 3.15), therefore effect of strain on the broad faces of the plate-like precipitates can be ignored.

The structure model for the twin containing supercell was modeled hypothetically. Since we were not able to obtain good enough images (HRTEM and HRSTEM) help drawing model structure.

For the model of a twist structure a Z-contrast HRSTEM image, presented in Fig. 4.4, obtained on a plate-like Al_9Ni_2 precipitate was used. In this image bright dots represent the positions of Ni atoms. A maximum-likelihood de-convoluted of the as-acquired image is seen in Fig. 4.5. A sharp interface separates the [010] and [001] orientated Al_9Ni_2 regions. In Fig 4.4, [010] oriented Al_9Ni_2 region (left part of the interface) has only one unit cell wide while the [001] oriented Al_9Ni_2 (right part of the interface) is five unit cell wide. It is clearly seen in the image that Ni atoms are shared by both the [010] and [001] oriented regions.

Lattice parameters of modeled structures are given in the Table 4.7. Supercells of twist and twin structures are both defined in triclinic unit cells so that no symmetry constraints on atoms at the interface is imposed. For twin structure both part across the interface is along the monoclinic **b** axis (See Fig.3.16(a)) the resulting supercell has orthogonal axes. A model structure that contains twinned Al_9Ni_2 is presented in Fig 4.6, seen through [001] axis which coincides with the monoclinic b axis of Al_9Ni_2 structure. The black rectangle in the Fig. 4.6 demonstrates the super cell projection along [001]. The twinned Al_9Ni_2 unit cells are shown in green.

Twist structure is more complicated compared to the twin structure due to monoclinic axis **b** rotates 90 degree (see Fig 3.18-3.19 and Fig.) and a supercell that contain twist is defined in non orthogonal axes. A supercell with 90 degree rotated Al_9Ni_2 unit cells is seen in Fig.4.7. In these pictures black parallelograms indicate unit cell projections for [001] and [010] oriented supercell. Green parallelogram indicates the Al_9Ni_2 crystal structure projections along [001] and [010]. HRSTEM simulation [5] of a model twist structure derived from image in Fig 4.4 in combination with taking Al-

Ni interatomic distances into an account shows a good fit between a simulated image of a model structure and an experimental image. This matching indicates that the initial model has probably a physically realistic structure.

Table 4.7 Structure details of twin and twist models.

Twin

Space-group	P 1 (1) – triclinic
Cell	a=8.63 Å b=6.19 Å c=6.26 Å α=90.00° β=90.00° γ=90.00° V=332.53 Å^3

Twist

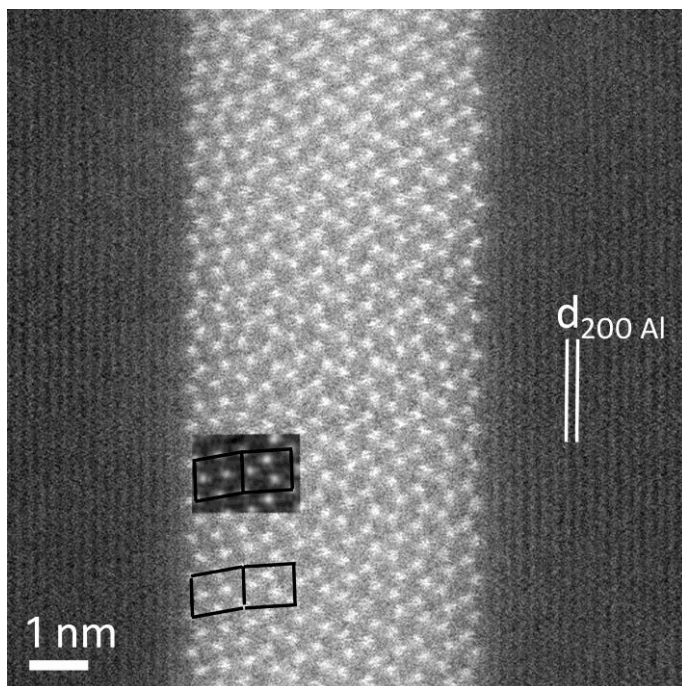| Space-group	P 1 (1) – triclinic
Cell	a=17.23 Å b=6.26 Å c=6.26 Å α=90.00° β=86.40° γ=86.40° V=0.666.10 nm^3

Figure 4.4 Z-Contrast HRSTEM image of a section of an Al_9Ni_2 precipitate recorded along [013] zone axis of Al. The precipitate contains a twist fault. Nickel atom columns appear brightest in the image. Al_9Ni_2 unit cell projections are outlined in black. The inlet shows the HRSTEM simulation [5] of the twist model.
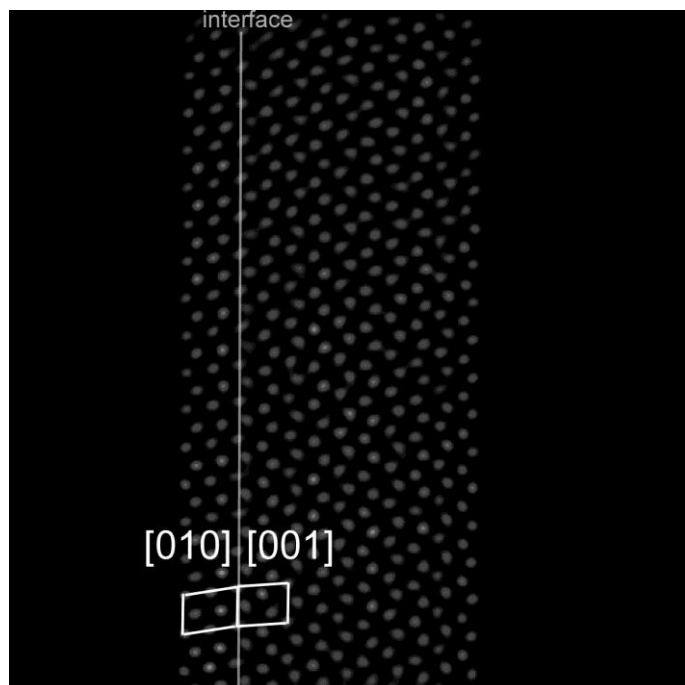
Figure 4.5 De-convoluted STEM image. Bright dots represent Ni columns. The interface, indicated by a white line, is sharp. Al_9Ni_2 unit cell projections are outlined in white. Right part is [001] oriented where as the left part is [010] oriented.
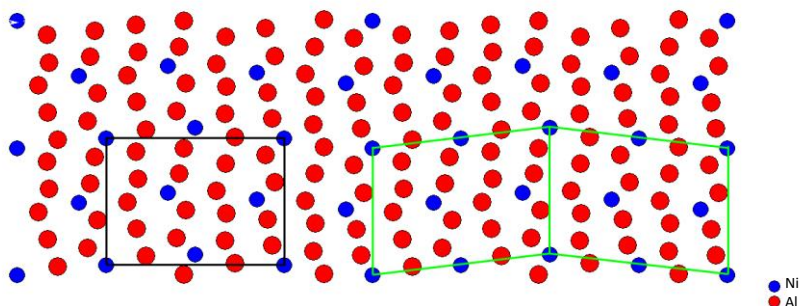

Figure 4.6 Modeled twin structure of Al_9Ni_2 phase. Red balls represent Al while blue ones indicate Ni positions. Thick black rectangle on the left part shows the smallest supercell that contains twin and is used for the ab-initio calculations. Since twin relation is along b axis of the Al_9Ni_2 cell resulting super cell has orthogonal axes. Green parallelograms represent the twin cells.
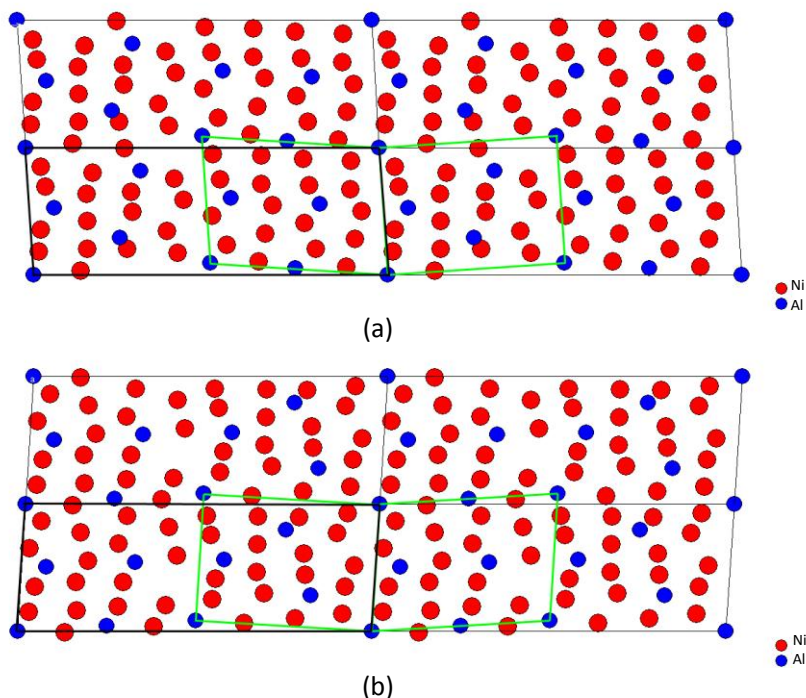
(a)

(b)

Figure 4.7 Modelled twist structure of Al_9Ni_2. Red balls represent Al while blue ones indicate Ni positions. Thick black lines represent the unit cell projection along (a)[001] and (b) [010] directions. Green lines show the twisted unit cells.

4.3.4 Computational details

The atomic positions and formation enthalpies of the three Al_9Ni_2 structure (basic structure, twin structure and twist structure) were calculated using the first-principles VASP code [6-8], using the projector augmented wave (PAW) method [9]. For all these spin-polarized calculations, the generalized gradient approximation (GGA) was used employing exchange-correlation functionals of Perdew, Burke and Ernzerhof (PBE) [10]. Energy and k-point convergence was ascertained and were performed with an energy cut-off of 350 eV. For all structures, the density of the Monkhorst-Pack k-point grid was increased until the abovementioned accuracy was reached. For all grids thus obtained, the linear k-point spacing was less than 0.020 Å^{-1}.

Because the three model structures (basic, twin and twist Al_9Ni_2) are identical in composition (Al_9Ni_2), and differ only in the atomic positions, the formation enthalpies of the three structures can be directly compared. As the calculations are performed at

zero temperature and allowing full relaxation of both the cell dimensions and the atomic positions, the Gibbs free energy equals the formation enthalpy H. The interface formation enthalpies of the twin interface and the twist interface can be calculated as follows:

$$\Delta\gamma_{\text{int}erface}^{formation} = \frac{\{H_{Al9Ni2}^{twist/twin} - H_{Al9Ni2}^{basic}\}}{2A}$$

4.1

Here γ is the interface formation enthalpy in Jm^{-2}, H is the formation enthalpy of the structure in J, A is the area of the interface in the twist or twin cell. H_{Al9Ni2}^{basic} contains the same number of atoms as $H_{Al9Ni2}^{twist/twin}$. The factor two arises because there are always two interfaces per twist or twin cell, which is required because of the periodic boundary conditions.

The cell dimensions and atomic positions of the experimentally observed structures, basic Al_9Ni_2, twinned Al_9Ni_2, and twisted Al_9Ni_2, were refined using the ab-initio first-principles VASP code, as described in the computational details section (Chapter 1 section 1.6). In the input structures, the interfaces of the twin and twist structures were constructed attempting to obtain realistic interatomic distances. The atomic positions were subsequently further refined in the calculations. The refined atomic positions are listed in Tables 4.8 and 4.9. Calculated energies and average interatomic distances are given in Table 4.9.

Table 4.8 Computationally refined lattice parameters and non-equivalent atomic positions of the twinned and twisted Al_9Ni_2 structures after full relaxation.

Structure Space Group		Al_9Ni_2 twinned P1 (No. 1)				Al_9Ni_2 twisted P1 (No. 1)		
Cell dims	a (Å)	8.84			a (Å)	17.72		
	b (Å)	6.31			b (Å)	6.26		
	c (Å)	6.17			c (Å)	6.24		
	α (°)	90.0			α (°)	89.6		
	β (°)	89.6			β (°)	84.0		
	γ (°)	90.3			γ (°)	83.5		
Atomic positions	Al1	0.945	0.795	0.075	Al1	0.903	0.322	0.950
	Al2	0.677	0.405	0.105	Al2	0.878	0.930	0.764
	Al3	0.422	0.233	0.342	Al3	0.934	0.503	0.523
	Al4	0.429	0.735	0.170	Al4	0.910	0.096	0.344
	Al5	0.907	0.303	0.440	Al5	0.900	0.728	0.135
	Al6	0.169	0.896	0.403	Al6	0.773	0.616	0.965
	Al7	0.617	0.555	0.510	Al7	0.792	0.306	0.650
	Al8	0.884	0.765	0.497	Al8	0.791	0.796	0.466
	Al9	0.184	0.268	0.612	Al9	0.773	0.115	0.155
	Al10	0.704	0.166	0.721	Al10	0.654	0.316	0.917
	Al11	0.434	0.921	0.646	Al11	0.660	0.703	0.708
	Al12	0.170	0.490	0.207	Al12	0.680	0.496	0.313
	Al13	0.683	0.998	0.297	Al13	0.660	0.097	0.509
	Al14	0.411	0.424	0.867	Al14	0.636	0.911	0.110
	Al15	0.137	0.658	0.782	Al15	0.528	0.637	0.942
	Al16	0.668	0.778	0.894	Al16	0.530	0.095	0.787
	Al17	0.958	0.259	0.014	Al17	0.543	0.785	0.459
	Al18	0.229	0.054	0.002	Al18	0.535	0.315	0.272
	Ni1	0.512	0.078	0.998	Al19	0.417	0.082	0.523
	Ni2	0.009	0.007	0.734	Al20	0.435	0.505	0.659
	Ni3	0.839	0.510	0.779	Al21	0.416	0.673	0.251
	Ni4	0.335	0.576	0.512	Al22	0.409	0.299	0.033
					Al23	0.308	0.418	0.418
					Al24	0.279	0.170	0.842
					Al25	0.305	0.800	0.603
					Al26	0.282	0.683	0.025
					Al27	0.325	0.029	0.230
					Al28	0.131	0.932	0.884
					Al29	0.172	0.532	0.737
					Al30	0.182	0.156	0.526
					Al31	0.162	0.754	0.379
					Al32	0.181	0.396	0.146
					Al33	0.044	0.288	0.771
					Al34	0.023	0.836	0.605
					Al35	0.060	0.134	0.264
					Al36	0.047	0.612	0.080
					Ni1	0.987	0.979	0.981
					Ni2	0.077	0.480	0.443
					Ni3	0.199	0.026	0.161
					Ni4	0.492	0.975	0.153
					Ni5	0.398	0.875	0.875
					Ni6	0.580	0.433	0.611
					Ni7	0.826	0.443	0.289
					Ni8	0.738	0.975	0.812

Table 4.9 Interface areas and interface formation enthalpies of the basic, twinned and twisted Al_9Ni_2 structures. The interface energies were calculated using Eq. 4.1.

		Al_9Ni_2 basic	Al_9Ni_2 twin	Al_9Ni_2 twist
Space group		P2$_1$/a	P1	P1
Relaxed cell dimensions	a (Å)	8.74	8.84	17.772
	b (Å)	6.26	6.31	6.26
	c (Å)	6.22	6.17	6.24
	α (°)	90.0	90.0	89.6
	β (°)	96.8	89.6	84.0
	γ (°)	90.0	90.3	83.5
number of atoms	-	22	22	44
average interatomic distance	(Å)	2.75	2.77	2.76
smallest interatomic distance	(Å)	2.44	2.37	2.29
interface plane	-	N.A.	(001)	(001)
interface area	(Å^2)	N.A.	38.9	39.1
ΔH	(eV/atom)	0.0	7.6	13.3
γ_{int}	(J m^{-2})	0.00	0.34	0.60

4.4 Conclusion

The calculated interface formation enthalpies, corresponding to twin and twist stacking fault energies, are 0.34 and 0.60 Jm^{-2}, respectively. Because the configurations are fully relaxed, strain energies caused by the interaction with the Al lattice are neglected and are not included in the energies listed in Table 4.4. Nonetheless, the calculations show that the constructed interfaces of the twinned and twisted structures (structural details given in Table 4.9) are realistic, considering that the interface energies are close to interface energies reported in several metals and intermetallics which are around 0.5 J m^{-2} [11,12,13,14] and that the interatomic distances are always larger than the shortest interatomic distance 0.229nm, in the ideal Al_9Ni_2 structure.

As shown in Chapter 3, twisted precipitates were observed much more frequently than twinned precipitates. Therefore twist formation is preferred over twin formation. Interface energies, on the other hand indicates that experimentally proven twist structure has higher energy compared to the hypothetically constructed twin interface. The interface formation energies suggest that twin structure should form easier.

Two factors must be considered to explain the discrepancy between the calculated and experimentally observed results.

First, ab-initio calculations of the interface formation energies are performed at 0 K but interfaces were formed after annealing at 573K and 698 K. The stability and structure of observed interfaces and interface energies can be compared directly but formation of interfaces is also kinetically controlled. This can be simply explained with the classical example of carbon allotropes, graphite and diamond. Formation enthalpy of diamond is lower than the graphite but diamond exists together with graphite and it does not transform into a graphite due to transformation is kinetically controlled.

Second, the strain energy and accommodation of the strain between the plate-like precipitates and the Al matrix must play a role for the formation and/or stability of twin twist interfaces. Analysis shows that twin formation does not alter the strain state of the precipitate/matrix interface. On the other hand thin twisted precipitates are better matched to the Al matrix as showed in Chapter3.

References

1. X.Z. Li et al., *Phil. Mag. B*, **61** 487 (1990)
2. C. Pohla et al., *Acta. Mater.*, **5** 2155 (1997)
3. D. L. Dorset, *Structural Electron Crystallography*, Plenum Press (1985)
4. J. Jansen et al. Acta. Cryst., **A54**, 91, (1998)
5. Dr. Probe by Juri Barthel, Forschung Zentrum Juelich
6. G. Kresse et al., *J. Phys Rev B.*, **47** 558 (1993)
7. G. Kresse et. al, *J. Comput Mater Sci.*, **6** 15 (1996)
8. G. Kresse et al., *J. Phys Rev B.*, **54** 11169 (1996)
9. G. Kresse et al., *J. Phys Rev B.*, **59** 1758 (1999)
10. Perdew JP et al., *Phys. Rev. Lett.*, **77** 3865 (1996)
11. A.P. Sutton and R.W Balluffi, *Interfaces in Crystalline Materials*, Oxford University Press (1996
12. C. Wolverton et al., *Phys. Rev. Lett.,* **86** 5518 (2001)
13. S.Y. Hu et al. *Acta Mater.*, **54** 4699 (2006)
14. V. Vaithyanathan et al., *Phys. Rev. Lett.*, **88** 125503 (2002)

Chapter 5

TEM Study of decomposition of Al-Zr alloy in the presence of Fe and Ni

This chapter reports the study the decomposition of aluminum solid solution containing Zr, Fe, Ni subjected to thermal treatment for 20 hours at two different temperatures. In the microstructure small Al-Zr and Al-Fe(Ni) intermetallic precipitates were observed as expected. $L1_2$-Al_3Zr precipitates with defects were found. The defect structure was explained. In addition to this, secondary precipitation of $L1_2$-Al_3Zr were detected on Al-Fe(Ni) intermetallics were observed.

5.1 Introduction

Several authors reported a positive effect of Zr addition to aluminum and aluminum alloys on the mechanical properties. The main benefits reported are

- Grain refinement, [1]
- Recovery and recrystallization retardation [2, 3, 4]
- Reduction on stress assisted corrosion [5]
- Age hardening response at relatively high temperature of use where other alloy systems do overage and therefore lose the age hardening characteristics) [4].
- Less Quench sensitivity [6]

The grain-refining effect of Zr in Al alloys stems from the fact that during solidification primary Al_3Zr crystals forms. Al_3Zr phase has very similar crystal structure to that of Al and once they are formed in the liquid the remaining can easily nucleate on these primary particles. The effectiveness of grain refinement by Zr is not as high that achieved by Ti/TiB_2. Therefore Zr based fine-grained Al alloys have not been produced commercially.

In the aluminum industry zirconium is used in several commercial Al alloys as a trace element, 0.1-0.15 wt. %. The key role of Zr in commercial alloys is to improve resistance of the alloy to recrystallization during solution heat treatment of the alloy. For instances, a few percent addition of Zr to Al-Mg-Zn (7xxx series) and Al-Mn-Mg alloys (3xxx series) alloys improve recovery and recrystallization resistance and result in a larger strength of the alloy [7].

During recrystallization of a deformed alloy, strain free grains form and grow. When an alloy recrystallizes it will lose part of its strength and thus recrystallization is often undesired. Recrystallization and strength loss at elevated temperatures may be prevented by the presence of small finely dispersed particles in the microstructure. These particles, referred as dispersoids, exert a retarding force against grain growth and impede sub-grains to reach critical size after which the sub-grains would further grow. This phenomena is known as Zener drag. To maximize the Zener drag and retard recrystallization it is important to increase the force exerted on sub-grains during growth by dispersoids. The density of dispersoids should be as high as possible whereas their size should be as small as possible for efficient recrystallization retardation. The low solid-solubility of Zr result in finely dispersed metastable cubic Al_3Zr precipitates. Low coarsening rates of these cubic Al_3Zr dispersoids at the solution heat treatment provides a good resistance to recrystallization[8].

5.1.1. Decomposition of Al-Zr solid solution

Fig. 5.1 shows the Al rich part of the Al-Zr phase diagram. There is a peritectic transformation at 0.083 at. % Zr 933.5 K where the liquid phase and solid Al_3Zr react forming an aluminum solid solution[1,2,3].

$$\text{Liquid} + Al_3Zr \rightarrow \alpha\text{-Al}$$
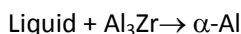
The equilibrium solid solubility of Zr in Al is 0.083 at. % at the peritectic temperature and according to phase diagram at the room temperature practically no Zr can be kept in the solid solution. During slow cooling close to equilibrium conditions the stable Al_3Zr phase forms. This phase has an ordered tetragonal unit cell which is designated as $D0_{23}$ in Strukturbericht notation. Generally cooling rates achieved in commercial practices are not slow enough for stable tetragonal ($D0_{23}$) Al_3Zr phase to form but metastable cubic ($L1_2$) Al_3Zr phase form. Apart from metastable $L1_2$ and stable $D0_{23}$ Al_3Zr Guo et. al identified another metastable Al_3Zr phase [10].This phase has same structure as tetragonal Al_3Ti phase and it is designated as $D0_{22}$ in Strukturbericht notation. The appearance of metastable tetragonal Al_3Zr is attributed incorporation of elements like Si, Ti, V in $D0_{22}$ structure [11,12]. Table 5.1 contains the structural information of the Al_3Zr intermetallics.
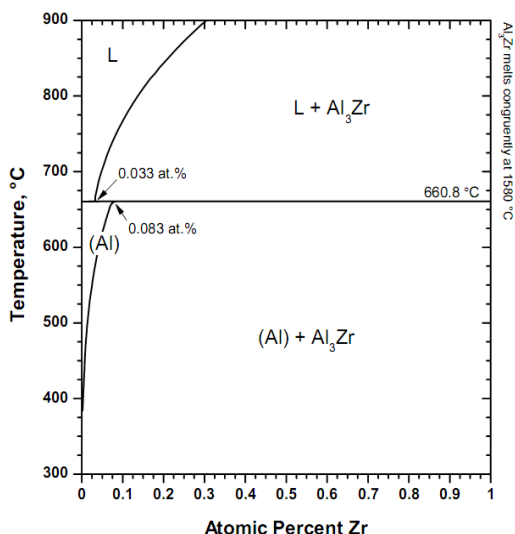
Figure 5.1 Al-Zr phase diagram [9]. Below the peritectic temperature (933.8 K) two phases exist; α-Al and $D0_{23}$-Al_3Zr. Maximum amount of Zr that can be retained in Al solid solution is indicated by a black arrow.

Table 5.1 Reported lattice parameters and the corresponding mismatch with Al for cubic L1$_2$ and related tetragonal D0$_{22}$ or D0$_{23}$ structures.

Al$_3$Zr	State	Lattice Parameters (nm)
L1$_2$ - Cubic	Metastable	a=0.408 [2,3]
D0$_{22}$ - Tetragonal	Metastable	a=0.38, c=0.82 [10]
D0$_{23}$ - Tetragonal	Stable	a=0.389, c=1.7321[2]

Both stable and metastable tetragonal structures of Al$_3$Zr have the I4/mmm space group which indicates that the structures are body centered (reflection condition h+k+l=2n) with 4 fold and two fold screw axis with mirror planes perpendicular. Tetragonal Al$_3$Zr are derivatives of basic L1$_2$ structure, see Fig. 5.2. These superstructures can be created by introducing anti phase boundary along <110> direction on {100} planes in the basic L1$_2$ structure. When an anti-phase boundary introduced in every (100) plane D0$_{22}$ superstructure is formed while when anti-phase boundary introduced in every second (100) plane D0$_{23}$ superstructure is created.
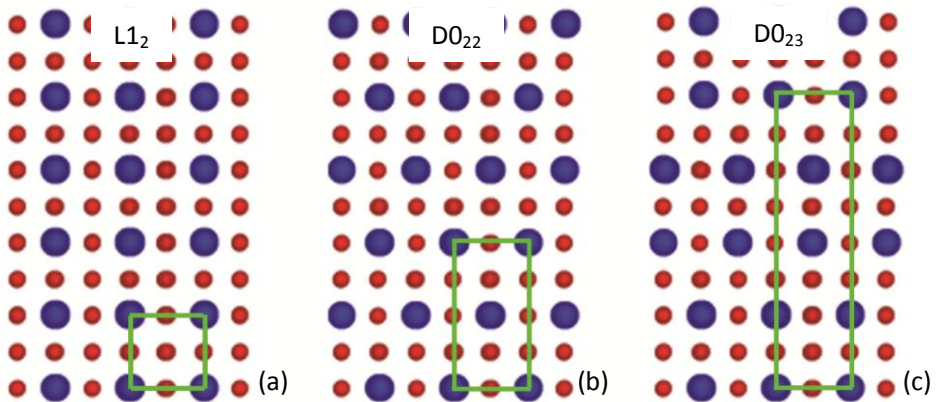
Figure 5.2 Unit cells of ordered Al$_3$Zr phases, (a) metastable cubic L1$_2$, (b) metastable tetragonal D0$_{22}$, (c) cubic tetragonal D0$_{23}$. Blue disks represent Zr atoms. Al atoms are shown as small red disks. Unit cell projections are in green.

The aim of this chapter is to study in detail the precipitation of Zr from Al solid solution containing Fe and Ni using transmission electron microscopy techniques. The as-cast microstructures often have gradient in grain size between top and bottom parts of the samples and shows segregations [13]. These features are especially reported in arc-melted alloys. Therefore contrary to the studies in the literature where Zr precipitated after annealing of as-solidified alloys, we studied the decomposition of the homogenized and then quenched alloys. In this way, the effect

of an as-cast microstructure on the Zr, Fe and Ni decomposition was avoided. All the alloying elements can be nucleated inside large grains. Especially role of Fe and Ni on the precipitation of $L1_2$ – Al_3Zr phase after annealing at 573 and 698 K is sought.

5.2 Experimental details

The sample (the as-cast alloy) was homogenized for 120h near eutectic temperature (905 K). As explained in Chapter 1. Homogenization is essential to obtain homogeneous solute distribution. Homogenization of the alloys with higher Zr concentration than maximum solid solubility results in the formation of stable phase $D0_{23}$ type Al_3Zr. This reduces the amount of Zr to be retained in solid solution after quenching and amount of precipitation will be lower consequently.

The alloy studied contains 0.06 at. % Zr which is lower than the maximum solubility at the peritectic temperature (see Fig. 5.1). Therefore, given the long homogenization at near peritectic temperature all Zr particles are expected to be dissolved. The solution heat treated alloy was immediately quenched into a water–ice mixture and then annealed at conditions described in Chapter 1.

5.3 Results and discussion

5.3.1 As-cast, as-quenched

The Microstructure of the as-cast alloy was investigated with SEM and (S)TEM. Back scattered SEM images in Fig. 5.3 show coarse, faceted intermetallic particles of size of few microns and smaller irregular shaped particles positioned along a line, thus forming casting grain boundary precipitates. Big particles show facets that suggest these particles formed probably in liquid state and were identified as primary Al_3Zr crystals by EDX.
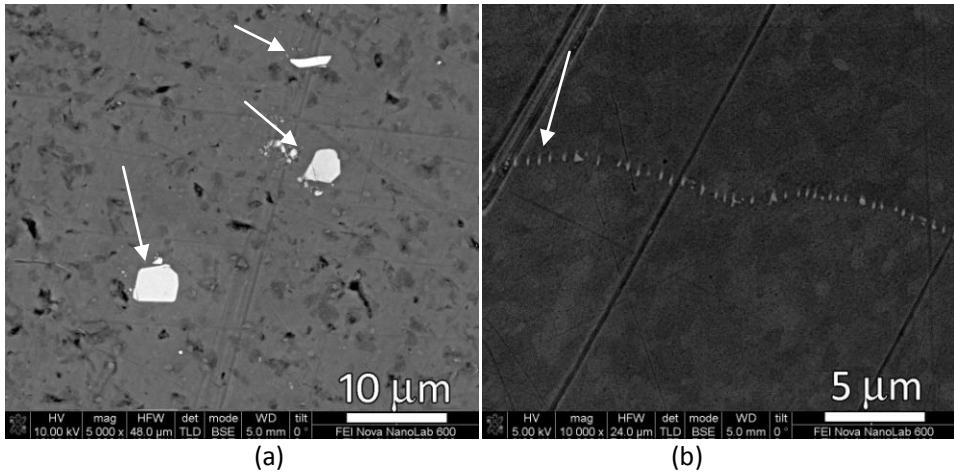
(a)   (b)

Figure 5.3 SEM images of microstructure of as-cast alloy. (a) Coarse Al_3Zr particles, (b) finely spaced smaller particles. The particles in the images are indicated by white arrows.
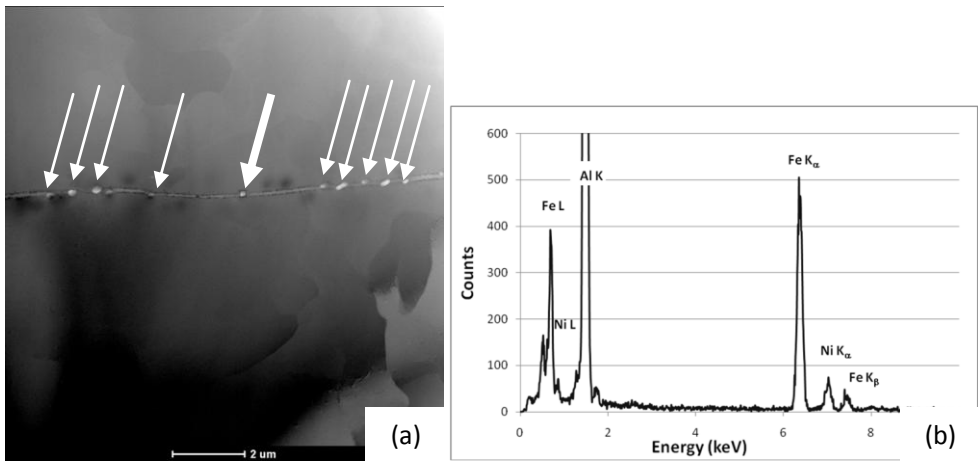

Figure 5.4 An ADF-STEM image of the microstructure of the as-cast alloy. (a) particles formed on high angle grain boundaries indicated by white arrows, (b) EDX spectra obtained on an $Al_9(Fe,Ni)_2$ particle indicated by a thick white arrow.

TEM investigation of a sample area with string of particles seen in the SEM image in Fig 5.3 reveals that these particles lie on a high angle grain boundary in the microstructure. Fig. 5.4 (a) shows the ADF STEM image of such a string of particles. Fig. 5.4 (b) shows the EDX spectrum obtained on a precipitate indicated by the thick white arrow in Fig. 5.4(a). Presence of Fe and Ni are clearly seen in the EDX spectra.

Quantification of EDX spectra obtained on different grain boundary particles show that particles on average contains 87 at. % Al, 12.2 at. % Fe and 0.8 at. % Ni. The Al richest Al-Fe-Ni intermetallic is monoclinic $Al_9(Fe,Ni)_2$ phase in which Al constitutes 82 at. % while sum of Fe and Ni 18 at. %. Particles probably sit on Al matrix and do not thread top to bottom. Therefore it is expected that Al signal is not only generated by the particles but also by Al matrix beneath the particles because of the interaction volume created by electron beam. The grain boundary particles most likely are $Al_9(Ni,Fe)_2$.

In addition to the coarse particles in Fig. 5.3(a), particles with a rod like morphology (deduced from tilting series) were also observed in the microstructure of as-cast alloy. A BF-TEM image of such a particle is presented in Fig. 5.5 (a). These particles are as long as 500 nm.
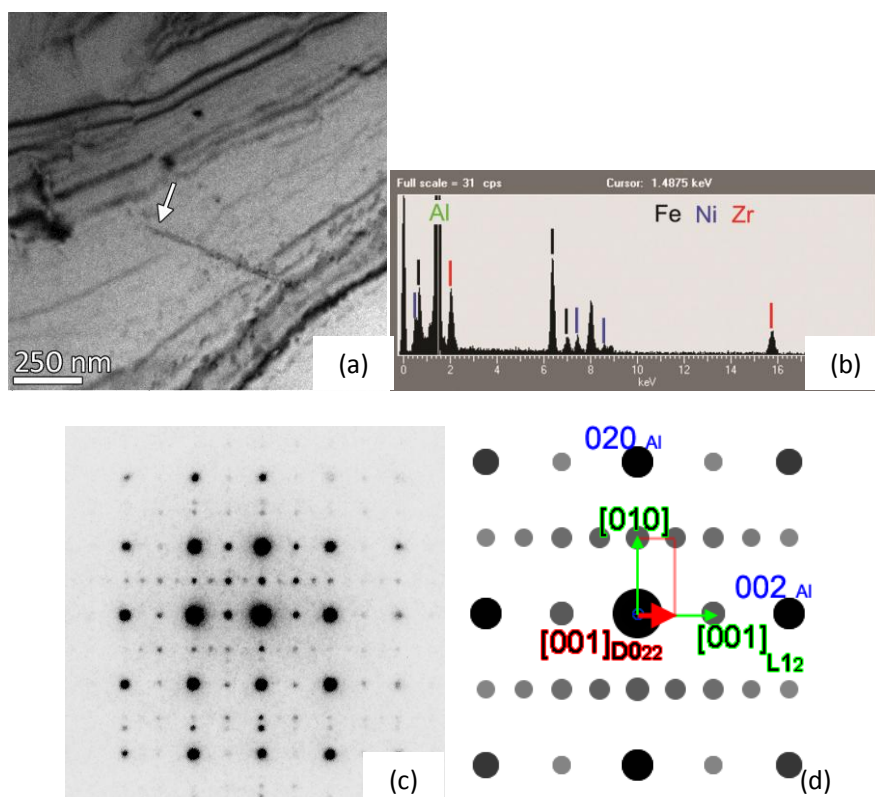
Figure 5.5 Particle in as-solidified structure. (a) Bright-Field TEM image, particle is indicated by an arrow (b) EDX spectrum obtained on the particle. (c) electron diffraction pattern acquired on the particle (d) simulation of the diffraction pattern

EDX analyses (Fig 5.5(b)) on long particles reveal that particles are rich in Zr but also contain Fe and Ni. Fig 5.5 (c) is a nano-beam electron diffraction pattern from such a particle. Analysis of a diffraction pattern reveals that the diffraction pattern contains spots from metastable tetragonal ($D0_{22}$) Al_3Zr phase and metastable cubic ($L1_2$) Al_3Zr. The simulated superimposed diffraction patterns from $D0_{22}$ and $L1_2$-Al_3Zr phases are shown in Fig 5.5 (d). The spot between central beam and Al 200 spot belongs to 100 and 002 spots of $L1_2$ and $D0_{22}$ structures respectively, while the spot between 020 Al and a central spot belongs to cubic direction of $L1_2$ structure. $D0_{22}$ structure is an ordered tetragonal unit cell and 010 and 001 spots are extinct since they do not fulfill the h+k+l=2n reflection condition for I4/mmm space group.

$D0_{22}$ phase has Al_3Zr stoichiometry [10]. According to the Al-Zr phase diagram it does not to form in dilute Al-Zr alloys. Experimental studies carried out since 1970s in binary Al-Zr alloy did not show this phase.

Recent studies show that $D0_{22}$-Al_3Zr phase is formed or stabilized with the incorporation of Si, Ti, Fe and Ni. Carlsson and Meschter and Xu and Freeman have shown by ab-initio calculations that the stability of the $D0_{22}$/$D0_{23}$ structure relative to the $L1_2$ increases rapidly as the transition metal d-electron count increases [12]

5.3.2 Annealed 573 K and 698 K

Typical low magnification ADF-STEM images of the 573 K and 698 K annealed samples are presented in Fig 5.6. The small bright areas are matrix precipitates. The contrast gradient (along the black arrows) seen in the images is due to increase of thickness in the scan area. In STEM imaging, the fraction of inelastic scattering events increases with thickness which causes an increase in the background and a reduction of the contrast.

Analysis of annealed samples reveals that matrix precipitates are not the only one kind. The several precipitate types observed in the annealed Al-Zr alloys are summarized in Table 5.2. The majority of the precipitates found in the annealed samples belong to $L1_2$-Al_3Zr cubic phase. Next to cubic Al_3Zr precipitates, $Al_{13}Fe_4$ and $Al_9(Ni,Fe)_2$ precipitates with different morphologies were also observed. The most striking finding is that these, Al-Fe and Al-Fe-Ni, precipitates are decorated with few nm thick $L1_2$-Al_3Zr phase. This phenomena (precipitation of $L1_2$-Al_3Zr on Fe/Ni intermetallics), will be referred as secondary precipitation throughout the text.
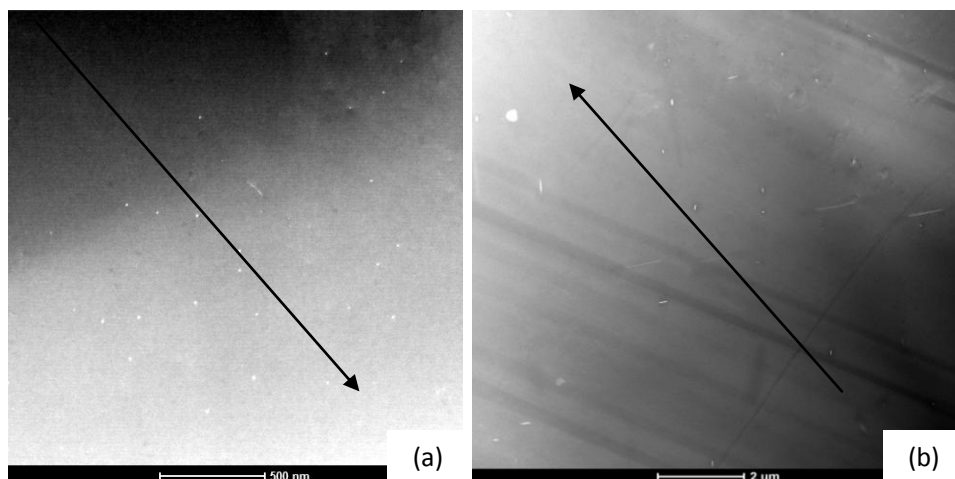
Figure 5.6 ADF STEM images of precipitates observed in microstructure of an annealed Al-Zr alloy. (a) 573 K, (b) 698 K. The bright spots in these images are from the precipitates. The black arrows indicate the contrast gradient in the images due to thickness change.

Table 5.2 Overview of precipitates structures formed in Al-Fe-Zr alloy.

Annealing Conditions	Intermetallic Phase	Shape/Morphology	Size (nm)	Figure
20h 573 K	$L1_2$-Al_3Zr	Cuboid	7-10	5.7(b,d)
20h 573 K	$Al_{13}(Fe,Zr)_4$	Thin-disc like	10-15	5.12
20h 573 K	$Al_9(Ni,Fe)_2$ with $L1_2$-Al_3Zr	Plate like with Cubic Al_3Zr on	100	5.16
20h 698 K	$Al_9(Ni,Fe)_2$ with $L1_2$-Al_3Zr	Plate like with Cubic Al_3Zr on	250	5.17
20h 698 K	$L1_2$-Al_3Zr	Truncated Octagonal prism	10-20	5.7(c,e)
20h 698 K	$Al_{13}Fe_4$ with $L1_2$-Al_3Zr	Rod like with Cubic Al_3Zr on	10-100	5.19(a,b) 5.20-21
		Plate like with Cubic Al_3Zr on	100	5.22-25

5.3.2.1 L1$_2$-Al$_3$Zr matrix precipitates after 573 K and 698 K annealing

Two different types of L1$_2$-Al$_3$Zr matrix precipitates are observed after annealing experiments: precipitates without defects and with defects. Defect free precipitates are 5-10 nm and 10-20 nm. Precipitates with defects are about 20 nm size.

Fig. 5.7(a) is a typical nano-beam electron diffraction pattern obtained on a L1$_2$-Al$_3$Zr precipitate. In Fig5.7 (b-e), small matrix L1$_2$-Al$_3$Zr precipitates observed in the samples annealed at 573 K and 698K are presented. As it can be seen from the diffraction pattern cubic Al$_3$Zr precipitates have cube on cube relationship with Al matrix.

$$\{100\}_{Al}//\{100\}_{Al3Zr}.$$

This orientation is expected because L1$_2$ phase and Al are similar in structure and L1$_2$-Al$_3$Zr lattice parameter differs only 0.8% and two structures can match. The precipitate matrix interface are primarily {100} planes.

L1$_2$-Al$_3$Zr particles formed during 573 K annealing are approximately 5-10 nm in size. The precipitates appear with {100} and {110} facets and it is observed that {100} faces are longer than {110} faces, shown in Fig 5.7(b), (d). This suggests that once particle forms on the {100} planes the initial growth direction is <100> and precipitate shape is observed as a cuboid.

As can be seen in Fig. 5.7(c) and (e), increase of the annealing temperature to 698 K results in bigger precipitates (15-20 nm). In these precipitates {110} facets are longer than {100} facets (in reality both {111} and {110} planes forms but we see 110 faces in 2-D projection). Therefore at 698 K as particles get bigger growth direction is switched to <110>. The shape of the precipitates is seen as octagonal prism in a TEM sample. Obviously, the precipitate growth direction and shape change between smaller and bigger precipitates (cuboid to octagonal prism).

For small L1$_2$-Al$_3$Zr precipitates formed at 573 K major interfacial planes are {100}Al$_3$Zr planes. The precipitates smaller than 10 nm appear as cuboids. In bigger precipitates the main interfacial planes are {110}Al$_3$Zr and {111}Al$_3$Zr.
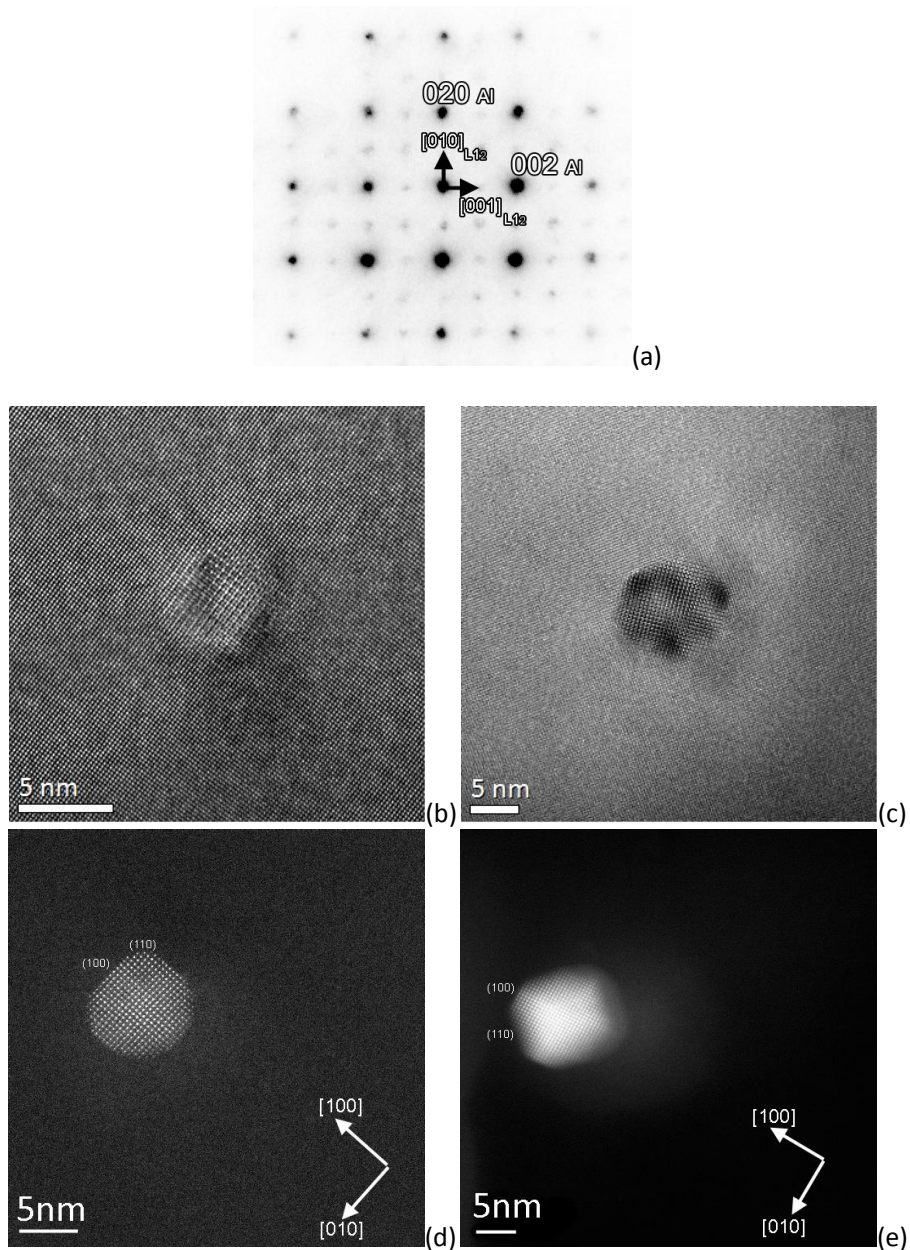
(a)

(b)

(c)

(d)

(e)

Figure 5.7 $L1_2$-Al_3Zr matrix precipitates formed after annealing 20 hours (a) typical nano-beam diffractio pattern from a matrix precipitate, superlattices reflections are weaker. HRTEM images (b) 573 K (c) 698 K and Z-contrast HRSTEM images obtained at, (d) 573 K (e) 698 K. Z-contrast STEM images show the facets clearly.

Observation of cuboid morphology is related to elastic strain between $L1_2$-Al_3Zr and Al lattices. Coherency across a precipitate-matrix interface is generally lost when the precipitate size exceeds a critical value [14], which typically corresponds to

$$n = 1/\delta,$$

where n is the number of atomic planes in the matrix and δ is the lattice parameter mismatch between the two phases [ref]. The misfit between $L1_2$-Al_3Zr precipitates and Al matrix is 0.8 %. With this misfit value precipitates can maintain the coherency up to 25 nm size. Then misfit dislocations will be introduced. The defect free precipitates are below 15 nm in size and thus no misfit dislocations are introduced.

For coherent cubic precipitates with the same basic structure as Al, the interfacial energy term determines the equilibrium shape of the precipitates and the equilibrium shape will be a sphere, ignoring the coherency strains [15]. On the other hand contribution of the elastic strain energy term cannot be ignored for $L1_2$-Al_3Zr precipitates due to 0.8% misfit between $L1_2$-Al_3Zr and Al lattices. Thus when the precipitates are small (such as ones formed during 573 K) misfit can be easily accommodated and elastic strain energy term overcomes interfacial energy term. As a result a cuboid precipitate shape observed. But as the precipitate sizes increases, strain energy reaches levels that cannot be accommodated and misfit dislocations are introduced. Thus the effect of elastic strain on the precipitate shape can be ignored since the contribution of elastic strain energy of misfit dislocations is not significant. Therefore interfacial energy determines the precipitate shape. And logically more favorable {110} and {111} planes are formed to minimize interfacial energy and the precipitate shape transforms into and eventually will be spherical upon longer annealing times. This is schematically shown in Fig. 5.8.
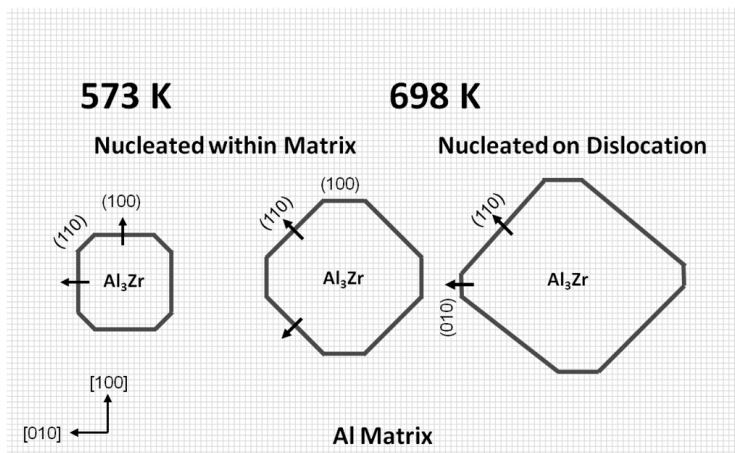

Figure 5.8 Pictorial representation of the evolution of the precipitate shape.

Some of precipitates such as those presented in Fig. 5.9 have defects. A detailed look at these precipitates reveal that the defects have planar character and are always parallel to the {100} planes of the $L1_2$ structure, for example in Fig. 5.9 (a). $L1_2$-Al_3Zr precipitates containing these planar faults have elongated shapes (such as one in Fig. 5.9) due to a preferential growth along the fault lines.

Close examination of this precipitate, in Fig. 5.9 (b), reveals that upper and lower part of Al_3Zr precipitates are separated by a block of 4 unit cell height. The contrast in this block indicates the presence of two anti phase boundaries separating two parts. A model for this block is presented in Fig. 5.10. It has the tetragonal $D0_{23}$ structure (which is superlattice of $L1_2$ as explained in the Fig. 5.2).

Similar structural faults have been reported by several authors on Al-Zr, Al-Ti-V-Zr and Al-Ti-Zr alloys [16,17,18]. These faults act as precursor for $L1_2$ to $D0_{23}$ transition. A study of Knipling reports the transformation of heterogeneously nucleated $L1_2 – Al_3Zr$ particles to stable $D0_{23}$–Al_3Zr after annealing at 698 K for 100 hour whereas homogeneously nucleated $L1_2 – Al_3Zr$ precipitates did not transform into the $D0_{23}$ structure.

A classical way to investigate $L1_2$ type precipitates is by Dark-Field TEM [1,2,3,4,13,17]. The DF-TEM images from $L1_2$-Al_3Zr precipitates are formed using {100} spots and then precipitates appear as bright in dark background. Such images from $L1_2$-Al_3Zr precipitates, reported by numerous researches often show sharp lines of dark contrast parallel to {100} planes inside the $L1_2$ precipitates [16,17,18]. These features in DF-TEM images indicate the coherency loss of in the precipitates and are generally attributed to antiphase boundaries (APB) generated during growth of the precipitates.

An APB can be created in two ways. The first way is, if two $L1_2$ particles nucleate at different positions in the matrix phase ($L1_2$ is an ordered structure with FCC lattice see Figures 5.2). A FCC cell contains four atom positions; 0 0 0, ½ ½ 0, ½ 0 ½ and 0 ½ ½ . In an ordered FCC crystal such as Al_3Zr, a Zr atom can occupy one of the four possible positions (let's say 0 0 0) and nucleate and form an Al_3Zr precipitate. Suppose another $L1_2$-Al_3Zr precipitate nucleates with a Zr atom occupying the same position (0 0 0); when these precipitates grow and meet each other the boundary between them cannot be distinguished and they will form a larger $L1_2$-Al_3Zr precipitate. On the other hand if the second precipitate nucleates with a Zr atom taking up one of the three positions other than 0 0 0 an APB will be created when these two precipitates meet. An anti phase boundary is characterized with a displacement vector **a**/2 <110> in a {100} plane, where **a** is the unit cell parameter of the $L1_2$ structure.

Dislocations also initiate creation of an anti phase boundary for ordered cubic phases. This is illustrated in Fig 5.11 for an edge dislocation. When an Al_3Zr nucleate on an edge dislocation, particle is sheared along the displacement vector of a/2<110> (for FCC) and can grow with a shift below and above the dislocation. This naturally creates an anti-phase boundary.
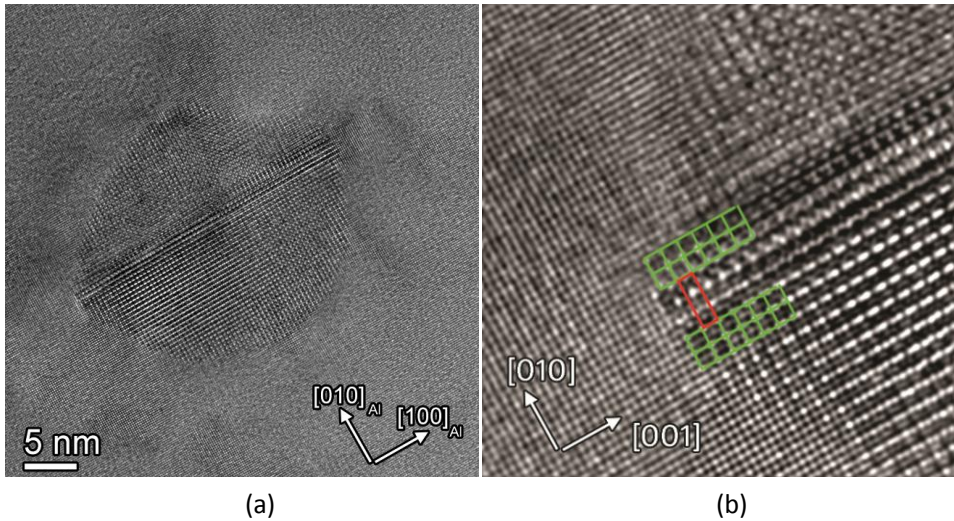

(a)   (b)

Figure 5.9 Heterogeneously nucleated $L1_2$- Al_3Zr precipitate. (a) entire HRTEM image (b) Detailed view of the structural fault. Green squares represent $L1_2$-Al_3Zr unit cell and the red rectangle indicates $D0_{23}$-Al_3Zr unit cell projection along [010].
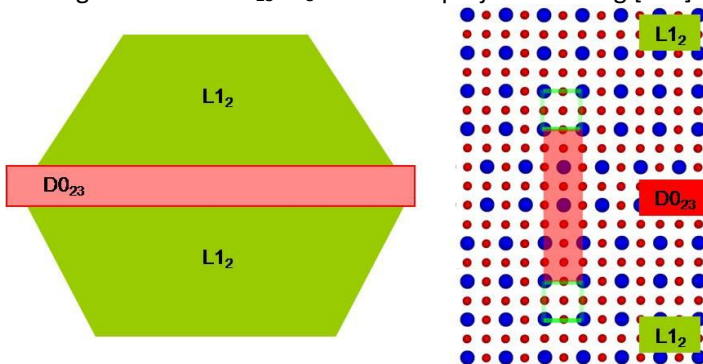
Figure 5.10 (a) Pictorial representation of the precipitate and (b) the structural model. $L1_2$ unit cells are indicated in green squares. $D0_{23}$ unit cell projection is shown in red rectangle. Blue balls represent Zr atoms while red ones are red.
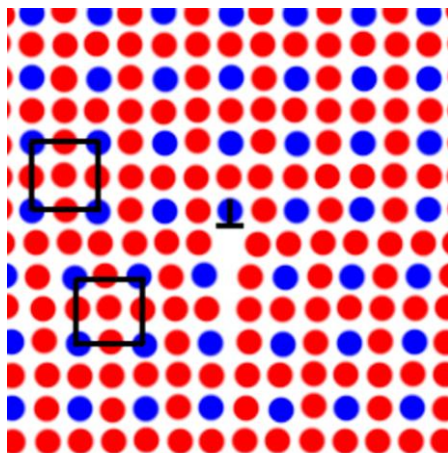
Figure 5.11 Illustration of creation of an antiphase boundary during nucleation of an ordered phase on a matrix dislocation. Red dots represent Al atoms while Blue dots show Zr atoms positions. L1$_2$ unit cells are indicated in black squares.

Increasing the aging temperature in precipitation reactions (effect similar to decrease undercooling) reduce the chemical driving force due to less oversaturation, on the other hand increases the diffusion speed which leads to formation of larger precipitates and lower density of the precipitates. This favors heterogeneous nucleation of precipitates at lattice defects such as dislocations, low and high angle grain boundaries. In the case of precipitation of L1$_2$-Al$_3$Zr phase, dislocations can reduce the lattice strain energy and interface energy, as well. Therefore, the activation energy barrier for heterogeneous nucleation is lowered [14] and L1$_2$-Al$_3$Zr precipitates form easier. On the other hand heterogeneously nucleated precipitates lose coherency and suffer from faster coarsening rates (compare images of the defect free precipitate in Fig 5.7(b) and the precipitate with a defect in Fig 5.9).

*5.3.2.2 Al$_{13}$(Fe,Zr)$_4$ intermetallic at 573K*

A thin disc like precipitate and its EDX spectrum are seen in Fig. 5.12. The EDX spectrum indicates that in addition to Al as the main constituent, this precipitate contains Fe and Zr. Fig 5.13 (a) shows a nano-beam electron diffraction pattern of this precipitate. The spots with strong intensities can be indexed with from the Al [011] zone axis and are to the Al matrix above/below the precipitate. The weaker spots visible in between the main Al spots are from the precipitate. The nano-beam electron diffraction pattern (in Fig 5. 13 (a)) can be indexed with Al$_{13}$Fe$_4$ phase. Given the EDX results, Zr must be dissolved in this phase. In its pure form Al$_{13}$Fe$_4$ structure [19] has monoclinic unit cell with 102 atoms of which 24 Fe atoms and 78 Al atoms.

The lattice parameters (determined from X-ray diffraction data) of the ideal $Al_{13}Fe_4$ structure is

$$a=1.54890 \text{ nm } b=8.0831 \text{ nm } c=1.24760 \text{ nm } \beta=107.7200°[19]$$
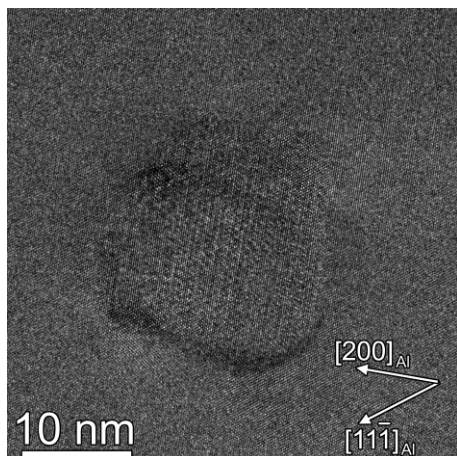
(a)
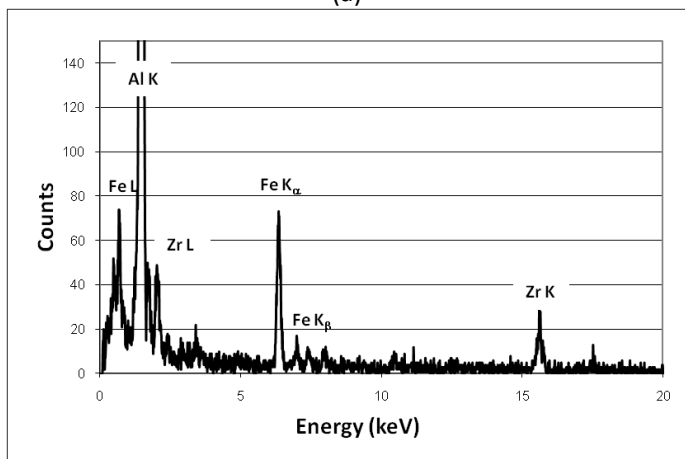
(b)

Figure 5.12 (a) HRTEM image of a disk like precipitate in the microstructure of the sample annealed at 573 for 20 h. Image obtained under <110> zone axis of Al. (b) EDX spectrum from the particle.

Analyses of DP indicates that precipitates have the orientation relationship

$$(010)_p \text{ // } (100)_{Al} \text{ and } [100]_p \text{ // } [011]_{Al}$$

A simulated diffraction pattern based on this orientation relationship is given in Fig. 5.13(b). As it is schematically explained Fig 5.13 (c), when the matrix is oriented along <110> the disc like precipitate morphology is observed parallel to the short axis of the disc. Under this condition/orientation the precipitate morphology reveals broad faces normal to the electron beam direction. If we would be able to tilt the specimen were able to be tilted to 001 zone axis of Al [010] precipitates would be observed along [010] $Al_{13}Fe_4$ and precipitates would probably appear as plates.

Comparison of superposition of simulated diffraction patterns, Fig 5.13(b), according to the orientation relationship using unit cell parameters of pure $Al_{13}Fe_4$ and Al with an experimental diffraction pattern, Fig 5.13(a), shows that precipitate unit cell and Al matrix are coherent and the $(60\text{-}6)_P$ reflection is matching with $(200)_{Al}$ and the $(060)_P$ reflection is matching with $(02\text{-}2)_{Al}$. As a result of plane matching the unit cell is increased in the [010] direction to 0.85 nm from 0.808 nm and the (10-1) planes expand from 1.1041 nm to 1.25 nm. Therefore with incorporation of Zr, the volume of the $Al_{13}Fe_4$ expands approximately 0.6 % larger compared to the original $Al_{13}Fe_4$ unit cell, illustrated in Fig 5.14. This is expected since Zr has larger atomic radii (206 pm) than Fe (156 pm) and Al (118pm) [20,21]. The better plane matching between the precipitate and Al matrix suggests that addition of Zr allows for an easier nucleation of $Al_{13}Fe_4$.

The diffraction patterns of the precipitates also show reflections that are extinct in pure $Al_{13}Fe_4$: h+k=2n and are due to C centering (+ ½ , ½, 0). It is probable that enlargement of the unit cell causes atoms to be displaced which break the C-centering. On the other hand to judge change in space group symmetry from single crystal diffraction patterns can be wrong because of defects present in the precipitates after nucleation and growth within a matrix.

Table 5.3 Averaged Quantification results on disk like particles with typical uncertainty, detector correction and k-factor values output from EDX quantification software.

Element	Weight %	Atomic %	Uncertainity %	k-Factor	Detector Correction
Al(K)	93.51	97.17	0.55	1.403	0.92
Fe(K)	4.26	2.14	1.027	0.17	0.99
Zr(K)	2.22	0.68	0.12	3.730	0.99

Al$_{13}$(Fe,Zr)$_4$ [101] / Al [011]   **Al$_{13}$Fe$_4$ [101] / Al [011]**

(a)

(b)

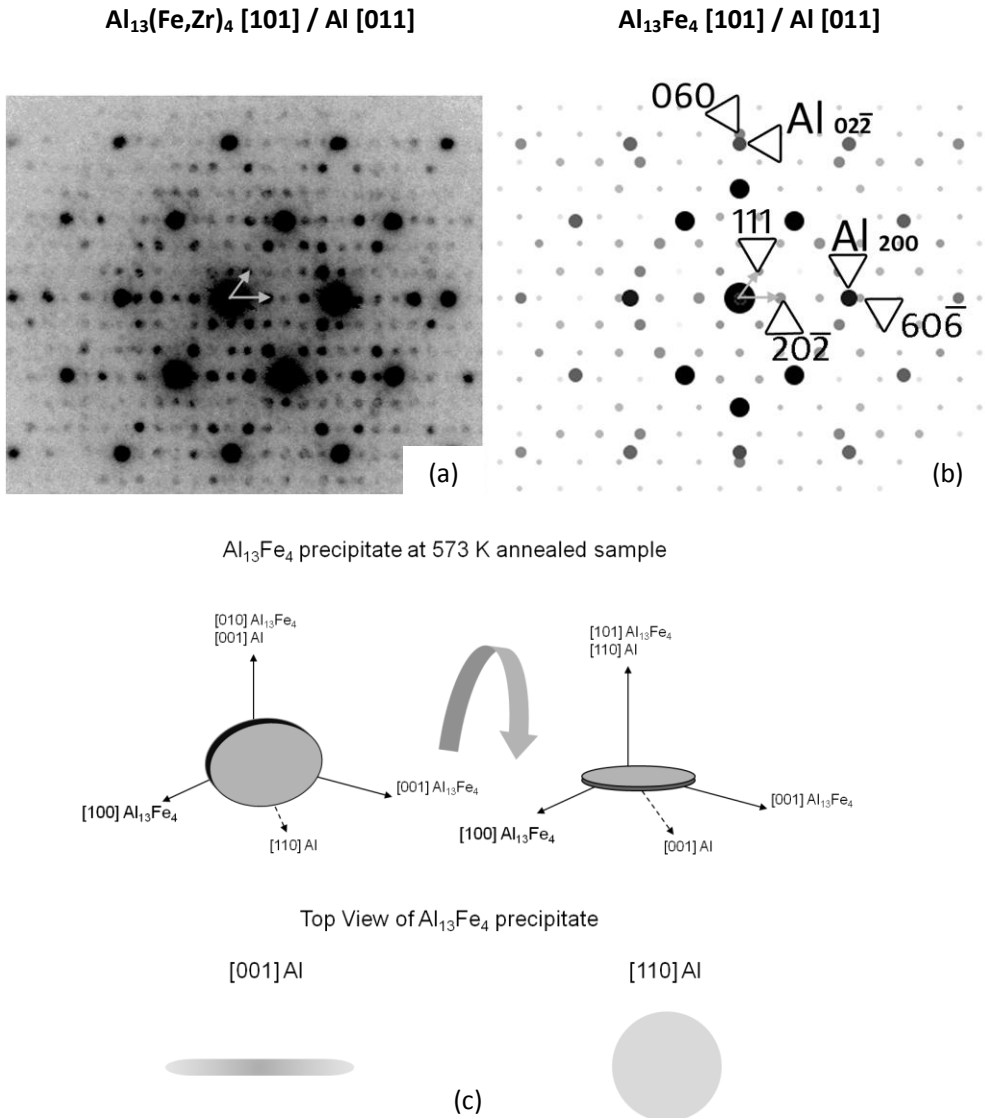Al$_{13}$Fe$_4$ precipitate at 573 K annealed sample

(c)

Figure 5.13 (a) Nano-beam electron diffraction pattern obtained on the particle seen in Fig 5.12(a). (b) Superimposed calculated diffraction patterns of Al$_{13}$Fe$_4$ and Al crystal. Diffraction patterns were calculated kinematically using JEMS[1][22]. Al$_{13}$Fe$_4$ zone axis is [101], Al zone axis is chosen as [011]. (c) Morphology of the Al$_{13}$(Fe,Zr)$_4$ precipitate are explained according to orientation relationship given in the text.

---

[1] Available from: http://cimewww.epfl.ch/people/stadelmann/jemswebsite/jems.html

Enlargement of $Al_{13}Fe_4$ unit cell by Zr

$Al_{13}Fe_4$ $Al_{13}(Fe,Zr)_4$

(010) is 0.808 nm
 measured (010) 0.859 nm   **Along [010] change is 6.3%**

(10-1) is 1.10412 nm
measured (10-1) 1.215 nm   **Along (10-1) change is 9.9 %**
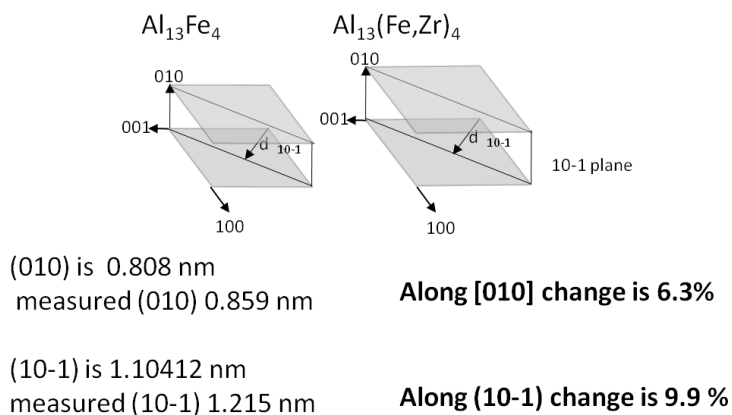
Figure 5.14 Schematic illustration of expansion in $Al_{13}Fe_4$ unit cell by Zr. Expansion of (010) and (10-1) planes are concluded from comparison of experimental and simulated diffraction pattern in Fig 5.13.

5.3.2.3 L1$_2$-Al$_3$Zr secondary precipitates on Al$_9$Ni$_2$ plates at after 573 K and 698 K Annealing

Plate-like precipitates were observed in the microstructure of samples annealed at 573 K and 698 K. A Z-contrast STEM image (see Fig. 5.15(a)) shows thin bright lines at the both side of the plates. EDX line scan experiments from the plate formed at 698 K annealed sample, presented in Fig. 5.15(b), shows that the plates contain Fe and Ni and Zr was detected at the plate/matrix interface. Analysis of electron diffraction patterns show that these plates are monoclinic the $Al_9(Ni,Fe)_2$ phase. In Chapter 3 of this thesis, plate like precipitates of monoclinic Al_9X_2 phase, where X is Co, Fe, Ni are described extensively. Monoclinic $Al_9(Fe,Ni)_2$ phase forms on {100} Al planes and grows along <013> direction of Aluminium. They can be long as several tens of nm while width of the plates is 5-7 nm. As a result the interface between the matrix and precipitates is flat and broad without steps forming a plate with curvature at the end of the plate which is shape is conceived as rectangular prism with rounded edges.
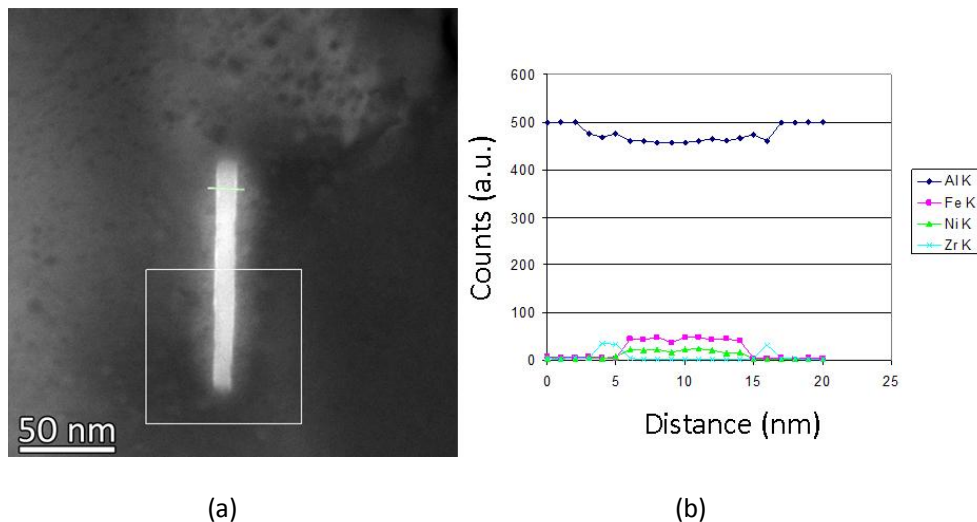
(a)   (b)

Figure 5.15 STEM EDX line profile experiment done on a plate like $Al_9(Ni,Fe)_2$ precipitate. Probe size is approximately 0.2 nm resolution. Profile size is 20 nm and 7 sec acquisition per pixel. (a) STEM image used for the experiment. EDX spectrums were obtained along the orange line. Red square was used for drift correction. (b) Extracted characteristic X-ray signals from Al, Fe , Ni and Zr.

In the Al-Zr system, the plate/ Al matrix interface observed by HRTEM shows the presence few mono layers thick $L1_2$-Al_3Zr phase at the interface. Thus, the interface between the Al matrix and the precipitate acts as a heterogeneous nucleation site for $L1_2$-Al_3Zr phase. A HRTEM image of such a precipitate is seen in Fig 5.16 (a). In this precipitate only 1-2 unit cell thick $L1_2$-Al_3Zr phase was observed on top of the plate/matrix interface formed after 573 K. Interestingly, $L1_2$-Al_3Zr phase was only observed on one of the two broad interfaces (top part of in Fig5.16(b)). This is remarkable since the interface between the precipitate and the matrix has the same atomic configuration (hence same interfacial and chemical energy) for both interfaces of the precipitate and if the Al matrix contain same amount of Zr in vicinity of the top and bottom part of the precipitate there is no reason why $L1_2$-Al_3Zr cannot be on both side of the precipitate. No cubic Al_3Zr was found in the bottom interface (Fig. 5.16(c)). This difference tells us that diffusion field of Zr is not same between top and bottom part of the plate. This might be due to chemical inhomogeneity as a result of microsegregation.
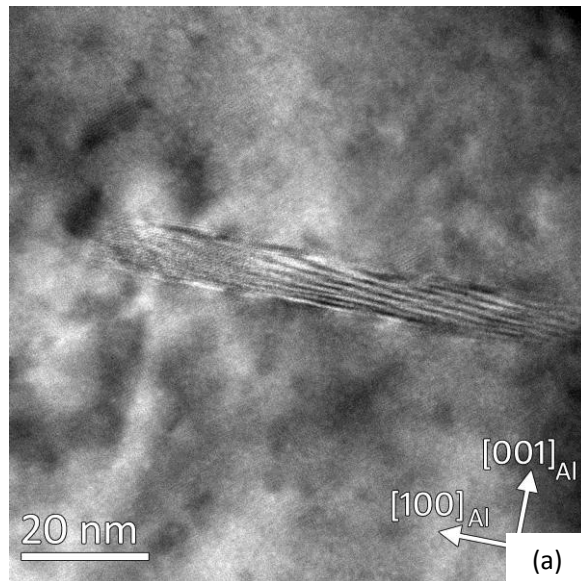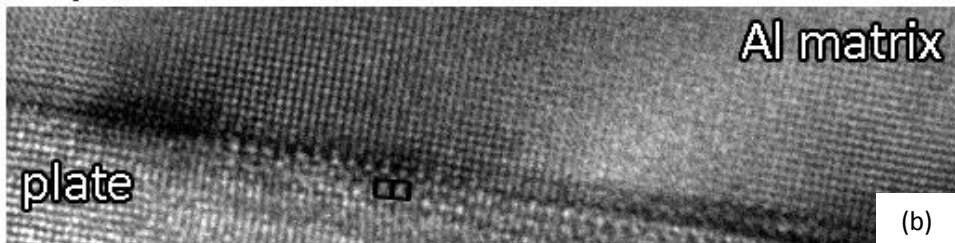
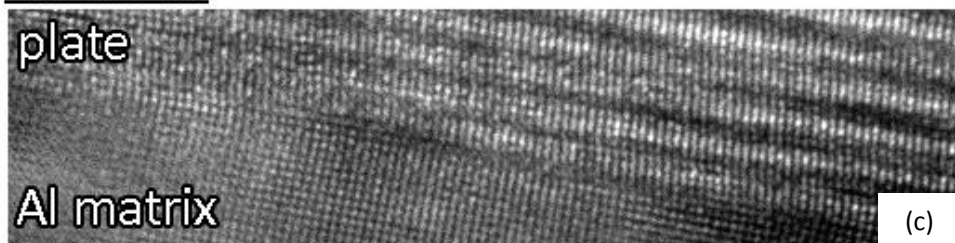**Figure 5.16** (a) HRTEM image of a plate-like precipitate observed along <100> zone axis of Aluminium. closer view of (b) the top and (c) the bottom interfaces between the plate and Aluminium matrix. 1-2 unit cell wide $L1_2$-Al_3Zr phase is present on the top interface. Unit cell $L1_2$-Al_3Zr is indicated by black squares.

Similar to 573 K annealed samples, $L1_2$-Al_3Zr phase was also found precipitated on $Al_9(Fe,Ni)_2$ plates in samples annealed at 698 K (Fig 5.17). In this sample $L1_2$-Al_3Zr forms on broad faces as thin plates size of 1-2 nm covering almost entire interface, (details can be seen in Fig. 5.17 (b)). The shape of $L1_2$-Al_3Zr secondary precipitates is half elliptical with very long size along the plate horizontal direction which is the long axis of the plate (as long as 40nm). The short axis (of the elliptical shaped Al_3Zr plate) is along the plate normal and at center of the width as high as 2 nm.

No secondary precipitates were observed at the plate ends for the plates formed at 573 K and 698 K. $L1_2$-Al_3Zr secondary precipitates on the broad faces of the plates with corresponding crystallographic directions are illustrated in Fig. 5.18. The flat interface between the $Al_9(Ni,Fe)_2$ plate like precipitates and Al matrix. The coherency with Al lattice makes easy for $L1_2$-Al_3Zr to nucleate along the interface.
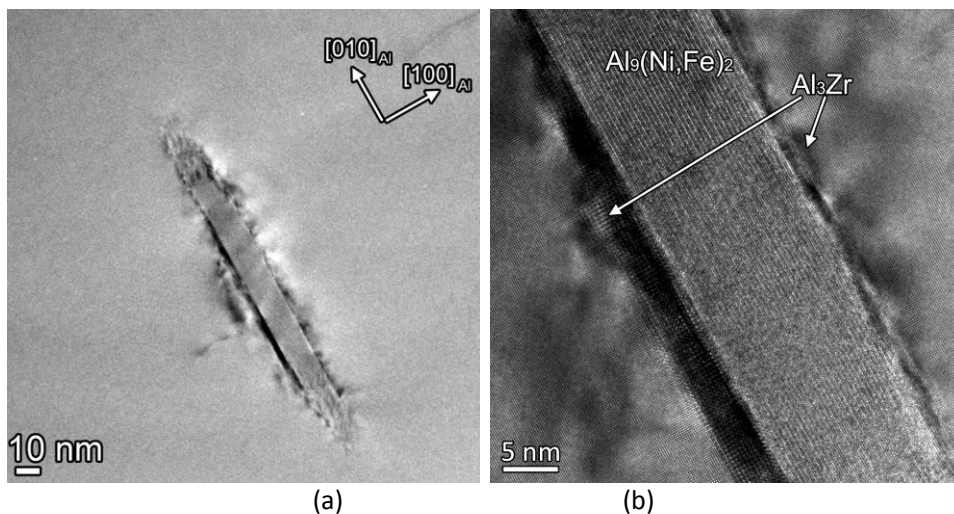

(a)   (b)

Figure 5.17 Al_3Zr phase nucleated and grown on an $Al_9(Ni,Fe)_2$ plate after 20 hours annealing at 698 K. (a) BF TEM image, (b) HRTEM image of the center part of (a). $L1_2$-Al_3Zr precipitates cover nearly the entire interface of the plate and appear as thin layers in the images.
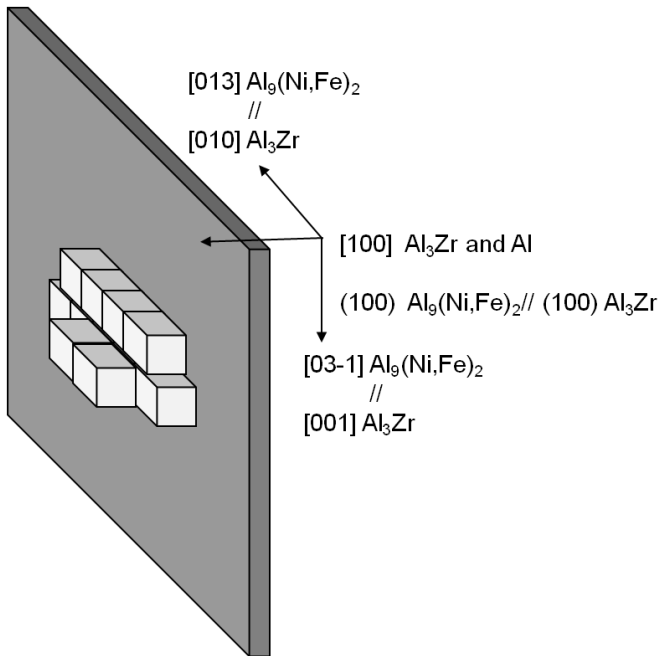
Figure 5.18 Flat broad interface of $Al_9(Ni,Fe)_2$ plates act as a heterogeneous nucleation sites for $L1_2$-Al_3Zr phase. Illustration of nucleation and growth of $L1_2$-Al_3Zr precipitates on an $Al_9(Ni,Fe)_2$ plate. Orientation relationship between the precipitate and plate is indicated.

5.3.2.4 $L1_2$-Al_3Zr secondary precipitates on $Al_{13}Fe_4$ particles after 698 K

Collection of Z-contrast STEM images from various $Al_{13}Fe_4$ precipitates formed during 698 K annealed sample are presented in Figures 5.19. These precipitates show simple rod and plate-like morphologies. Irregular shaped $Al_{13}Fe_4$ precipitates were observed, as well. Images of $Al_{13}Fe_4$ plates presented in Fig. 5.19 show that shape and morphology of $L1_2$-Al_3Zr secondary precipitates depend on the morphology of $Al_{13}Fe_4$ precipitates. Below, characteristics of $L1_2$-Al_3Zr secondary precipitates observed on different type $Al_{13}Fe_4$ precipitates are described (see Table 5.2).
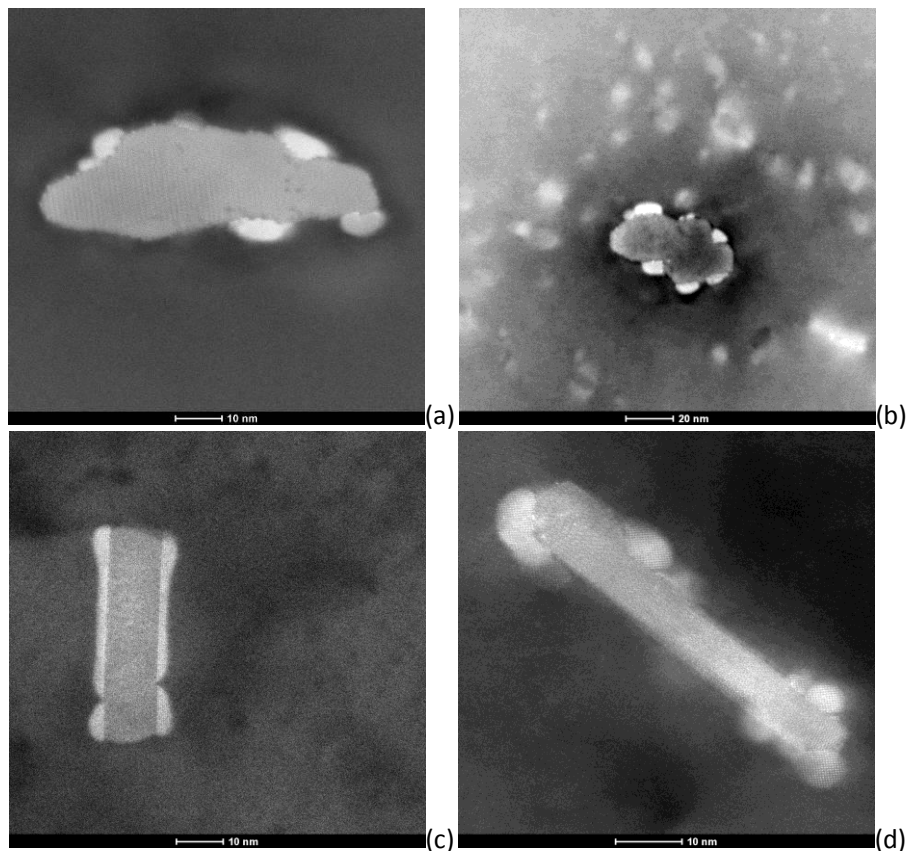
Figure 5.19 HAADF STEM images acquired on a sample annealed at 698 K for 20 hours. Various precipitate morphologies: (a) and (b) rod-like. (c), (d) plate-like precipitates. The bright contrast regions around the precipitates are due to formation of L1$_2$-Al$_3$Zr phase. Since atomic weight of Zr is higher than Fe and Ni, Al$_3$Zr regions appear brighter in Z-contrast STEM images.

On Rod-Like Al$_{13}$Fe$_4$ precipitates

Rod like Al$_{13}$Fe$_4$ precipitates are the most frequent precipitate type observed in the microstructure of the sample annealed at 698 K for 20 hours. The shape and size of these Al$_{13}$Fe$_4$ are found to vary; from small (Fig. 5.20-21) rod like Al$_{13}$Fe$_4$ precipitates, 10 nm the smallest, to large precipitates near 100 nm in length and 25 nm wide, such as one in Fig 5.19(a-b). All the rod-like precipitates over 10 nm in size contain twins and planar faults. L1$_2$-Al$_3$Zr secondary precipitates were found on all Al$_{13}$Fe$_4$ precipitates independent of the size of the Al$_{13}$Fe$_4$ rod-like precipitates. The size of the secondary precipitates varies from 2 nm (Fig. 5.21) to 10 nm (Fig. 5.20). These L1$_2$-

Al_3Zr secondary precipitates show facets on {100} and {110} planes. These can be clearly seen in Fig.5.21. The morphology of the secondary precipitates is found to be as cuboids and octagonal prisms under projection in TEM images.
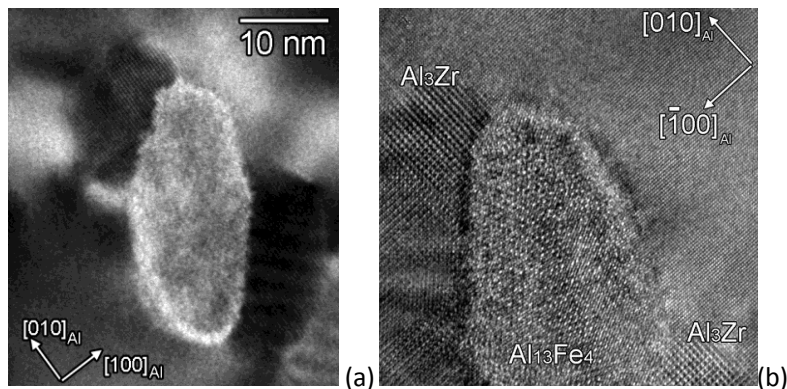

Figure 5.20 (a) Low magnification Bright-Field TEM and (b) HRTEM images from top part of rod-like $Al_{13}Fe$ precipitate. Taken along <100> zone axis of aluminum. Note the presence of Anti-phase boundaries in $L1_2$-Al_3Zr seen in left part of (b).
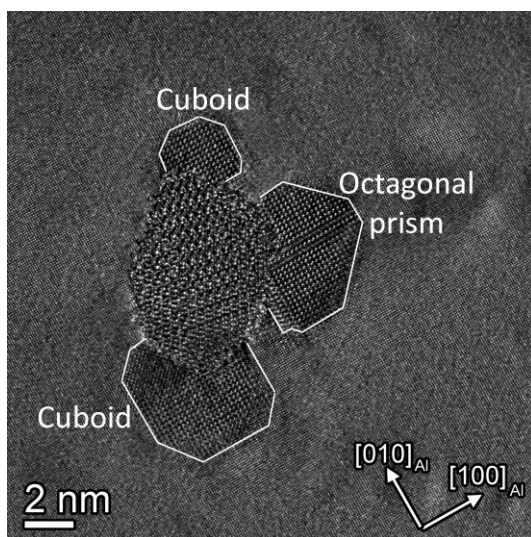
Figure 5.21 An aberration-corrected HRTEM image from a small $Al_{13}Fe_4$ rod-like precipitate with $L1_2$-Al_3Zr precipitated on it. Note the facets (outlined) in the $L1_2$-Al_3Zr precipitates and the anti-phase boundary in the precipitate seen in the right part of the $Al_{13}Fe_4$ precipitate, indicated by a white arrow. Particles on top and bottom have cuboid morphology while the particle with anti-phase boundary has octagonal prism.

On Plate-Like Al$_{13}$Fe$_4$ precipitates

Al$_{13}$Fe$_4$ plate-like precipitates with two distinct orientation relationships with respect to Al matrix were observed in the specimens after annealing at 698 K for 20 hours. The plates with different orientation relationships are designated as *type1* and *type2*. Morphologies of the secondary precipitates on Al$_{13}$Fe$_4$ plates depend on the orientation relationship of Al$_{13}$Fe$_4$ plate-like precipitates. Observed morphologies of the secondary precipitates on Al$_{13}$Fe$_4$ plates are organized in Table 5.4.

Table 5.4 Morphology of the cubic Al$_3$Zr secondary precipitates on Al$_{13}$Fe$_4$ plate-like precipitates.

Al$_{13}$Fe$_4$ Plates	L1$_2$-Al$_3$Zr Secondary Precipitate Shape	
	At Plate/matrix end interface	At Plate/matrix long interface
Type1	not observed	As thin layer / half ellipsoid
Type2	Cuboid-octagonal	Half cuboid/ half spherical

Al$_{13}$Fe$_4$ plates of *type1* were most frequently observed and have the following orientation relationship;

$$(010)Pr//\{100\} \text{ Al and } [001]Pr//<010>Al.$$

Al$_{13}$Fe$_4$ plates with *type1* orientation form {100}Al planes (this is called as the habit plane of the precipitates) as seen in Fig. 5.22-24. The all plate types were often found to be twinned. However plates of *type1* were often observed to be twinned multiple times. This eventually causes Al$_{13}$Fe$_4$ precipitates to lose their plate character as it can be seen for the case of a plate presented in Fig. 5.24(b).

L1$_2$-Al$_3$Zr secondary precipitates on *type1* Al$_{13}$Fe$_4$ plates have different shapes. Plates with twins contain half ellipsoid to half spherical L1$_2$-Al$_3$Zr, Fig. 5.24(a), whereas on non-twinned Al$_{13}$Fe$_4$ plates, L1$_2$-Al$_3$Zr phase forms thin platelets covering the broad faces of the Al$_{13}$Fe$_4$ plates, Fig 5.22. Like in the case of Al$_9$(Ni,Fe)$_2$ plates, no secondary L1$_2$-Al$_3$Zr precipitates were observed at the Al$_{13}$Fe$_4$ plates of *type1* and Al matrix ends. This is logical since both Al$_9$(Ni,Fe)$_2$ plates and Al$_{13}$Fe$_4$ plates of *type1* form on {100} Al planes with broad coherent interfaces.
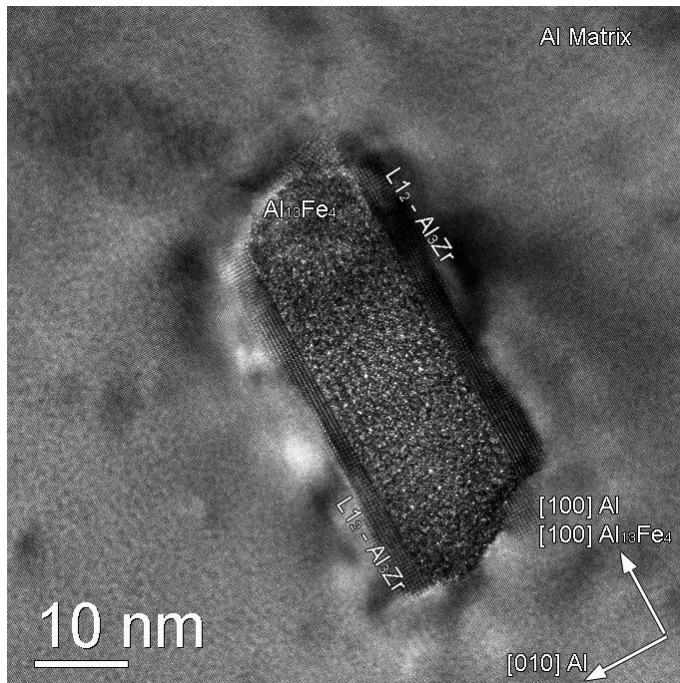
Figure 5.22 An aberration-corrected HRTEM image of a plate-like $Al_{13}Fe_4$ precipitate (type1) after 20 hours annealing at 698 K. The broad faces of plates are entirely covered with $L1_2$-Al_3Zr phase. At the plate ends no secondary precipitates present.

Plates of *type1* without twinning contains thin layer of $L1_2$-Al_3Zr. In some cases, probably related to relatively low supply of Zr atoms, there is only 1-2 monolayer of $L1_2$-Al_3Zr are found [Fig 5.23].

$L1_2$-Al_3Zr secondary precipitates are found to be on multiple twinned plates, such as Fig 5.24(b). On broad faces of these $Al_{13}Fe_4$ plates, it is possible to see well grown $L1_2$-Al_3Zr secondary precipitates of spherical shape with radius of 1-5 nm. Next to the spherical Al_3Zr there is also Al_3Zr in the form of half ellipsoid shape as it can be seen in Fig 5.24 (a). These half ellipsoid shaped $L1_2$-Al_3Zr regions have their have long axis parallel to plate growth direction and they can be as long as 20nm. The short axis of these regions is the plate growth direction and it is found between 1-3 nm.
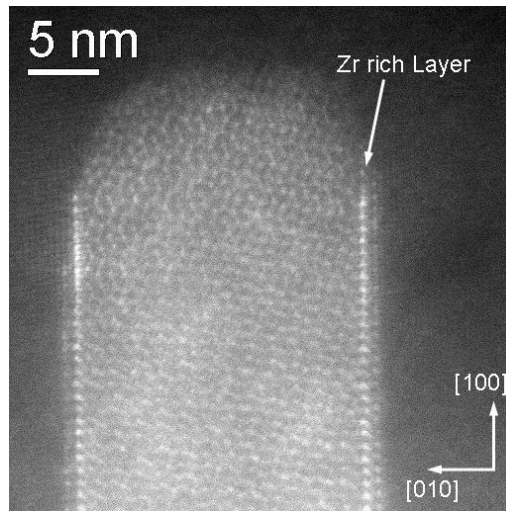
Figure 5.23 Z-Contrast HRSTEM image of an $Al_{13}Fe_4$ precipitate (type1) with secondary $L1_2$-Al_3Zr precipitates after 20 hours annealing at 698 K. $L1_2$-Al_3Zr formed
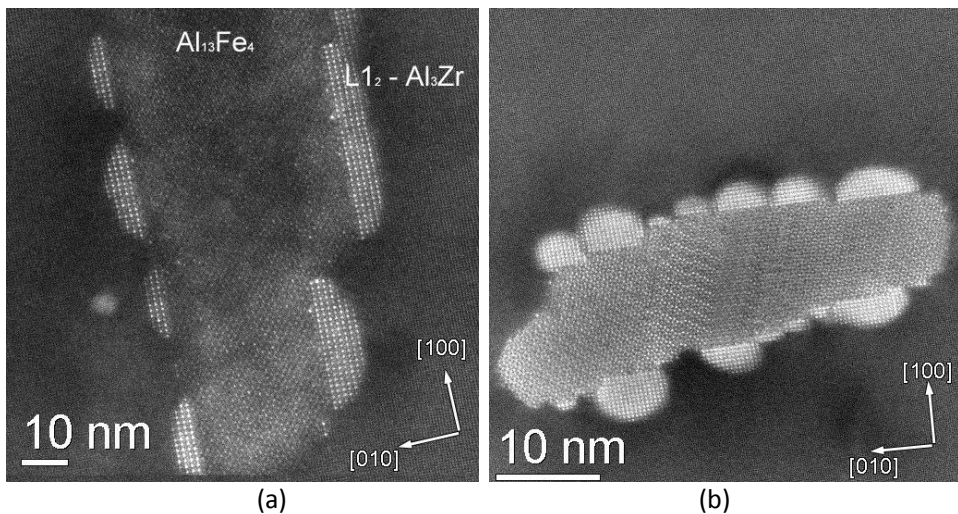

(a)   (b)

Figure 5.24 Z-contrast HRSTEM images from type1 $Al_{13}Fe_4$ plate-like precipitates after 20 hours annealing at 698 K. Precipitate in (a) is twinned. Precipitates in (b) are twinned multiple times. $L1_2$-Al_3Zr formed on flat stepped and kinked interfaces. Multiple twinned precipitate lost plate characteristics.

$Al_{13}Fe_4$ plates of *type2* have the following orientation relationship;

$$(100)Pr//\{110\}Al \text{ and } [010]Pr//<110>Al$$

An example of such a plate is demonstrated in Fig. 5.19(d) and Fig. 5.25. In *type2* plates habit plane is $\{110\}Al$. As can be seen in Fig.5.25, $L1_2$-Al_3Zr secondary precipitates with different morphologies were formed on these plates.

$Al_{13}Fe_4$ plates of *type2* forms on $\{110\}Al$. different to the secondary precipitation on type1 plates, $L1_2$- Al_3Zr secondary precipitates were found on the broad faces and end of the plates of type2. As seen in the images, Fig. 5.25 $L1_2$-Al_3Zr secondary precipitates:

- On the broad faces of the plates. The shape is a cuboid cut along the face diagonal $\{110\}$ planes
- On the corner plate matrix interface. Shape is octagonal
- At the end of plate. Both cuboid and octagonal shapes were observed.

On the broad face of the *type2* plates atomic/plane matching is not as good as in the case of type1 plates. Therefore secondary precipitates do not form thin layer along the $<110>$ interface plane. Compared to *type1* plates the interfacial area between Al_3Zr and $Al_{13}Fe_4$ precipitates is small, often confined to few nm where as in *type1* plates entire interface covered with secondary $L1_2$-Al_3Zr precipitates were seen.

When $L1_2$- Al_3Zr precipitates on the edge of *type2* $Al_{13}Fe_4$ plates they appear similar to the secondary precipitates observed on rod like $Al_{13}Fe_4$ precipitates (compare Fig.5.21 and Fig 5.25(b-c)); facets on 110 and 100 planes are observed. It is clearly seen in Fig, 5.25(b) that 110 facets are shorter than 100 facets thus the morphology of the secondary precipitates can be concluded as cuboid.

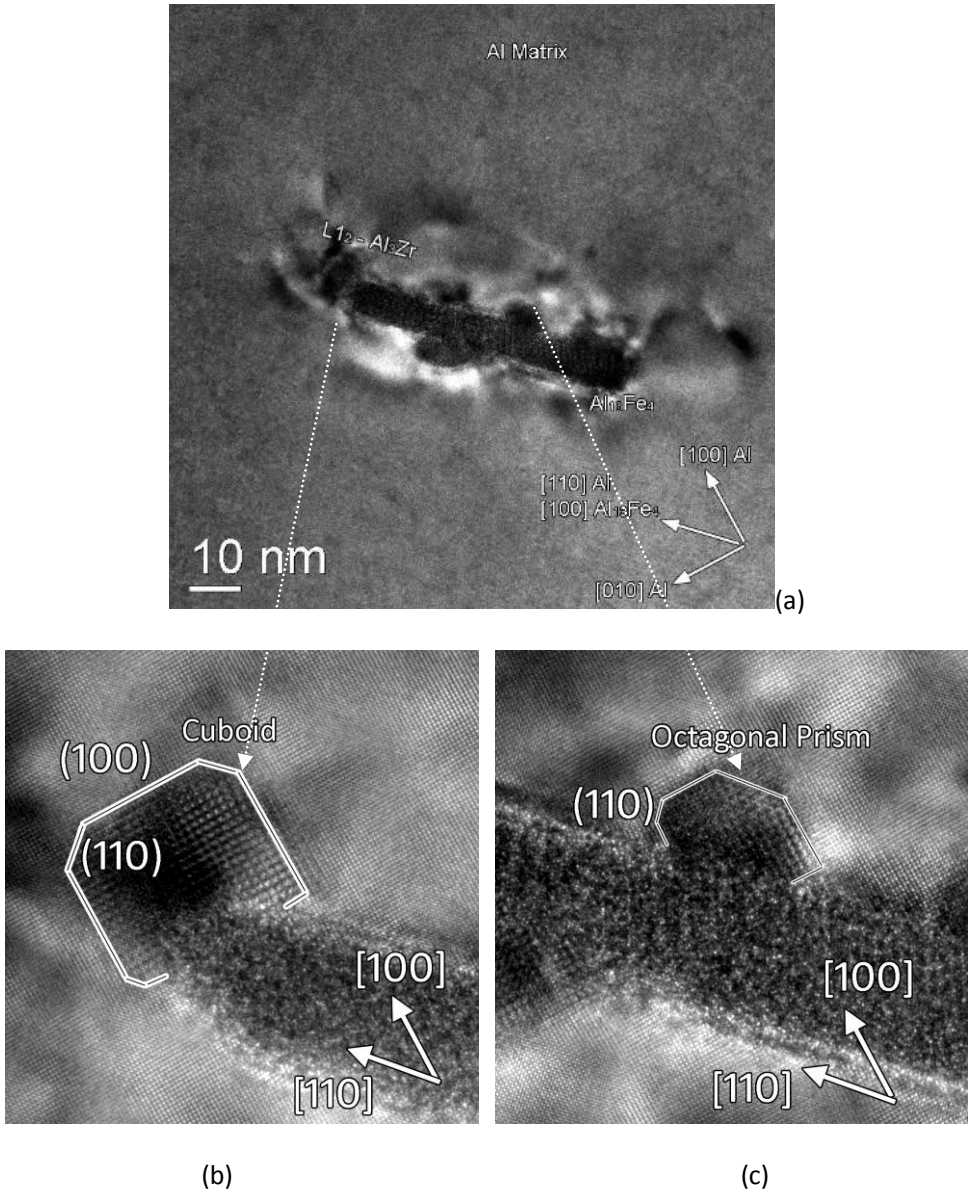**Figure 5.25** (a) An aberration-corrected HRTEM images of plate like $Al_{13}Fe_4$ precipitates of *type2* seen under <100> zone axis of Al. (b) At the plate ends secondary precipitates with cuboid morphology forms. (c) Along the long axis of the plate secondary precipitates with octagonal prism form. The (100) and (110) facets In $L1_2$-Al_3Zr/Al-matrix interfaces are indicated by white lines.

5.3.3 Characteristics of interface between $L1_2$-Al_3Zr secondary precipitates on $Al_{13}Fe_4$ plate like precipitates and Zr in $Al_{13}Fe_4$ structure

Probe corrected Z-contrast STEM images of the $Al_{13}Fe_4$ plates with orientation *type1* are shown in 5.26. These plates are covered with $L1_2$-Al_3Zr secondary precipitates. Z-contrast HRSTEM image in Fig. 5.27 shows details of the interface between $L1_2$-Al_3Zr and $Al_{13}Fe_4$. Since Zr has higher atomic number than Fe, regions decorated with $L1_2$-Al_3Zr look brighter in STEM images. The interface between $L1_2$-Al_3Zr secondary precipitates and the $Al_{13}Fe_4$ plates is sharp. Thus $L1_2$-Al_3Zr covers the large part of the interface as thin layers, as seen in Fig 5.26. When there is a disruption in $Al_{13}Fe_4$ precipitate/Al interface as such in lower part of the plate in Fig. 5.26(a), $L1_2$-Al_3Zr will not cover the entire interface but rather forms half spherical (indeed half octagonal prism) precipitates such as one shown in Fig. 5.27.

(a)   (b)

Figure 5.26 An aberration-corrected (optimized 25 mrad[2] semi convergence angle) HRSTEM images from plate like $Al_{13}Fe_4$ precipitates (*type1*) and secondary $L1_2$-Al_3Zr precipitates. Bright dots inside the $Al_{13}Fe_4$ plates are Zr atom columns. In (a) top part of the plate is almost entirely covered while in (b) the bottom part of the plate is covered by $L1_2$-Al_3Zr entirely. No secondary precipitates at the plate/matrix ends.

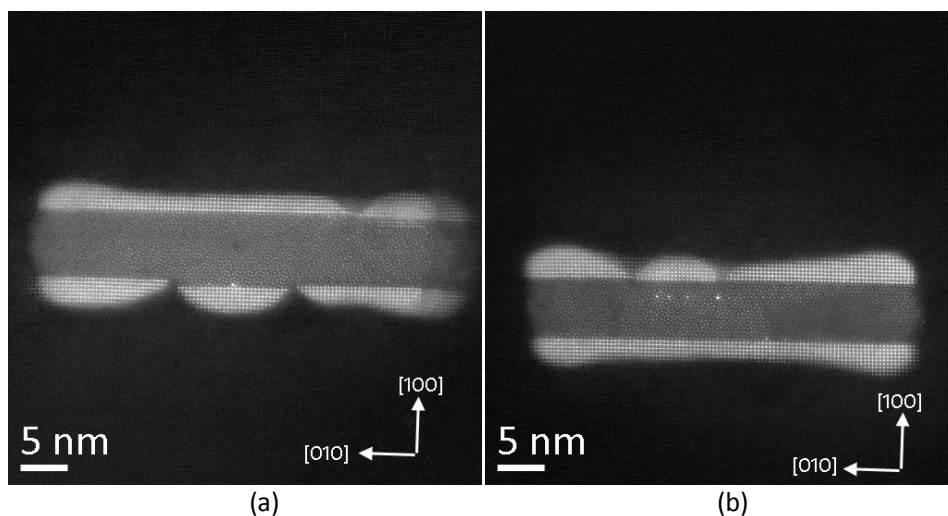[2]Correction limit of the hardware aberration corrector used in the present study.
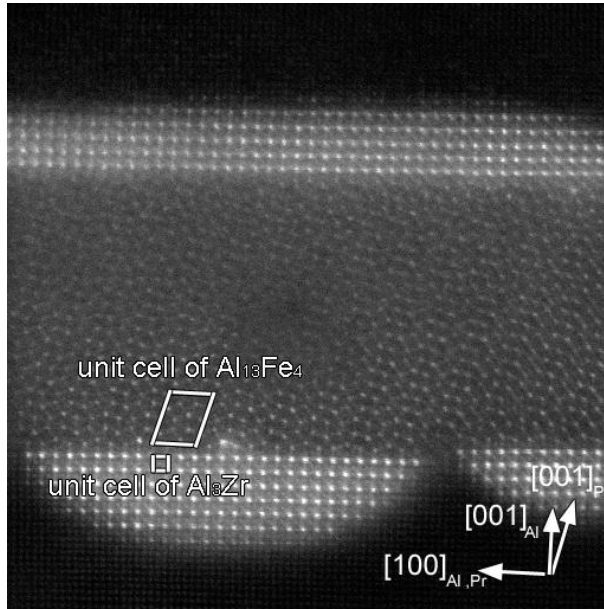
Figure 5.27 An aberration-corrected (optimized for 25 mrad semi convergence angle) HRSTEM image of plate like $Al_{13}Fe_4$ precipitates and secondary $L1_2$-Al_3Zr precipitates. Steps on $Al_{13}Fe_4$ plate causes formation of half spherical $L1_2$-Al_3Zr phases.

In order to understand the relationship between $L1_2$-Al_3Zr and $Al_{13}Fe_4$, the details of $Al_{13}Fe_4$ structure and its orientation with Al lattice must be explained.

In the $Al_{13}Fe_4$, structure which has a monoclinic lattice (parameters are given in section 5.2.3) the Al and Fe atoms lie in four well defined layers, (040) planes, perpendicular to the [010] axis. Two of these layers lie on the mirror-planes at y = 0 and y = ½, and are related by the C centering. These layers are flat. The layer in between them is puckered (see Fig.5.28(a)). These 4 layers, ((040) planes), are separated by 0.202 nm. This results in a good plane matching Al {200} planes. Therefore, $Al_{13}Fe_4$ naturally form on {200}Al planes. Fe atoms in the flat layers form pentagons. These pentagons make a 2-D tiling, known as Dürer tiling [21], as presented in Fig.5.28(b). The Al atoms (in the same plane with pentagon forming Fe atoms) are found in the center of the Fe pentagons and the Fe atoms in the puckered layers are positioned directly beneath the center of Fe pentagons. Z-Contrast HRSTEM image in Fig 5.29 shows Dürer tiling [23] of Fe pentagons, two connected on an edge forms a pair. Pairs are connected at corners then form a chain.

Analysis of HRTEM and HRSTEM suggests that the [001] direction of the $Al_{13}Fe_4$ is parallel to the <001>Al and hence $L1_2$-Al_3Zr. Thus $Al_{13}Fe_4$ plates grow along <100>Al. The lattice mismatch between <100> Al and [001]$Al_{13}Fe_4$ is -2.7% whereas the mismatch between $L1_2$-Al_3Zr and $Al_{13}Fe_4$ is -1.3%. Although the lattice parameter match between $L1_2$-Al_3Zr and $Al_{13}Fe_4$ is relatively good, there is no easy plane matching due to complicated structure of $Al_{13}Fe_4$. On the other hand, high magnification Z-contrast STEM images reveal sharp and strain free, almost epitaxial, interface. In these images (Fig. 5.30), three $L1_2$-Al_3Zr unit cells fit with one peridocity of $Al_{13}Fe_4$ along the [001] direction. Moreover the atoms are positioned regularly at the interface and the tip of Fe pentagons in $Al_{13}Fe_4$ are shared with Zr atoms of $L1_2$-Al_3Zr structure and thus perfect matching between two structures are achieved. Interestingly, see Fig.5.30, Fe pentagons with Zr, next to the interface, is elongated compared to the pure Fe pentagons inside the $Al_{13}Fe_4$ plates.

(a)

(b)
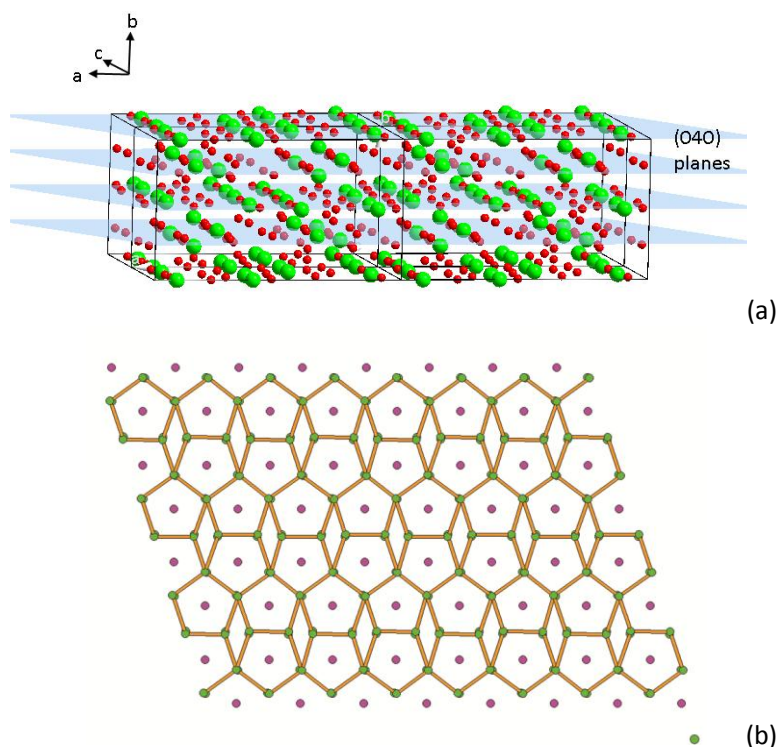
Figure 5.28 $Al_{13}Fe_4$ structure (2x1x2 time unit cell). (a) Organization of Al and Fe atoms in (040) planes. Al atoms are red while Fe atoms are green. Planes are indicated in light blue colour. (b) organization of Fe atoms in plane y=0 and and y=1/4. Fe atoms form pentagons (Green) and these pentagons are shown forming Dürer tiling, seen in orange. Fe atoms (magenta) in the puckered layers are seen in the center of pentagons**.**
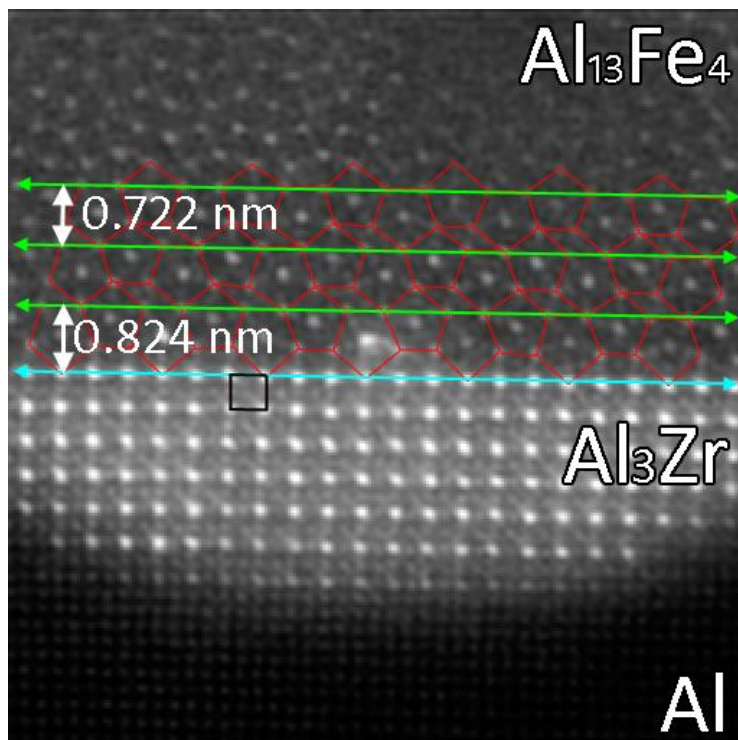
Figure 5.29 Low-pass filtered, an aberration-corrected Z-contrast HRSTEM image of a section the interface. Unit cell projection of $L1_2$-Al_3Zr is indicated by a black square. The line in cyan colour indicates the interface. Fe pentagons are completed at the interface. The width of Fe pentagons directed towards the interface is shown as green lines. Pentagons with Zr is elongated towards to the interface.

In Z-contrast HRSTEM images of $Al_{13}Fe_4$ precipitates along the monoclinic axis, the positions of Fe columns are clearly discerned (Fig 5.29). In these images the network of Fe pentagons with Fe columns in the can be seen. Inside $Al_{13}Fe_4$ precipitates covered with $L1_2$-Al_3Zr layers, one can often observe atom columns that are brighter than the similar columns. These brighter columns are always at center of pentagons. The brightness of these columns indicates a high concentration of Zr atoms as in $L1_2$-Al_3Zr secondary precipitates. Since the alloy contains only Zr, Fe and Ni, we conclude that the bright columns must represent a high content of Zr atoms in these columns.

In the HRSTEM images, which are 2-D projections of the crystal structure, we see that the brighter contrast is always observed in center of the pentagons. As explained above, the center of pentagons represents the Fe atom position in the puckered layer

and the Al atom position in plane with Fe pentagons. Therefore there are two possible atom positions for Zr atom to replace.

These images obtained at samples annealed after 698 K can also provide insight into where Zr atoms can be located in the $Al_{13}Fe_4$ structure. This can be helpful to explain the stability of $Al_{13}(Fe,Zr)_4$ precipitates observed in 573 K annealed samples.

Incorporation of Zr in $Al_{13}Fe_4$ structure raises the question in which location Zr can be hosted in this structure. Atom positions are given in Table 5.5. In $Al_{13}Fe_4$ structure Al to Fe interatomic distances vary between 0.23 nm and 0.29 nm and every Al atom has the shortest distance to one of the Fe atoms which vary between 0.23-0.25 nm. Replacement of Al and Fe by Zr atoms in $Al_{13}Fe_4$ should result in physically meaningful interatomic distances.

Therefore it was checked which ones are the two shortest Fe-Zr distances (in Table 5.6) in various Fe rich FeZr intermetallics ($Fe_{12}Zr$, $Fe_{17}Zr_2$ $Fe_{23}Zr_6$, Fe_7Zr_2, Fe_3Zr and Fe_2Zr) found in computational Alloy database of M. Widom, Cornell University [24][3].

Based on the Fe-Zr interatomic distances replacements of Al positions by Zr atoms would result in too short Zr-Fe interatomic distances in the $Al_{13}Fe_4$ structure. According to the Fe-Zr distances found in FeZr intermetallics, Zr cannot replace every Fe positions in the $Al_{13}Fe_4$ structure due to too short interatomic distances. The only available positions with short Fe-Fe distances are Fe05, Fe04 and Fe03.

$Al_{13}Fe_4$ precipitates with $L1_2$-Al_3Zr obtained annealing after 698 K. They have flat interfaces covered with Al_3Zr. HAADF HRSTEM images of the $Al_{13}Fe_4$/Al_3Zr shows brighter contrast in $Al_{13}Fe_4$. This must represent atom columns with Zr. In the images we see that Zr atoms sit on center of pentagons which contains Al02 and Fe05 atoms.

Al02 sits on mirror planes with multiplicity 4 and Fe05 belongs to the puckered layer on a general Wyckoff position with multiplicity of 8. Along the [010] direction columns, the Al02-Fe05 distance is 0. 23045 nm and Fe05-Fe05 distance is 0.34757 nm. The distance between Fe05 to other Fe atoms vary between 0.42-0.47 nm. Therefore if Zr takes Al02 position the resulting Fe-Zr interatomic distance will be too short. On the other hand If Zr takes Fe05 position Fe-Zr interatomic distances will be larger (see table 5.6) compared to Fe-Zr intermetallics shown in Table 5.6 and Zr to Al distance will be shorter compared Al-Zr distance (0.285 nm) in Al_3Zr structure. Therefore we can conclude that best available atom position for Zr to replace is Fe05 (Table 5.5).

---

[3] http://alloy.phys.cmu.edu/

Table 5.5 Position of atoms in $Al_{13}Fe_4$ structure given in lattice coordinates [19].

Atoms	x	y	z
|01| Fe	0.086	0.000	0.383
|02| Fe	0.401	0	0.624
|03| Fe	0.090	0.000	0.989
|04| Fe	0.400	0.000	0.985
|05| Fe	0.318	0.285	0.277
|01| Al	0.064	0.000	0.173
|02| Al	0.322	0.000	0.277
|03| Al	0.235	0.000	0.539
|04| Al	0.081	0.000	0.582
|05| Al	0.231	0.000	0.972
|06| Al	0.480	0.000	0.927
|07| Al	0.500	0.000	0.500
|08| Al	0.310	0.000	0.769
|09| Al	0.086	0.000	0.781
|10| Al	0.188	0.216	0.111
|11| Al	0.373	0.211	0.107
|12| Al	0.176	0.216	0.314
|13| Al	0.495	0.283	0.329
|14| Al	0.366	0.223	0.479
|15| Al	0.000	0.244	0.000

Table 5.6 Interatomic distances between Fe and Zr in various FeZr intermetallics [24].

1st order Interatomic Distances (nm) of Zr replaced Fe05 position	
Al	Fe
0.262	0.440
0.253	0.431
0.256	0.435
0.247	0.347
0.244	0.428
0.245	0.431
0.230	0.478
0.258	0.472
0.261	0.474

Table 5.7. Interatomic distances of Zr to Fe and Al first neighbor distances in $Al_{13}Fe_4$ structure [24].

Interatomic distances (nm)	Fe-Zr 1st
$Fe_{12}Zr$	0.29-0.32
$Fe_{17}Zr_2$	0.28-0.31
$Fe_{23}Zr_6$	0.29
Fe_7Zr_2	0.28
Fe_3Zr (stable)	0.28-0.31
Fe_2Zr (stable)	0.29

5.4 Conclusion

5.4.1 D0$_{22}$ phase

The stable D0$_{23}$-Al$_3$Zr phase is expected to form during solidification with slow cooling rates. As it is shown in the present study under the cooling conditions in addition to D0$_{23}$, D0$_{22}$ particles also form. Once D0$_{22}$ particles are formed they also act as a heterogonous nucleation site for cubic L1$_2$-Al$_3$Zr phase, and consequently during cooling a mixture of particles of D0$_{22}$ and L1$_2$ mixture is formed.

Despite the binary Al-Zr phase diagram, the formation D0$_{22}$ phase containing Fe and Ni in the present study is in agreement with the reports of D0$_{22}$-Al$_3$Zr precipitation in rapidly solidified Al-Zr alloys containing transition metals.

5.4.2 L1$_2$ - Al$_3$Zr Matrix Precipitates

Small coherent L1$_2$-Al$_3$Zr precipitates in the Al matrix are formed through homogeneous nucleation. The precipitation of this form is expected since at low annealing temperatures the driving force for precipitation is high due to limited solid solubility.

The elongated L1$_2$-Al$_3$Zr precipitates such as in Fig. 5.9, with structural faults suggest that matrix dislocations are preferential nucleation site for L1$_2$-Al$_3$Zr precipitates.

Heterogeneously nucleated L1$_2$-Al$_3$Zr particles contain D0$_{23}$–Al$_3$Zr domains. Lattice dislocations are responsible for the formation of these domains. L1$_2$-Al$_3$Zr particles with structural faults represent the early stages of the transformation to the equilibrium D0$_{23}$-Al$_3$Zr precipitates.

5.4.3. Al$_{13}$(Fe,Zr)$_4$ precipitates

Incorporation of Zr in to Al$_{13}$Fe$_4$ precipitates provide better match between the precipitates and the Al matrix and possibly lower the interface energy. These factors easier the nucleation of Al$_{13}$Fe$_4$ precipitates.

References

1. E. Nes et al.,*Acta Metall*, **20**/4, 499, (1971)
2. N. Ryum, *Acta. Metall*, **17**, 269, (1969)
3. N. Ryum, *J. Inst. Metals*, **94**/5, 191, (1996)
4. E. Nes et al., *Scr. Metall.*, Vol 5, 987, (1971)
5. H.C. Fang, et al., *Corr. Sci.*, **21**, 62, (2009)
6. W. Dahl et al., *Z. Metallkd*, **68**/3, 188, (1977)
7. H. Westengen, *Z. Metallkd.*, **73**, 360, (1982)
8. H. Westengen et al., *Aluminium*, **57**/12, 797, (1981)
9. T.B. Massalski (editor), *Binary Alloy Phase Diagrams*, ,**Vol. 1** (1990)
10. J.Q. Guo et al., *Mater. Lett.,***27**, 343, (1996)
11. C. Amador et al., *Phys. Rev. Lett.*, **74**/24, 4955, (1996)
12. A.E. Carlsson et al., *J. Mater. Res.*, **5**/12, 2813, (1990)
13. K. Knipling et al., *Acta Mater.*, Vol 56, 114, (2008)
14. R.Cahn, P. Haasen (Editors), *Physical Metallurgy*, Vol 2
15. J.D. Robson, *Acta Mater.*, Vol 49, 599, (2001)
16. L. Litynska et al., *J. of Micr*, Vol 223, 182, (2006)
17. K. Knipling et al., *Acta Mater.*, Vol 56, 1182, (2008)
18. Y.C. Chen, et al, *Acta Metall. Mater.*, Vol 38, 771, (1990)
19. P.J. Black, *Acta Cryts.*, Vol 8, 43, (1955)
20. E. Clementi et al., *J. of Chem. Phys.*, **38** 2686, (1963)
21. E. Clementi et al., *J. of Chem. Phys.*, **47** 1300, (1967)
22. P.A. Stadelmann, *Ultramicroscopy*, **21** 13 (1987)
23. B. Grünbaum, C.G. Shephard, *Tilings and Patterns*, Freeman (1986)
24. M.Widom Computational Alloy data base Cornell University

Chapter 6

Aberration corrected high resolution TEM imaging at 80 kV

The latest advances in electron optics using spherical aberration correctors and improvements in the stability of the microscope platform enable to lower the acceleration voltage without suffering from substantial loss of lateral resolution in atomic resolution imaging. Lower accelerating voltages minimize knock on damage effects and allows atomic resolution imaging of beam sensitive materials. The benefits to study electron beam sensitive materials with unprecedented resolution and opens a door for these material classes to be examined in a transmission electron microscope down to the atomic level.

This chapter consists of two parts. In the first part of this chapter we discuss the effects the fifth order spherical aberration on contrast transfer function for simulated atomic resolution images at 80 kV. In the second part, using atomic resolution HRTEM imaging and exit-wave restoration, individual atoms in graphene sheets were examined quantitatively

6.1 High Resolution Transmission Electron Microscopy[1]

Round electromagnetic lenses (rest of the only objective lens is considered) inherently suffer from spherical and chromatic aberrations and have always positive values as shown by Scherzer [1]. These aberrations cannot be made zero by perfecting lens manufacturing. Until 2000 the main trend was to lower spherical aberration of the objective lenses to achieve better resolution in 200-300 kV transmission electron microscopes. By then high voltage approach was abandoned due to cost of such microscopes and irradiation damage imposed on the samples. Therefore atomic resolution transmission electron microscopes mainly have the 200-300 kV accelerating voltage with low-spherical aberration objective lenses of which spherical aberration coefficient varying between 0.5-1.5 mm. The reduction of the spherical aberration scales with the size of the objective lens and brings few disadvantages. Firstly, this causes magnetic saturation. Secondly, in low spherical aberration objective lenses the available space for the specimen is limited [2]. This has important consequences since it limits the maximum achievable tilt angle and the space inside the objective lens area for in-situ experiments.

Spherical aberration, C_S, is the major limitation for conventional transmission electron microscopy [1]. It limits the point resolution and also causes blurring in the image known as delocalisation. Next to the spherical aberration another characteristics lens aberration is the chromatic aberration, C_C, which determines the amount of information to be transferred by the objective lens.

During the last three decades, several information processing methods have been developed to improve point resolution and to reduce the image delocalization. These methods are all based on holographic reconstruction principles originally proposed by Gabor [3]; such as through-focus series reconstruction [4] or off-axis holography [5]. However, a major breakthrough was achieved by the introduction of hardware C_S-correctors in the TEM [6]. After this, it took few years to implement C_S-corrector in TEM production line and now C_S-correctors are available to wider research community. C_C correctors have only been recently implemented in TEM and still waiting to be explored for various material problems [7].

---

[1] This section was adopted from references 2,8,9

In this chapter we will briefly introduce the essential concepts of the theory of image formation in TEM. Aberration and envelope functions control the contrast transfer of the objective lens. The effect of the hardware spherical aberration correction on the contrast transfer at 80 kV accelerating voltage images will be explained with the help HRTEM multislice image simulations. As a test structure, Si <110> and a super cell consisting of mono and double layer graphene are used. The effect of the fifth order spherical aberration on the HRTEM images and in the exit wave reconstruction will be discussed.

6.1.1 Image Formation

The image formation in HRTEM is fairly well developed [8-9]. Direct/primary and scattered/diffracted electron waves emanating from a thin specimen (typically 1-5nm for 300 kV) are collected by an objective lens focused into a diffraction pattern at back focal plane. The diffracted beams are then interfere with primary beam and form an image at the image plane of the objective lens. The image is then magnified by the projector system of a TEM and then captured on a recording media, e.g., CCD devices. The recorded image is then altered projection of electron exit wave. The alteration is due to effect of objective lens aberrations as extra phase shifts during interference of primary and diffracted beams. Therefore the recorded image cannot be directly linked to electron exit wave and thus the structure of the observed material. The crucial question for HRTEM images is how these images are related to the specimen structure. For a moment if we assume perfect lens without aberrations electron exit wave relation to projected potential can only be restored for very thin crystals i.e. generally accepted below 5 nm but depends heavily on the scattering power of an atom.

Image formation in HRTEM is expressed in two steps, illustrated in Fig 6.1. The first step is the specimen electron beam interaction. This results in electron wavefunction at the exit surface the specimen. The second step is the propagation of the exit wave through imaging system and defined as information transfer by the objective lens.
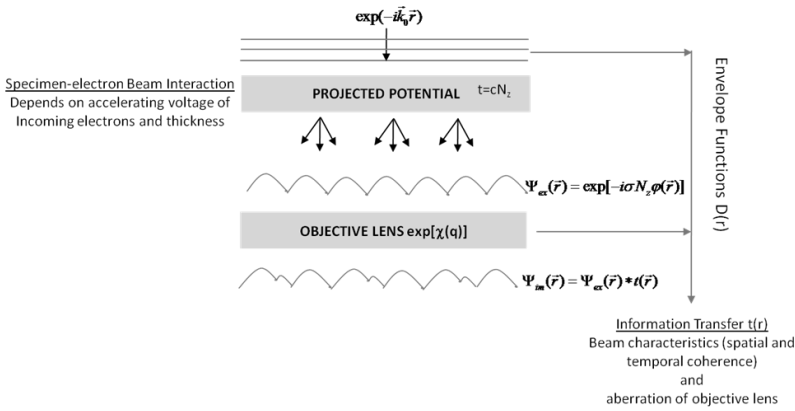
Figure 6.1 The phase object approximation. Phase object modulates an incoming plane wave and electron exit wave is further modulated by the objective lens.

Assume that when a plane electron wave enters into the specimen, the electron wave as it travels down the specimen amplitude remains unchanged while its wavelength is modified due to crystal potential which is periodic and changing with an atom position. This is known as <u>P</u>hase <u>O</u>bject <u>A</u>pproximation, POA. In that case, electron exit wave reflects potential distribution of the crystal structure.

$$\Psi_{ex}(\vec{r}) = \exp[-i\sigma N_z \varphi(\vec{r})] \tag{6.1}$$

N_z is the thickness traversed by electron wave and $\varphi(\vec{r})$ is the projected potential of the crystal/material, σ is the interaction coefficient which is measure of interaction strength of electrons with matter. The exit wave is the result of interference between the unscattered electron wave and scattered electron waves that travel in different directions (eventually they would form a Fraunhofer diffraction pattern at infinity). These diffraction waves are Fourier components of the exit wave as a function of *q*, scattering vector, and are collected then focused to a diffraction pattern by the objective lens at the back focal plane of the objective lens. Wave function of each scattered wave is expressed as Fourier transform of Eq. 6.1.

$$\Psi_{ex}(\vec{q}) = F[\Psi_{ex}(\vec{r})] = \exp[-i\sigma N_z \phi(\vec{q})] \tag{6.2}$$

ϕ(*q*) is the Fourier transform of the projected potential and related to the structure factors, F(*q*)

$$\phi(\vec{q}) = \frac{\lambda}{\sigma S} F(\vec{q})$$ 6.3

S is the area of unit cell projection and λ is the wavelength of incoming electron wave.

The objective lens imposes phase shifts to the electron wave due to imperfections in the objective lens. And various instabilities cause modifications in the electron wave. These factors are expressed as transfer function written in formula by $t(r)$. Intensity of electron wave in image plane

$$\Psi_{im}(\vec{r}) = \Psi_{ex}(\vec{r}) * t(\vec{r})$$ 6.4

Image intensity is square modulus of wave function at imaging plane

$$I_{im}(\vec{r}) = \left| \Psi_{im}(\vec{r}) \right|^2 = \Psi_{im}(\vec{r}) \Psi_{im}^{*}(\vec{r})$$ 6.5

If we assume an ideal and focused lens, the intensity distribution would be unity. This means no contrast would be in the image corresponding to the projected potential.

We can better describe image formation and transmission function in reciprocal space since information formed can be conveniently described by the number of Fourier components present in the back focal plane. Tranmission function in reciprocal space:

$$T(\vec{q}) = D(\vec{q}) e^{i\chi(\vec{q})}$$ 6.6

$D(q)$, expressed in Eq.6.6, is overall envelope function and contains several term: $A(q)$, $E_s(q)$ and $E_\Delta(q)$. $A(q)$, aperture function which functions as selecting spatial frequency at the back focal plane. It is usually defined as top-hat function, usually circular but special shape functions can be also considered. In modern TEMs, HRTEM imaging is usually performed without an objective aperture and thus $A(q)$ can be included when an objective aperture used. $E_s(q)$ partial spatial coherence due to beam convergence. It limits spatial resolution. $E_\Delta(q)$ represent the partial temporal coherence causes defocus spread and limits the highest spatial frequency transmitted by the objective lens.

$$D(\vec{q}) = A(\vec{q}) E_s(\vec{q}) E_\Delta(\vec{q})$$ 6.7

Therefore the electron exit wave at the back focal plane of the objective lens is expressed as

$$\Psi_{im}(\vec{q}) = D(\vec{q})e^{i\chi(\vec{q})}\Psi_{ex}(\vec{q})$$
6.8

Image intensity in reciprocal space is the Fourier transform of the real image intensity distribution.

$$I_{im}(\vec{q}) = F\left|I_{im}(\vec{q})\right| = \Psi_{im}(\vec{q}) * \Psi_{im}^*(-\vec{q})$$
6.9

Using the convolution theorem, the Fourier transform can be expressed as discrete sum and if we replace $-Q$ by q', the image intensity distribution in real space can be expressed as sum of image intensity of discrete spatial frequencies in reciprocal space.

$$\Psi_{im}(\vec{q}) * \Psi_{im}^*(-\vec{q}) = \sum_{q'} \Psi_{im}(\vec{q}-\vec{Q}) \cdot \Psi_{im}^*(-\vec{Q})$$
6.10

$$I_{im}(\vec{q}) = \sum_{q'} \Psi_{im}(\vec{q}+\vec{q}') \cdot \Psi_{im}^*(\vec{q}')$$
6.11

For the image intensity, the relevance of equation 6.11 is, it can be expressed as discrete sum over all wave vectors q'. This expression contains the interference between unscattered and scattered waves as well as the interference between scattered waves,

$$\sum_{q'} \Psi_{im}(\vec{q}+\vec{q}')\Psi_{im}^*(\vec{q}') =$$
$$\Psi_{im}(\vec{q})\Psi_{im}^*(0) + \Psi_{im}(0)\Psi_{im}^*(-\vec{q}) + \sum_{q'\neq 0,-q} \Psi_{im}(\vec{q}+\vec{q}')\Psi_{im}^*(\vec{q}')$$
6.12

It is seen in 6.12 that if the electron wave has a strong primary beam, Ψ_{im} *(0)*, and a weakly scattered, $\Psi_{im}(q)$, beams the image intensity can be expressed;

$$I_{im,Linear}(\vec{q}) = \Psi_{im}(\vec{q})\Psi_{im}^*(0) + \Psi_{im}(0)\Psi_{im}^*(-\vec{q})$$
6.13

Image intensity of a phase object thus can be expressed by replacing Eq.6.8 (and its complex conjugate) in Eq. 6.13;

$$I_{im,Linear}(\vec{q}) = D(\vec{q}) \left[\Psi_{ex}(\vec{q}) e^{i\chi(\vec{q})} + \Psi_{ex}^{*}(-\vec{q}) e^{i\chi(\vec{q})} \right]$$ 6.14

In Eq.6.14, the exponential (phase shift contribution) within the bracket can be exchanged with $\cos\chi(\mathbf{q})$ + i$\sin\chi(\mathbf{q})$. In order to simplify the problem, the exit wave (expressed in reciprocal space), given Eq. 6.2., can be expanded as Taylor series. The terms in the expanded wavefunction represent the contribution of uncscattered, single, double and triple scattered waves. If we only consider the first three terms the image intensity becomes:

$$I_{im}(\vec{q}) = \delta(\vec{q}) + 2D(\vec{q}) \sin[\chi(\vec{q})] \sigma N_z \phi(\vec{q})$$
$$+ \left\{ D(\vec{q}) e^{i\chi(\vec{q})} \sigma N_z \phi(\vec{q}) \right\} * \left\{ D(\vec{q}) e^{i\chi(\vec{q})} \sigma N_z \phi(\vec{q}) \right\}$$ 6.15(a)

$$I_{im}(\vec{q}) = \delta(\vec{q})$$
$$+ D(\vec{q}) \left[2\sigma N_z \phi(\vec{q}) \sin[\chi(\vec{q})] - (\sigma N_z)^2 \phi(\vec{q}) \phi(\vec{q}) \cos[\chi(\vec{q})] \right]$$ 6.15(b)

The first term in the above equation is a delta function and represents the unscattered electron wave. The first term, within the brackets represent the contribution of single scattered event to the image intensity which is modulated by $\sin\chi(\mathbf{q})$ function. The second term is the contribution of double scattering event and contrary to single scattering event and it is transferred with $\cos\chi(\mathbf{q})$. Therefore in the case of multiple scattering events, the projected potential is no longer linearly related to image intensity. For thin specimens but without weak phase object character (such CdSe, PbSe, Au nano particles etc), contrast transfer will be different for single and double scattered electron waves.

As shown in Eq. 6.13, in the presence of strong primary beam and weak scattered beams, the image intensity is linearly related to the wave function. This approximation known as linear image formation and it is valid for very thin crystals/objects. For example, a few nm thin Al crystal imaged at 300 kV under [100] zone axis, it will probably contain 25 beams at the back focal plane (experimental observation). Interference between the direct beam and 24 diffracted beams would yield 48 terms will be in the equation 6.12 (total 2(n-1) terms). And HRTEM images can be considered to form linearly. For a thicker part of Al crystal, few tens of nm, HRTEM image will be formed after interference of all diffracted beams with each other as well as with the direct beam and total number of interference would be 625

(multiplication within summation will cause n^2 terms to be summed). On the other hand this simple assumption can be relaxed since the intensity of low index (low spatial frequencies) reflections are far more stronger than high index reflections (high spatial frequencies) therefore number of non-linear terms may reduce to a lower number.

Both dynamic scattering and non-linear contributions to the image intensity make the relation between image and projected potential very complex and such images cannot tell us about the structure of the crystal except few direct conclusions about uniformity of crystals and presence of defects which is the result of breaking of translational of the lattice.

However these difficulties can be relaxed for very thin crystals or by using higher accelerating voltages[2]. As it is mentioned in previous paragraphs for very thin crystals the projected potential is related to image intensity. This condition is known as Weak Phase Object Approximation, WPOA, and it is assumed that only kinematical scattering occurs and multiple scattering is ignored. Under WPAO, the second term within the bracket in Eq.6.15(b) is ignored and thus exit electron wave function becomes linearly related to the projected potential of the crystal for very thin crystals.

$$\Psi_{ex}(\vec{q}) = [\delta(\vec{q}) - i\sigma N_z \phi(\vec{q})]$$

6.16

derived linear image intensity spectrum and intensity distribution in real space are

$$I_{im}(\vec{q}) = \delta(\vec{q}) + 2D(\vec{q})\sigma N_z \phi(\vec{q})\sin[\chi(\vec{q})]$$

6.17

$$I_{im}(\vec{r}) = 1 - 2\sigma N_z \varphi(\vec{r}) * t(\vec{r})$$

6.18

Eq. 6.18 simply means that for a phase object (thin samples) there will be no contrast observed when the objective lens is in focus (or ideal) because of the scattered and unscattered waves are differ in phase by $\pi/2$. If the phase of scattered waves can be shifted additional $\pi/2$ projected potential of the crystal structure will be revealed. For imaging of biological samples with a light microscope, Zernike proposed to use a phase plate to increase the contrast. For a classical TEM such a phase shift can be introduced by defocusing the objective lens. In addition to phase changes, amplitude

---

[2] High Voltage (1-3 MV) Transmission Electron Microscopy approach is almost abandoned nowadays.

of the scattered waves is altered by the temporal and spatial coherence envelopes (classically defined in reciprocal space). All these effects are expressed as complex transfer function of the microscope.

For a thin crystal that behaves like weak phase object, the amplitude of the unscattered wave is much stronger than the scattered waves. If the multiple scattering is ignored the real part of $e^{-i\chi(q)}$, which is $\cos\chi(q)$, do not contribute to the image. Therefore image intensity in Eq.6.17 is modulated only by imaginary part of $e^{-i\chi(q)}$. This, $\sin\chi(q)$, is known as <u>P</u>hase <u>C</u>ontrast <u>T</u>ransfer <u>F</u>unction, PCTF. Optimum image transfer with strong contrast variation occurs when $\sin\chi(q)=\pm1$ where the $\chi(q)$ is an odd multiple of $\pi/2$.

6.1.2 Aberration function

The most important property of an objective lens is the spherical aberration, C_S. It is an intrinsic property of the lens [1]. For a perfect lens, electrons emanating from a point in the object plane are brought back to a point in the image plane of the lens. A spherical aberration causes a variation of the focusing power of across the lens. Electrons are far from optical axis are deflected much more strongly compared the electrons near optical axis. Thus a point source is imaged as a disc with diameter, d, known as disc of confusion. Change of focus, Δf, of an objective lens causes the blur in the image similar like the effect of C_S. We will follow the notation of Typke and Dierksen [10] where coherent circular aberrations of the objective lens referred as C_1, C_3, C_5 and so on. C_1 is the defocus. C_3 is the third order spherical aberration[3]. It is the dominant aberration for conventional TEMs. Typical values of C_s are 0.5-1.5 mm. C_5 is the fifth order spherical aberration which is important for the aberration corrected instruments and its value is of the order of few millimetres.

The phase shift that the objective lens imposes on the electron exit wave is defined as $\chi(q)$. Aberration function of the objective lens, thus is expressed as

$$\chi\left(\vec{q}\right) = 2\pi \left[\frac{1}{2}C_1\lambda\vec{q}^{\,2} + \frac{1}{4}C_3\lambda^3\vec{q}^{\,4} \right] \qquad 6.19$$

---

[3] For conventional TEMs C_3 is often denoted as C_S.

This equation has two outcomes. Firstly, phase changes are a function of spatial frequency for constant objective lens parameters. This means information at back focal plane will be transferred by different shifts to the image plane. Secondly for a constant spatial frequency, different phase shifts are introduced by changing the objective lens parameters. Therefore the objective lens parameters can be tuned to achieve the highest spatial frequency transferred into the image intensity spectrum with same sign of the phase shift.

As seen in Eq.6.19, phase shifts are dependent on C_3 and C_1 differently. Therefore it is not possible to maintain constant phase shift for all spatial frequencies since $sin\chi(\boldsymbol{q})$ function will oscillate. In conventional TEMs, where C_3 is fixed, a good compromise is achieved by balancing positive phase shift caused due to C_3 by underfocussing, $-\Delta f$, the objective lens. This condition is known as Scherzer defocus [11], Δf_{Sch}, for which $sin\chi(\boldsymbol{q})$ is close to -1.

$$\Delta f_{Sch} \approx -\sqrt{\frac{4}{3}|C_s|\lambda}$$

6.20

Δf_{Sch}, is the defocus value at which maximum range of spatial frequencies is transferred with almost constant phase shift. The smallest spatial frequency transferred where the PCTF becomes zero for Δf_{Sch} is called the point resolution and expressed as

$$d_{Sch} \approx \sqrt[4]{\frac{16}{3}|C_s|\lambda^3}$$

6.21

In order to explain general behaviour of PCTF, so far we ignored the contribution of envelope functions in the Eq. 6.6 and assumed both spatially and temporally coherent illumination source. These functions defines the effect of coherence lose in the electron wave and causes dampening of the PCTF, limiting the resolution of a TEM [2,8,9].

The chromatic aberration causes loss of image contrast at decreasing detail size, up to a point where the transferred signal lose signal and eventually lower to the noise level [2,8,9]. The effect of C_C is that electrons with different energies are focused differently. This causes spread in focal strength, Δ, which depends on the energy spread of the electron source ΔE and the instabilities of the accelerating voltage $\Delta V/V$

$\approx 0.5 \cdot 10^{-6}$ (RMS). Instabilities of the objective lens current $\Delta I/I \approx 1.0 \cdot 10^{-6}$ (RMS) also contribute to the focal spread

$$\Delta = C_c \sqrt{\left(\frac{\Delta E}{eV}\right)^2 + \left(\frac{\Delta V}{V}\right)^2 + \left(\frac{2\Delta I}{I}\right)^2}$$ 6.22

$_\Delta(\mathbf{q})$, is expressed as a function of $\mathbf{q}$ and its strength is mainly controlled by the defocus spread, Δ;

$$E_\Delta(\vec{q}) = e^{\left(\frac{\pi\Delta\lambda}{2}\right)^2 \vec{q}^{4}}$$ 6.23

The incoming electron wavefunction is not a single plane-wave of one wave vector but superposition of wavefunctions travelling in slightly different directions. The dampening caused by this effect is described as partial spatial coherence $E_s(\mathbf{q})$ envelope. Expression for $E_s(\mathbf{q})$ is

$$E_s(\vec{q}) = e^{-\left(\frac{q_0}{2}\right)^2 \left[\frac{\partial}{\partial q}\chi(\vec{q})\right]^2}$$ 6.24

It is seen in Eq 6.24, the dampening effect of partial spatial coherence is controlled by the gradient of PCTF and increases with increasing beam semi-convergence angle $\alpha = \lambda q_0$. Effect of the $\chi(\boldsymbol{q})$ function on the dampening has important consequences and both large C_S and Δf values causes strong dampening of the PCTF (see the effect of C_S in the Fig. 6.2).
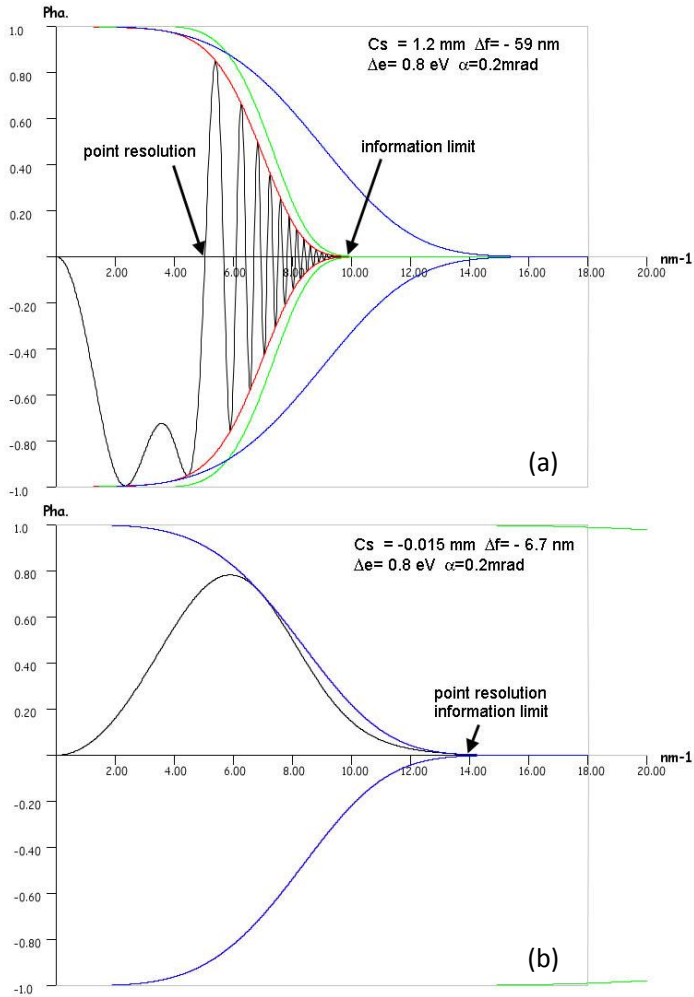
Figure 6.2 Calculated Phase Contrast Transfer Functions (black curve) at Scherzer focus for (a) a conventional TEM with objective lens of 1.2 mm C_S. (b) C_S-corrected TEM, C_3 value set to -0.015mm. Vertical axis indicates the phase shift while horizontal axis is the reciprocal distance. Point resolution and information transfer is indicated. Envelope functions are given in colour. Spatial coherence envelope is in green, temporal coherence envelope is in blue. Product of two envelopes is in red. C_S-correction improves the point resolution and decreases dampening effect of the spatial coherence envelope greatly.

An example of PCTFs of a TEM with large and small negative C_S at 300 kV is presented in Fig. 6.2. The first crossing of the PCTF of the horizontal axis defined the highest spatial frequency to be transferred with constant phase shift and defines the point

resolution of a TEM. The large gap where constant phase shift is maintained in Fig.6.2(a) is usually referred as pass-band. At Scherzer imaging condition the projected potential (in Eq. 6.16), will experience negative phase shift within the pass-band. Thus atom columns will show dark contrast regions in the bright background. Beyond the point resolution the PCTF will oscillate rapidly, as seen in Fig. 6.2(a), and accordingly sign of phase shift. Therefore the images cannot be interpreted directly.

Correction of the spherical aberration improves the point resolution according to Eq. 6.21 and reduces the effect of dampening due to partial spatial coherence. These improvements can be seen in the PCTF displayed in Fig. 6.2(b). Spherical aberration correction improves the PCTF up to the limit of the temporal coherence envelope and thus greatly improves the performance of HRTEM. A notable difference between non-corrected and C_S-corrected PCTFs is that low spatial frequency components of the projected potential are transferred with smaller phase shifts than non-corrected PCTF.

Classically, HRTEM images reveal atom columns as a dark contrast in bright background as explained above [2,8,9]. With the hardware C_S-correctors it is possible to tune the C_S so that optimum bright atom contrast in up to the information limit can be achieved. This method known as negative spherical aberration imaging technique has several advantages; visibility of weak scattering atoms and improvement in the contrast due to superposition of linear and non-linear terms with the same sign [12].

Hardware based aberration correctors for TEM are mainly based on hexapole design [6]. This corrector type eliminates the spherical aberration of third order, C_3, (and also reduce the parasitic aberrations caused by multipole elements) and hence improves the information transfer of the microscope and reduce the delocalization of image features. Hardware spherical aberration correction improves the aberration measurement accuracy since larger beam tilts can be applied. This enables to access residual intrinsic wave aberrations which cannot be accessed in classical HRTEM. Such an aberration with high importance is the spherical aberration of the fifth order, C_5. The aberration function including only rotational aberrations up to fifth order

$$\chi\left(\vec{q}\right) = 2\pi\left[\frac{1}{2}C_1\lambda\vec{q}^2 + \frac{1}{4}C_3\lambda^3\vec{q}^4 + \frac{1}{6}C_5\lambda^5\vec{q}^6\right] \qquad 6.25$$

As was shown by Scherzer phase shifts of the spherical aberration of the uncorrected objective lens (this is expressed as C_3) can be compensated by changing the objective lens focus to achieve almost constant phase shift with broad pass-band. Scherzer in

his original paper [13] also showed the optimum conditions for the PCTF for the case of fixed C_5 and derive the optimum values C_1 and C_3

$$C_{1,Scherzer} = 2\sqrt[3]{\lambda^2 C_5}$$
$$\text{6.26}$$

$$C_{3,Scherzer} = -3.2\sqrt[3]{\lambda C_5^2}$$
$$\text{6.27}$$

Chang et al carried out a similar analysis [14] and solved the Eq.6.25 analytically for a fixed positive value of C_5

$$C_{1,Chang} = 1.56\sqrt[3]{\lambda^2 C_5}$$
$$\text{6.28}$$

$$C_{3,Chang} = -2.88\sqrt[3]{\lambda C_5^2}$$
$$\text{6.29}$$

Lentzen found optimum conditions using the least-squares optimization of the aberration function in Eq.6.25, taking two-dimensional information transfer of the microscope [15]. This method also allows including non-rotational aberration such as parasitic aberrations from the multipole elements of the corrector. Lentzen derived the optimum conditions of C_1 and C_3 for the fixed C_5 value.

$$C_{1,Lentzen} = \frac{2}{\lambda q_{max}^2} + \frac{2}{15} C_5 \lambda^4 q_{max}^4$$
$$\text{6.30}$$

$$C_{3,Lentzen} = -\frac{10}{3\lambda^2 q_{max}^4} - \frac{8}{9} C_5 \lambda^2 q_{max}^2$$
$$\text{6.31}$$

In these equations q_{max} represent the maximum information transfer of the microscope.

The effect of C_5 on PCTF curves was compared and discussed for 200 kV and 300 kV in [16]. But its effect on the PCTF was not discussed for 80 kV (or lower accelerating voltages). Below we will investigate the impact of the C_5 on the PCTF and draw a general strategy for atomic resolution imaging at 80 kV.

6.1.3 C_S-corrected HRTEM Imaging at 80 kV: Discussion

Atomic resolution imaging of beam sensitive materials at high accelerating voltages (200-300 kV) cannot be achieved due to rapid degradation of the material structure by a mechanism known as knock-on damage [17]. Carbon based materials, light atomic number elements containing ceramics and alloys especially suffer from the knock-on damage [18]. The lower accelerating voltages reduce or even may prevent knock-on damage but at the same time resolution get worse due to increase in the electron wavelength. However achievement in hardware aberration correctors and electron sources with low energy spread (cold FEG, monochromators) made it possible to achieve 0.1 nm resolution at 80 kV [19].

For the spherical aberration correctors with conventional Schottky FEG electron source, the information transfer is limited by C_c and partial temporal coherence envelope dampens the phase transfer quickly. Typical PCTF curve, shown in blue colour, is displayed in Fig. 6.3. Therefore in a conventional TEM equipped with a C_S-corrector, approximately 0.2 nm information limit is expected at 80 kV which is also the point resolution of the instrument. Experimental HRTEM images obtained at 80 kV often show information transfer far better than 0.2 nm but this is attributed to effect of multiple scattering. One way to improve PCTF is to reduce the dampening effect of partial temporal coherence in Eq. 6.23. The defocus spread in Eq 6.22. controls the partial temporal coherence envelope function. The main parameter responsible for the temporal coherence is the C_c which is an inherent aberration of the objective lens. C_c can be eliminated therefore the partial temporal coherence envelope function approaches to unity. C_c correctors for TEM are recently available [7] but not widespread due to high investment amount required. As was shown by Freitag et al. an electron source with small energy spread will reduce the amount of defocus spread [19]. This will cause decrease in the dampening effect of partial temporal coherence envelope and improve the information limit. The PCTF curve of small energy spread system, shown in green colour, is presented in Fig.6.3.
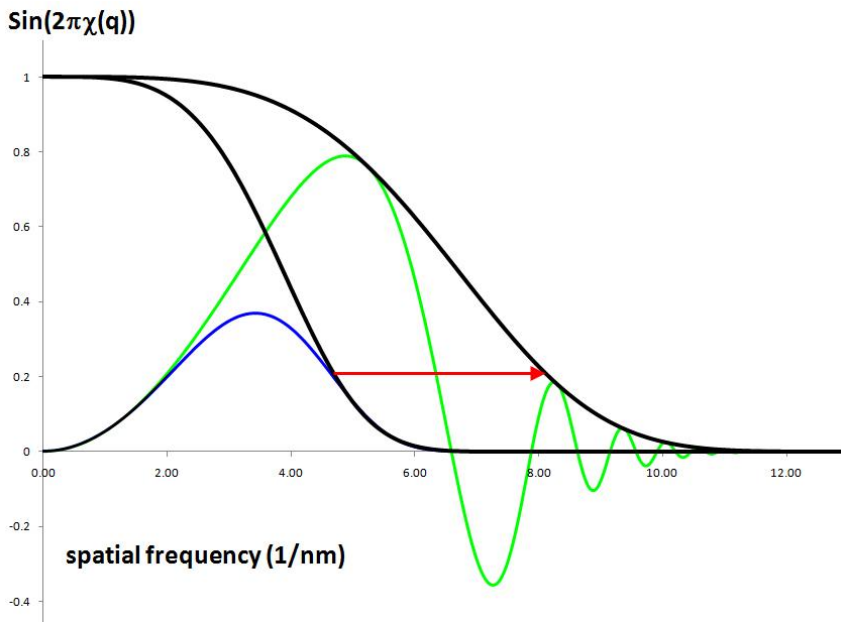
Figure 6.3 Calculated 80kV Phase Contrast Transfer Functions of the Cs-corrected TEM. Typical aberration values for daily use are assumed: C_3=-3 um. C_1 is 4 nm, C_5 is 13 mm. Energy spread high (blue curve) and low (green curve). Dampening effect of partial temporal coherence envelope (in black) envelope is reduced for low energy spread case.

In a C_3-corrected TEM, as a strategy, C_5 is fixed by adjusting the stage height of a TEM at the main accelerating voltage to be used (generally 300 kV). For lower accelerating voltages adjustment of C_5 would require a new stage height establishment, which is not practical. Recent methodology is to minimize the effect of off-axial coma which would also result in minimization in C_5. In this way effect of C_5 at 80 kV imaging was minimized (TEAM 0.5). This causes the reduced field of view and can be only managed very experienced person [16]. Therefore effect of C_5 at 80 kV, generally speaking at low accelerating voltages, is often not measured accurate enough and ignored or considered with less care using unrealistic values.

It is logical to consider C_5 value as fixed at 80 kV. The theoretical calculation estimates 13.43 mm of residual C_5 at 80 kV [20]. For the C_3-corrected microscopes with conventional FEG sources, 0.7-0.8 eV, the PCTF curve is limited by temporal coherence envelope regardless of C_5. Therefore the PCTF shows same sign phase shift and resolution is limited to around 0.2 nm. The situation changes when the low

energy spread electron sources, cold FEG or monochromator are used to increase the spatial resolution. As seen in Fig. 6.3 dampening effect of partial temporal coherence envelope function is lowered and thus higher spatial frequencies transmitted. However unwanted oscillations are noticed in the PCTF and as a result phase reversal occurs. This complicates the image interpretation. This situation represents the C_5 limiting imaging. As shown in previous section it is possible to compensate phase shifts due to fixed C_5 value with adjusting C_3 and C_1. Using Scherzer, Chang and Lentzen optimized values we calculated the coherent PCTF curves (in Fig. 6.4(a)). As a reference we also included the PTCF curve for the classical Scherzer condition. For this curve, fixed C_5 is assumed in Eq. 6.25 but phase shift of C_3 is balanced by C_1. This situation (C_5 ignored) often represents the daily experimental setup, ignoring the presence of C_5 and use of conventional Scherzer focus value to optimize the PCTF.

As seen in coherent PCTF in Fig. 6.4 (a), Scherzer and Lentzen conditions almost provide constant phase shift. Chang optimization has narrower constant phase range. When the effect of the envelope functions is included in PCTF (in Fig. 6.4(b)) all the optimized PCTFs shows strongly dampened curves but the phase shift is maintained in the same sign. The PCTF curves for Chang and Lentzen optimized C_1 and C_3 values are similar. But under Chang's conditions smaller spatial coherency range is achieved than Lenzten and Scherzer conditions as seen in the PCTF curves.

Table 6.1 Summary of conditions for PCTF at 80 kV C_5 fixed at 13.43mm. Low energy source is assumed.

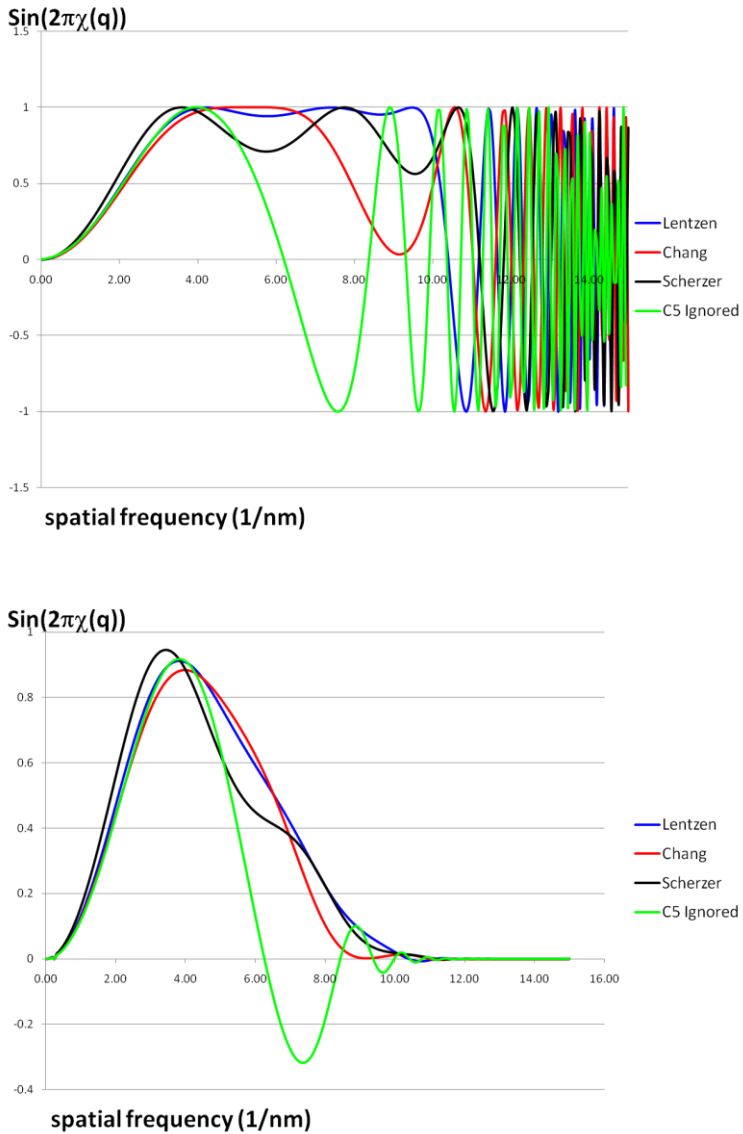|	**Scherzer**	**Chang**	**Lentzen**	**C_5 ignored**
C_1 (nm)	12.32	9.61	10.23	9.23
C_3 (nm)	-29000	-26000	-25000	-15000

Figure 6.4 PCTF curves are calculated at 80 kV for fixed C_5. Parameters are given in Table 6.1. Green curves represent Lentzen optimized, Red Curves represents Chang optimized, Black curves represent Scherzer optimized C_1 and C_3. (a) is the coherent PCTF (b) is the PCTF with partial temporal and spatial coherence envelopes. $\Delta e = 0.2$ eV, $Cc = 1.4$ mm, $\alpha = 0.3$ mrad

In order to test the balance of C_5 according to conditions defined above, HRTEM Si <110> images were simulated for optimized PCTF curves. As it is expected Si dumbbells whose spacing is 0.136 nm cannot be resolved conventional FEG sources (Fig. 6.5(a)). A C_5 ignored PCTF optimized the C_3 phase shift alone, have information limit down to 0.1 nm but oscillations of the CTF and due to this HRTEM simulated image at Scherzer defocus does not show the dumbbell structure of the silicon. HRTEM images simulated according to C_5 optimized PCTF curves resolves dumbbell structure of silicon but individual atom peaks in each dumbbell become less distinct for the Scherzer optimized condition. This is can be explained due to decrease in phase shift forming a small plateau in Scherzer optimized PCTF (see black curve in Fig. 6.4(b)), between approximately 6 -8 1/nm. Thus Scherzer condition will make poorly resolved images with image features roughly between 0.16-0.12 nm (dumbbell distance in <110> oriented semiconductors like Si, GaAs etc and C-C distance in Graphene will fall between this plateau).

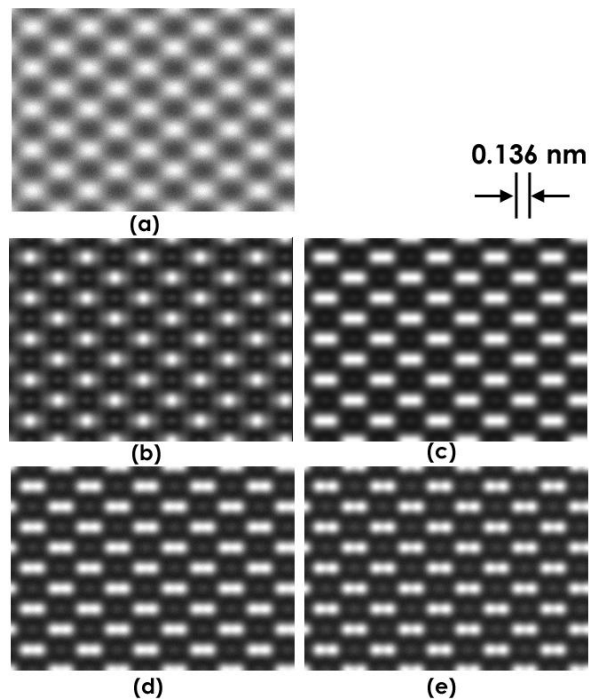**Figure 6.5** Multi-Slice simulated HRTEM images of Si <110> at 80 kV. Specimen thickness was chosen as 3 nm. (a) Energy spread 0.8eV (b) C_5 ignored, PCTF at classical Scherzer defocus. Optimized C_1 and C_3 for (c) Scherzer (d) Lentzen (e) Chang.

In commercial spherical aberration correctors the C_3 value can be set to the optimized values shown in Table 6.1 and thus a smooth PCTF curve with positive phase shift can be achieved. In practice, the finite aberration measurement precision makes it difficult to differentiate small the differences between the optimized C_3 values for Chang and Lentzen conditions. At 80 kV the best PCTF therefore can be achieved setting the C_3 value close the -25/26 µm. Atomic resolution HRTEM images can be achieved by taking focal series around the optimized C_1 value. An alternative method is to combine HRTEM imaging and exit wave reconstruction so that any effect of oscillatory behaviour of PCTF can be removed. This is tested for hypothetical graphene structure displayed in Fig. 6.6. In next section experimental verification is also shown for quantitative analysis of single/double graphene sheets.
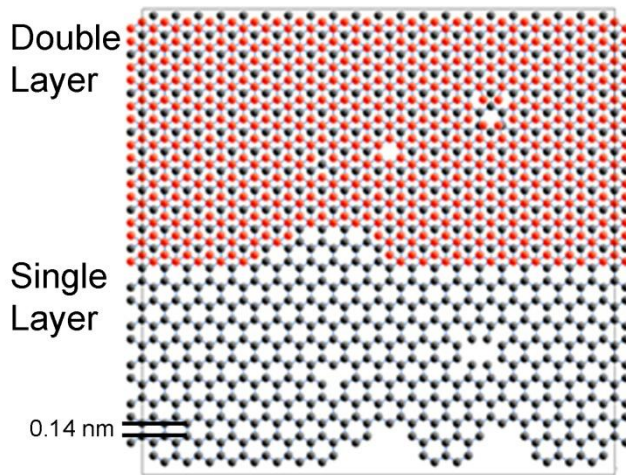
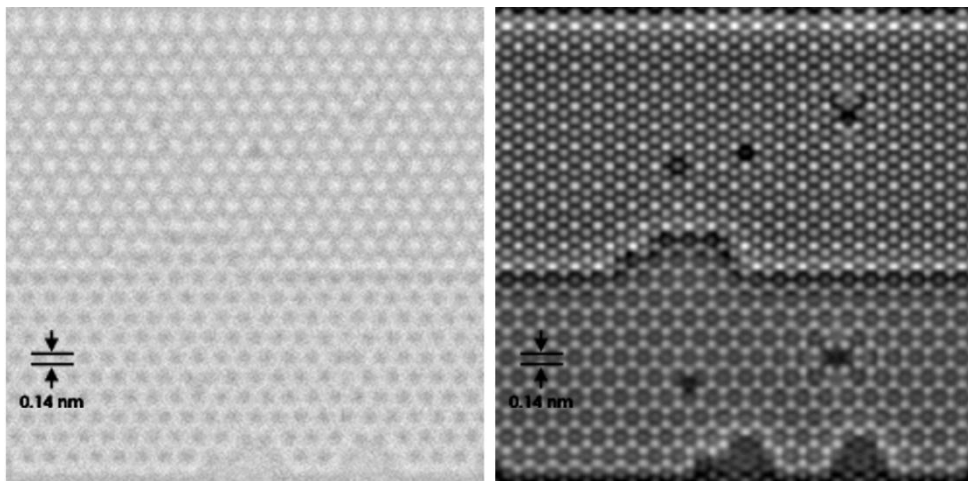**Figure 6.6** Modelled graphene cell. Black dots represent bottom sheet. The red dots represent upper sheet.

Figure 6.7 (a) Multi-slice simulated Graphene HRTEM image at 80 kV for C_5 ignored PTCF. C_3 = 0.015mm and C_1= 9.5 nm. Information limit as seen in Fig.6.4(b) is approximately 0.10 nm. In order to represent realistic situation 2% shot noise is included in the simulated images (b) The phase of the reconstructed exit wave, after reconstruction of 20 simulated images. Reconstruction limit was chosen as 0.115 nm. Simulated/reconstructed images and the model structure in Fig. 6.6 have the same scale and can be directly compared.

6.2 Imaging of carbon based nanostructures

New manmade nanomaterials, especially carbon-based (C, atomic number Z= 6) nanostructures, are considered to be essential new building blocks for bottom-up nanotechnology as they exhibit unusual electronic and structural properties. For example, graphene - a one-atom thick single sheet of graphite has already arouse great research interest [21] especially as it was found to exist with extraordinary electronic structure [22-24]. This extraordinary behaviour of electrons is directly related to the crystal structure and the arrangement of every individual carbon atom in this single sheet in 2-D, as well as, in case of few-layer graphene (FLG) in 3-D.

Comparison between theoretical models as well as their predictions and the atomic positions - revealed by atomic-resolution experiment at the same length scale - is therefore a fundamental request before applications [24] in nanoscale science and technology can be defined.

Atomic resolution and, equally important, the sensitivity to detect individual atoms advanced dramatically in Scanning / Transmission Electron Microscopy (S/TEM) by means of improving the sophisticated electron optics, such as aberration correctors [25]. Especially in the case of carbon-based nanomaterials, the TEM imaging "quality" progressed in the last decade from "seeing" carbon-based particles [26] to "seeing" columns of light atoms [28] as well as "seeing" single individual heavy atoms [29] inside carbon-based cage structures. Finally, the atomic structure of the carbon framework of graphene itself has been directly made visible by 80 kV HRTEM lattice images using NCEM's TEAM instrument [30,31]. On such a basis, most images shown for the structure of graphene are directly taken and procedures using long-time observations such as exit wave function (EW) reconstruction in TEM mode have mostly been avoided. But using complex EW for structure interpretations has important advantages in terms of definite contrast interpretations, especially if the signal is used to reveal the atomic 3-D structure [33]. This makes the use of such an approach very attractive to characterize carbon-based nanostructures.

Here, we present a comparison between experimental data and simulations, and thereby demonstrate "seeing" single carbon atoms in 3-D on single/double layer graphene. The method to accomplish these results is C_S-corrected high-resolution transmission electron microscopy (HRTEM) at 80 kV acceleration voltage. By focus series reconstruction we obtain the complex exit wave images and understand the 3-D atomic structure quantitatively [3].

6.3 Experimental section

6.3.1 Transmission Electron Microscopy (TEM) at lower accelerating voltage (HT)

For our TEM investigation, graphene sheets have been carefully prepared (details in [31]). TEM experiments have been performed using a FEI TitanG2 60-300 microscope operated at 80 kV and equipped with a high brightness field emission source, a monochromator, as well as a CEOS aberration corrector to correct the spherical aberration C_S of the objective lens. The CEOS aberration corrector has been tuned to a spherical aberration C_S value of about -15μm.

Drawbacks of imaging nanostructures using accelerated electrons are ionization damage by exciting electronic states and knock-on damage caused by collisions of beam electrons with specimen atoms. In graphene, the ionization damage is considered to be less important due to its high conductivity. And, the knock-on damage can be minimized by operating state-of-the-art electron microscopes at acceleration voltages below the material's knock-on damage threshold - such as in our case at 80 kV. The knock-on damage threshold for carbon atoms in perfect graphene structure is estimated to be 113 kV [36].

As another advantage of using 80 kV accelerating voltage is that the electron scattering becomes stronger at lower acceleration voltages [19]. Scattering amplitude of a carbon atom at an accelerating voltage of 80 kV has been derived from Fourier transform of an exit electron wave using multislice algorithm in ELSTRU software package[4], and has been compared to carbon's scattering amplitude at 300 kV. It is obvious in Figure 6.8(a), a drop in voltage to 80 kV from 300 kV improves the 'signal' of carbon atoms, allows for better S/N ratios, and therefore better sensitivity to detect small phase shifts carrying the 3-D structural information described in the paper. At these low voltages usage of a spherical aberration (C_S) corrector is essential to reduce imaging artefacts caused by spherical aberration and imperfections of the objective lens, and, in this way, is essential to increase the achievable interpretable resolution and sensitivity to the point that atomic-scale structures and one-atom columns can be resolved.

---

[4] ELSTRU software package, National Centre for HREM, Delft University of Technology, The Netherlands, http://nchrem.tnw.tudelft.nl/elstru/
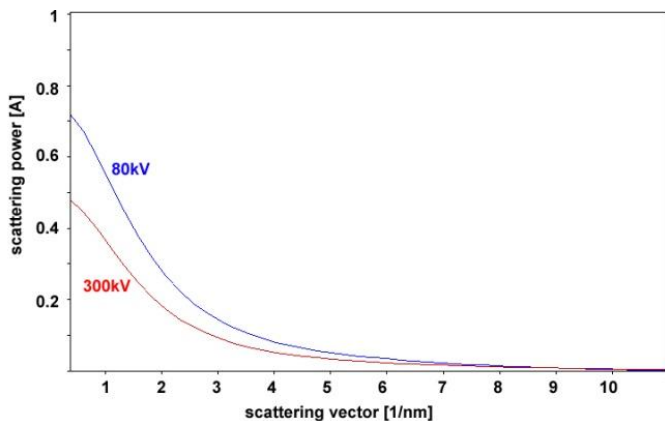
(a)
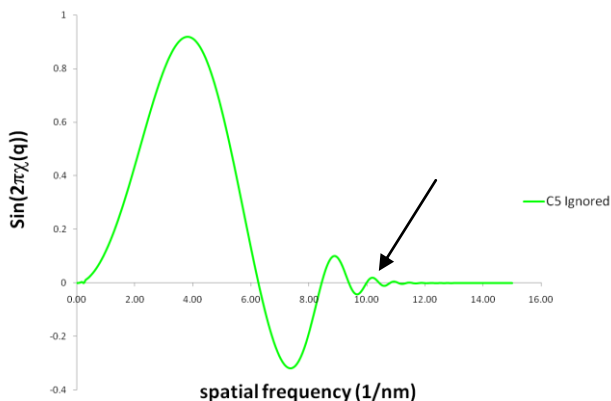
(b)

Figure 6.8 (a) Electron scattering power of carbon at 80kV (blue) vs. 300kV (red) Scattering amplitude of a carbon atom at accelerating voltages of 80 kV and 300 kV were derived from Fourier transform of an exit electron wave. The exit wave of a large unit cell (25nmx25nmx0.3nm) containing a single carbon was calculated using multislice algorithm in ELSTRU software package where Peng-Ren-Dudarev-Whelan electron scattering factors have been chosen. Effect of absorption in scattering amplitudes has been ignored. (b) Calculated PCTF (green curve) of the used microscope setting: 80 kV, defocus = -9 nm, C_S = -0.015 mm, C_C = 1.4 mm, C_5=13.43 mm , ΔE = 0.2eV, focal spread = 2.07 nm. Transfer of information at least up to a resolution of 0.10 nm (see indication).

With those settings the energy spread is now limiting the achievable information limit in a non-chromatic-aberration corrected microscope [20,21] at a spatial resolution above the C-C bond length in graphene of 0.142 nm. In the "rainbow illumination" approach [19], the XFEG gun and monochromator setting leads to a lower energy spread of about 0.2 eV, and therefore the tuned temporal coherence damping envelope of the phase contrast transfer function (PCTF) allows an achievable spatial resolution down to at least 0.10 nm (Figure 6.8b).

6.3.2 Exit-wave reconstruction

The EW reconstruction procedure [4] has been performed using a through focal series of HRTEM images of a graphene layer structure by utilizing FEI's TrueImage package. The images were captured onto a 2k×2k pixel CCD array (Gatan US1000).
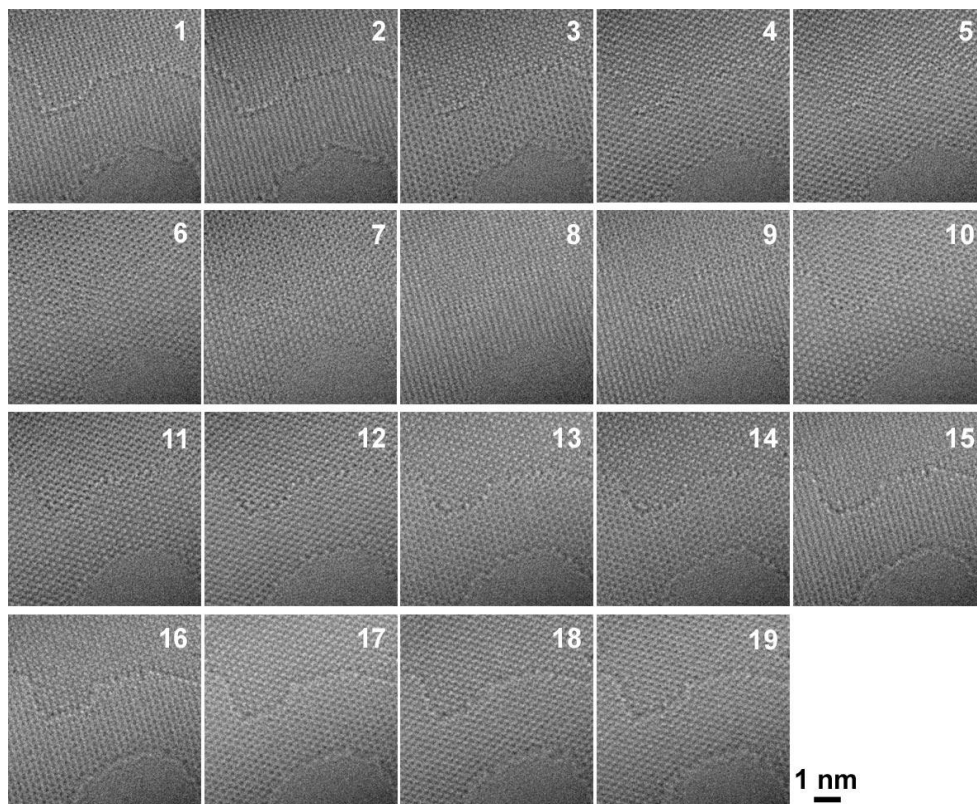

Figure 6.9 Through-focal series of HRTEM lattice images of graphene (19 images, starting defocus Δf = +11 nm, focal step = -1.7 nm)

A short acquisition time of 0.1 sec has been very carefully chosen to fulfill lower dose constraints. This minimizes the possibility of the already less important ionization damage in graphene at 80 kV and sample instabilities. Under fixed TEM beam settings the mean electron count per pixel was about 100 e⁻/pixel (average count per pixel of 800 with a conversation rate of ~ 8 counts per electron of this camera at 80 kV). With a sampling rate of 0.00937 nm/pixels and an exposure time of 0.1 sec, this electron count rate refers to an electron dose rate of ~$1.1 \cdot 10^5$ e⁻/s Å².

The EW reconstruction procedure has been performed using 19 images using same image conditions in a through focal series starting from Δf ~+11 nm and a focal step of about -1.7 nm. As a note: the resulting dose in a series of 19 images (see Figure 6.9) is about 2.2 10^5 e⁻/Å². Taking 100 e⁻/pixel in a single shot and 19 images for reconstructing the complex EW function into account, a *shot noise* estimation [38] for analyzing intensities on the pixel level is about 2.3%.

Contrast features visible in vacuum close to the edge of the single graphene sheet are artefacts, which may result from small differences in edge atom configuration, image quality and image registry between successive frames in the focal series (see Figure 6.9), as well as from the difficulty of recovering the lowest spatial frequency components in the reconstructed phase shift from a defocus series [39] (see later in Figure 6.11). These factors are less likely to influence the reconstructed phase shift away from the specimen edge, and will be discussed in detail elsewhere through comparisons with image simulations.

6.3.3 Image analysis and aberration correction

Each focal series has been analyzed to verify if the imaged structure has not been modified during the experiment. Only the edge-vacuum structure, which we are not analyzing here, is slightly changing. No MTF correction of the camera has been used since the sampling was 0.00937 nm/pixels, and therefore the results did not require this correction.

Complex EW image has been obtained. Thereby, analyses of the expected structure and symmetry as well as the intensity at atom positions in the single graphene sheet region in the EW images have been used to correct for residual aberrations in the iterative reconstruction procedure. Residual aberrations, even present while using an "aberration corrector", can be corrected on the nm level if the complex electron wave is accessible. This residual aberration correction can be done up to the third order [40] by application of a numerical phase plate while reconstructing the complex EW wave function using the professional version of FEI's TrueImage software package.

6.3.4 Image simulation

Intensity differences in HRTEM lattice images and EW functions could lead to various non-unique interpretations. Therefore, our analysis is supported by image simulation of the graphene structure in (001) projection as basis for quantifying values of 'intensities' in EW images.

In detail, through focus series of graphene single/double layer structures have been calculated using the multi-slice algorithm in MacTempas (Total Resolution®) [5]. Simulation parameters have been chosen to match our experimental settings, such as start defocus, focal step, electron dose and S/N in the focal-series (see example images in Figure 6.10).The complex EW function has then been reconstructed by using again FEI's TrueImage package.

It is worth mentioning here that in single HRTEM images in Figure 6.10(a-b) it is not obvious what part of the image depicts single or the double layer graphene. It would even suggest that in the double layer region it would be possible to resolve the C-C dumbbells of a single sheet displayed in Figure 6.10(b). Hence, care is needed to interpret single HRTEM images, and misinterpretation can be avoided by including EW image analysis and image simulation.

---

[5] CrystalKit/MacTempas package. Total Resolution LLC, Berkeley/CA, U.S.A.,
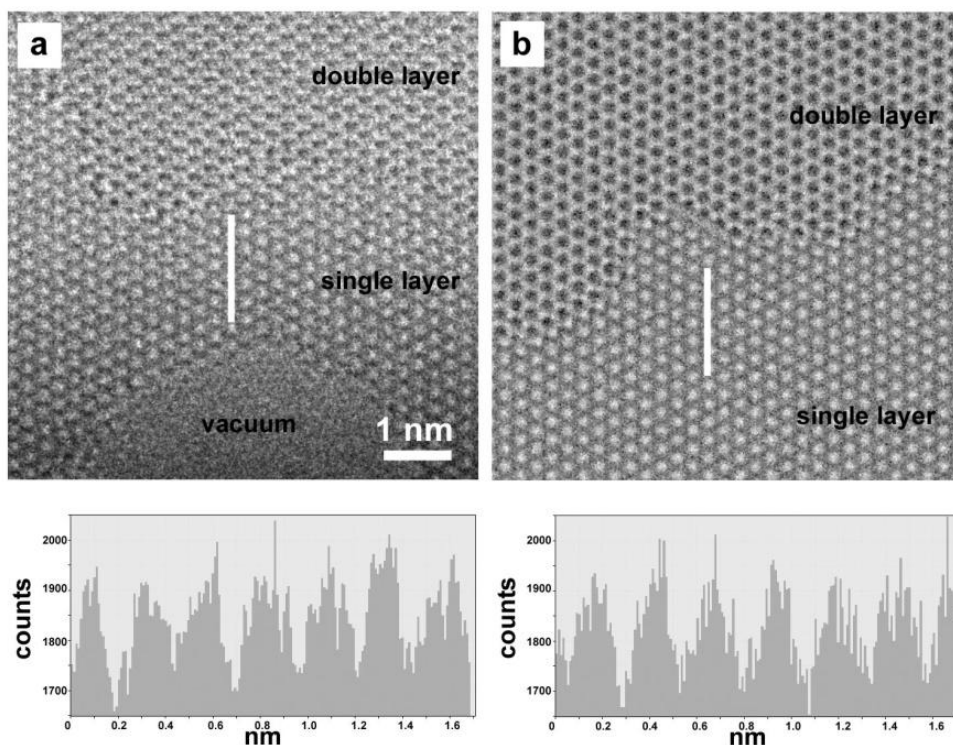http://totalresolution.com

Figure 6.10 HRTEM lattice images of graphene: (a) experimental (image 10 of the focal series – see Figure 6.9), (b) simulated based on multi-slice algorithm. Both are 'taken' at about $\Delta f \sim$ -4nm. Line scans in the lower part show comparable S/N and noise levels between experiment and simulation based on the finding in the single sheet area. However, in the experimental image residual aberrations are present that distort the image (visible in the double layer region).

6.4 Results and discussion

Using a model graphene structure, simplified image in Figure 6.11(a), HRTEM images and EW function simulations, Figure 6.11(b), have also been used to verify that the experimental EW image shows the "correct" graphene pattern at the precise propagated defocus.
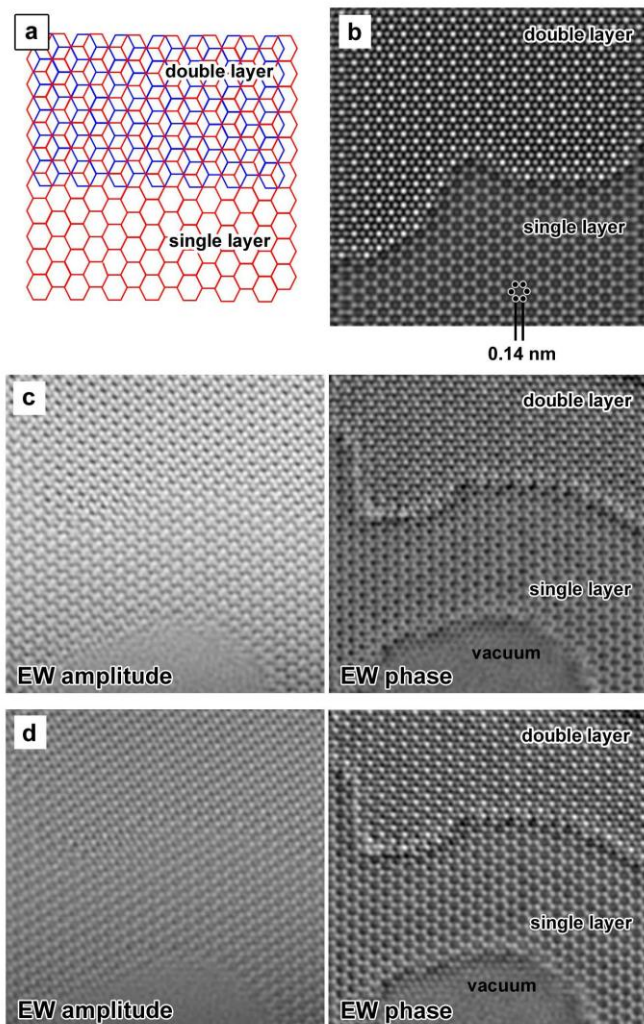
Figure 6.11 EW reconstruction results (a) model graphene structure with a single layer area and a hexagonal-stacked double layer (Bernal stacking) (b) simulated EW phase images of graphene sheet(s) has been obtained by reconstructing it from experiment-matching through-focus series (one image is shown in Figure 6.10(b) based on a single/double layer graphene model structure (c), (d) EW amplitude and phase images of graphene sheet(s): (c) experimental with residual aberrations, (d) experimental with correction of residual aberrations (defocus = 0.3nm , 2-fold astigmatism = 3.0nm (azimuth = 94degree), axial coma = 25.0nm (azimuth = 210degree), 3-fold astigmatism = 35.0nm (azimuth =102degree)) by application of numerical phase plate on complex EW function

The final amplitude and phase images of the EW function, in Figure 6.11(c), still contain minimal residual aberrations - even present when using an "aberration corrector". Since the complex EW is accessible, analysis of the EW images and intensities in the single graphene sheet area have been used to determine the values of the residual aberrations up to the third order [25]. Application of a numerical phase plate in reciprocal space results in EW phase image in Figure 6.11(d) that is in very good agreement with our simulated image in Figure 6.11(b).
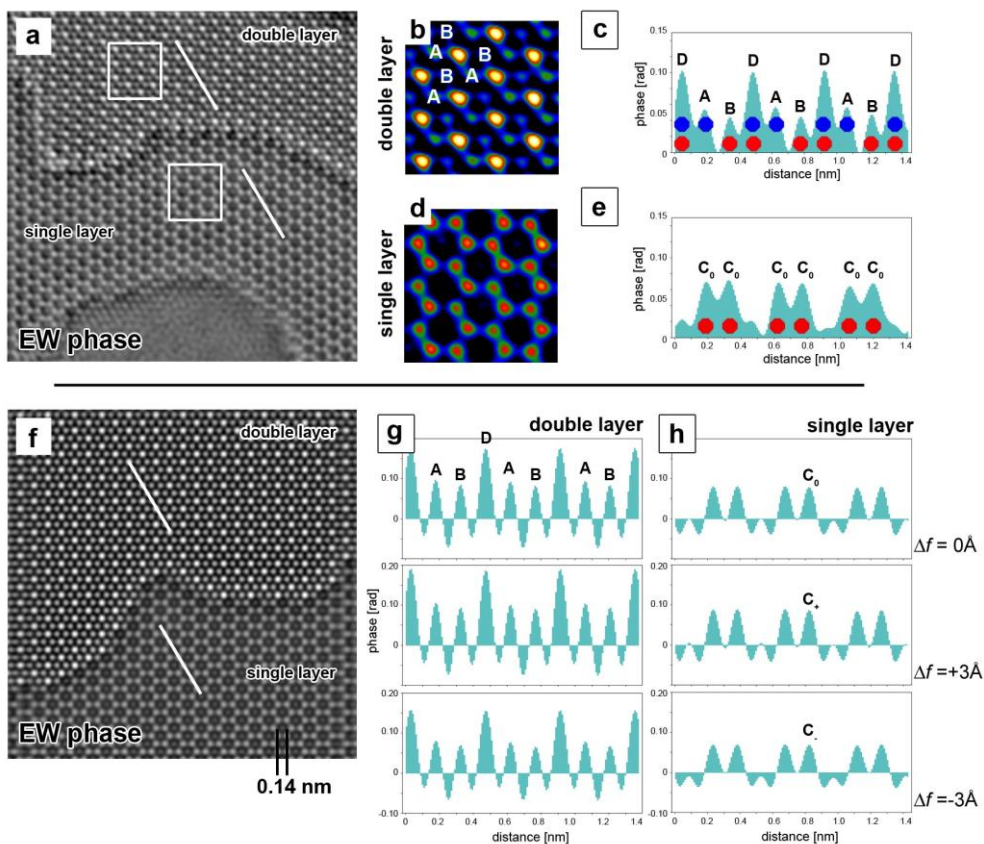

Figure 6.12 (a) experimental EW phase images of graphene sheets – same as Figure 6.11d (right-hand side), (b), (d) higher magnification in RGB colour scale: b – from the double layer area, d – from the single layer area, indicated by "↑" in Figure 6. 5a
(c), (e) line scans of experimental phase image: c – from the double layer area, e – from the single layer area (f) Simulated EW phase image of graphene sheet(s) – same as Figure 6.11b (g,) (h) line scans (as indicated in (f) in "double layer" and "single layer" region) on EW phase images propagated by a defocus of +3 Å and -3 Å.

Both, the experimental and the model-based EW images, in Figures 6.12(a) and 6.12(f) respectively, show the single carbon atoms and two-carbon-atom atomic columns in the hexagonal Bernal-stacked single/double layer graphene. The brightest contrast in the double layer, ergo larger phase shifts, indicates the two-carbon-atom atomic columns, marked as "D" in higher magnification image in Figure 6.12(b). Between these two-carbon-atom columns, the bright features indicate individual single C atoms - either in the first or in the second layer caused by the hexagonal Bernal stacking.

In the EW phase image from the Bernal-stacked double layer region in Figure 6.12(b), the larger phase value at carbon atom position "A" vs. phase value at position "B" is clearly resolved. Also the expected 3-fold symmetry of this atomic arrangement in the different layers "A" and "B" in respect to the two-carbon-atom column positions "D" can be distinguished in Figure 6.12b. The line scan analysis in Figure 6.12(c) confirms this result and reveals an intensity pattern containing three maxima separated by ~0.14 nm, corresponding to the separation between the atomic columns of Bernal-stacked double-layer graphene in (001) projection. The EW phase value of the carbon atom in the second sheet (indexed by "A") is ~9.5% larger than the phase shift caused by the carbon atom in the first sheet (indexed by "B"). This is clearly above the noise level of ~2.3% estimated by *shot noise* considerations (given by the total electron dose) [23]. Analysis of EW function from single sheet region, in Figure 6.12(d), was used to estimate the residual aberration and their influence on the measured phase value for single carbon atoms ("C_0") in the two different graphene sublattices. The line scan analysis in Figure 6.12(e) illustrates that this phase difference is much smaller (~ 0.002rad = noise level) than the phase difference between the two single carbon atoms belonging to the two different layers in the double-layered region (~ 0.010rad).

Line scan analyses, indicated in Figure 6.12(f), on simulated EW phase images reveal that there is a measurable phase difference of 0.014rad between these individual single-carbon-atom "columns", depending on if they are in the second layer ("A" in line scan in Figure 6.12g) or at the same height as the single sheet ("B" in line scan in Figure 6.12g). Those two atom positions are ~0.35nm (3.5Å) different in height in beam direction.

In the line scan analyses seen in Figure 6.12(g,h), propagated EW functions (by +3Å and by -3Å defocus) have been used. The measured phase changes on the carbon atom position in the single sheet area ("C" in line scan in Figure 6.12h) by propagating the EW functions by +3Å and by -3Å is +0.010rad (phase difference between "C_+" and "C_0") and -0.014rad (phase difference between "C_-" and "C_0"), respectively. Thereby it has been verified that the measurable phase difference between the single-C-atom "columns" in the double layer area is caused by a difference of atom position in beam

direction.

It is worth noting that the phase shift by single carbon atoms and two-carbon-atom columns, "D" in line scan in Figure 6.12(c), is almost linear in our experimental single/double layer case. (Further analysis needs to be done to claim this also for few-layer-graphene containing more than 2 sheets). Hence, the complex EW function can be used not only to identify carbon atom positions in 3-D - very important in identifying intrinsic defect structures - but also to chemically identify "doping" of graphene structure, graphene oxide, graphane, and surfaces with different atomic species. This is part of our on-going research.

6.4 Conclusion

The corrected S/TEM optics and the tuned beam coherence allowed us to achieve the required resolution and, more important, the necessary sensitivity in complex exit-wave images at 80kV to perform single carbon atom 3-D imaging. The use of a lower dose setting assured that the needed sensitivity (S/N) to detect the individual carbon atom is achieved limiting e-beam damage on the crystal structure.

Graphene provides an ideal platform for demonstrating the potential of our achievement. The data presented can unambiguously distinguish between single and two atom columns in a double layer of graphene. Dopant of foreign atoms can be excluded by the linearity in the phase shift in the double atom positions. The sensitivity is even sufficient that a phase change caused by single carbon atom positions can be obtained well above the noise level, which clearly quantitatively matches a position height change of 0.35nm in double layers. The presented single atom sensitivity provides an unprecedented view of the atom arrangement in graphene(-based) nanostructures.

This quantitative understanding based on experimentally quantified 3-D atomic positions will finally lead to the long by theoreticians' desired information to predict the properties of the specific carbon-based nanostructures. To the best of our knowledge, this should be generally applicable to other nanomaterials containing light elements, such as "doped" graphene, boron nitride and similar low-dimensional structures.

References

1. Scherzer, O. *Z. Physik,* **101,** 593, (1936)
2. J. Spence, *High Resolution Electron Microscopy*, Oxford University Press (2000)
3. D. Gabor, *Nature,* **161**, 777, (1948)
4. Coene, W et al., *Phys. Rev. Lett.,* **69,** 3743 (1992)
5. H. Lichte et al, *Ultramicroscopy*, **54** 310 (1994)
6. M. Haider et al*., Nature* **392,** 768 (1998)
7. B. Kabius et al., *J. of Elec. Micro.*, **21** 1 (2009)
8. J. Cowley, *Diffraction Physics*, Elsevier Press (1995)
9. P.Buseck, J. Cowley, L. Eyring, *High Resolution Electron Microscopy and Associated Techniques*, Oxford University Press (1992)
10. D. Typke et al., *Optik*, **99** 155 (1995)
11. O. Scherzer, *J. Appl. Phys.*, **20** 20 (1948)
12. C.L. Jia et al., *Science,* **299** 870 (2003).
13. O. Scherzer, *Berichte der Bunsengesellschaft für physikalische Chemie*, **74**, 1154 (1970)
14. L.Y. Chang et al., *Ultramicroscopy*, **106** 301 (2006)
15. M. Lentzen, *Microsc. & Microanal.*, **14** 16 (2008)
16. R. Erni, *Intro. to Aberration Corrected TEM*, Imperial College Press (2009)
17. L.Reimer, *Transmission Electron Microscopy: Physics of Image Formation*, Springer (2008)
18. W. Brian et al. *J of Appl. Phys.*, **90**, 3509 (2001)
19. B. Freitag et al. *Ultramicroscopy*, **102** 205 (2005)
20. Discussion with Dr. M. Bischoff
21. K.S. Novoselov et al., *Science*, **306** 666 (2009)
22. K.S. Novoselov et al., Nature, **438** 197 (2005)
23. A.H. Castro et al., *Reviews of Modern Physics* , **81** 109 (2009)
24. Y-M Lin et al., *Science*, **347** 662 (2010)
25. M. Haider et al., *Ultramicrosopy*, **108** 167-78. 2008
26. S. Iijima et al. *Nature*, **363** 603 (1993)
27. B.W. Smith et al., *Nature*, **396** 323 (1998)
28. R. Erni et. al., *Microsc & Microanal.*, **12** 492 (2006)
29. R. R. Meyer et al., *Science*; **289** 1324 (2000)
30. J.C. Meyer, et al., *Nano Letters*; **8** 3582 (2008)
31. C.O. Girit et al., *Science*, **323** 1705 (2009)
32. J.R. Jinschek et al., *Ultramicroscopy*, **108** 589 (2008)

33. J. Sloan et al., *Acc Chem Res,* **35** 1054 (2002)
34. J.R. Jinschek et al., *Proceedings of SPIE*, 54 (2004)
35. L. G. Cervera et. al., *Angewandte Chemie Int. Ed.*, **46** 3685 (2007)
36. A. Zobelli et al., *Phys Rev B,*; **75** 2454 (2007)
37. J. Barthel, et al., *Phys Rev Let*; **101** 200801 (2008)
38. P. Bevington, D.K. Robinson, *Data Reduction and Error Analysis for the Physical Sciences*, McGraw-Hill (2002)
39. C. T. Koch, *Ultramicroscopy,* **108** 141 (2008)
40. A Thust et al., *Ultramicroscopy*, **64** 249 (1996)

Summary

Low-dimensional structures

Low-dimensional structures have the property that their structures extend over fever than three dimensions. This may be because their shape is a sheet e.g. two dimensional graphene or BN-like) or a chain (one-dimensional molecules), or because they exist as interfaces (in thin films or in precipitate/matrix systems) or surface layer, or as defects (line or point defects such as dislocations and vacancies).

Such structures have often electronic, magnetic and mechanical properties that are different and sometimes better than their bulk counterparts, which make them key components for novel technological applications. Their properties are controlled by the organization of the atoms within them. Therefore characterization with the highest possible detail is an important step for establishing their structure-property relationships. High Resolution Tranmission Electron Microscopy (HRTEM) techniques are very useful for providing structural details at atomic resolution. When combined with electron energy loss spectrometers, chemical information at atomic resolution can also be obtained. HREM has been successfully applied to characterize defect structures in nanoprecipitates and at interface in precipitate/matrix systems and organizations of atoms in nanotubes/rods, graphene structures and nanoparticle systems.

The importance and impact of HREM

The work in this thesis benefited from the advances in transmission electron microscopy that have been achieved in the last decade. A key breakthrough for TEM imaging came with the introduction of spherical aberration correctors for the objective lens, electron monochromators and the enhanced stability of mechanical and electronic components. Spherical aberration correctors can be used to push the Scherzer resolution close to the information limit of the microscope and also reduce delocalization in HRTEM images. Correction of spherical aberration of the objective lens results not only in sub-Ångstrom resolution but also greatly improved precision in the measurement of atom positions and greater phase sensitivity in the recorded electron exit wave. For, High Resolution-Scanning Transmission Electron Microscopy (HRSTEM) the impact is bigger since atom positions in images can be directly deduced.

This thesis describes method development in TEM-related techniques and their application to the study of nanoprecipitates and low-dimensional structures. The work is divided into two parts.

- The first part is focused on the structures of nanoprecipitates found in Al-Co, Al-Ni and Al-Fe-Zr alloys.
- The second part describes the effect of accelerating voltage and its direct impact on image formation in different materials including the application of low acceleration voltages to the imaging of graphene single/double sheets quantitatively.

In Chapter 1, general information is given about the materials studied in this thesis and on the experimental methods used focusing on transmission electron microscopy techniques.

Chapter 2 contains the results of a study of precipitates in Al-Co. By using non-aberration corrected HRTEM and nano-beam electron diffraction, Al-Co alloys were examined and fine precipitates of Al_9Co_2 phase identified. These precipitates have plate-like shapes. At an early stage of annealing they are confined to only a few {200} Al planes and are coherent with the Al matrix. If the annealing temperature is increased, these planar precipitates grow and turn into plate-like precipitates with semi-coherent interfaces.

In Chapters 3 and 4 a study of binary Al-Ni alloys and the structure of Al_9Ni_2 plate-like precipitates using nano beam electron diffraction, HRTEM and HRSTEM is reported. The Al_9Ni_2 precipitates are identified from nano beam electron diffraction patterns acquired on different precipitates, by tilting each selected precipitate to obtain diffraction patterns at different zone axes. Electron diffraction patterns obtained in this way from nanoprecipitates contain more information than selected area diffraction patterns. At an early stage of annealing, the Al_9Ni_2 precipitates have plate-like morphologies (similar to Al_9Co_2 precipitates) and are coherent with the matrix. As the annealing temperature increases, the precipitates lose coherency, develop semi-coherent interfaces with the matrix and are often found to contain defects. These faults can be planar or more ordered, similar to well defined twin and twist structures. The structures of the defects were modeled using supercells that contain twist and twin interfaces, using interatomic distances between Al and Ni atoms found in Al-rich AlNi intermetallics. Twin and twist models were tested and atom positions in the models were refined with ab-initio Density Functional Theory (DFT) calculations. The calculations showed that the defect models have realistic interface energies comparable to similar twin interface structures in metals and intermetallics. Neither Aberration-corrected nor conventional, HRTEM images of very small strained plate-

like precipitates with a sample thickness of 20-30 nm are directly interpretable to retrieve structural information. Thickness and strain factors also hinder the use of quantitative high-resolution electron microscopy techniques such as exit wave reconstruction to deduce interface structure from reconstructed electron exit waves. The quantitative interpretation of electron diffraction patterns obtained from the precipitates is difficult and did not yield reliability factors that were low enough for successful structure refinement. The main limitation was small plate thickness and the presence of defects which caused strong streaking in electron diffraction patterns and made it difficult to extract reliable electron diffraction intensities. Under these conditions it was only possible to infer a rough model structure for Al_9Ni_2 phase. HRSTEM imaging and ab-initio DFT calculations proved to be very successful with HRSTEM providing direct access to transition metal positions and DFT calculations refining the Al and Ni atom positions.

In Chapter 5, a detailed study of precipitation in a ternary Al-Fe-Zr alloy is reported. Here, in contrast reports in the literature, the experiment was designed and performed on alloys where both Fe and Zr were present in the solid solution prior to precipitation. Meta-stable cubic $L1_2$-Al_3Zr matrix precipitates and $Al_{13}Fe_4$ and $Al_9(Fe,Ni)_2$ intermetallic particles were observed after annealing the supersaturated solid solution. $L1_2$-Al_3Zr precipitates were found to nucleate homogenously within the matrix (at 573 K) and heterogeneously on dislocations (at 698 K). Heterogeneously-nucleated $L1_2$-Al_3Zr particles have more rounded shapes compared to homogenously nucleated ones and are found to contain planar faults. These planar faults were identified to comprise unit cell of the tetragonal $D0_{23}$-Al_3Zr structure. Formation of the tetragonal phase is associated with dislocations creating anti-phase boundaries during growth of the precipitate. The presence of this structure provides proof for the rapid coarsening behavior of heterogeneously-nucleated $L1_2$-Al_3Zr precipitates and eventually of the transformation to undesired tetragonal $D0_{23}$-Al_3Zr particles, as reported in the literature. Apart from Al_3Zr matrix precipitates, $Al_{13}Fe_4$ precipitates containing some Zr were also observed in the samples annealed at 573 K. Incorporation of Zr into the $Al_{13}Fe_4$ structure was observed to cause the $Al_{13}Fe_4$ unit cell to enlarge by about 0.6%. Interestingly, secondary precipitation of a metastable cubic Al_3Zr phase was discovered on $Al_{13}Fe_4$ and $Al_9(Fe,Ni)_2$ intermetallics. The formation mechanisms and shapes of the secondary precipitates are explained on the basis of the shapes of $Al_{13}Fe_4$ and $Al_9(Fe,Ni)_2$ precipitates and on the interface structure. Structural details of the interface between the secondary $L1_2$-Al_3Zr precipitates and $Al_{13}Fe_4$, studied by aberration-corrected HRSTEM, were reported. $L1_2$-Al_3Zr phase found to be aligned with the **b** direction of $Al_{13}Fe_4$ phase. The interface between these two phases is sharp and coherent. However the network of Fe pentagons in $A_{l13}Fe_4$ structure near the interface is elongated towards Al_3Zr. A supercell containing the interface was constructed based on HRSTEM images and

interatomic distances between Fe-Zr atoms. The model was compared with HRSTEM simulations.

Chapter 6 consists of two parts. In the first part, HRTEM imaging at lower electron acceleration voltages is discussed. The effect of accelerating voltage on information transfer and image contrast is illustrated using image simulations. The use of an electron gun monochromator and an aberration-corrector make it possible to study materials that are affected by 300 kV electrons through knock-on damage with a spatial resolution better than 0.1 nm. The second part of the chapter is devoted to quantitative HRTEM imaging of single/double graphene sheets at 80kV. The experimental conditions and methodology for imaging graphene structure with high phase sensitivity where C-C distance of 0.14 nm A is directly resolved, are described. Using the phase of the reconstructed electron exit wave a quantitative analysis of the atomic positions in single/double layer sheets is reported.

Samenvatting

Karakterisering van laag-dimensionale structuren met geavanceerde transmissie-elektronenmicroscopie.

Laag-dimensionale structuren

Laag-dimensionale structuren hebben een dimensie kleiner dan drie. Dit is het geval voor structuren in een vlak (bijvoorbeeld enkellaags grafeen of BN-achtig) of een ketting (één-dimensionale moleculen) en in het geval van grensvlakken (een dunne film of een precipitaat/matrix systeem) of defecten (dislocaties of vacatures).

Zulke structuren vertonen vaak superieure elektronische, magnetische of mechanische eigenschappen vergeleken met bulkmateriaal, waardoor ze als componenten kunnen dienen in nieuwe technologische toepassingen. Deze eigenschappen worden bepaald door de rangschikking van de atomen in de structuur. De bepaling van die rangschikking is dus van primair belang om de structuur/eigenschap relatie vast te stellen. Hoge-Resolutie Transmissie Elektronenmicroscopie (HRTEM) technieken kunnen kleinere structuren dan de afstanden van de atomen zichtbaar gemaakt worden. Tevens kan chemische informatie op atomair niveau verkregen worden, indien gecombineerd met elektronen-energieverlies spectroscopie. HRTEM is succesvol toegepast op de organisatie van atomen in bovengenoemde laag-dimensionale structuren en ook in bijvoorbeeld nanodeeltjes en nanobuizen.

De invloed van HREM

Het werk beschreven in dit proefschrift is gebaseerd op de vooruitgang in de transmissie-elektronenmicroscopie in het laatste decennium. Een doorbraak in deze vooruitgang kwam tot stand met het gebruik van sferische aberratiecorrectoren voor de objectieflens, elektronen monochromatoren en de verbeterde stabiliteit van elektronische en mechanische componenten. Sferische aberratiecorrectoren kunnen worden gebruikt om de Scherzer resolutie dicht bij de informatielimiet van een microscoop te brengen en ook om delocalisatie in HRTEM beelden te verminderen. Op deze manier wordt zowel sub-Ångström resolutie bereikt als verbeterde plaatsbepaling van atomen en verhoogde gevoeligheid in de geregistreerde uitgaande golf van de elektronen. Voor Hoge-Resolutie Scanning Transmissie elektronenmicroscoop (HRSTEM) beelden is de invloed van sferische aberratiecorrectoren nog groter waardoor de atoom posities direct uit de beelden bepaald kunnen worden.

Dit proefschrift beschrijft de methoden ontwikkeling van TEM gerelateerde technieken en hun toepassing op de bestudering van nanoprecipitaten en laag-dimensionale structuren. Het werk is onderverdeeld in twee delen:

- Het eerste deel behandelt de structuurbepaling van nanoprecipitaten in Al-Co, Al-Ni en Al-Fe-Zr legeringen.
- Het tweede deel beschrijft de invloed van de versnelspanning op de beeldvorming van verschillende materialen, inclusief de toepassing van een lage versnelspanning op het afbeelden van enkel- en dubbellaags grafeen op een kwantitatieve manier.

In hoofdstuk 1 wordt algemene informatie gegeven over de bestudeerde materialen in dit proefschrift en de gebruikte experimentele methoden met de nadruk op HR(S)TEM technieken.

Hoofdstuk 2 bevat de resultaten van een studie van precipitaten in Al-Co met niet aberratie gecorrigeerde HRTEM beelden en nano-bundel-diffractie. Kleine plaatvormige precipitaten met de Al_9Co_2 fase werden geïdentificeerd. Tijdens de eerste fase van een gloeibehandeling beperken deze precipitaten zich tot slechts enkele {200} Al vlakken en zijn ze coherent met de Al matrix. Met toenemende gloeitemperatuur groeien ze uit tot plaatvormige precipitaten met semi-coherente grensvlakken met de matrix.

In de hoofdstukken 3 en 4 wordt onderzoek naar binaire Al-Ni legeringen en de structuur van plaatvormige Al_9Ni_2 precipitaten beschreven, waarbij gebruik gemaakt wordt van nano-bundel-elektronendiffractie, HRTEM en HRSTEM. De Al_9Ni_2 fase werd geïdentificeerd   door analyse van nano-bundel-elektronendiffractiepatronen afkomstig van verschillende precipitaten. Door middel van kanteling van het precipitaat werd de gewenste zone-as ingesteld. De op deze wijze verkregen elektronen-diffractiepatronen bevatten meer informatie dan *geselecteerd-gebied* diffractiepatronen. Tijdens de eerste fase in een gloeibehandeling zijn de Al_9Ni_2 precipitaten plaatvormig (net als Al_9Co_2 precipitaten) en coherent met de matrix. Met toenemende gloeitemperatuur verliezen de precipitaten coherentie, ontwikkelen semi-coherente grensvlakken met de matrix en bevatten vaak defecten. Deze fouten kunnen zich voordoen als vlakken of als meer geordende structuren, zoals de goed beschreven tweeling- en draaistructuren. De structuren van de defecten werden beschreven met behulp van supercellen, die draai- en tweelinggrensvlakken bevatten, gebruikmakend van de atoomafstanden tussen Al en Ni in AlNi intermetallische verbindingen, die rijk zijn aan Al. Zowel tweeling als draaimodellen werden getest. Van alle modellen werden de atoomposities verfijnd met behulp van *ab-initio* Density Functional Theory (DFT) berekeningen. De berekeningen lieten zien dat de modellen van de defecten een realistisch grensvlak weergeven welke vergelijkbaar zijn met tweelinggrensvlakstructuren van metalen en intermetallische verbindingen. Noch aberratie gecorrigeerde noch conventionele HRTEM beelden van zeer kleine opgerekte plaatvormige precipitaten met een monsterdikte van 20-30 nm leveren direct informatie over de structuur op. Factoren als monsterdikte en oprekking hebben een negatieve invloed bij het gebruik van hoge-resolutie elektronenmicroscopietechnieken, zoals reconstructie van de uitgaande golf om het grensvlak te beschrijven. De kwantitatieve interpretatie van elektronendiffractiepatronen, verkregen uit de precipitaten, is moeilijk en resulteerde

niet in R-waarden die laag genoeg waren voor een succesvolle structuurverfijning. De voornaamste beperking was de geringe dikte van de platen en de aanwezigheid van defecten, die een sterke uitsmering van het diffractiepatroon veroorzaakten. Hierdoor was het moeilijk om betrouwbare diffractie intensiteiten te bepalen. Onder deze omstandigheden was het slechts mogelijk om een ruw structuurmodel voor de Al_9Ni_2 fase te bepalen. HRSTEM afbeeldingen en *ab-initio* DFT berekeningen bleken erg succesvol, HRSTEM voor het direct bepalen van de transitiemetaalposities en DFT berekeningen voor het verfijnen van de Al- en Ni-atoomposities.

In hoofdstuk 5 wordt een gedetailleerd onderzoek beschreven naar de precipitatie van een ternaire Al-Fe-Zr legering. In dit geval, anders dan in de literatuur wordt beschreven, werden de experimenten ontworpen en uitgevoerd met behulp van legeringen waar zowel Fe en Zr in de matrix opgelost waren voorafgaande aan de precipitatie. Meta-stabiele kubische $L1_2$-Al_3Zr matrix precipitaten en $Al_{13}Fe_4$ deeltjes werden waargenomen na het gloeien van de superverzadigde oplossing. Er werd gevonden dat $L1_2$-Al_3Zr precipitaten homogeen groeiden in de matrix (bij een temperatuur van 573K) en heterogeen bij dislocaties (bij een temperatuur van 698K). Heterogeen gegroeide $L1_2$-Al_3Zr deeltjes hebben een meer ronde vorm vergeleken met de homogeen gegroeiden. De heterogeen gegroeide precipitaten bevatten vlakke defecten. Vlakke defecten bleken de eenheidscel van tetragonaal $D0_{23}$-Al_3Zr te bevatten. De vorming van de tetragonale fase wordt in verband gebracht met dislocaties, die tijdens het groeien van de precipitaten anti-fasegrenzen creëren. De aanwezigheid van deze structuur verklaart de snelle groei van heterogeen gegroeide $L1_2$-Al_3Zr precipitaten en het eventueel omvormen tot de ongewenste tetragonale $D0_{23}$-Al_3Zr deeltjes, zoals al beschreven is in de literatuur. Behalve in de Al_3Zr matrixprecipitaten, werd ook enig Zr gevonden in de $Al_{13}Fe_4$ precipitaten in de monsters die gegloeid waren bij een temperatuur van 573K. Insluiting van Zr in de $Al_{13}Fe_4$ structuur veroorzaakte een vergroting van de eenheidscel met ongeveer 0.6%. Interessant was dat er secundaire precipitaten bestaande uit de meta-stabiele kubische Al_3Zr fase ontdekt werden in de $Al_{13}Fe_4$ en de $Al_9(Fe,Ni)_2$ intermetallische verbindingen. De vormingsmechanismen en de vorm van de secundaire precipitaten worden verklaard aan de hand van de vormen van de $Al_{13}Fe_4$ en de $Al_9(Fe,Ni)_2$ precipitaten en de structuur van de grenslaag. Details van de structuur van de grenslaag tussen de secundaire $L1_2$-Al_3Zr precipitaten en $Al_{13}Fe_4$ werden bestudeerd met behulp van aberratie-gecorrigeerde HRSTEM. De $L1_2$-Al_3Zr fase bleek gericht te

zijn langs de b-as van de $Al_{13}Fe_4$ fase. De grenslaag tussen deze twee fasen is scherp en coherent. Het netwerk van Fe-pentagons in de $Al_{13}Fe_4$ structuur vlak bij de grenslaag is echter uitgerekt in de richting van Al_3Zr.

Hoofdstuk 6 bestaat uit twee delen. In het eerste deel wordt de HRTEM afbeelding bij lagere elektronenversnelling besproken. Het effect van de versnelspanning op de informatie overdracht en beeldcontrast wordt geïllustreerd aan de hand van beeldsimulaties. Het gebruik van een monochromator bij de elektronenbron en een aberratiecorrector maken het mogelijk om materialen te bestuderen die schade oplopen door botsingen met 300 keV elektronen. De ruimteresolutie is hierbij beter dan 0.1nm. Het tweede deel van het hoofdstuk is gewijd aan kwantitatieve HRTEM afbeeldingen van enkel/dubbellaags grafeen met behulp van 80 keV elektronen. Experimentele condities en methodes worden beschreven om de grafeenstructuur af te beelden, met voldoende gevoeligheid in de fase van de uitgaand golf voor oplossing van de C-C afstand van 0.14nm. Gebruikmakend van de fase van de gereconstrueerde uitgaand golf wordt een kwantitatieve analyse van de atoomposities in enkel/dubbellaags grafeen beschreven.

Dankwoord

Work presented in this thesis is a result of several years of effort and dedication and it would not be possible if without the understanding, inspiration and teaching of Prof. Henny Zandbergen whom hereinafter I call my Ph.D. father.

Jörg, your support and guidance in various areas my career was very crucial and I really appreciate it.

Wim, you, never give up on me and kept pushing me to complete. Teşekkür ederim.

Dong and Steve you allow enough time for me to complete my Ph.D and I cannot find words to match how thankful I am to you.

Special thanks go to Dr. Vasili Sechnikov and Tom R. de Kruijff teaching me the art of specimen preparation for transmission electron microscopy.

My special gratitude and thanks go to;

> Dr Jouk Jansen for helping with crystallography and our discussions on scientific and various non-scientific topics,
>
> Dr. Frans Tichelaar for his patience support during the problems I experience with microscopes,
>
> Dr. Bert Freitag, for inspiring me with his huge enthusiasm,
>
> Dr. Qiang Xu for our in depth discussions on various subjects and helping with the final stage of my thesis,
>
> Prof. Jiang Hua Chen for his introduction me to high resolution electron microscopy,
>
> Dr. Marijn van Huis for his help with DFT calculations,

Curriculum Vitae

Emrah Yücelen was born on April 27, 1978 in Istanbul, Turkey. He received his bachelor degree from Istanbul Technical University and Master degree from Christian-Albrechts University of Kiel, in 1999 and 2002 respectively, majoring in Materials Science and Engineering. Between January 2002 and December 2006, he worked as a research engineer for the Netherlands Institute of Metals Research. He has been employed for FEI Electron Optics BV as a research scientist, since 2007. Between January 2008 and July 2011 he was a Ph.D candidate at the National Center for High Resolution Electron Microscopy, Kavli Institute of NanoScience at the Delft University of Technology, Delft, The Netherlands, carrying out research on characterization of low-dimensional structures by transmission electron microscopy.

Publications

1. Paper in preparation, 'Detailed TEM Study of precipitates and particles formed in dilute Al-Ni alloys'.

2. Paper in preparation, 'Structure of Al_9Ni_2 precipitates in Al-Ni alloys'.

3. Paper in preparation 'TEM Study of decomposition of Al-Zr alloy in the presence of Fe and Ni'.

4. Chapter 6 was partly published in

   - Joerg R. Jinschek, Emrah Yucelen, Bert Freitag, Hector A. Calderon, Andy Steinbach *Microscopy Today*, Volume19, Issue 03 May 2011, pp 10 – 14.
   - J.R. Jinschek, E. Yucelen, H.A. Calderon, B. Freitag, Carbon, Volume 49, Issue 2, February 2011, Pages 556-562.